frontiers | Research Topics

Calculation and design of two-dimensional thermoelectric and piezoelectric materials

Edited by
San-Dong Guo, Guangzhao Wang, Yee Sin Ang and Huabing Yin

Published in
Frontiers in Physics
Frontiers in Materials
Frontiers in Chemistry

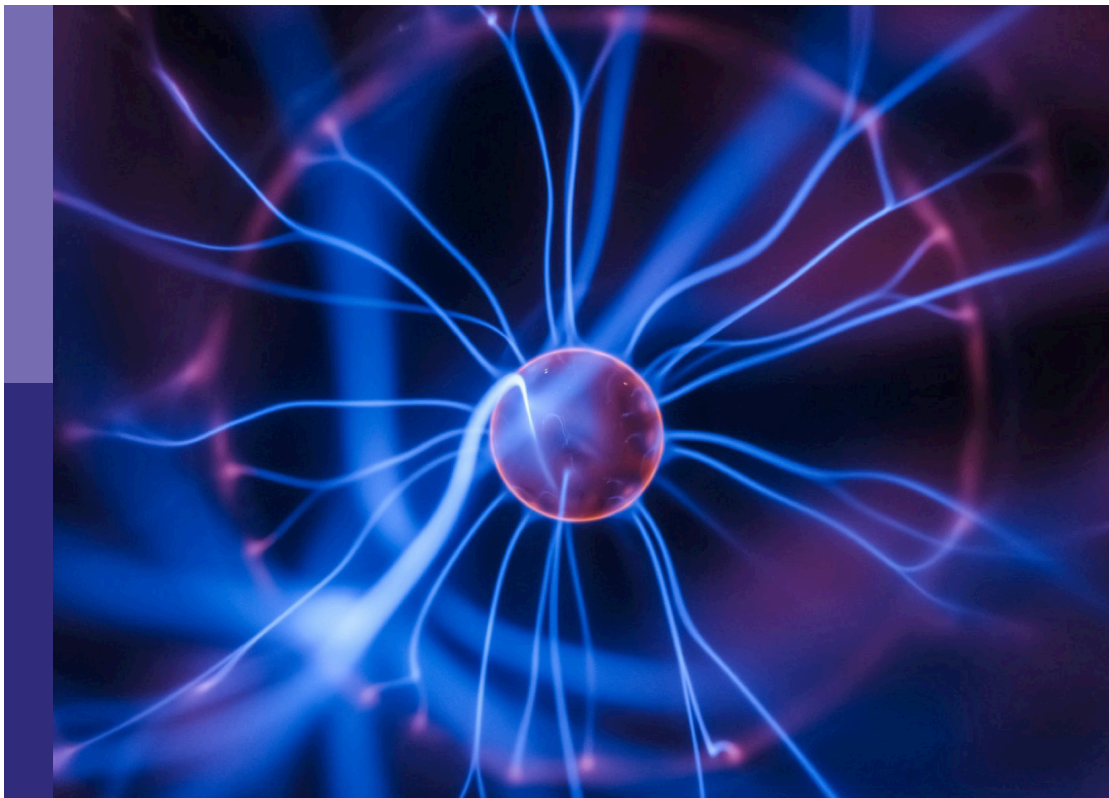

ISSN 1664-8714
ISBN 978-2-8325-3163-1
DOI 10.3389/978-2-8325-3163-1

About Frontiers

Frontiers is more than just an open access publisher of scholarly articles: it is a pioneering approach to the world of academia, radically improving the way scholarly research is managed. The grand vision of Frontiers is a world where all people have an equal opportunity to seek, share and generate knowledge. Frontiers provides immediate and permanent online open access to all its publications, but this alone is not enough to realize our grand goals.

Frontiers journal series

The Frontiers journal series is a multi-tier and interdisciplinary set of open-access, online journals, promising a paradigm shift from the current review, selection and dissemination processes in academic publishing. All Frontiers journals are driven by researchers for researchers; therefore, they constitute a service to the scholarly community. At the same time, the *Frontiers journal series* operates on a revolutionary invention, the tiered publishing system, initially addressing specific communities of scholars, and gradually climbing up to broader public understanding, thus serving the interests of the lay society, too.

Dedication to quality

Each Frontiers article is a landmark of the highest quality, thanks to genuinely collaborative interactions between authors and review editors, who include some of the world's best academicians. Research must be certified by peers before entering a stream of knowledge that may eventually reach the public - and shape society; therefore, Frontiers only applies the most rigorous and unbiased reviews. Frontiers revolutionizes research publishing by freely delivering the most outstanding research, evaluated with no bias from both the academic and social point of view. By applying the most advanced information technologies, Frontiers is catapulting scholarly publishing into a new generation.

What are Frontiers Research Topics?

Frontiers Research Topics are very popular trademarks of the *Frontiers journals series*: they are collections of at least ten articles, all centered on a particular subject. With their unique mix of varied contributions from Original Research to Review Articles, Frontiers Research Topics unify the most influential researchers, the latest key findings and historical advances in a hot research area.

Find out more on how to host your own Frontiers Research Topic or contribute to one as an author by contacting the Frontiers editorial office: frontiersin.org/about/contact

Calculation and design of two-dimensional thermoelectric and piezoelectric materials

Topic editors

San-Dong Guo — Xi'an University of Posts and Telecommunications, China
Guangzhao Wang — Yangtze Normal University, China
Yee Sin Ang — Singapore University of Technology and Design, Singapore
Huabing Yin — Henan University, China

Citation

Guo, S.-D., Wang, G., Ang, Y. S., Yin, H., eds. (2023). *Calculation and design of two-dimensional thermoelectric and piezoelectric materials*. Lausanne: Frontiers Media SA. doi: 10.3389/978-2-8325-3163-1

Table of contents

frontiers | Frontiers in Physics

TYPE Editorial
PUBLISHED 21 July 2023
DOI 10.3389/fphy.2023.1244195

OPEN ACCESS

EDITED AND REVIEWED BY
Malgorzata Biczysko,
Shanghai University, China

*CORRESPONDENCE
Guangzhao Wang,
wangyan6930@yznu.edu.cn
San-Dong Guo,
sandongyuwang@163.com
Yee Sin Ang,
yeesin_ang@sutd.edu.sg

†These authors have contributed equally to this work

RECEIVED 22 June 2023
ACCEPTED 12 July 2023
PUBLISHED 21 July 2023

CITATION
Wang G, Yin H, Guo S-D and Ang YS (2023), Editorial: Calculation and design of two-dimensional thermoelectric and piezoelectric materials.
Front. Phys. 11:1244195.
doi: 10.3389/fphy.2023.1244195

Editorial: Calculation and design of two-dimensional thermoelectric and piezoelectric materials

Guangzhao Wang[1*†], Huabing Yin[2†], San-Dong Guo[3*] and Yee Sin Ang[4*]

[1]Key Laboratory of Extraordinary Bond Engineering and Advanced Materials Technology of Chongqing, School of Electronic Information Engineering, Yangtze Normal University, Chongqing, China, [2]Institute for Computational Materials Science, School of Physics and Electronics, Henan University, Kaifeng, China, [3]School of Electronic Engineering, Xi'an University of Posts and Telecommunications, Xi'an, China, [4]Science Mathematics and Technology Cluster, Singapore University of Technology and Design, Singapore, Singapore

KEYWORDS

thermoelectricity, piezoelectricity, magnetism, topology, photocatalysis

Editorial on the Research Topic
Calculation and design of two-dimensional thermoelectric and piezoelectric materials

Introduction

Two-dimensional (2D) materials have been widely applied in various fields from science to engineering due to their fascinating physical and chemical properties [1–3]. 2D thermoelectric/piezoelectric materials could directly convert thermal/mechanical energy into electrical energy, which could solve the energy problems and relieve environmental pollution. Though the thermoelectric or piezoelectric properties of a large amount 2D materials including graphene, hexagonal boron nitride, arsenene, metal carbides and nitrides (MXenes), and transition metal dichalcogenides (TMDs) have been detailedly investigated, these performance has not yet met the requirements for commercial applications. Usually, the thermoelectric/piezoelectric properties could be improved by developing 2D material, doping, straining engineering, chemical functionalization, *etc.* [4–7] Furthermore, some novel physical properties including magnetism, topology, and valley may appear in some 2D materials. The combination of thermoelectricity/piezoelectricity with other unique properties may lead to novel device applications or scientific breakthroughs in new physics. Combining the advantages of thermoelectricity/piezoelectricity with other unique properties may result in new physical breakthroughs or novel device applications. Thus, designing and developing novel thermoelectric/piezoelectric materials is full of significance.

In this Research Topic "*Calculation and design of two-dimensional thermoelectric and piezoelectric materials*," we have collected a total of 13 articles including the recent progress

in thermoelectricity, magnetism, topology, photocatalysis, and noise reduction. Next, we briefly summarize the research highlights about these fascinating studies.

Thermoelectricity

The thermoelectric effect could convert mechanical energy into electrical energy, thus providing a considerable solution to address environmental and energy issues. With the help of first-principles calculations and Boltzmann transport theory, Li et al. predicted the electronic and thermoelectric properties of pentagonal PdX_2 (X = Se, Te) monolayers (MLs). The maximum thermoelectric figure of merit (ZT) reaches 6.6 (or 4.4) for p-type (or n-type) $PdTe_2$, which is a potential thermoelectric candidate. Yin et al. theoretically predicted 2D $TlInSe_3$ to be a promising thermoelectric material with a high ZT value of 4.15 at 500 K. Cui et al. explored the thermal properties of biphenylene by non-equilibrium molecular dynamics calculations, and they found that the thermal conductivity of biphenylene is isotropic and sensitive to size and temperature. The graphene/biphenylene lateral heterojunction possesses an interface thermal conductance of about 2.84×10^9 $WK^{-1}m^{-2}$. Furthermore, the interface thermal conductance could be obviously tuned by strain.

Magnetism

2D ferromagnetic and antiferromagnetic materials provides a novel platform for the application of spintronics. Tu et al. summarized the recent progress of 2D intrinsic Cr-based ferromagnetic semiconductors from the theoretical perspective, and showcased the importance of first-principles calculations in designing new 2D ferromagnetic semiconductors. Wang et al. summarized the magnetic, electronic, topological, spin-transport properties, and potential applications of a series of spin-gapless semiconductors including 2D oxalate-based metal-organic frameworks (MOFs), Fe_2I_2 ML, Cr_2X_3 (X = S, Se, and Te) ML, $CrGa_2Se_4$ ML, HK Mn-cyanogen lattice, MnNF ML, and Fe_4N_2 pentagon crystal. Kang et al. found that $Cr_2Ge_2Te_6$ switches from semiconductor to metal by adsorption Ti or Fe atoms, while $Cr_2Ge_2Te_6$ changes from semiconductor to half-metal by adsorption of Sc, V, Co., Ni, or Cu atoms. Moreover, the adsorption of 3d transition metal atoms obviously enhance the Curie temperature $Cr_2Ge_2Te_6$. Chen et al. predicted $MnSi_2N_4$ ML to be an antiferromagnetic semiconductor, and external strain could effectively tune its antiferromagnetic coupling. Furthermore, $MnSi_2N_4$ ML shows half-metallic ferromagnetism when an external magnetic field is applied. Wang et al. predicted 2D ferromagnetic GdScSi and GdScGe MLs to possess good dynamical, thermal, and mechanical stabilities. More excitingly, the Curie temperatures of GdScSi ML (470 K) and GdScGe ML (495 K) are above room temperature. Zhang et al. found that Ti and Ge doped 2D SiC systems are nonmagnetic semiconductors, Sc and Al doped 2D SiC systems are magnetic metals, and V, Cr, Mn, Fe, Co., and Zn doped 2D SiC systems are magnetic semiconductors. Yang et al. summarized the electronic, magnetic, and transport properties of Mn_2CoAl bulk and Mn_2CoAl-based films including Mn_2CoAl bulk, Mn_2CoAl 001 surface, various types of Mn_2CoAl films, Mn_2CoAl/GaAs, MgO/Mn_2CoAl/Pd, Mn_2CoAl/Ag/Mn_2CoAl.

Topology, photocatalysis, and noise reduction

Yang et al. demonstrated tetragonal $Na_2Zn_2O_3$ to host charge-two Dirac point phonons and charge-two Weyl point phonons at high-symmetry points. Shen et al. prepared a three-dimensional porous structured ZnO/graphene/graphene oxide/multi-walled carbon nanotube (ZnO/G/GO/MCNT) composite aerogels and reported its photocatalytic efficiency for Rhodamine B (RhB) degradation is 3.3 times higher than that of ZnO. Ren et al. performed a structural model of a stranding machine to obtain the first eight orders of inherent frequencies and vibration patterns, and found that the resonant frequency could be avoided and the vibration reduction could be achieved by increasing the wall thickness of the bearing seat.

We hope that this Research Topic could provide guidance for developing novel thermoelectric, magnetic, topological, photocatalytic materials, and reducing noise. Finally, we thank to all the authors, reviewers, and editors who have made contributions to this Research Topic.

Author contributions

GW and HY prepared the first draft, while S-DG and YSA revised the manuscript. All authors contributed to the article and approved the submitted version.

Funding

This work was supported by the Science and Technology Research Program of Chongqing Municipal Education Commission, China under grant No. KJQN202201405.

Conflict of interest

The authors declare that the research was conducted in the absence of any commercial or financial relationships that could be construed as a potential conflict of interest.

Publisher's note

References

1. Mas-Balleste R, Gomez-Navarro C, Gomez-Herrero J, Zamora F. 2D materials: To graphene and beyond. *Nanoscale* (2011) 3(1):20–30. doi:10.1039/C0NR00323A

2. Novoselov KS, Mishchenko A, Carvalho A, Castro Neto AH. 2D materials and van der Waals heterostructures. *Science* (2016) 353(6298):aac9439. doi:10.1126/science.aac9439

3. Wang G, Chang J, Tang W, Xie W, Ang YS. 2D materials and heterostructures for photocatalytic water-splitting: A theoretical perspective. *J Phys D: Appl Phys* (2022) 55(29):293002. doi:10.1088/1361-6463/ac5771

4. Shi XL, Zou J, Chen ZG. Advanced thermoelectric design: From materials and structures to devices. *Chem Rev* (2020) 120(15):7399–515. doi:10.1021/acs.chemrev.0c00026

5. Liu W, Hu J, Zhang S, Deng M, Han CG, Liu Y. New trends, strategies and opportunities in thermoelectric materials: A perspective. *Mater Today Phys* (2017) 1:50–60. doi:10.1016/j.mtphys.2017.06.001

6. Cui C, Xue F, Hu WJ, Li LJ. Two-dimensional materials with piezoelectric and ferroelectric functionalities. *npj 2D Mater Appl* (2018) 2(1):18. doi:10.1038/s41699-018-0063-5

7. Zhang Q, Zuo S, Chen P, Pan C. Piezotronics in two-dimensional materials. *InfoMat* (2021) 3(9):987–1007. doi:10.1002/inf2.12220

frontiers | Frontiers in Materials

ORIGINAL RESEARCH
published: 19 July 2022
doi: 10.3389/fmats.2022.956675

First-Principles Study of Metal Impurities in Silicon Carbide: Structural, Magnetic, and Electronic Properties

Lin Zhang[1] *and Zhen Cui*[2]*

[1]School of Science, Xi'an University of Technology, Xi'an, China, [2]School of Automation and Information Engineering, Xi'an University of Technology, Xi'an, China

The configurations of 10 types of metal-doped silicon carbide (SiC) systems were investigated by the first-principles calculations. The dopants include eight types of 3d-series transition metal atoms, one semi-metal Ge atom, and one other metal Al atom. For all the metal-doped SiC systems, the steadiest doping sites are fixed at the substituted Si site, while the Ti-SiC system exhibits the most potent binding activity. The properties of these new systems vary with the doping atoms. The SiC- and Al-SiC systems convert to magnetic metals. The Ti- and Ge-SiC systems remain non-magnetic semiconductors, while the V-, Cr-, Mn-, Fe-, Co-, and Zn-SiC systems turn into magnetic semiconductors with magnetic moments related to the valence electron number of dopants. Partial charge transfers from the metal atoms to the adjacent C atoms accompanied the change in the electron-emitting capacity of the new systems. The work function achieves the minimum of 3.439 eV in the Co-SiC system, just 71.6% of the original SiC system. Our analysis indicates that the potent binding energy of the Ti-SiC system is due to the complete bonding states between the transition metal Ti and the adjacent C atoms. The magnetism evolution in semiconducting metal-doped SiC is attributed to the occupation mode of the hybridization orbitals nearby the Fermi level, which are determined by the coupling of the 3d orbital of transition metal atoms and the defect states of the vacancy atoms. The adjustable magnetic and electronic properties of the metal-doped SiC systems provide a flexible method in designing more suitable SiC-based spintronics and field electron-emitting devices.

Keywords: metal-doped silicon carbide, magnetism, transition metal, hybridization orbitals, work function

OPEN ACCESS

Edited by:
Guangzhao Wang,
Yangtze Normal University, China

Reviewed by:
Sihao Xia,
Nanjing University of Aeronautics and Astronautics, China
Junjie He,
Charles University, Czechia

***Correspondence:**
Zhen Cui
zcui@xaut.edu.cn

Specialty section:
This article was submitted to Smart Materials, a section of the journal Frontiers in Materials

Received: *30 May 2022*
Accepted: *16 June 2022*
Published: *19 July 2022*

Citation:
Zhang L and Cui Z (2022) First-Principles Study of Metal Impurities in Silicon Carbide: Structural, Magnetic, and Electronic Properties. Front. Mater. 9:956675. doi: 10.3389/fmats.2022.956675

INTRODUCTION

Two-dimensional silicon carbide (2D SiC) has become the hot spot (Mélinon et al., 2007; Castelletto et al., 2014) of 2D materials (Li and Kaner, 2008; Luo et al., 2021; Cui et al., 2022) for the virtues, such as the high thermal capacity (Hsueh et al., 2011; Chowdhury et al., 2017) and the graphene-like planar structure (Eddy and Gaskill, 2009; Susi et al., 2017; Ferdous et al., 2019). The high thermal capability makes 2D SiC competent not only as high-power electronic and optoelectronic devices (Zhang and Cui, 2022a) but also in high-temperature circumstances and quantum information processing (Chabi and Kadel, 2020). The two-dimensional structure induces unique optical and electronic properties which are essential in optoelectronics (Stankovich et al., 2006; Bratschitsch, 2014; Sun et al., 2017a; Cui et al., 2021a; Sun et al., 2021), catalysis (Komsa et al., 2012; Ziletti et al.,

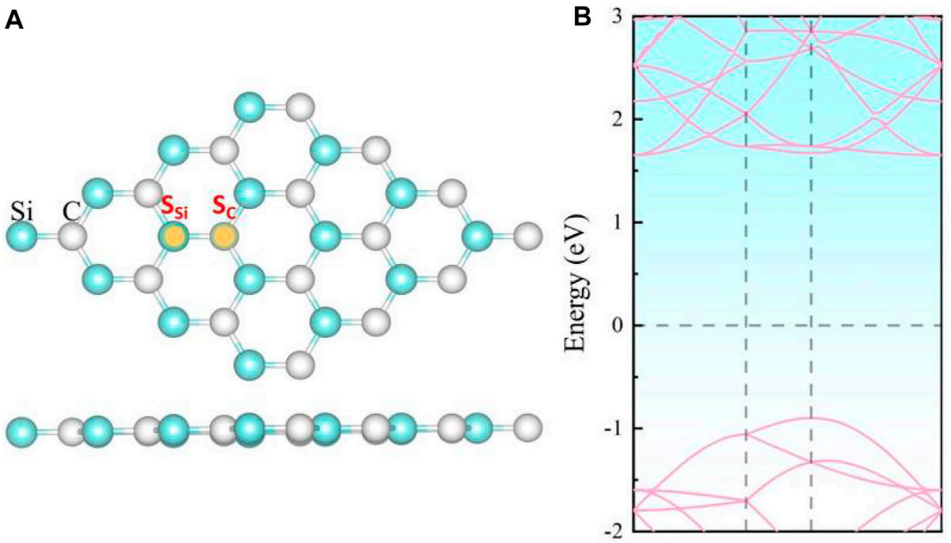

FIGURE 1 | (A) Top and side views of the crystal structure and **(B)** the energy band structure of intrinsic 2D SiC.

TABLE 1 | Doping site, binding energy (E_b), charge transfer (C), magnetic moment (M_{total}), and bandgap (E_g) of the metal-doped SiC systems.

Metal style	Doping	Site	E_b (eV)	C (e)	M_{total} (μ_B)	E_g (eV)
3d-series transition metal	Sc	S_{Si}	−11.341	−1.525	0.512	0
	Ti	S_{Si}	−18.625	−1.534	0	2.583
	V	S_{Si}	−14.723	−1.291	1.003	2.574
	Cr	S_{Si}	−13.293	−1.171	2.003	2.681
	Mn	S_{Si}	−12.783	−1.070	3.001	2.257
	Fe	S_{Si}	−12.014	−0.979	4.509	2.331
	Co	S_{Si}	−4.942	−0.596	5.004	2.572
	Zn	S_{Si}	−5.931	−0.832	1.984	0.112
Other metal	Al	S_{Si}	−11.323	−2.201	0.492	0
Semi-metal	Ge	S_{Si}	−12.411	−1.245	0	2.516

2015), spintronic devices (Wang et al., 2018; Li et al., 2021), energy conversion (Pospischil et al., 2014; Cui et al., 2020a; Sun et al., 2020; Sun and Schwingenschlögl, 2020), and gas sensing (Lin et al., 2013; Kooti et al., 2019; Cui et al., 2020b). The success in the wet exfoliation of 2D SiC accelerates the further investigation of the SiC-based system (Chabi et al., 2021).

The previous studies on other 2D materials and dopants provide many predictive references (He et al., 2010; Tang et al., 2018; Cui et al., 2020b; Cui et al., 2021b). In non-metal doped SiC (NM-SiC), the sp^2 hybridization orbitals of NM atoms form more robust coupling interactions, inducing the magnetism of the systems (Bekaroglu et al., 2010). When the transition metal (TM) atom is doped in 2D material, the occupation mode of d hybridization orbitals of TM atoms determines the magnetism of the systems (Santos et al., 2010; He et al., 2014a; He et al., 2014b; Sun et al., 2017b; Yuan et al., 2020; Cui et al., 2021c). All these results indicate that the electronic and magnetic properties of 2D-SiC can be adjusted by the doping of atoms effectively. Although SiC systems have been studied while doping some TM and NM atoms, the discussion on the law of universality is relatively few, especially the effects of the valence electron number of the dopant on magnetism are seldom discussed (Luo et al., 2017; Luo and Shen, 2018; Wu et al., 2019). In this work, the configurations of 10 types of the metal-doped SiC systems were investigated. The doping atoms include not only eight 3d-series TM atoms but also one semi-metal atom and one other metal atom. The electronic and magnetic performances were investigated at the most stable structures systematically. The high stability in Ti-SiC was explained by the complete bonding states between the Ti atom and the neighboring C atoms because of the same valence electron number with the substituted Si atom. The magnetism evolution in transition metal-doped SiC was attributed to the occupation mode of hybridization orbitals nearby the Fermi level.

COMPUTATIONAL DETAILS

The first-principles theory calculations are based on the density functional theory and executed by the Vienna *Ab initio* simulation package (VASP) (Kresse and Furthmüller, 1996)

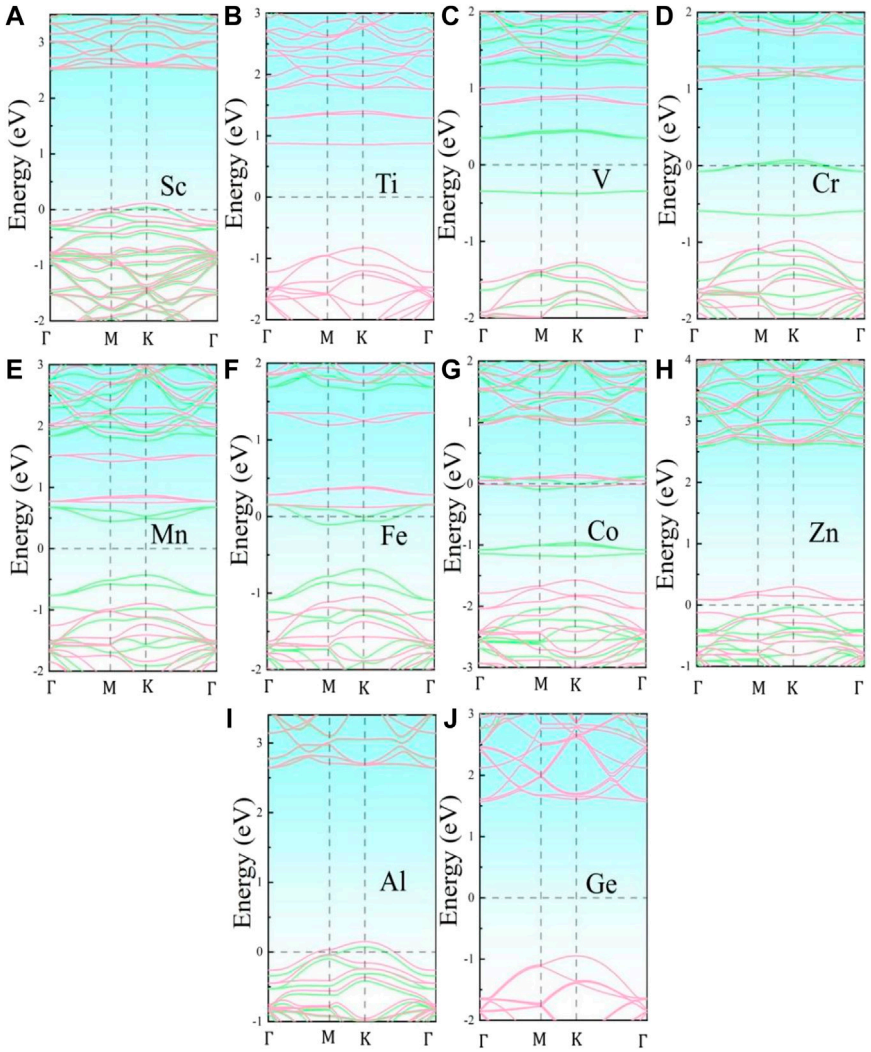

FIGURE 2 | Band structures of the metal-doped SiC systems: **(A)** Sc-SiC, **(B)** Ti-SiC, **(C)** V-SiC, **(D)** Cr-SiC, **(E)** Mn-SiC, **(F)** Fe-SiC, **(G)** Co-SiC, **(H)** Zn-SiC, **(I)** Al-SiC, and **(J)** Ge-SiC. The green and the pink lines represent the spin-up and the spin-down component of the energy levels, respectively. The Fermi level is shifted to zero.

and Perdew–Burke–Ernzerhof functions (PBE) (Perdew et al., 1996; Kresse and Joubert, 1999). Projector-augmented wave (PAW) schemes (Kresse and Joubert, 1999) are employed in the electron–ion interaction. To expand the Kohn–Sham orbitals, the cut-off energy for plane-waves basis is set to 550 eV. To minimize the interaction between the metal atoms, a 4 × 4×1 supercell with one vacancy atom is selected, corresponding to a 3.125% doping concentration. To eliminate the molecular interactions between layers, a vacuum layer of 15 Å height was constructed along the normal direction of the SiC plane. The first Brillouin zone was structured with a 3 × 3 × 1 k-point grid (Grimme et al., 2010). The final stable system is achieved until all the particles experience enough relaxation, the Hellmann–Feynman force on each atom is less than 0.01 eV/Å, and the total energy change is lower than 10^{-5} eV/atom. The magnetic and electronic properties of the metal-doped SiC systems are explored in their steadiest configurations.

RESULTS AND DISCUSSION

Our calculation shows that the pristine SiC exhibits a two-dimensional planar structure with a lattice parameter of 3.10 Å, as depicted in **Figure 1**. The 2D SiC system is a direct band semiconductor with a band gap 2.5 eV, whose band edge of the conduction band and the valence band are both located at the K point. These calculation results are similar to those of the other groups (Luo et al., 2017; Chabi et al., 2021), which demonstrates the correctness of our method.

The practical application of 2D materials is based on the structural stability, which is evaluated by the binding energy of the new system:

$$E_b = E_{metal+\ SiC} - (E_{SiC} + E_{metal}), \quad (1)$$

where E_b represents the binding energy of the metal-doped SiC system. $E_{metal+SiC}$, E_{SiC}, and E_{metal} denote the energies of the final

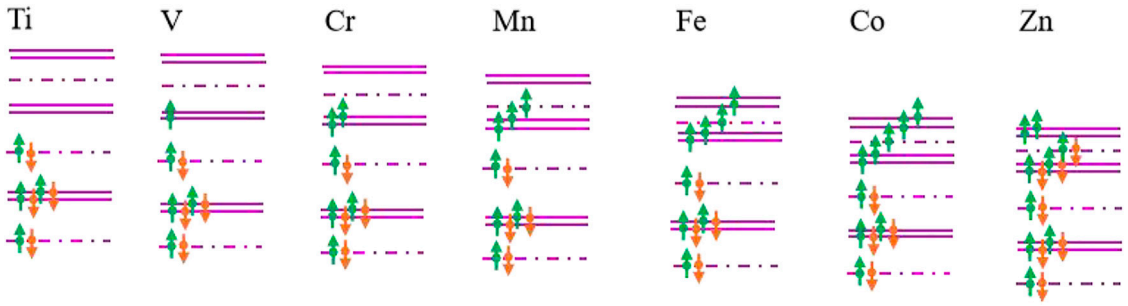

FIGURE 3 | Evolution of the occupation mode of the hybridization orbitals nearby the Fermi level for the transition metal-doped SiC systems. The purple double lines represent the electronic states with E-symmetry, while the short line point represents the electronic states with A-symmetry. The green and the orange arrows denote the spin-up and the spin-down components, respectively. The distances between the lines reflect the energy variation between the energy levels.

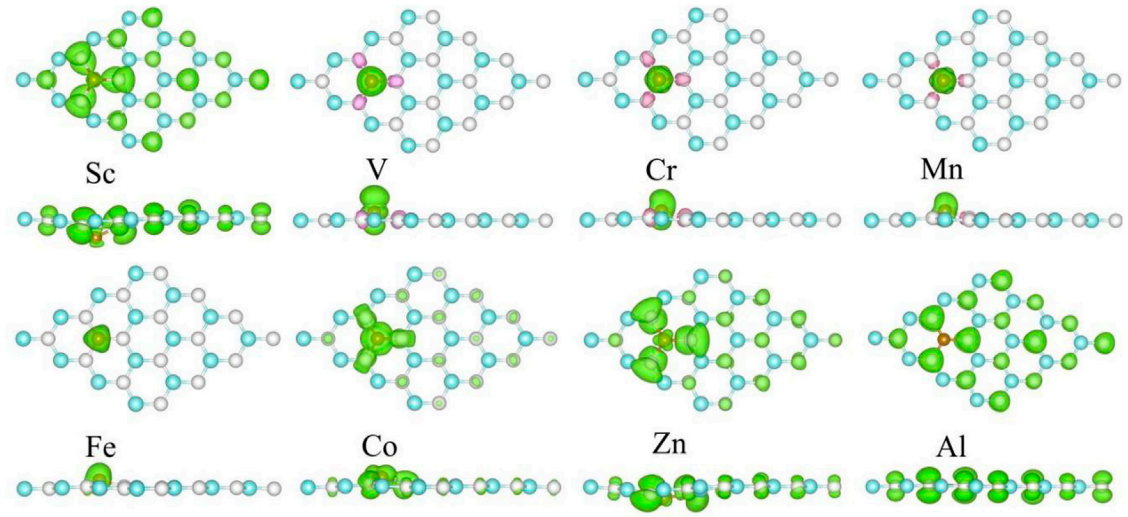

FIGURE 4 | Spin-polarized charge density of the metal-doped SiC system. The green and the pink areas represent the spin-up and the spin-down regions, respectively. The isovalue is set to 0.001 e/Å^3.

metal-doped SiC, the original SiC with one vacancy, and the doping atom. Negative binding energy indicates that the metal-doped SiC system is more stable than the original SiC system with one vacancy. The most possible configuration corresponds to the structure with the largest binding energy.

In our work, the doping atoms include not only the eight 3d-series transition metal atoms but also one semi-metal Ge, and one other metal Al atom. The binding energies for metal-doped SiC system are investigated at the two possible symmetry sites, the Si-substituted site S_{Si} and the C-substituted site S_C, as depicted in **Figure 1A**. Our calculation shows that all the doping atoms exhibit more powerful bindings when doped at the site S_{Si}, and the systems with the maximum of binding energies are listed in **Table 1**. All these systems exhibit binding energies larger than 4.9 eV, indicating that these substitutional doping atoms are very favorable in thermodynamics for the original system with the vacancy atom. The semi-metal Ge and other metal Al atoms present weaker bindings with the SiC systems than the TM atoms do. The binding energy achieves the maximum of 18.625 eV in the Ti-SiC system, presenting a monotonous decrease with the increase in the atomic number from the 3d-series TM atom Ti to Co. The most robust binding in the Ti-SiC system is because the Ti atom substitutes the Si atom with the same number of valence electrons and reconstructs the complete bonding states with the adjacent C atoms. Potent coupling forms between the 3d hybridization orbital of Ti atoms and the neighboring defect states of C atoms. As the electron number of the dopant increases, the energy of the TM-SiC system decreases, and the coupling degree of the hybridization orbitals nearby the Fermi energy level reduces, diminishing the binding energy of the corresponding system, which agrees with the results in 4d TM atom-doped graphene (Santos et al., 2010). The larger binding energy of 12.411 eV

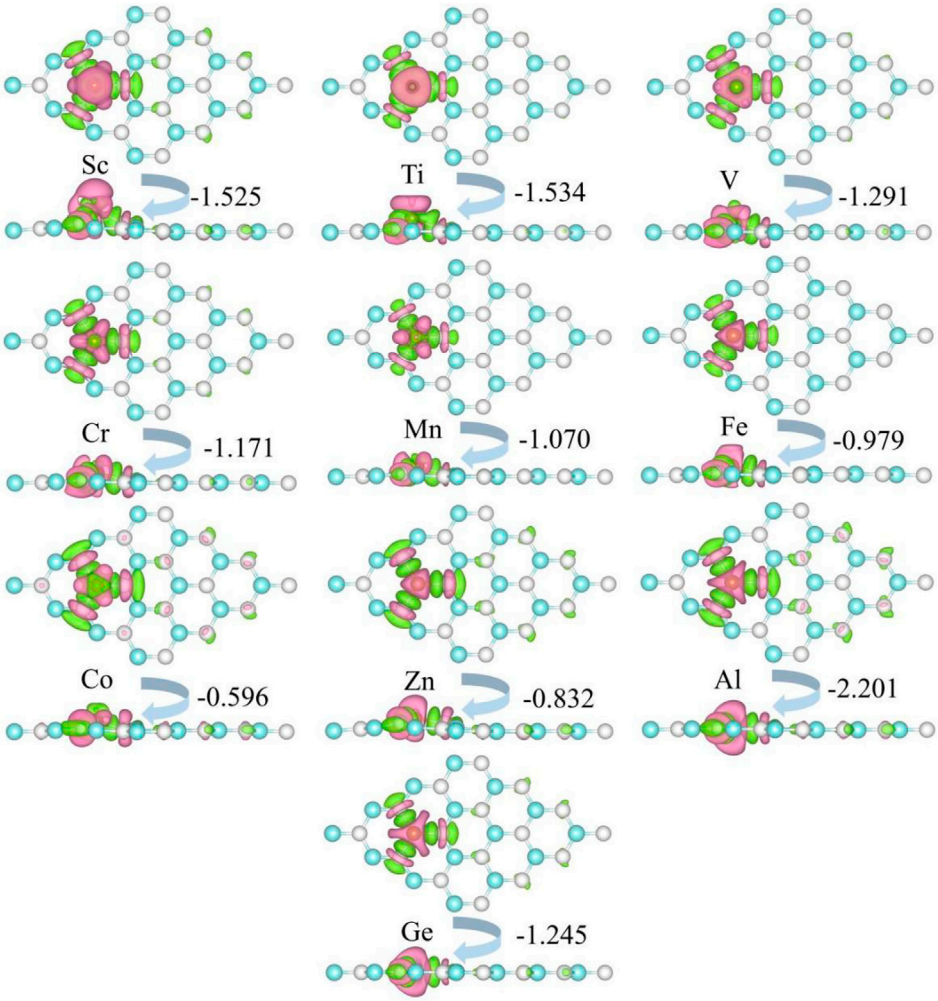

FIGURE 5 | Charge density difference of the metal-doped SiC system. The green and the pink areas represent the loss and the obtained charge, respectively. The isovalue is set to 0.001 e/Å^3.

in Ge-SiC is also attributed to the complete metal-carbon bonding states, while the less binding energy relative to Ti-SiC is due to the lower orbital hybridization degree in Ge-SiC.

Figure 2 illustrates the energy band structures of the 10 metal-doped SiC systems. All these energy band structures are similar to those of the original SiC system, with several impurity energy levels appearing in the forbidden band. In the Al- and Sc-SiC systems, the spin-up and spin-down components of the SiC energy levels intersect with the Fermi level, and the corresponding Al- and Sc-SiC systems turn into the magnetic metals. Considering the energy levels intersected by the Fermi level are the hybridization result of the impurity levels and the vacancy states of C atoms, the Cr-, Fe- and Co-SiC systems remain the properties of semiconductors. The corresponding bandgaps are calibrated by the nearest electronic states above and below those impurity energy levels. The metal-doped SiC system exhibit an adjustable band gap: 2.583 eV (Ti), 2.574 eV (V), 2.681 eV (Cr), 2.257 eV (Mn), 2.331 eV (Fe), 2.572 eV (Co), 0.112 eV (Zn), and 2.516 eV (Ge), respectively. Among them, the Ge- and Ti-SiC systems are still non-magnetization for the consistency of the spin-up and the spin-down components of energy levels, while the other 3d-series transition metal-doped SiC systems exhibit the behaviors of magnetic semiconductors for the asymmetry in the spin-up and the spin-down components of energy levels, as shown in the V-, Cr-, Mn-, Fe-, Co-, and Zn-SiC systems.

To estimate the magnetism of TM-SiC roughly, a hybridization orbital model of E.J.G. Santos (Santos et al., 2010; Sun et al., 2017b) was employed based on the energy band structure. Considering that the energy of 4s orbitals of metal atoms is much higher than the Fermi level, the contribution of 4s orbitals is neglected. When the 3d-series transition metal is doped in SiC, the 3d orbitals of TM atoms split into one A and two twofold-degenerate E levels, while the p orbitals of the vacancy C atom split and form two A and one twofold-degenerate E levels. Magnetic coupling occurs between the electron states of 3d TM atoms and the localized defect states

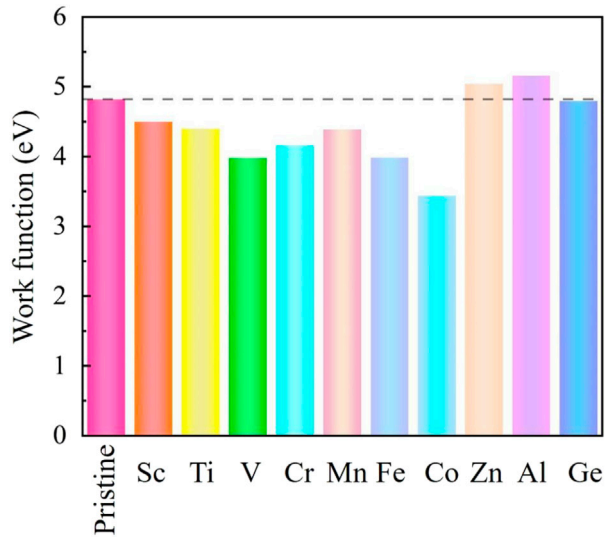

FIGURE 6 | Work function of the intrinsic SiC and metal-doped SiC systems.

of the C atom. Based on A or E irreducible representations, the coupling just occurs under the same irreducible representation. The corresponding band structures of TM-SiC are schemed in **Figure 3**, where the energy values are calibrated by the first-principles calculations and orbital theory. It can be seen that the energy of systems decreases with the valence electron number, accompanying the change in the energy variation between energy levels. Electrons occupy the energy levels from low-energy to high-energy gradually, while the hybridization orbitals are filled based on the Hund's rule. When Ti atom is injected, the four valence electrons of the Ti atom form complete bonding states with the defect states of the C atoms, and the corresponding Ti-SiC exhibits no magnetism. With the increase in the valence electron number along the 3d Ti atom to Co atom, the electrons of TM atoms fill the hybridization orbital with the same spinned direction, and the magnetism moments increase with the valence electron number. When all the hybridization orbitals are occupied with the same spin-polarized charge, the system presents the largest magnetism, as depicted in Co-SiC. With the further increase in the valence electron number, the remaining electrons start to fill these hybridization orbitals with an opposite spinned direction, and the magnetism of system decreases, as shown in the Zn-SiC system. The occupation mode of the hybridization orbitals nearby the Fermi level determines the magnetism of the TM-SiC system. Based on this simple principle, the magnetism moments of the transition metal-doped SiC can be acquired roughly, about 0 μ_B (Ti), 1 μ_B (V), 2 μ_B (Cr), 3 μB (Mn), 4 μ_B (Fe), 5 μ_B (Co), and 2 μ_B (Zn).

The spin-polarized charge distributions near the metal atom are calculated, as illustrated in **Figure 4**. It can be seen that the three surrounding C atoms of the TM atom-doped SiC make equal contribution to the spin-polarized charge distribution. In the Sc- and Al-SiC systems, the spinned-polarized charge density exhibits a long-range distribution, even the atoms far away make a strong contribution, similar to the results shown in the GeC adsorbed by the F or Cl atom (Zhang and Cui, 2022b). However, Fe atom makes a decisive effect on the spin-polarized charge distributions of Fe-SiC, and the contributions of the adjacent C atoms are hard to be seen. In the V-, Cr-, Mn-, and Co-SiC systems, the TM atoms make more dominant effects than the adjacent C atoms. The magnetic moments of the metallic Sc- and Al-SiC systems are further calculated 0.512 μ_B (Sc) and 0.492 μ_B (Al), while the magnetic moments in semiconducting TM-SiC are 0 μ_B (Ti), 1.003 μ_B (V), 2.003 μ_B (Cr), 3.001 μ_B (Mn), 4.509 μ_B (Fe), 5.004 μ_B (Co), and 1.984 μ_B (Zn), respectively. Although there is a 0.5 μ_B variation in the Fe-SiC system, the magnetic moments of the other six TM-SiC systems are consistent with the forecasting results in **Figure 3** as well, which demonstrates the validity of the hybridization orbital model.

To investigate the change in the electronic properties of metal-atom–doped SiC, the charge transfer between doping and the adjacent atoms is studied. The charge density difference (CDD) of metal-doped SiC is calculated by the Bader charges (Henkelman et al., 2006; Sanville et al., 2007),

$$\Delta\rho = \rho_{\text{Total}} - (\rho_{\text{SiC}}+\rho_{\text{NM}}), \tag{2}$$

where $\Delta\rho$ is the difference in the charge density, ρ_{Total}, ρ_{SiC}, and ρ_{NM} represent the charge densities of the metal-doped SiC, the pristine SiC, and the metal atom, respectively.

The charge density difference of metal-doped SiC is illustrated in **Figure 5**. It can be seen that the metal atoms act as charge donors, transferring some charges to the adjacent C atoms. The charge transfers are F02D1$^-$.525|e| (Sc), F02D1$^-$.534|e| (Ti), F02D1$^-$.291|e| (V), F02D1$^-$.171|e| (Cr), F02D1$^-$.070|e| (Mn), F02D0$^-$.979|e| (Fe), F02D0$^-$.596|e| (Co), F02D0$^-$.832|e| (Zn), F02D2$^-$.202|e| (Al), and F02D1$^-$.245|e| (Ge), respectively. New metal-carbon bonds are formed to achieve the stability of the metal-doped SiC systems. The systems with semiconducting properties (the V-, Cr-, Mn-, Fe-, Co-, Zn, and Ge-SiC systems) exhibit relatively weak transfer charges than those with the metallic properties (the Sc- and Al-SiC systems). Among the semiconducting doped SiC systems, the most robust metal-carbon bonds are formed in the Ti-SiC system for the larger binding energy than the others, while Co-SiC exhibits weaker metal-carbon bonds for the smaller binding energy.

The formation of the new metal-carbon bonds induces the change in the system work function, leading to the variation in the electron-emitting capacity. A weak metal-carbon bond indicates a smaller work function and a stronger electron-emitting capacity. The work functions of the conventional 2D field electron emission devices are about several eV (Yu et al., 2009; Jiao et al., 2012; Cai et al., 2014; Soo et al., 2014), such as 4.50 eV (phosphorene), 4.60 eV (graphene), 4.90 eV (boron nitride), and 5.15 eV (MoS_2). In our work, the calculated work function of the pristine SiC is 4.80 eV, while the metal-doped SiC systems change from 3.439 to 5.158 eV, as depicted in **Figure 6**. Although the work function increases in the Al- and Zn-SiC systems, it decreases in the Sc-, Ti-,V-, Cr-, Mn-, Fe-, Co-, and Ge-SiC

systems. The minimum work function of 3.439 eV is in the Co-SiC system, just 71.16% of the pristine SiC. The adjustment on the work function causing by metal dopants expands the application of the SiC-based system in the field emission devices.

CONCLUSION

We investigated the structural, electronic, and magnetic performances of 10 metal-doped SiC systems. The doping metal atoms include eight 3d-series transition metals, one semi-metal Ge, and one other metal Al atom. Our calculations indicate that the steadiest doping sites for all metal-doped SiC systems are located at the substituted Si site. Ti-SiC presents the most stable configuration for the largest binding energy. Although the Ti- and Ge-SiC systems remain nonmagnetic semiconductors, the Sc- and Al-SiC systems convert to magnetic metals, and the V-, Cr-, Mn-, Fe-, Co-, and Zn-SiC systems turn into magnetic semiconductors whose magnetic moments are related to the valence electron number of dopants. With the doping of the metal atoms, particle charge transfers from the metal atoms to the adjacent C atoms, causing the variation in the work function. Except for the increase in the Zn- and Al-SiC systems, the work function of the other metal-doped SiC systems decreases and achieves the minimum of 3.439 eV in the Co-SiC system, just 71.6% of the original SiC system. Our analysis indicates that the intense binding energy in the Ti-SiC system is due to the complete bonding states between the transition metal Ti and the adjacent C atoms. The magnetism in 3d TM-SiC is attributed to the occupation mode of the hybridization orbitals contributed by the coupling of 3d orbitals of the TM atom and the defect states of the vacancy. The adjustment on the electronic and magnetic performances by metal atoms extends the applications of SiC, especially in the design of field emission and spin electronic devices.

DATA AVAILABILITY STATEMENT

The original contributions presented in the study are included in the article/Supplementary Material; further inquiries can be directed to the corresponding author.

AUTHOR CONTRIBUTIONS

LZ: conceptualization, methodology, and validation. ZC: supervision, software, and writing—reviewing and editing.

ACKNOWLEDGMENTS

We gratefully acknowledge the funding support from the National Natural Science Foundation of China 11904285.

REFERENCES

Bekaroglu, E., Topsakal, M., Cahangirov, S., and Ciraci, S. (2010). First-principles Study of Defects and Adatoms in Silicon Carbide Honeycomb Structures. *Phys. Rev. B, Condens. Matter Mat. Phys.* 81, 1–9. doi:10.1103/physrevb.81.075433

Bratschitsch, R. (2014). Monolayer Diodes Light up. *Nat. Nanotech* 9, 247–248. doi:10.1038/nnano.2014.66

Cai, Y., Zhang, G., and Zhang, Y.-W. (2014). Layer-dependent Band Alignment and Work Function of Few-Layer Phosphorene. *Sci. Rep.* 4, 6677. doi:10.1038/srep06677

Castelletto, S., Johnson, B. C., Ivády, V., Stavrias, N., Umeda, T., Gali, A., et al. (2014). A Silicon Carbide Room-Temperature Single-Photon Source. *Nat. Mater* 13, 151–156. doi:10.1038/nmat3806

Chabi, S., Guler, Z., Brearley, A. J., Benavidez, A. D., and Luk, T. S. (2021). The Creation of True Two-Dimensional Silicon Carbide. *Nanomaterials* 11, 1799. doi:10.3390/nano11071799

Chabi, S., and Kadel, K. (2020). Two-dimensional Silicon Carbide: Emerging Direct Band Gap Semiconductor. *Nanomaterials* 10, 2226. doi:10.3390/nano10112226

Chowdhury, C., Karmakar, S., and Datta, A. (2017). Monolayer Group IV-VI Monochalcogenides: Low-Dimensional Materials for Photocatalytic Water Splitting. *J. Phys. Chem. C* 121, 7615–7624. doi:10.1021/acs.jpcc.6b12080

Cui, Z., Bai, K., Ding, Y., Wang, X., Li, E., Zheng, J., et al. (2020). Electronic and Optical Properties of Janus MoSSe and ZnO vdWs Heterostructures. *Superlattices Microstruct.* 140, 106445. doi:10.1016/j.spmi.2020.106445

Cui, Z., Luo, Y., Yu, J., and Xu, Y. (2021). Tuning the Electronic Properties of $MoSi_2N_4$ by Molecular Doping: A First Principles Investigation. *Phys. E Low-dimensional Syst. Nanostructures* 134, 114873. doi:10.1016/j.physe.2021.114873

Cui, Z., Lyu, N., Ding, Y., Bai, K., and Bai, K. F. (2021). Noncovalently Functionalization of Janus MoSSe Monolayer with Organic Molecules. *Phys. E Low-dimensional Syst. Nanostructures* 127, 114503. doi:10.1016/j.physe.2020.114503

Cui, Z., Wang, M., Lyu, N., Zhang, S., Ding, Y., and Bai, K. (2021). Electronic, Magnetism and Optical Properties of Transition Metals Adsorbed Puckered Arsenene. *Superlattices Microstruct.* 152, 106852. doi:10.1016/j.spmi.2021.106852

Cui, Z., Wang, X., Ding, Y., Li, E., Bai, K., Zheng, J., et al. (2020). Adsorption of CO, NH_3, NO, and NO_2 on Pristine and Defective g-GaN: Improved Gas Sensing and Functionalization. *Appl. Surf. Sci.* 530, 147275. doi:10.1016/j.apsusc.2020.147275

Cui, Z., Zhang, S., Wang, L., and Yang, K. (2022). Optoelectronic and Magnetic Properties of Transition Metals Adsorbed Pd_2Se_3 Monolayer. *Micro Nanostructures* 167, 207260. doi:10.1016/j.micrna.2022.207260

Eddy, C. R., and Gaskill, D. K. (2009). Silicon Carbide as a Platform for Power Electronics. *Science* 324, 1398–1400. doi:10.1126/science.1168704

Ferdous, N., Islam, M. S., Park, J., and Hashimoto, A. (2019). Tunable Electronic Properties in Stanene and Two Dimensional Silicon-Carbide Heterobilayer: A First Principles Investigation. *AIP Adv.* 9, 025120. doi:10.1063/1.5066029

Grimme, S., Antony, J., Ehrlich, S., and Krieg, H. (2010). A Consistent and Accurate Ab Initio Parametrization of Density Functional Dispersion Correction (DFT-D) for the 94 Elements H-Pu. *J. Chem. Phys.* 132, 154104. doi:10.1063/1.3382344

He, J., Jiao, N., Zhang, C., Xiao, H., Chen, X., and Sun, L. (2014). Spin Switch of the Transition-Metal-Doped Boron Nitride Sheet through H/F Chemical Decoration. *J. Phys. Chem. C* 118, 8899–8906. doi:10.1021/jp410716q

He, J., Wu, K., Sa, R., Li, Q., and Wei, Y. (2010). Magnetic Properties of Nonmetal Atoms Absorbed MoS_2 Monolayers. *Appl. Phys. Lett.* 96, 082504. doi:10.1063/1.3318254

He, J., Zhou, P., Jiao, N., Ma, S. Y., Zhang, K. W., Wang, R. Z., et al. (2014). Magnetic Exchange Coupling and Anisotropy of 3d Transition Metal Nanowires on Graphyne. *Sci. Rep.* 4, 4014. doi:10.1038/srep04014

Henkelman, G., Arnaldsson, A., and Jónsson, H. (2006). A Fast and Robust Algorithm for Bader Decomposition of Charge Density. *Comput. Mater. Sci.* 36, 354–360. doi:10.1016/j.commatsci.2005.04.010

Hsueh, H. C., Guo, G. Y., and Louie, S. G. (2011). Excitonic Effects in the Optical Properties of a SiC Sheet and Nanotubes. *Phys. Rev. B* 84, 085404. doi:10.1103/physrevb.84.085404

Jiao, N., He, C., Zhang, C. X., Peng, X., Zhang, K. W., and Sun, L. Z. (2012). Modulation Effect of Hydrogen and Fluorine Decoration on the Surface Work Function of BN Sheets. *AIP Adv.* 2, 022125. doi:10.1063/1.4719097

Komsa, H. P., Kotakoski, J., Kurasch, S., Lehtinen, O., Kaiser, U., and Krasheninnikov, A. V. (2012). Two-dimensional Transition Metal Dichalcogenides under Electron Irradiation: Defect Production and Doping. *Phys. Rev. Lett.* 109, 035503. doi:10.1103/PhysRevLett.109.035503

Kooti, M., Keshtkar, S., Askarieh, M., and Rashidi, A. (2019). Progress toward a Novel Methane Gas Sensor Based on SnO_2 Nanorods-Nanoporous Graphene Hybrid. *Sensors Actuators B Chem.* 281, 96–106. doi:10.1016/j.snb.2018.10.032

Kresse, G., and Furthmüller, J. (1996). Efficient Iterative Schemes Forab Initiototal-Energy Calculations Using a Plane-Wave Basis Set. *Phys. Rev. B* 54, 11169–11186. doi:10.1103/physrevb.54.11169

Kresse, G., and Joubert, D. (1999). From Ultrasoft Pseudopotentials to the Projector Augmented-Wave Method. *Phys. Rev. B* 59, 1758–1775. doi:10.1103/physrevb.59.1758

Li, D., and Kaner, R. B. (2008). Graphene-based Materials. *Science* 320, 1170–1171. doi:10.1126/science.1158180

Li, D., Li, S., Zhong, C., and He, J. (2021). Tuning Magnetism at the Two-Dimensional Limit: a Theoretical Perspective. *Nanoscale* 13, 19812–19827. doi:10.1039/d1nr06835k

Lin, X., Lin, S., Xu, Y., Hakro, A. A., Hasan, T., Zhang, B., et al. (2013). Ab Initio study of Electronic and Optical Behavior of Two-Dimensional Silicon Carbide. *J. Mat. Chem. C* 1, 2131–2135. doi:10.1039/c3tc00629h

Luo, M., and Shen, Y. H. (2018). Magnetic Properties of SiC Monolayer with Different Nonmagnetic Metal Dopants. *J. Supercond. Nov. Magn.* 31, 3277–3282. doi:10.1007/s10948-018-4589-8

Luo, M., Shen, Y. H., and Yin, T. L. (2017). Ab Initio study of Electronic and Magnetic Properties in TM-Doped 2D Silicon Carbide. *Phys. E Low-dimensional Syst. Nanostructures* 85, 280–284. doi:10.1016/j.physe.2016.08.028

Luo, Y., Ren, C. D., Xu, Y. J., Yu, J., Wang, S., and Sun, M. L. (2021). A First Principles Investigation on the Structural, Mechanical, Electronic, and Catalytic Properties of Biphenylene. *Sci. Rep.* 11, 19008. doi:10.1038/s41598-021-98261-9

Mélinon, P., Masenelli, B., Tournus, F., and Perez, A. (2007). Playing with Carbon and Silicon at the Nanoscale. *Nat. Mat.* 6, 479–490. doi:10.1103/PhysRevB.90.205421

Perdew, J. P., Burke, K., and Ernzerhof, M. (1996). Generalized Gradient Approximation Made Simple. *Phys. Rev. Lett.* 77 (18), 3865–3868. doi:10.1103/physrevlett.77.3865

Pospischil, A., Furchi, M. M., and Mueller, T. (2014). Solar-energy Conversion and Light Emission in an Atomic Monolayer P-N Diode. *Nat. Nanotech* 9, 257–261. doi:10.1038/nnano.2014.14

Santos, E. J. G., Ayuela, A., and Sánchez-Portal, D. (2010). First-principles Study of Substitutional Metal Impurities in Graphene: Structural, Electronic and Magnetic Properties. *New J. Phys.* 12, 053012. doi:10.1088/1367-2630/12/5/053012

Sanville, E., Kenny, S. D., Smith, R., and Henkelman, G. (2007). Improved Grid-Based Algorithm for Bader Charge Allocation. *J. Comput. Chem.* 28, 899–908. doi:10.1002/jcc.20575

Soo, H. C., Zhang, S. L., and Woo, C. Y. (2014). Layer-number-dependent Work Function of MoS_2 Nanoflakes. *J. Kor. Phys. Soc.* 64, 1550–1555.

Stankovich, S., Dikin, D. A., Dommett, G. H. B., Kohlhaas, K. M., Zimney, E. J., Stach, E. A., et al. (2006). Graphene-based Composite Materials. *Nature* 442, 282–286. doi:10.1038/nature04969

Sun, M., Chou, J.-P., Ren, Q., Zhao, Y., Yu, J., and Tang, W. (2017). Tunable Schottky barrier in van der Waals heterostructures of graphene and g-GaN. *Appl. Phys. Lett.* 110, 173105. doi:10.1063/1.4982690

Sun, M. L., and Schwingenschlögl, U. (2020). A Direct-Band-Gap Semiconductor Combining Auxeticity, Ferroelasticity, and Potential for High-Efficiency Solar Cells. *Phys. Rev. Appl.* 14, 044015. doi:10.1103/physrevapplied.14.044015

Sun, M., Luo, Y., Yan, Y., and Schwingenschlögl, U. (2021). Ultrahigh Carrier Mobility in the Two-Dimensional Semiconductors B8Si4, B8Ge4, and B8Sn4. *Chem. Mat.* 33, 6475–6483. doi:10.1021/acs.chemmater.1c01824

Sun, M., Ren, Q., Zhao, Y., Chou, J.-P., Yu, J., and Tang, W. (2017). Electronic and Magnetic Properties of 4d Series Transition Metal Substituted Graphene: a First-Principles Study. *Carbon* 120, 265–273. doi:10.1016/j.carbon.2017.04.060

Sun, M., Yan, Y., and Schwingenschlögl, U. (2020). Beryllene: A Promising Anode Material for Na- and K-Ion Batteries with Ultrafast Charge/Discharge and High Specific Capacity. *J. Phys. Chem. Lett.* 11, 9051–9056. doi:10.1021/acs.jpclett.0c02426

Susi, T., Skákalová, V., Mittelberger, A., Kotrusz, P., Hulman, M., Pennycook, T. J., et al. (2017). Computational Insights and the Observation of SiC Nanograin Assembly: Towards 2D Silicon Carbide. *Sci. Rep.* 7, 4399. doi:10.1038/s41598-017-04683-9

Tang, W., Sun, M., Yu, J., and Chou, J.-P. (2018). Magnetism in Non-metal Atoms Adsorbed Graphene-like Gallium Nitride Monolayers. *Appl. Surf. Sci.* 427, 609–612. doi:10.1016/j.apsusc.2017.08.210

Wang, S., Ren, C., Tian, H., Yu, J., and Sun, M. (2018). MoS_2/ZnO van der Waals heterostructure as a high-efficiency water splitting photocatalyst: a first-principles study. *Phys. Chem. Chem. Phys.* 20, 13394–13399. doi:10.1039/c8cp00808f

Wu, C.-W., Huang, J.-H., and Yao, D.-X. (2019). Tunable Room-Temperature Ferromagnetism in the SiC Monolayer. *J. Magnetism Magnetic Mater.* 469, 306–314. doi:10.1016/j.jmmm.2018.08.054

Yu, Y.-J., Zhao, Y., Ryu, S., Brus, L. E., Kim, K. S., and Kim, P. (2009). Tuning the Graphene Work Function by Electric Field Effect. *Nano Lett.* 9, 3430–3434. doi:10.1021/nl901572a

Yuan, J., Chen, Y., Xie, Y., Zhang, X., Rao, D., Guo, Y., et al. (2020). Squeezed Metallic Droplet with Tunable Kubo Gap and Charge Injection in Transition Metal Dichalcogenides. *Proc. Natl. Acad. Sci. U.S.A.* 117, 6362–6369. doi:10.1073/pnas.1920036117

Zhang, L., and Cui, Z. (2022). Electronic, Magnetic, and Optical Performances of Non-metals Doped Silicon Carbide. *Front. Chem.* 10, 898174. doi:10.3389/fchem.2022.898174

Zhang, L., and Cui, Z. (2022). Theoretical Study on Electronic, Magnetic and Optical Properties of Non-metal Atoms Adsorbed onto Germanium Carbide. *Nanomaterials* 12, 1712. doi:10.3390/nano12101712

Ziletti, A., Carvalho, A., Campbell, D. K., Coker, D. F., and Castro Neto, A. H. (2015). Oxygen Defects in Phosphorene. *Phys. Rev. Lett.* 114, 046801. doi:10.1103/PhysRevLett.114.046801

Conflict of Interest: The authors declare that the research was conducted in the absence of any commercial or financial relationships that could be construed as a potential conflict of interest.

Publisher's Note: All claims expressed in this article are solely those of the authors and do not necessarily represent those of their affiliated organizations, or those of the publisher, the editors, and the reviewers. Any product that may be evaluated in this article, or claim that may be made by its manufacturer, is not guaranteed or endorsed by the publisher.

frontiers | Frontiers in Chemistry

TYPE Original Research
PUBLISHED 15 August 2022
DOI 10.3389/fchem.2022.992482

OPEN ACCESS

EDITED BY
Guangzhao Wang,
Yangtze Normal University, China

REVIEWED BY
Guoqing Zhang,
Xi' an Polytechnic University, China
Zhifang Zhao,
Zhejiang University of Technology, China

*CORRESPONDENCE
Yang Shen,
shenyang@xaut.edu.cn
Zhen Cui,
zcui@xaut.edu.cn
Enling Li,
lienling@xaut.edu.cn

SPECIALTY SECTION
This article was submitted to Physical Chemistry and Chemical Physics, a section of the journal Frontiers in Chemistry

RECEIVED 12 July 2022
ACCEPTED 21 July 2022
PUBLISHED 15 August 2022

CITATION
Shen Y, Yuan Z, Cheng F, Cui Z, Ma D, Bai Y, Zhao S, Deng J and Li E (2022), Preparation and characterization of ZnO/graphene/graphene oxide/multi-walled carbon nanotube composite aerogels.
Front. Chem. 10:992482.
doi: 10.3389/fchem.2022.992482

Preparation and characterization of ZnO/graphene/graphene oxide/multi-walled carbon nanotube composite aerogels

Yang Shen[1]*, Zhihao Yuan[1], Fengjiao Cheng[2], Zhen Cui[3]*, Deming Ma[1], Yueyue Bai[1], Shuqing Zhao[1], Jieyao Deng[1] and Enling Li[1]*

[1]School of Science, Xi'an University of Technology, Xi'an, China, [2]School of Electrical Engineering, Xi'an University of Technology, Xi'an, China, [3]School of Automation and Information Engineering, Xi'an University of Technology, Xi'an, China

ZnO/Graphene (G)/Graphene Oxide (GO)/Multi-walled Carbon Nanotube (MCNT) composite aerogels with a three-dimensional porous structure were prepared by the sol-gel method under average temperature and alkaline conditions, combined with freeze-drying process and heat treatment process. The photocatalytic degradation of Rhodamine B (RhB) was mainly studied. The scanning electron microscope (SEM) test results showed that the morphology uniformity of the ZnO/G/GO/MCNT composite aerogel was significantly enhanced, which effectively solving the agglomeration problem of MCNT and ZnO. The photocatalytic degradation test results of RhB show that due to the synergistic effect of physical adsorption and photocatalytic degradation, the total degradation efficiency of RhB by ZnO/G/GO/MCNT could reach 86.8%, which is 3.3 times higher than that of ZnO. In addition, the synergistic effect of ZnO and G effectively hinders the recombination of photo-generated electron-hole pairs and enhances photocatalytic activity. The ZnO/G/GO/MCNT composite aerogel can be applied in the visible light catalytic degradation of water pollution.

KEYWORDS

ZnO, graphene, multi-walled carbon nanotube, aerogels, photocatalytic

Introduction

In recent years, with the rapid economic development and the increasing environmental pollution (Cui et al., 2020), the management of organic pollutants in water bodies has attracted great concern (Tang et al., 2022). Traditional methods of treating organic contaminants in wastewater include physical adsorption (Cui et al., 2022a; Das et al., 2022; Wang et al., 2022), chemical oxidation (Li et al., 2021; Yan et al., 2021; Zhang et al., 2021), and biological degradation (Sun K et al., 2021; Marciano et al., 2021; Zou et al., 2021). Compared with traditional methods, photocatalytic technology, as a new "green sustainable technology," features the advantages of environmental

protection, high efficiency, low energy consumption (Shen et al., 2016), no secondary pollution, and a wide range of applications, etc. It has rapidly emerged as a research hotspot for academics and industry in various countries. Meanwhile, many methods of photocatalyst surface modification modification such as adsorption, doping, and compounding have also emerged (Cui et al., 2019; Zhang and Cui, 2022).

The photocatalytic oxidation reaction uses semiconductors, such as titanium oxide (TiO_2) (Gopinath et al., 2020; Li et al., 2020), zinc oxide (ZnO) (Kegel et al., 2018), vanadium oxide (VO_2) (Zhu et al., 2018), molybdenum disulphide (MoS_2) (Yin et al., 2018; Sun and Schwingenschlögl, 2021a), etc., as catalysts (Sun and Schwingenschlögl, 2020). Under light irradiation, the electrons in the valence band (VB) of the semiconductor are excited and shifted to the conduction band (CB). The holes in the VB capture electrons from the hydroxyl groups in the surrounding environment, generating free radicals with strong oxidizing properties (Sun and Schwingenschlögl, 2021b; Shen et al., 2022a). The free radicals degrade the organic matter adhering to the surface of the semiconductor into carbon dioxide and water, thus achieving efficient purification of organic pollutants (Sun M.et al., 2021).

ZnO is the II-VI direct bandgap novel inorganic semiconductor material (Shen et al., 2022a). It has high photocatalytic activity (Yang et al., 2004; Sun C et al. 2018), cheap availability, and abundant reserves. So its application (Wang et al., 2018) for efficient photocatalysis (Yan et al., 2017) is one of the hottest research topics at present. However, due to the small size effect, ZnO can achieve high photocatalytic efficiency only at the nanoscale size. For nanoscale ZnO, it has a large specific surface area and high specific surface energy, and it is easy to agglomerate by itself. It has a strong surface polarity, which makes it difficult to disperse uniformly in the medium, resulting in few active sites for the photocatalytic oxidation of ZnO. In addition, ZnO exhibits the characteristics of a wide bandgap, whose bandgap is about 3.37 eV at room temperature (Shen et al., 2022b). As a result, it has poor electrical conductivity and a tendency to compound photo-generated electron-hole pairs, resulting in low quantum efficiency and a narrow response range to the solar spectrum. Moreover, although using metals or organic materials as loading materials for ZnO may compensate for these deficiencies, photo corrosion effects cause the loading materials to decompose and the shedding of catalytic particles, which may result in secondary pollution to the environment. These factors significantly limit the photocatalytic performance of ZnO. Therefore, solving the problems of complex dispersion, poor electrical conductivity, low solar light utilization, and severe photo corrosion of nanoscale ZnO is the challenge to achieve a significant increase in ZnO photocatalytic efficiency and improved cycling stability.

Graphene oxide (GO) has a high specific area. Its surface is rich in hydrophilic functional groups, and GO has a good affinity for dye molecules. So it is easy to achieve uniform dispersion of GO and adsorption of organic dye molecules dissolved in water. Removal of hydrophilic functional groups from the surface of GO, thereby reducing GO to graphene (G), can improve the electrical conductivity of the material.

It is reported that using G as a carrier for ZnO can improve its photocatalytic properties. Due to the good electrical conductivity of G, it creates a shallow potential Schottky barrier at the contact interface between ZnO and G. This reduces the compounding of photo-generated carriers in ZnO, thus improving the photocatalytic performance of ZnO. Sun et al. (2019) compounded ZnO with G. They found that this compound enabled photo-generated charge carrier transfer and effectively hindered electron-hole pair recombination, degrading 95.9% of methylene blue dye under UV irradiation conditions for 60 min. Pant et al. (2013) prepared Ag/ZnO/Reduced Graphene Oxide (RGO) composites, they found that it has suitable photocatalytic and antibacterial activities. The efficiency of perfect recovery and recycling of the catalyst after the reaction remains unchanged. In addition, Ahmad et al. (2018) combined nickel oxide and RGO to enhance the photocatalytic activity of the metal oxides. The formation of P-N heterojunctions and the strong interaction between nickel oxide and RGO dictated a high separation efficiency of photo-generated electrons and holes, enhancing the photodegradation activity of methylene blue dyes. However, the methods reported in these studies require UV light to achieve the photocatalytic reaction, indicating the need for severe conditions of use. Efficient photocatalytic reactions under visible light require more in-depth research.

Aerogels are nanomaterials with micro, mesoporous and microporous multilevel fractal network structures (Shen et al., 2019), which also can provide a good support skeleton for semiconductors. Besides, it can provide a special contact

TABLE 1 The chemical reagent for preparing the sample.

Reagent name	Chemical formula	Specification
Zinc acetate dihydrate	$C_4H_6O_4Zn{\cdot}2H_2O$	Analysis pure
Sodium hydroxide	NaOH	Analysis pure
Multi-walled Carbon Nanotubes (MCNT)	C	>95wt%
Graphene Oxide (GO)	—	>98wt%
Rhodamine B (RhB)	$C_{28}H_{31}ClN_2O_4$	Analysis pure

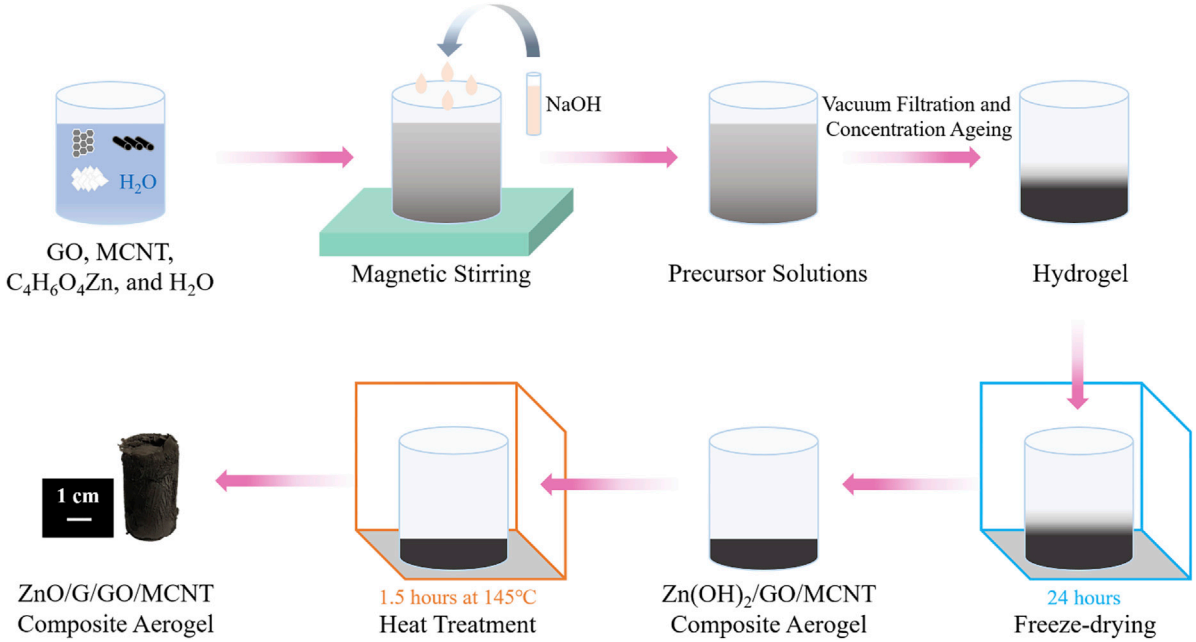

FIGURE 1
The preparation process of ZnO/G/GO/MCNT composite aerogel.

interface for photocatalytic reactions and accelerate the diffusion of photoelectrons in water (Li and Zhang, 2022).

Here, we have developed a method for assembling ZnO, G, GO, and Multi-Walled Carbon Nanotube (MCNT) into composite aerogels with a three-part porous structure. The composite material allows the nano-ZnO to be uniformly dispersed in water, reducing the compounding of photo-generated carriers in the ZnO, enhancing the electrical conductivity, and enabling efficient photocatalytic reactions to be developed under visible light conditions.

Experimental

Materials

The reagents used in this paper include Zinc acetate dihydrate, sodium hydroxide (NaOH), and Rhodamine B (RhB), which are all analytically pure and purchased from Sinopharm Chemical Reagent Co. Ltd., MCNT and GO are purchased from Suzhou Tanfeng Graphene Technology Co. Ltd., as shown in Table 1.

Preparation of composite aerogels

The preparation process of ZnO/G/GO/MCNT composite aerogel is shown in Figure 1. GO aqueous solution, MCNT aqueous solution, zinc acetate dihydrate solution, and distilled water mixed well at room temperature and pressure. Then, add NaOH solution in 4 equal parts, once at an interval of 1 min, 5–10 ml each time, with a drop acceleration rate of 5–10 drops per second, stirring continuously at room temperature to make the alkali fully react with the mixed solution. And precursor sols were obtained. The precursor sols were vacuum filtered to achieve hydrogels. Next, the hydrogel is placed in a freeze dryer for 1–2 h to ice entirely, then vacuum freeze-dried for 24 h to produce a $Zn(OH)_2$/GO/MCNT composite aerogel.

TABLE 2 The raw material ratio of aerogel.

Sample #	6 mg/ml MCNT (ml)	6 mg/ml GO (ml)	1 mol/L $C_4H_6O_4Zn$ (ml)	1 mol/L NaOH (ml)
1	0	0	2.5	4 × 0.625
2	40	0	2.5	4 × 0.625
3	20	40	2.5	4 × 0.625

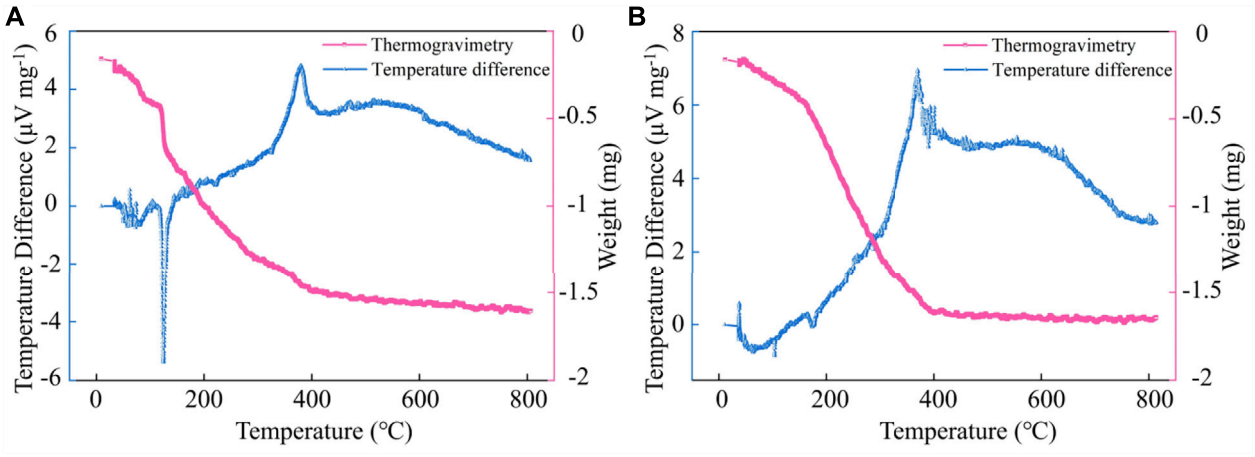

FIGURE 2
The TG and DTA curves of ZnO (sample #1) before **(A)** and after **(B)** 1.5 h heat treatment.

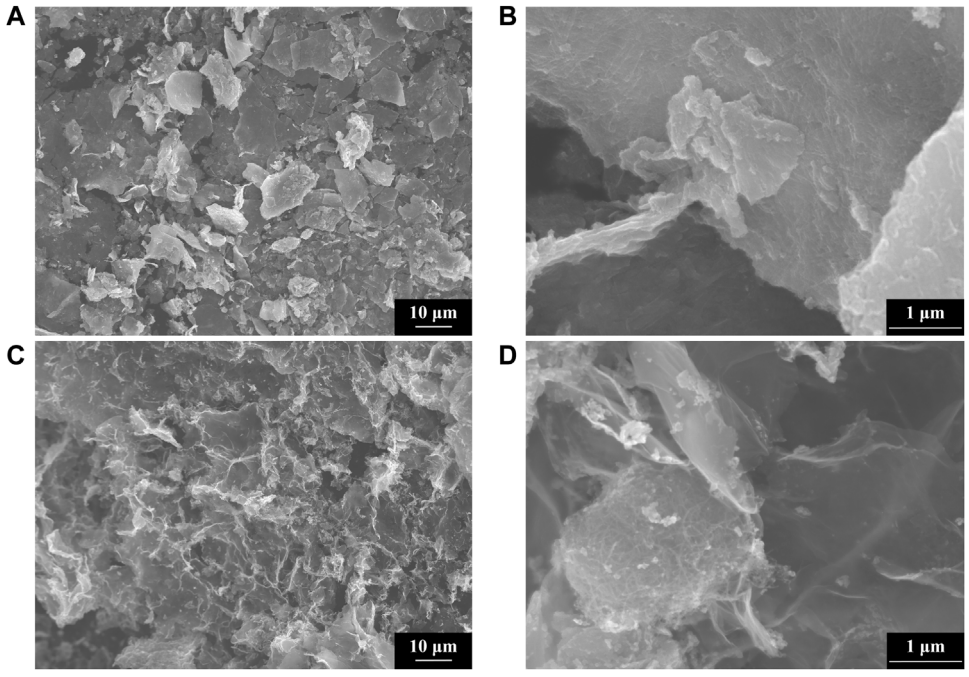

FIGURE 3
SEM of ZnO (sample A) at magnifications of **(A)** 1,000 and **(B)** 20,000 times. SEM of ZnO/G/GO/MCNT composite aerogel (sample C) at a multiplicity of **(C)** 1,000 and **(D)** 20,000 times.

Finally, the $Zn(OH)_2$/GO/MCNT composite aerogel is heat-treated in a thermostat or tube furnace for 1.5 h at 145°C. The $Zn(OH)_2$ decomposes to ZnO, while GO is partially restored to G, obtaining ZnO/G/GO/MCNT composite aerogel.

To accurately describe the properties of ZnO/G/GO/MCNT composite aerogels, Different sample ratios are shown in Table 2. ZnO (sample #1), ZnO/MCNT composite aerogel (sample #2), and ZnO/G/GO/MCNT composite aerogel (sample #3).

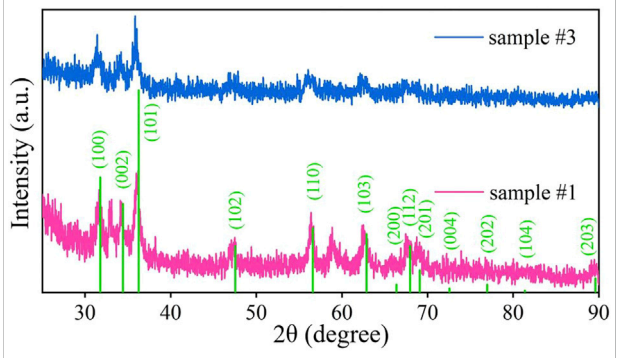

FIGURE 4
XRD images of ZnO (sample #1) and ZnO/G/GO/MCNT composite aerogel (sample #3). The green vertical line represents the peak position corresponding to the ZnO standard XRD standard card.

Characterization

The micrograph of samples was characterized by a scanning electron microscope (SEM, Japan Electronics Corporation, JSM-6700F). X-ray diffractometer (XRD, Shimadzu Japan, XRD-7000) was used to describe the internal atomic or molecular structure of samples. TG-DTA curve of the material using a comprehensive thermal analyzer (Beijing Hengjiu, HCT-3). UV-Visible spectrophotometer (Unico, United States, UV-2355) is used to measure the absorbance of samples at wavelengths between 200 and 800 nm.

The wavelength-absorbance curve is plotted, and the absorption edge is estimated by the tangent method. Using monochromatic light of 200–800 nm to irradiate the composite material, obtaining the light absorption of composite material at different wavelengths. The bandgap (E_g) is calculated as follows (Sauer et al., 2002):

$$E_g = \frac{hc}{\lambda_m} \tag{1}$$

where h, c, and λ_m denote Planck's constant, speed of light in a vacuum, and maximum wavelength of absorbed light, respectively. λ_m can be estimated from the UV-Vis absorption spectrum. The absorption efficiency of composite aerogels for sunlight can be obtained by calculating the proportion of wavelengths less than λ_m in the solar range.

The photocatalytic activity of the resulting composite aerogel was investigated by the rapid degradation of RhB under visible light radiation. Firstly, 20 mg of the samples were added into a 100 ml range quartz beaker, and add 50 ml of RhB staining solution at a concentration of 10 mg/L. Secondly, by the water bath method, maintain a speed of 1,000 r/min at 30°C with a heated magnetic mixer to mix well. At the same time, the dark reaction under shade for 30 min to reach adsorption equilibrium. After that, 5 ml of solution from the dark reaction system was taken with a pipette for testing. Then, it was switched on a 350 W xenon cold light source for light reaction, and the light source 13.5 cm from the bottom of the beaker. 5 ml of solution is removed from the photoreaction system every 5 min with a pipette for testing. After six extractions, the test samples were centrifuged, and the absorbance of the supernatant was measured.

According to the Beer-Lambert law, the absorbance (A) of a dye solution is proportional to its concentration. In addition, the dye removal rates (D) are computed as follows (Cui et al., 2022b):

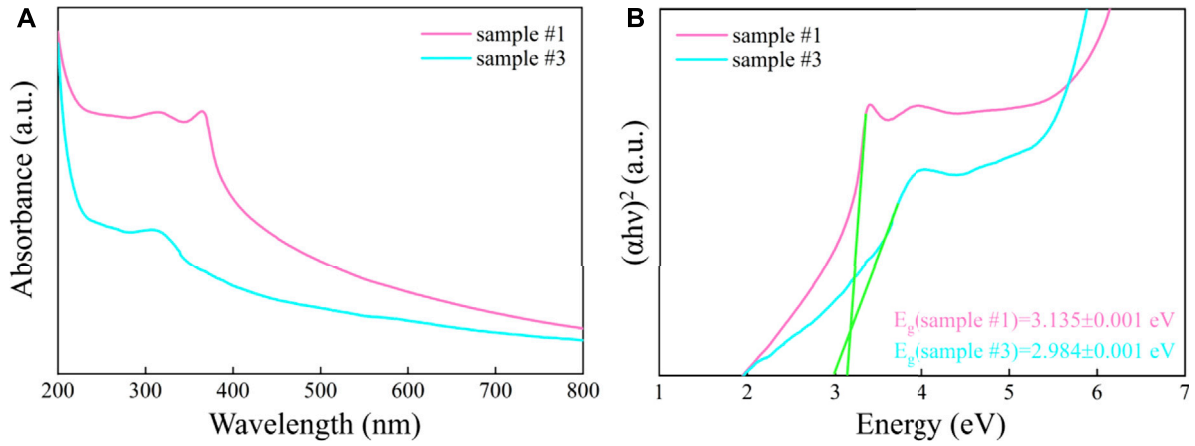

FIGURE 5
(A) The UV-Vis spectrum and **(B)** the relation between Kubelka-Munk function and photon energy of ZnO (sample #1) and ZnO/G/GO/MCNT composite aerogel (sample #3).

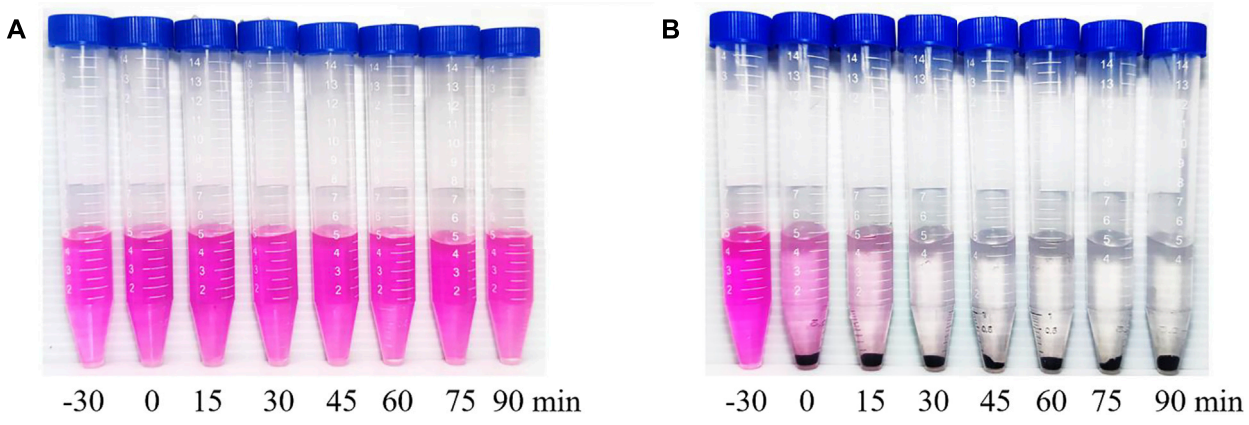

FIGURE 6
Experimental results of photocatalytic degradation of RhB by **(A)** ZnO (sample #1) and by **(B)** ZnO/G/GO/MCNT composite aerogel (sample #3).

$$D = \left(1 - \frac{C}{C_0}\right) \times 100\% = \left(1 - \frac{A_t}{A_0}\right) \times 100\% \quad (2)$$

where C_0, C, A_0, and A_t represent the initial concentration of the fuel solution, the concentration of the dye solution after t minutes, the initial absorbance of the dye solution, and the absorbance of the dye solution after t minutes, respectively. The value of A_t/A_0 can be calculated from the relative absorption intensity of the UV-Vis absorption spectrum.

The photocatalytic degradation process of dyes mainly consists of mass transfer and photocatalytic reactions. The kinetic constants of photocatalytic reaction degradation are described by the Langmuir–Hinshelwood model as follows (Sauer et al., 2002):

$$R = -\frac{dC}{dt} = \frac{\kappa K C}{1 + KC} \quad (3)$$

where R, κ, K, and C represent the total reaction rate of the dye at time t, the Langmuir rate constant, the equilibrium constant for the adsorption and desorption of the paint on the catalyst, and the concentration of the dye at time t, respectively. The Eq 3 can be simplified to a primary reaction kinetic model when the concentration of the paint is relatively low. The calculation is as follows (Cui et al., 2022b):

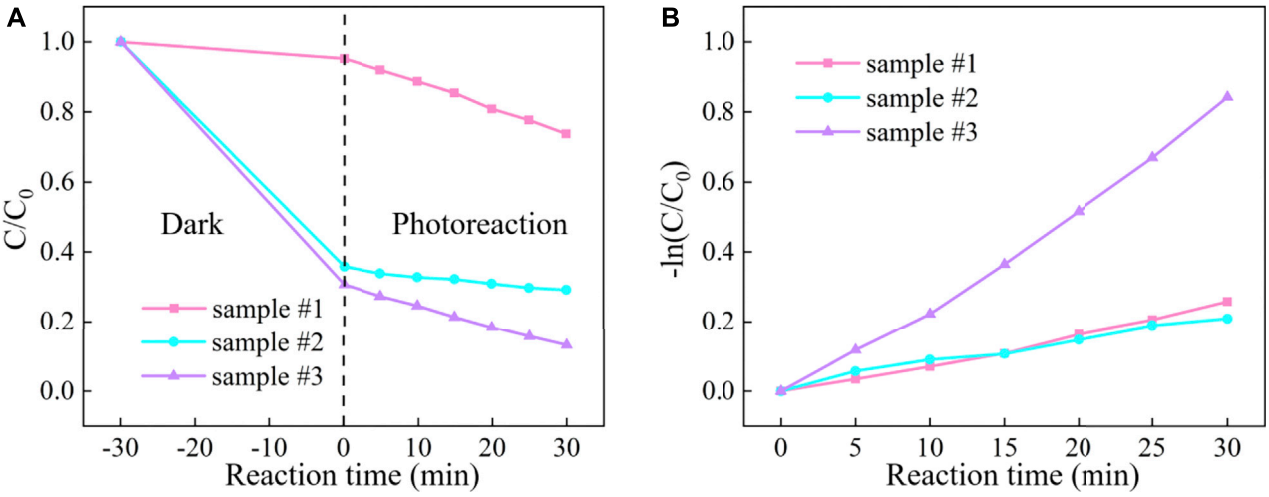

FIGURE 7
(A) RhB degradation curve and **(B)** reaction kinetic curve under visible light for ZnO (sample #1), ZnO/MCNT composite aerogel (sample #2), and ZnO/G/GO/MCNT composite aerogel (sample #3).

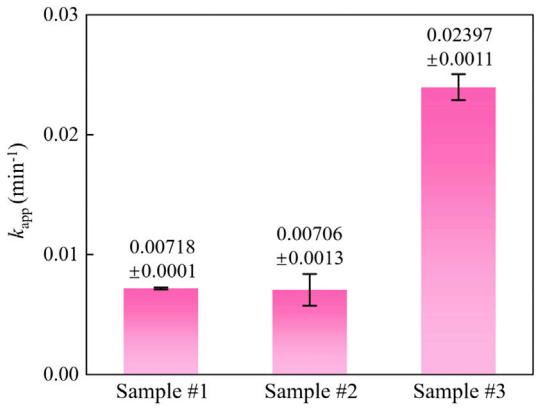

FIGURE 8
Reaction kinetic constant histogram for ZnO (sample #1), ZnO/MCNT composite aerogel (sample #2), and ZnO/G/GO/MCNT composite aerogel (sample #3).

$$\ln \frac{C_0}{C} = \kappa K t = k_{app} t \quad (4)$$

where k_{app} indicates the primary reaction rate constant. Linear fit of ln (C_0/C) and t, and the slope is k_{app}, which can be used to characterize the photocatalytic reaction efficiency quantitatively.

Results and discussion

Morphology and compositional characterization

To accurately describe the thermal decomposition of $Zn(OH)_2$, the Thermogravimetry (TG) and Temperature difference (DTA) curves of sample #1 before and after heat treatment are shown in Figures 2A,B, respectively. From Figure 2A, It can be observed that an endothermic peak appears at 124°C, which is mainly due to the absorption of heat by the thermal decomposition of $Zn(OH)_2$, and the overall weight of the sample is decreasing. From Figure 2B, No vigorous endothermic or exothermic peaks were observed in the range of 0–150°C. Altuntasoglu et al. (2010) performed TG-DTA analysis on $Zn(OH)_2$. They found an endothermic peak appeared at 134°C, and the final decomposition product was ZnO. Related reports are consistent with our results. Therefore, it proved that $Zn(OH)_2$ in the $Zn(OH)_2$/GO/MCNT composite aerogel could be converted entirely into ZnO after heat treatment at 145°C.

The Scanning Electron Microscope (SEM) of sample #1 is shown in Figures 3A,B, respectively. Figure 3C,D exhibit the SEM of sample #3, respectively. By Figures 3A,C, it can be observed that the morphology uniformity of sample #3 was enhanced after adding graphene and Multi-walled carbon nanotubes. The dense adhesion of Multi-walled carbon nanotubes and ZnO particles to graphene sheets was observed under the SEM graph of Figures 3B,C, and ZnO/G/GO/MCNT composite aerogel (sample #3) effectively solved the clustering problem of ZnO.

The XRD patterns of samples #1 and #3 are shown in Figure 4. The test range is 2θ = 25–90°. It can be observed that sample #3 has prominent narrow characteristic peaks at 31.42°, 34.2°, and 36.04°. Compared with the ZnO standard card, it is found that the corresponding crystal planes are (100), (002), and (101). In addition, broad characteristic peaks appear at 47.62°, 55.72°, 62.72°, and 67.58°, corresponding to the (102), (110), (103), and 112) crystal planes, respectively. It is verified that Z $(OH)_2$, in sample #3, has been completely converted into ZnO. It is consistent with the results of the TG-DTA analysis.

Optical absorption and photocatalytic degradation of RhB

To demonstrate the change in the response range of the ZnO/G/GO/MCNT composite aerogel to the solar spectrum, we further studied the UV-Vis absorption spectra of sample #1 and sample #3, which are shown in Figure 5A. The relation between the Kubelka-Munk function and photon energy is shown in Figure 5B. For sample #1, the tangent (extrapolation method) calculates that the absorption edge is around 396 nm. For sample #3, its absorption edge is at 416 nm. Meanwhile, the band gap of samples #1 and #3 are calculated to be 3.135 and 2.984 eV, respectively. The reduction of the band gap may be due to the adsorption between different materials (Sun M et al., 2018; Cui et al., 2021a; Cui et al., 2021b). This will improve the photocatalytic degradation of pollutants by the composite material under visible light conditions.

The photocatalytic efficiency is the focus of our inquiry (Cui et al., 2022b). Sample #3 was subjected to photocatalytic experiments, and its photocatalytic activity was evaluated by comparing its photocatalytic degradation rate to RhB. The experimental results are shown in Figure 6B. −30–0 min is the dark reaction stage, and the light reaction starts from 0 min. To reach the experimental results, the same photocatalytic efficiency experiment was applied to sample #1 (Figure 6A). For sample #3, photocatalytic experiments proved that RhB achieved efficient degradation after 30 min of visible light irradiation.

The reaction curves and photocatalytic kinetics curves of different samples are depicted in Figures 7A,B, respectively. The results indicated that RhB adhered to the sample surface by adsorption within 30 min of the dark reaction phase until the adsorption and desorption reached equilibrium. At this stage, it mainly relies on the van der Waals forces between molecules to reach equilibrium quickly, and the adsorption or desorption process is physical adsorption. Besides, compared with sample

#1, the physical adsorption is enhanced due to the introduction of MCNT, G, and GO. In the photoreaction stage, after 30 min, the degradation efficiency of ZnO (sample #1) was only 26.3%, and the degradation effect was the worst. The degradation efficiency of ZnO/MCNT composite aerogel (sample #2) was 70.8%, and the degradation effect was good. The degradation efficiency of ZnO/G/GO/MCNT composite aerogel (sample #3) is as high as 86.8%, and the degradation effect is the best. Cui et al. (2022b) reported a degradation rate of 99.4% at 90 min for g-C_3N_4/MoS_2 composites. Similar results can be obtained based on the trend of our results. In addition, it can be observed from Figure 7B that the degradation rate of sample #3 accelerates from the photoreaction for 10 min, and it is also the fastest overall among all samples. Figure 8 more intuitively compares the kinetic reaction constants of each sample. It can be observed that the reaction kinetic constant of ZnO/G/GO/MCNT (sample #3) is 0.02497, which is larger than that of ZnO (0.00718, sample #1) and ZnO/MCNT composite aerogel (0.00706, sample #2). In conclusion, compared with single ZnO, the physical adsorption effect, photocatalytic degradation efficiency, and photocatalytic degradation rate of the ZnO/G/GO/MCNT composite aerogels were significantly improved. And it have higher application value.

Conclusion

ZnO/G/GO/MCNT composite aerogels with a three-dimensional porous structure were prepared by the sol-gel method under average temperature and alkaline conditions, combined with a freeze-drying and heat treatment process. The photocatalytic degradation of RhB was mainly investigated. The SEM test results show that the morphology uniformity of the ZnO/G/GO/MCNT composite aerogel is significantly enhanced, effectively solving the agglomeration problem of MCNT and ZnO. TG-DTA analysis and XRD pattern showed that $Zn(OH)_2$ was wholly decomposed into ZnO after heat treatment. The physical adsorption capacity of ZnO/G/GO/MCNT for RhB is significantly improved. And its total degradation efficiency can reach 86.8%, which is 3.3 times higher than that of ZnO (26.3%), indicating that the ZnO/G/GO/MCNT composite aerogels have high photocatalytic activity. In addition, the synergistic effect of ZnO and G can also enable photogenerated carrier transfer to hinder electron-hole pair recombination, enhancing the photocatalytic activity effectively. Therefore, the ZnO/G/GO/MCNT composite aerogel can be applied in the visible light catalytic degradation of water pollution.

Data availability statement

The original contributions presented in the study are included in the article/supplementary material, further inquiries can be directed to the corresponding authors.

Author contributions

YS, ZC, and EL contributed to conception and design of the study. ZY organized the database. FC and DM performed the statistical analysis. YS and ZY wrote the first draft of the manuscript. YB, SZ, and JD wrote sections of the manuscript. All authors contributed to manuscript revision, read, and approved the submitted version.

Funding

This work was funded by Natural Science Basic Research Program of Shaanxi (Program No. 2022JM-176), Scientific Research Program Funded by Shaanxi Provincial Education Department (Program No. 21JK0789), the Opening Project of Shanghai Key Laboratory of Special Artificial Microstructure Materials and Technology (Program No. ammt2020A-6), College Students' Innovative Entrepreneurial Training Plan Program (Program No. 202210700008 and Program No. 202210700105), the National Natural Science Foundation of China (No. 12104362) and China Postdoctoral Science Foundation (Program No. 2020M683684XB).

Conflict of interest

The authors declare that the research was conducted in the absence of any commercial or financial relationships that could be construed as a potential conflict of interest.

Publisher's note

All claims expressed in this article are solely those of the authors and do not necessarily represent those of their affiliated organizations, or those of the publisher, the editors and the reviewers. Any product that may be evaluated in this article, or claim that may be made by its manufacturer, is not guaranteed or endorsed by the publisher.

References

Ahmad, J., Majid, K., and Dar, M. A. (2018). Controlled synthesis of p-type NiO/n-type GO nanocomposite with enhanced photocatalytic activity and study of temperature effect on the photocatalytic activity of the nanocomposite. *Appl. Surf. Sci.* 457, 417–426. doi:10.1016/j.apsusc.2018.06.200

Altuntasoglu, O., Matsuda, Y., Ida, S., and Matsumoto, Y. (2010). Syntheses of zinc oxide and zinc hydroxide single nanosheets. *Chem. Mat.* 22 (10), 3158–3164. doi:10.1021/cm100152q

Cui, Z., Luo, Y., Yu, J., and Xu, Y. (2021a). Tuning the electronic properties of $MoSi_2N_4$ by molecular doping: A first principles investigation. *Phys. E Low-dimensional Syst. Nanostructures* 134, 114873. doi:10.1016/j.physe.2021.114873

Cui, Z., Wang, M., Lyu, N., Zhang, S., Ding, Y., and Bai, K. (2021b). Electronic, magnetism and optical properties of transition metals adsorbed puckered arsenene. *Superlattices Microstruct.* 152, 106852. doi:10.1016/j.spmi.2021.106852

Cui, Z., Ren, K., Zhao, Y., Wang, X., Shu, H., Yu, J., et al. (2019). Electronic and optical properties of van der Waals heterostructures of g-GaN and transition metal dichalcogenides. *Appl. Surf. Sci.* 492, 513–519. doi:10.1016/j.apsusc.2019.06.207

Cui, Z., Wang, X., Ding, Y., Li, E., Bai, K., Zheng, J., et al. (2020). Adsorption of CO, NH_3, no, and NO_2 on pristine and defective g-GaN: Improved gas sensing and functionalization. *Appl. Surf. Sci.* 530, 147275. doi:10.1016/j.apsusc.2020.147275

Cui, Z., Zhang, S., Wang, L., and Yang, K. (2022a). Optoelectronic and magnetic properties of transition metals adsorbed Pd_2Se_3 monolayer. *Micro Nanostructures* 167, 207260. doi:10.1016/j.micrna.2022.207260

Cui, Z., Wu, H., Bai, K., Chen, X., Li, E., Shen, Y., et al. (2022b). Fabrication of a g-C_3N_4/MoS_2 photocatalyst for enhanced RhB degradation. *Phys. E Low-dimensional Syst. Nanostructures* 144, 115361. doi:10.1016/j.physe.2022.115361

Das, R., Lindström, T., Sharma, P. R., Chi, K., and Hsiao, B. S. (2022). Nanocellulose for sustainable water purification. *Chem. Rev.* 1 (2), 8936–9031. doi:10.1021/acs.chemrev.1c00683

Gopinath, K. P., Madhav, N. V., Krishnan, A., Malolan, R., and Rangarajan, G. (2020). Present applications of titanium dioxide for the photocatalytic removal of pollutants from water: A review. *J. Environ. Manag.* 270, 110906. doi:10.1016/j.jenvman.2020.110906

Kegel, J., Zubialevich, V. Z., Schmidt, M., Povey, I. M., and Pemble, M. E. (2018). Effect of surface and defect chemistry on the photocatalytic properties of intentionally defect-rich ZnO nanorod arrays. *ACS Appl. Mat. Interfaces* 10 (21), 17994–18004. doi:10.1021/acsami.8b05130

Li, R., Li, T., and Zhou, Q. (2020). Impact of titanium dioxide (TiO_2) modification on its application to pollution treatment-a review. *Catalysts* 10 (7), 804. doi:10.3390/catal10070804

Li, Y., Dong, H., Li, L., Tang, L., Tian, R., Li, R., et al. (2021). Recent advances in waste water treatment through transition metal sulfides-based advanced oxidation processes. *Water Res.* 192, 116850. doi:10.1016/j.watres.2021.116850

Li, Y., and Zhang, X. (2022). Electrically conductive, optically responsive, and highly orientated $Ti_3C_2T_x$ MXene aerogel fibers. *Adv. Funct. Mat.* 32 (4), 2107767. doi:10.1002/adfm.202107767

Marciano, J. S., Ferreira, R. R., de Souza, A. G., Barbosa, R. F., de Moura Junior, A. J., and Rosa, D. S. (2021). Biodegradable gelatin composite hydrogels filled with cellulose for chromium (VI) adsorption from contaminated water. *Int. J. Biol. Macromol.* 181, 112–124. doi:10.1016/j.ijbiomac.2021.03.117

Pant, H. R., Pant, B., Kim, H. J., Amarjargal, A., Park, C. H., Tijing, L. D., et al. (2013). A green and facile one-pot synthesis of Ag-ZnO/RGO nanocomposite with effective photocatalytic activity for removal of organic pollutants. *Ceram. Int.* 39 (5), 5083–5091. doi:10.1016/j.ceramint.2012.12.003

Sauer, T., Neto, G. C., Jose, H., and Moreira, R. (2002). Kinetics of photocatalytic degradation of reactive dyes in a TiO2 slurry reactor. *J. Photochem. Photobiol. A Chem.* 149 (1-3), 147–154. doi:10.1016/s1010-6030(02)00015-1

Shen, Y., Du, A., Cheng, F., Li, X., Liu, C., Liu, Y., et al. (2019). Preparation and characterization of inhomogeneous RF aerogels with continuously varying densities. *J. Solgel. Sci. Technol.* 90 (3), 478–486. doi:10.1007/s10971-019-04989-2

Shen, Y., Du, A., Li, X., Huang, X., Ye, J., Xie, Z., et al. (2016). Preparation and optimization of aerogel flyer-plates with graded density. *Mater. Des.* 110, 225–232. doi:10.1016/j.matdes.2016.07.142

Shen, Y., Yuan, Z., Cui, Z., Ma, D., Yuan, P., Yang, K., et al. (2022). The electronic properties of g-ZnO modulated by organic molecules adsorption. *Crystals* 12 (7), 882. doi:10.3390/cryst12070882

Shen, Y., Yuan, Z., Cui, Z., Ma, D., Yang, K., Dong, Y., et al. (2022b). Electronic, magnetic, and optical properties of metal adsorbed g-ZnO systems. *Front. Chem.* 10, 943902. doi:10.3389/fchem.2022.943902

Sun, C., Xu, Q., Xie, Y., Ling, Y., and Hou, Y. (2018). Designed synthesis of anatase-TiO_2 (B) biphase nanowire/ZnO nanoparticle heterojunction for enhanced photocatalysis. *J. Mat. Chem. A Mat.* 6 (18), 8289–8298. doi:10.1039/c7ta10274g

Sun, M., Chou, J. P., Gao, J., Cheng, Y., Hu, A., Tang, W., et al. (2018). Exceptional optical absorption of buckled arsenene covering a broad spectral range by molecular doping. *ACS omega* 3 (8), 8514–8520. doi:10.1021/acsomega.8b01192

Sun, H., Cui, M., Chen, C., Zhu, S., Zhang, L., and Shang, P. (2019). Study on mechanism of photocatalytic performance enhancement for RGO loaded nano-ZnO composites. *Mater. Sci.* 9 (4), 428–435. doi:10.12677/ms.2019.94055

Sun, K., Hong, D., Liu, J., Latif, A., Li, S., Chu, G., et al. (2021). *Trametes versicolor* laccase-assisted oxidative coupling of estrogens: Conversion kinetics, linking mechanisms, and practical applications in water purification. *Sci. Total Environ.* 782, 146917. doi:10.1016/j.scitotenv.2021.146917

Sun, M., Luo, Y., Yan, Y., and Schwingenschlogl, U. (2021). Ultrahigh carrier mobility in the two-dimensional semiconductors B_8Si_4, B_8Ge_4, and B_8Sn_4. *Chem. Mat.* 33 (16), 6475–6483. doi:10.1021/acs.chemmater.1c01824

Sun, M., and Schwingenschlögl, U. (2020). δ-CS: A direct-band-gap semiconductor combining auxeticity, ferroelasticity, and potential for high-efficiency solar cells. *Phys. Rev. Appl.* 14 (4), 044015. doi:10.1103/physrevapplied.14.044015

Sun, M., and Schwingenschlögl, U. (2021a). Structure prototype outperforming MXenes in stability and performance in metal-ion batteries: A high throughput study. *Adv. Energy Mat.* 11 (14), 2003633. doi:10.1002/aenm.202003633

Sun, M., and Schwingenschlögl, U. (2021b). Unique omnidirectional negative Poisson's ratio in δ-phase carbon monochalcogenides. *J. Phys. Chem. C* 125 (7), 4133–4138. doi:10.1021/acs.jpcc.0c11555

Tang, W., Pei, Y., Zheng, H., Zhao, Y., Shu, L., and Zhang, H. (2022). Twenty years of China's water pollution control: Experiences and challenges. *Chemosphere* 295, 133875. doi:10.1016/j.chemosphere.2022.133875

Wang, F., Wu, P., Shu, L., Huang, D., and Liu, H. (2022). High-efficiency adsorption of Cd (II) and Co (II) by ethylenediaminetetraacetic dianhydride-modified orange peel as a novel synthesized adsorbent. *Environ. Sci. Pollut. Res.* 29 (17), 25748–25758. doi:10.1007/s11356-021-17501-7

Wang, S., Kuang, P., Cheng, B., Yu, J., and Jiang, C. (2018). ZnO hierarchical microsphere for enhanced photocatalytic activity. *J. Alloys Compd.* 741, 622–632. doi:10.1016/j.jallcom.2018.01.141

Yan, B., Wang, Y., Jiang, X., Liu, K., and Guo, L. (2017). Flexible photocatalytic composite film of ZnO-microrods/polypyrrole. *ACS Appl. Mat. Interfaces* 9 (34), 29113–29119. doi:10.1021/acsami.7b08462

Yan, H., Lai, C., Wang, D., Liu, S., Li, X., Zhou, X., et al. (2021). *In situ* chemical oxidation: Peroxide or persulfate coupled with membrane technology for wastewater treatment. *J. Mat. Chem. A Mat.* 9 (20), 11944–11960. doi:10.1039/d1ta01063h

Yang, J. L., An, S. J., Park, W. I., Yi, G. C., and Choi, W. (2004). Photocatalysis using ZnO thin films and nanoneedles grown by metal-organic chemical vapor deposition. *Adv. Mat.* 16 (18), 1661–1664. doi:10.1002/adma.200306673

Yin, L., Hai, X., Chang, K., Ichihara, F., and Ye, J. (2018). Synergetic exfoliation and lateral size engineering of MoS2 for enhanced photocatalytic hydrogen generation. *Small* 14 (14), 1704153. doi:10.1002/smll.201704153

Zhang, L., and Cui, Z. (2022). Theoretical study on electronic, magnetic and optical properties of non-metal atoms adsorbed onto germanium carbide. *Nanomaterials* 12 (10), 1712. doi:10.3390/nano12101712

Zhang, M., Yang, Y., An, X., and Hou, L.-a. (2021). A critical review of g-C_3N_4-based photocatalytic membrane for water purification. *Chem. Eng. J.* 412, 128663. doi:10.1016/j.cej.2021.128663

Zhu, M., Sun, Z., Fujitsuka, M., and Majima, T. (2018). Z-scheme photocatalytic water splitting on a 2D heterostructure of black phosphorus/bismuth vanadate using visible light. *Angew. Chem. Int. Ed. Engl.* 57 (8), 2182–2186. doi:10.1002/ange.201711357

Zou, Y., Wu, X., Li, H., Yang, L., Zhang, C., Wu, H., et al. (2021). Metal-phenolic network coated cellulose foams for solar-driven clean water production. *Carbohydr. Polym.* 254, 117404. doi:10.1016/j.carbpol.2020.117404

frontiers | Frontiers in Chemistry

TYPE Mini Review
PUBLISHED 25 August 2022
DOI 10.3389/fchem.2022.996344

OPEN ACCESS

EDITED BY
Guangzhao Wang,
Yangtze Normal University, China

REVIEWED BY
Hao Guo,
Hebei Normal University of Science and Technology, China
Junjie He,
Charles University, Czechia

*CORRESPONDENCE
Dandan Wang,
wangdandan@swu.edu.cn

SPECIALTY SECTION
This article was submitted to Physical Chemistry and Chemical Physics, a section of the journal Frontiers in Chemistry

RECEIVED 17 July 2022
ACCEPTED 26 July 2022
PUBLISHED 25 August 2022

CITATION
Wang J and Wang D (2022), Two-dimensional spin-gapless semiconductors: A mini-review. *Front. Chem.* 10:996344. doi: 10.3389/fchem.2022.996344

Two-dimensional spin-gapless semiconductors: A mini-review

Jianhua Wang and Dandan Wang*

School of Physical Science and Technology, Southwest University, Chongqing, China

In the past decade, two-dimensional (2D) materials and spintronic materials have been rapidly developing in recent years. 2D spin-gapless semiconductors (SGSs) are a novel class of ferromagnetic 2D spintronic materials with possible high Curie temperature, 100% spin-polarization, possible one-dimensional or zero-dimensional topological signatures, and other exciting spin transport properties. In this mini-review, we summarize a series of ideal 2D SGSs in the last 3 years, including 2D oxalate-based metal-organic frameworks, 2D single-layer Fe_2I_2, 2D Cr_2X_3 (X = S, Se, and Te) monolayer with the honeycomb kagome (HK) lattice, 2D $CrGa_2Se_4$ monolayer, 2D HK Mn–cyanogen lattice, 2D MnNF monolayer, and 2D Fe_4N_2 pentagon crystal. The mini-review also discusses the unique magnetic, electronic, topological, and spin-transport properties and the possible application of these 2D SGSs. The mini-review can be regarded as an improved understanding of the current state of 2D SGSs in recent 3 years.

KEYWORDS

two-dimensional material systems, spin-gapless materials, Dirac point, nodal line, spin transport properties

1 Introduction

Due to their unique physical and chemical characteristics induced by low-dimensionality and electronic constraints, as well as their potential applications in spintronics, high-temperature ferromagnetic two-dimensional (2D) materials (Lee et al., 2010; Li and Yang, 2014; Wang et al., 2016a; Zhou et al., 2016; Ashton et al., 2017; Benmansour et al., 2017; Gong and Zhang, 2019; Kim et al., 2019; Zhou et al., 2019; Chen et al., 2020; Torelli et al., 2020; Xu et al., 2020; Zhang et al., 2021a; Tang et al., 2021; Miao and Sun, 2022) have attracted a great deal of attention in recent years. Nevertheless, the majority of prepared 2D materials that resemble graphene are not magnetic (Wang et al., 2012; Liu and Zhou, 2019), magnetic ordering has not been observed in the 2D material family for more than 10 years since the discovery of graphene (Hashimoto et al., 2004; Novoselov et al., 2004; Huang et al., 2017) in 2004. Recently, only some intriguing 2D magnetic materials, such as CrI_3 (Huang et al., 2017), $CrGeTe_3$ (Gong et al., 2017; Wang et al., 2018a), Fe_3GeTe_2 (Deng et al., 2018a; Fei et al., 2018), VSe_2 (Bonilla et al., 2018) and $CrTe_2$ (Sun et al., 2020a), have been experimentally realized. Furthermore, it should be noticed that, the 2D magnetic material is far from the actual spintronic application at room temperature due to the low Curie temperature T_c and low spin polarization. Thus, it is significant and urgent

to develop ferromagnetic 2D materials with high spin-polarization and T_c via theory and experiment.

Among different types of 2D ferromagnetic materials, 2D spin-gapless semiconductors (SGSs) (Li et al., 2009; Zhang et al., 2015; Gao et al., 2016; Zhu and Li, 2016; Wang et al., 2017a; He et al., 2017; Lei et al., 2017; Wang, 2017; Deng et al., 2018b; Wang et al., 2018b; Wu et al., 2020a; Yang et al., 2020a; Wu et al., 2020b; Deng et al., 2020; Feng et al., 2020; Li et al., 2020; Nadeem et al., 2020; Rani et al., 2020; Wang et al., 2020; Yue et al., 2020; Şaşıoğlu et al., 2020; Feng et al., 2021; Phong and Nguyen, 2022) are ideal candidates for high-efficient spintronic devices. Wang (Wang, 2008) first proposed the concept of SGSs in 2008, and the SGSs can be viewed as a bridge to connect the magnetic semiconductors (Haas, 1970; Dietl, 2010; Sato et al., 2010) and half-metals (Wang et al., 2016b; Wang et al., 2017b; Wang et al., 2017c; Liu et al., 2017; Wang et al., 2018c; Han et al., 2019; Wang et al., 2019; Yang et al., 2020b; Tang et al., 2021; Yang et al., 2021). It is well known that the SGSs (Wang et al., 2018b) can host parabolic and linear dispersion between energy and momentum (see Figure 1A–H). Moreover, SGSs (Wang, 2017) can be categorized into four different types depending on the touching types of the valence band maximum (VBM) and the conduction band minimum (CBM) in both spin directions. We take the SGSs with parabolic dispersion as examples to introduce the above four types (see Figure 1A–D). In Figure 1A, one finds the CBM and VBM touch each other at the Fermi level (FL) in the spin-up (SU) channel, whereas a semiconducting gap appears in the spin-down (SD) channel. The VBM in the SD channel touches the FL. Figure 1B shows the semiconducting gaps in both spin channels. However, the VBM in the SU channel

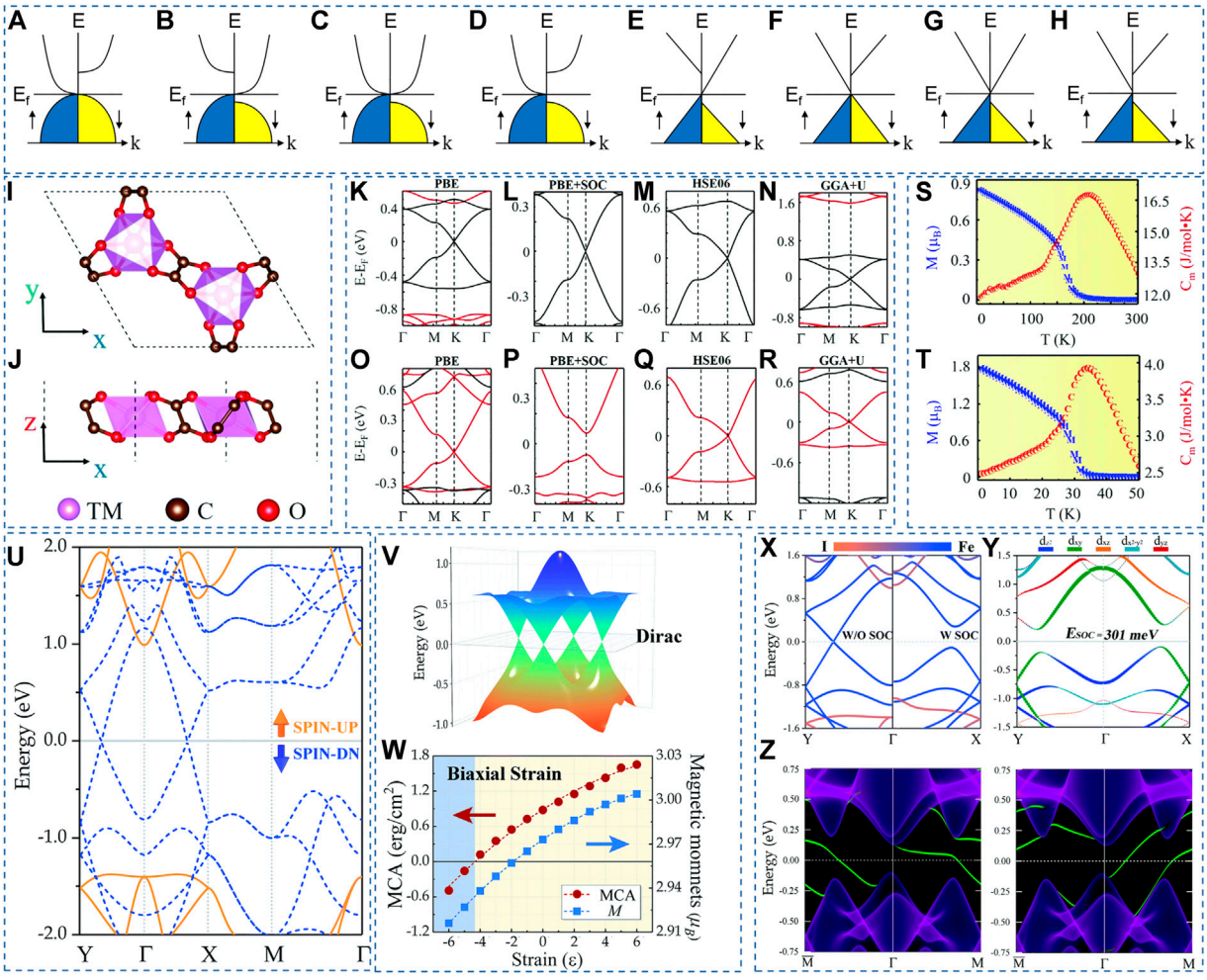

FIGURE 1
(A–H) Different SGSs. **(I–J)** Top and side views of the $TM_2(C_2O_4)_3$ structure. The calculated band structures (BSs) of $Ni_2(C_2O_4)_3$ **(K–N)** and $Re_2(C_2O_4)_3$ **(O–R)** with different methods. M and C_m of $Ni_2(C_2O_4)_3$ **(S)** and $Re_2(C_2O_4)_3$ **(T)** as a function of temperature. **(I–T)** Reproduced from (Xing et al., 2022) with permission from RSC publishing **(U)** BS of the Fe_2I_2 monolayer. **(V)** 3D plot of Dirac point **(W)** Magnetic anisotropy and magnetic moment of the Fe_2I_2 as a function of biaxial strain. **(X)** and **(Y)** atom-resolved BSs without and with SOC. **(Z)** Edge states of 2D Fe_2I_2 **(U–Z)** Reproduced from (Sun et al., 2020b) with permission from RSC publishing.

touches the CBM in the SD channel, forming an indirect zero-gap state. The case of Figure 1C is similar to that of Figure 1B. However, the CBM touches the FL in the SD channel. Figure 1D is the standard form of SGSs with parabolic dispersion: a zero-gap in the SU channel and a semiconducting gap in the SD channel. Similarly, the cases of SGSs with linear dispersion are listed in Figure 1E–H. Note that, for cases I, III and IV (see Figures 1A,C, D, E, G, F), depending on how the VBM and CBM touch each other, the zero-gap in one spin channel can be direct (VBM and CBM touch each other at the same *k* point) or indirect (they touch each other at different *k* points) (Wang et al., 2020).

SGSs may host the following advantages: 1) the excitation of electrons from the valence band to the conduction band requires only a tiny amount of energy. 2) the excited carriers (electrons and holes) can be fully spin-polarized (S-P) simultaneously. 3) one can use the Hall effect to separate the 100% S-P electrons and holes. 4) for the case II SGSs (See Figure 1B and Figure 1F), one can control the gate voltage to manipulate the SU and SD electrons and holes. 5) researchers proposed nodal point SGSs and nodal line SGSs in 2D and 3D materials, which can be excellent candidates for studying the relationship between topological and spintronics. For example, Dirac SGSs may induce low energy consumption and ultrafast transport because of their unique linear band dispersion. Hence, Dirac SGSs can cohost 100% spin-polarization and linear Dirac point at the FL.

Although there were several reviews on the research topic of SGSs, these articles (Wang, 2017; Wang et al., 2020; Yue et al., 2020) all focused on SGSs from 2008 to 2020. To our best knowledge, other researchers have not reviewed the recent advances in 2D SGSs from 2020 to 2022. From 2020 to 2022, a series of ideal 2D SGSs are proposed via first-principles calculations, and the related novel properties are also investigated. Therefore, for spintronics and topology, a mini-review of 2D SGSs seems necessary. It is noteworthy that Dirac SGSs and nodal line SGSs are new cross concepts in spintronics and topology. Although in almost all the reported 2D (2D) materials, the twofold degenerate nodal points in their band structures are misused as "Dirac points" due to a historical issue (Yang, 2016). The correct naming of these nodal points should be "Weyl", and then each twofold degenerate point is described by the Weyl model in 2D. This review follows the common practice of using "Dirac point" SGSs in 2D materials.

In this review, we divided 2D SGSs into four classes: 2D SGSs with direct band crossing points at high-symmetry (H-S) points and along the H-S paths, 2D SGSs with indirect zero-gap states, and 2D SGSs with zero-gap nodal ring states. Note that this is the first time to review SGSs based on classification as mentioned above.

Herein, we will review the most recent investigations of 2D SGSs from 2020 to 2022. Section 2 introduces the proposed 2D SGSs with band crossing points at the H-S point. Section 3 introduces the proposed 2D SGSs with band crossing points along the H-S paths and their unique behaviors. Section 3 reviews 2D SGSs with indirect zero-gap states and their possible application. Section 4 introduces the case of 2D SGSs with zero-gap nodal ring states. Section 5 is the conclusion.

2 2D SGSs with band crossing points at H-S points

In 2022, Xing *et al.* (Xing et al., 2022) proposed a family of 2D oxalate-based metal-organic frameworks (MOFs) that possed the SGS characteristic. Figures 1I,J show the structure and reciprocal lattice of a 2D MOF $TM_2(C_2O_4)_3$ with a honeycomb-kagome (HK) lattice. Figure 1K–R show the electronic BSs of $Ni_2(C_2O_4)_3$ and $Re_2(C_2O_4)_3$ calculated by different methods along the Γ-M-K-Γ high symmetry paths. Without SOC, the valence band and conduction band in one spin channel touch the FL at the K point, and the other spin channel has a semiconducting band gap of 1 eV (see Figure 1K, O). Meanwhile, spin-gapless Dirac points with linear dispersion appear at the FL in one spin channel, which is beneficial for dissipationless spin transport. The influence of SOC on the Dirac point at the K H-S point is considered, and the results are shown in Figure 1L, P. One finds that the SOC triggers a band gap of about 7.6 meV in $Ni_2(C_2O_4)_3$ and 143 meV in $Re_2(C_2O_4)_3$, respectively. Compared with $Ni_2(C_2O_4)_3$, the SOC-induced gap of $Re_2(C_2O_4)_3$ is more significant than that of $Ni_2(C_2O_4)_3$ because the relative atomic mass of the Re atom is heavier than that of the Ni atom, and the Dirac point of $Re_2(C_2O_4)_3$ only contributes the *d* orbital of Re atom. Figure 1M, Q show the BSs calculated by the HSE06 method, and Figure 1N, R show the BSs calculated by the GGA + U method. One finds that the spin-gapless Dirac point is still maintained at the K point under both HSE06 and GGA + U methods.

With the PBE functional, the calculated Fermi velocity (v_F) values (Xing et al., 2022) are up to 2.0×10^5 m s^{-1} and 1.86×10^5 m s^{-1} for $Ni_2(C_2O_4)_3$ and $Re_2(C_2O_4)_3$, respectively. When using the HSE06 functional, the obtained v_F values are relatively higher, up to 2.78×10^5 m s^{-1} and 2.58×10^5 m s^{-1} for $Ni_2(C_2O_4)_3$ and $Re_2(C_2O_4)_3$, respectively. As seen in Figure 1S, T, M and C_m exhibit a sudden change at a temperature of 208 K for $Ni_2(C_2O_4)_3$ and 34 K for $Re_2(C_2O_4)_3$, respectively. Note that the ultimate goals of spintronic or electronic devices in the future are ultra-fast transmission and extremely low energy consumption. The massless charge should ideally be fully S-P, and the (effective) mass of electrons or holes should be eliminated. Therefore, a class of magnetic materials called 2D SGSs with Dirac points at high symmetry points can be considered ideal for the use of next-generation spintronics (Wang et al., 2018b).

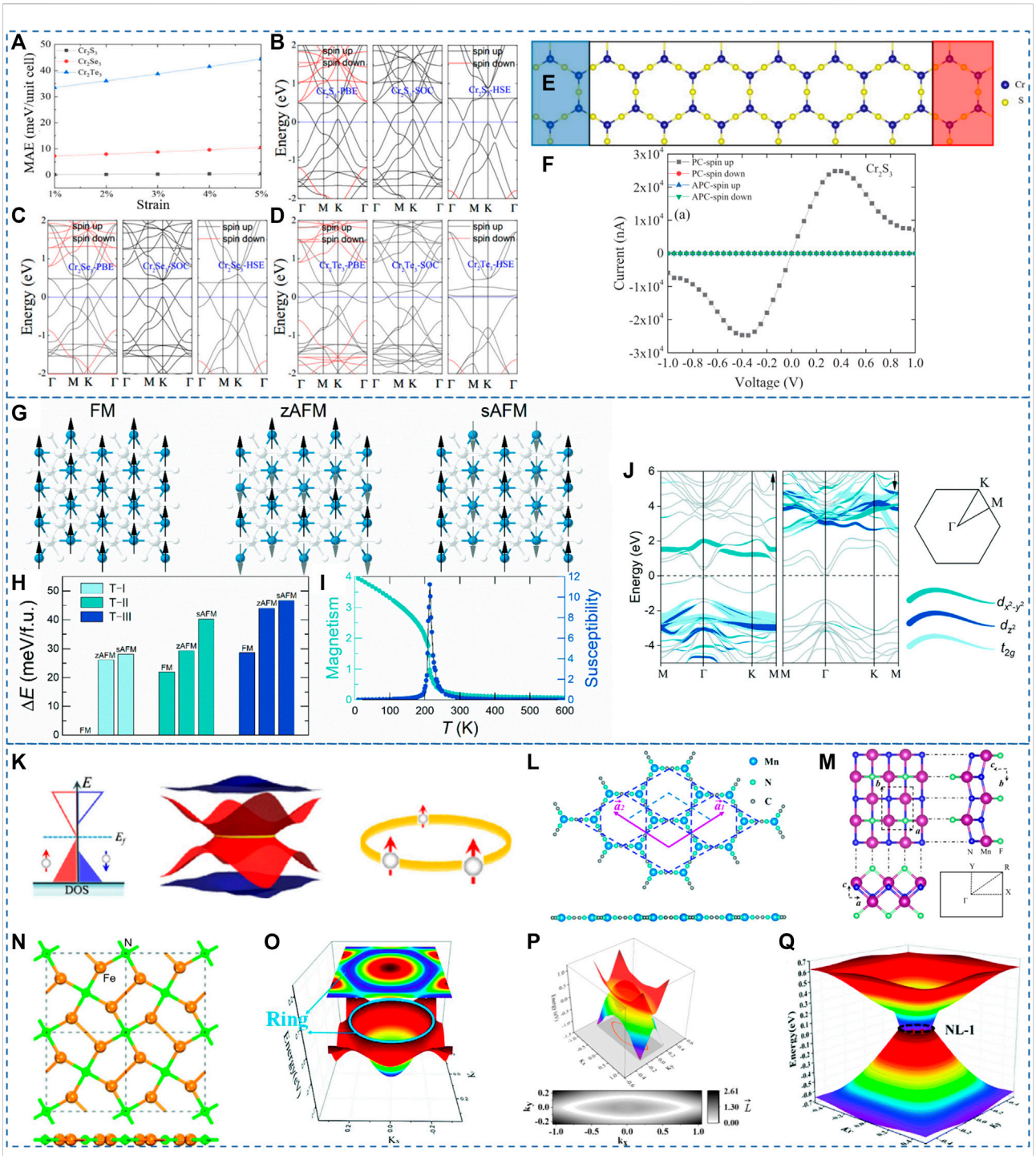

FIGURE 2
(A) The relationship between the MAE and strain. **(B–D)** BS of the Cr_2X_3 monolayers calculated with different methods. **(E)** The Cr_2S_3 device model. **(F)** The spin-resolved current-voltage curves for the PC and the APC of the device. **(A–F)** Reproduced from (Feng et al., 2021) with permission from AIP publishing. **(G)** Schematics for the FM and AFM states of the $CrGa_2Se_4$ monolayer. **(H)** Energy difference with respect to the ground state for T-I, T-II and T-III configurations. **(I)** The simulated Curie temperature **(J)** The calculated BSs by the HSE06 method. **(G–J)** Reproduced from (Chen et al., 2021) with permission from RSC publishing. **(K)** The schematic diagram of NRSGSs. Reproduced from (Zhang et al., 2020b) with permission from APS. **(L–N)** Structures of 2D HK Mn-cyanogen lattice, 2D MnNF monolayer, and 2D Fe_4N_2 pentagon crystal, respectively. **(O–Q)** 3D plot of the gapless NR states in 2D HK Mn–cyanogen lattice, 2D MnNF monolayer, and 2D Fe_4N_2 pentagon crystal, respectively. **(L–Q)** Reproduced from (Zhang et al., 2018; Hu et al., 2019; Zhang et al., 2021b) with permission from RSC and ACS publishing.

3 2D SGSs with band crossing points along the H-S paths

3.1 Example 1: 2D single-layer Fe_2I_2

In 2020, Sun, Ma, and Kioussis (Sun et al., 2020b) proposed single-layer Fe_2I_2, with space group *P4/nmm* (nop. 129) and calculated lattice constants a = b = 3.81 Å, is a 2D SGS. The calculated BSs for single-layer Fe_2I_2 without SOC and with GGA + U are shown in Figure 1U. One finds that the SU bands show a semiconducting behavior, whereas the SD bands show a zero-gap behavior. Two gapless band crossing points appear at the FL in the SD channel. Unlike the gapless point at the H-S point in $Ni_2(C_2O_4)_3$ and $Re_2(C_2O_4)_3$, the gapless points in Fe_2I_2 are along the H-S paths. As shown in Figure 1U, the gapless points appear along the Y-Γ-X H-S paths. The 3D plot of these gapless points (named as Dirac points in Ref. (Sun et al., 2020b)) is shown in Figure 1V. The obtained v_F with the help of GGA + U and HSE06 is 4.66×10^5 m s^{-1} and 6.39×10^5 m s^{-1}, respectively. As we all know, the massless Dirac fermions will lead to low effective masses and high carrier mobility. Further, as shown in Figure 1W, single-layer Fe_2I_2 undergoes a spin reorientation transition to an in-plane magnetization orientation beyond -4% compressive strain. As shown in Figure 1X, one finds that the SD bands arise from the Fe-d orbital, whereas the SU bands are from the I-p orbital. Hence, the Fe-d orbital contributes solely to the Dirac points at the FL. When SOC is added, significant band gaps (~301 meV) appear along the Y-Γ-X H-S paths (see Figure 1Y) and a nonzero Chern number ($|C| = 2$). The edge states for the single-layer Fe_2I_2 are shown in Figure 1Z; one finds that two chiral topologically protected gapless edge states, which are consistent with the obtained $|C| = 2$. The SOC induces a physics nature transition from Driac SGS to quantum anomalous Hall (QAH) state in single-layer Fe_2I_2.

3.2 Example 2: 2D Cr_2X_3 monolayer with the HK lattice

In 2021, Feng, Liu, and Gao (Feng et al., 2021) proposed the spin-gapless semiconducting states in 2D Cr_2X_3 monolayers (X = S, Se, and Te) via first-principle calculations. The estimated Curie temperatures for these three monolayers are about 420, 480, and 510 K, respectively. The S-P BSs and the calculated MAE for these three monolayers are collected in Figures 2B–D. One finds these three monolayers belong to 2D SGSs with zero-gap Dirac points along the H-S paths, i.e., K-Γ-M. As shown in Figure 2A one finds that the MAEs for these three monolayers increase with the increasing tensile strains from 1% to 5%. Unfortunately, the SGS behaviors in Cr_2Te_3 at the FL are destroyed within HSE06. For the Cr_2S_3 and Cr_2Se_3, the Dirac points along the K-Γ-M paths are still maintained within PBE and HSE06. The effect of SOC to the Dirac points is also examined by Feng, Liu, and Gao (Feng et al., 2021); they stated that the SOC effect is weak for the proposed monolayers.

Feng, Liu, and Gao (Feng et al., 2021) also studied the nonequilibrium spin transport properties of monolayer Cr_2S_3, and the device model is shown in Figure 2E. From Figure 2F, for the APC in both spin directions, one finds the values of spin-currents are extremely small. For the PC, one finds the spin-current of the PC-spin down can be neglected, whereas the spin-current of PC-spin up increased at first and then decreased with the increase of voltage form 0.0 V–1.0 V. The maximum value of spin current of PC-spin up appears at about+/-0.35 V. Hence, the device model in Figure 2E should host a perfect spin filtering effect (Chen et al., 2019; Zhang et al., 2020a; Han et al., 2022).

4 2D SGSs with indirect zero-gap states

In 2021, Chen *et al.* (Chen et al., 2021) predicted a 2D spin gapless ferromagnetic semiconductor of $CrGa_2Se_4$ monolayer with indirect zero-gap state. As shown in Figures 2G,H, one finds that the magnetic ground state is the FM state with a T-I configuration. It can be seen from Figure 2I that the Curie temperature of the $CrGa_2Se_4$ monolayer is about 220 K. Chen *et al.* calculated the BSs of the $CrGa_2Se_4$ monolayer with HSE06 functional. The results are collected in Figure 2J. At first glance, one finds that the $CrGa_2Se_4$ monolayer is a ferromagnetic semiconductor. The bands in SU and SD channels host semiconducting gaps of 0.36 eV and 1.36 eV, respectively. Interestingly, the lowest conduction band state in the SD channel touches the FL, and the highest valence band states in the SU channel touch the FL, forming an indirect zero-gap state. Hence, the $CrGa_2Se_4$ monolayer can also be seen as an SGS with an indirect spin-gapless semiconducting state.

We would like to point out that the indirect zero gap states occur because the two spin components at different *k* points accidentally have their extreme values at the FL. Therefore, in general, they are not protected from the symmetry of systems due to the indirect band touching. However, the SGSs with indirect band touching usually host bipolar magnetic behavior. That is, by changing the sign of the applied gate voltage, one can achieve the electrical manipulation of spin-polarization orientation in SGSs (with indirect band touching).

5 2D SGSs with zero-gap nodal ring states

Compared to the Dirac SGSs with single or multiple nodal point states, Zhang *et al.* (Zhang et al., 2018) proposed a new class of 2D SGSs with a gapless nodal ring (NR) in the momentum space and 100% spin polarization. That is, the SGSs, with a one-dimensional topological signature, have zero-gap band crossing points that form a line in the momentum space. Typically, they are named as NRSGSs. The schematic diagram of NRSGSs is shown in Figure 2K. One finds that the SU channel shows a zero-gap NR state in the momentum space and the SD channel shows a semiconducting state.

To this date, 2D HK Mn–cyanogen lattice (Zhang et al., 2018), 2D MnNF monolayer (Hu et al., 2019), and 2D Fe_4N_2 pentagon crystal (Zhang et al., 2021b) are proposed to be 2D NR SGSs. The structural model and the 3D plot of the gapless NR state in one spin channel are shown in Figure 2L–Q. We would like to point out that the gapless NR state in one spin channel may suffer sizable SOC-induced gaps. Hence, searching for NRSGSs with light elements to reduce the value of SOC-induced gaps.

6 Conclusion and remarks

In this mini-review, we introduced a series of ideal 2D SGSs, including 2D SGSs with band-crossing points at H-S points or along the H-S paths, 2D SGSs with S-P NR states, and 2D SGSs with indirect zero-gap states.

The Dirac SGSs with band-crossing points at H-S points or along the H-S paths show massless fermions around the FL, ideal dissipation-less properties, and 100% spin-polarization. Furthermore, the band crossing points may not isolate in the momentum space and form an NR in 2D SGSs. The NRSGSs will exhibit more intensive nonlinear electromagnetic responses than a single Dirac point. It should be noted that the 2D SGSs are hopped to host a high Curie temperature and a robust FM state at room temperature. Finally, a major challenge for 2D SGSs is that no 2D SGSs has been experimentally realized. The reason is that the 2D SGSs are monolayer materials, and they are hard to synthesize. Moreover, some monolayer materials are not stable in the ambient environment. Thus, new nanotechnology is needed for fabricating 2D monolayer SGSs.

Author contributions

JW wrote the manuscript. DW revised and approved the manuscript.

Funding

This work is financially supported by the Fundamental Research Funds for the Central Universities (SWU019030).

Conflict of interest

The remaining author declares that the research was conducted in the absence of any commercial or financial relationships that could be construed as a potential conflict of interest.

The handling editor GW declared a past co-authorship with the author DW.

Publisher's note

References

Ashton, M., Gluhovic, D., Sinnott, S. B., Guo, J., Stewart, D. A., and Hennig, R. G. (2017). Two-dimensional intrinsic half-metals with large spin gaps. *Nano Lett.* 17 (9), 5251–5257. doi:10.1021/acs.nanolett.7b01367

Benmansour, S., Abhervé, A., Gómez-Claramunt, P., Vallés-García, C., and Gómez-García, C. J. (2017). Nanosheets of two-dimensional magnetic and conducting Fe(II)/Fe(III) mixed-valence metal-organic frameworks. *ACS Appl. Mat. Interfaces* 9 (31), 26210–26218. doi:10.1021/acsami.7b08322

Bonilla, M., Kolekar, S., Ma, Y., Diaz, H. C., Kalappattil, V., Das, R., et al. (2018). Strong room-temperature ferromagnetism in VSe2 monolayers on van der Waals substrates. *Nat. Nanotech* 13 (4), 289–293. doi:10.1038/s41565-018-0063-9

Chen, Q., Wang, R., Huang, Z., Yuan, S., Wang, H., Ma, L., et al. (2021). Two dimensional CrGa2Se4: A spin-gapless ferromagnetic semiconductor with inclined uniaxial anisotropy. *Nanoscale* 13 (12), 6024–6029. doi:10.1039/d0nr08296a

Chen, Z., Fan, X., Shen, Z., Luo, Z., Yang, D., and Ma, S. (2020). Two-dimensional intrinsic ferromagnetic half-metals: Monolayers Mn3X4 (X = Te, Se, S). *J. Mat. Sci.* 55 (18), 7680–7690. doi:10.1007/s10853-020-04582-x

Chen, Z., Li, T., Yang, T., Xu, H., Khenata, R., Gao, Y., et al. (2019). Palladium (III) fluoride bulk and PdF3/Ga2O3/PdF3 magnetic tunnel junction: Multiple spin-gapless semiconducting, perfect spin filtering, and high tunnel magnetoresistance. *Nanomaterials* 9 (9), 1342. doi:10.3390/nano9091342

Deng, Y. X., Chen, S. Z., Zeng, Y., Feng, Y., Zhou, W. X., Tang, L. M., et al. (2018). Spin gapless semiconductor and half-metal properties in magnetic penta-hexa-graphene nanotubes. *Org. Electron.* 63, 310–317. doi:10.1016/j.orgel.2018.09.046

Deng, Y. X., Chen, S. Z., Zhang, Y., Yu, X., Xie, Z. X., Tang, L. M., et al. (2020). Penta-hexa-graphene nanoribbons: Intrinsic magnetism and edge effect induce spin-gapless semiconducting and half-metallic properties. *ACS Appl. Mat. Interfaces* 12 (47), 53088–53095. doi:10.1021/acsami.0c14768

Deng, Y., Yu, Y., Song, Y., Zhang, J., Wang, N. Z., Sun, Z., et al. (2018). Gate-tunable room-temperature ferromagnetism in two-dimensional Fe3GeTe2. *Nature* 563 (7729), 94–99. doi:10.1038/s41586-018-0626-9

Dietl, T. (2010). A ten-year perspective on dilute magnetic semiconductors and oxides. *Nat. Mater* 9 (12), 965–974. doi:10.1038/nmat2898

Fei, Z., Huang, B., Malinowski, P., Wang, W., Song, T., Sanchez, J., et al. (2018). Two-dimensional itinerant ferromagnetism in atomically thin Fe3GeTe2. *Nat. Mater* 17 (9), 778–782. doi:10.1038/s41563-018-0149-7

Feng, Y., Liu, N., and Gao, G. (2021). Spin transport properties in Dirac spin gapless semiconductors Cr2X3 with high Curie temperature and large magnetic anisotropic energy. *Appl. Phys. Lett.* 118 (11), 112407. doi:10.1063/5.0045262

Feng, Y., Wu, X., and Gao, G. (2020). High tunnel magnetoresistance based on 2D Dirac spin gapless semiconductor VCl3. *Appl. Phys. Lett.* 116 (2), 022402. doi:10.1063/1.5128204

Gao, G., Ding, G., Li, J., Yao, K., Wu, M., and Qian, M. (2016). Monolayer MXenes: Promising half-metals and spin gapless semiconductors. *Nanoscale* 8 (16), 8986–8994. doi:10.1039/c6nr01333c

Gong, C., Li, L., Li, Z., Ji, H., Stern, A., Xia, Y., et al. (2017). Discovery of intrinsic ferromagnetism in two-dimensional van der Waals crystals. *Nature* 546 (7657), 265–269. doi:10.1038/nature22060

Gong, C., and Zhang, X. (2019). Two-dimensional magnetic crystals and emergent heterostructure devices. *Science* 363 (6428), eaav4450. doi:10.1126/science.aav4450

Haas, C. (1970). Magnetic semiconductors. *C R C Crit. Rev. Solid State Sci.* 1 (1), 47–98. doi:10.1080/10408437008243418

Han, J., Chen, X., Yang, W., Lv, C., Lin, X., Wang, X., et al. (2022). Promising spin caloritronics and spin diode effects based on 1T-FeCl2 nanotube devices. *J. Mat. Chem. C* 10 (2), 607–615. doi:10.1039/d1tc05094j

Han, Y., Chen, Z., Kuang, M., Liu, Z., Wang, X., and Wang, X. (2019). 171 scandium-based full heusler compounds: A comprehensive study of competition between xa and L21 atomic ordering. *Results Phys.* 12, 435–446. doi:10.1016/j.rinp.2018.11.079

Hashimoto, A., Suenaga, K., Gloter, A., Urita, K., and Iijima, S. (2004). Direct evidence for atomic defects in graphene layers. *nature* 430 (7002), 870–873. doi:10.1038/nature02817

He, J., Li, X., Lyu, P., and Nachtigall, P. (2017). Near-room-temperature chern insulator and Dirac spin-gapless semiconductor: Nickel chloride monolayer. *Nanoscale* 9 (6), 2246–2252. doi:10.1039/c6nr08522a

Hu, Y., Li, S. S., Ji, W. X., Zhang, C. W., Ding, M., Wang, P. J., et al. (2019). Glide mirror plane protected nodal-loop in an anisotropic half-metallic MnNF monolayer. *J. Phys. Chem. Lett.* 11 (2), 485–491. doi:10.1021/acs.jpclett.9b03320

Huang, B., Clark, G., Navarro-Moratalla, E., Klein, D. R., Cheng, R., Seyler, K. L., et al. (2017). Layer-dependent ferromagnetism in a van der Waals crystal down to the monolayer limit. *Nature* 546 (7657), 270–273. doi:10.1038/nature22391

Kim, J., Kim, K. W., Kim, B., Kang, C. J., Shin, D., Lee, S. H., et al. (2019). Exploitable magnetic anisotropy of the two-dimensional magnet CrI3. *Nano Lett.* 20 (2), 929–935. doi:10.1021/acs.nanolett.9b03815

Lee, E. C., Choi, Y. C., Kim, W. Y., Singh, N. J., Lee, S., Shim, J. H., et al. (2010). A radical polymer as a two-dimensional organic half metal. *Chem. Eur. J.* 16 (40), 12141–12146. doi:10.1002/chem.201000858

Lei, J., Xu, M. C., and Hu, S. J. (2017). Anchoring transition metal elements on graphene-like ZnO monolayer by CO molecule to obtain spin gapless semiconductor. *Appl. Surf. Sci.* 416, 681–685. doi:10.1016/j.apsusc.2017.04.169

Li, L., Kong, X., Chen, X., Li, J., Sanyal, B., and Peeters, F. M. (2020). Monolayer 1T-LaN2: Dirac spin-gapless semiconductor of p-state and chern insulator with a high chern number. *Appl. Phys. Lett.* 117 (14), 143101. doi:10.1063/5.0023531

Li, X., and Yang, J. (2014). CrXTe3(X = Si, Ge) nanosheets: Two dimensional intrinsic ferromagnetic semiconductors. *J. Mat. Chem. C* 2 (34), 7071–7076. doi:10.1039/c4tc01193g

Li, Y., Zhou, Z., Shen, P., and Chen, Z. (2009). Spin gapless Semiconductor–Metal–Half-metal properties in nitrogen-doped zigzag graphene nanoribbons. *ACS Nano* 3 (7), 1952–1958. doi:10.1021/nn9003428

Liu, B., and Zhou, K. (2019). Recent progress on graphene-analogous 2D nanomaterials: Properties, modeling and applications. *Prog. Mater. Sci.* 100, 99–169. doi:10.1016/j.pmatsci.2018.09.004

Liu, J., Liu, Z., Song, T., and Cui, X. (2017). Computational search for two-dimensional intrinsic half-metals in transition-metal dinitrides. *J. Mat. Chem. C* 5 (3), 727–732. doi:10.1039/c6tc04490e

Miao, N., and Sun, Z. (2022). Computational design of two-dimensional magnetic materials. *WIREs Comput. Mol. Sci.* 12 (2), e1545. doi:10.1002/wcms.1545

Nadeem, M., Hamilton, A. R., Fuhrer, M. S., and Wang, X. (2020). Quantum anomalous Hall effect in magnetic doped topological insulators and ferromagnetic spin-gapless semiconductors-A perspective review. *Small* 16 (42), 1904322. doi:10.1002/smll.201904322

Novoselov, K. S., Geim, A. K., Morozov, S. V., Jiang, D. E., Zhang, Y., Dubonos, S. V., et al. (2004). Electric field effect in atomically thin carbon films. *science* 306 (5696), 666–669. doi:10.1126/science.1102896

Phong, P. N., and Nguyen, H. V. (2022). Spin gapless semiconductors in antiferromagnetic monolayer HC4N3BN under strain. *Comput. Mater. Sci.* 203, 111110. doi:10.1016/j.commatsci.2021.111110

Rani, D., Bainsla, L., Alam, A., and Suresh, K. G. (2020). Spin-gapless semiconductors: Fundamental and applied aspects. *J. Appl. Phys.* 128 (22), 220902. doi:10.1063/5.0028918

Şaşıoğlu, E., Aull, T., Kutschabsky, D., Blügel, S., and Mertig, I. (2020). Half-metal-spin-gapless-semiconductor junctions as a route to the ideal diode. *Phys. Rev. Appl.* 14 (1), 014082. doi:10.1103/physrevapplied.14.014082

Sato, K., Bergqvist, L., Kudrnovský, J., Dederichs, P. H., Eriksson, O., Turek, I., et al. (2010). First-principles theory of dilute magnetic semiconductors. *Rev. Mod. Phys.* 82 (2), 1633–1690. doi:10.1103/revmodphys.82.1633

Sun, Q., Ma, Y., and Kioussis, N. (2020). Two-dimensional Dirac spin-gapless semiconductors with tunable perpendicular magnetic anisotropy and a robust quantum anomalous Hall effect. *Mat. Horiz.* 7 (8), 2071–2077. doi:10.1039/d0mh00396d

Sun, X., Li, W., Wang, X., Sui, Q., Zhang, T., Wang, Z., et al. (2020). Room temperature ferromagnetism in ultra-thin van der Waals crystals of 1T-CrTe2. *Nano Res.* 13 (12), 3358–3363. doi:10.1007/s12274-020-3021-4

Tang, C., Zhang, L., Jiao, Y., Zhang, C., Sanvito, S., and Du, A. (2021). First-principles prediction of polar half-metallicity and out-of-plane piezoelectricity in two-dimensional quintuple layered cobalt selenide. *J. Mat. Chem. C* 9 (36), 12046–12050. doi:10.1039/d1tc02727a

Torelli, D., Moustafa, H., Jacobsen, K. W., and Olsen, T. (2020). High-throughput computational screening for two-dimensional magnetic materials based on experimental databases of three-dimensional compounds. *npj Comput. Mat.* 6 (1), 158. doi:10.1038/s41524-020-00428-x

Wang, A., Zhang, X., Feng, Y., and Zhao, M. (2017). Chern insulator and chern half-metal states in the two-dimensional spin-gapless semiconductor Mn2C6S12. *J. Phys. Chem. Lett.* 8 (16), 3770–3775. doi:10.1021/acs.jpclett.7b01187

Wang, Q. H., Kalantar-Zadeh, K., Kis, A., Coleman, J. N., and Strano, M. S. (2012). Electronics and optoelectronics of two-dimensional transition metal dichalcogenides. *Nat. Nanotech* 7 (11), 699–712. doi:10.1038/nnano.2012.193

Wang, X., Cheng, Z., Jin, Y., Wu, Y., Dai, X., and Liu, G. (2018). Magneto-electronic properties and tetragonal deformation of rare-earth-element-based quaternary heusler half-metals: A first-principles prediction. *J. Alloys Compd.* 734, 329–341. doi:10.1016/j.jallcom.2017.10.277

Wang, X., Cheng, Z., Liu, G., Dai, X., Khenata, R., Wang, L., et al. (2017). Rare earth-based quaternary Heusler compoundsMCoVZ(M= Lu, Y;Z= Si, Ge) with tunable band characteristics for potential spintronic applications. *Int. Union Crystallogr. J.* 4 (6), 758–768. doi:10.1107/s2052252517013264

Wang, X., Cheng, Z., Wang, J., and Liu, G. (2016). A full spectrum of spintronic properties demonstrated by a C1b-type Heusler compound Mn2Sn subjected to strain engineering. *J. Mat. Chem. C* 4 (36), 8535–8544. doi:10.1039/c6tc02526a

Wang, X., Cheng, Z., Yuan, H., and Khenata, R. (2017). L21 and XA ordering competition in titanium-based full-Heusler alloys. *J. Mat. Chem. C* 5 (44), 11559–11564. doi:10.1039/c7tc03909c

Wang, X., Cheng, Z., Zhang, G., Yuan, H., Chen, H., and Wang, X. L. (2020). Spin-gapless semiconductors for future spintronics and electronics. *Phys. Rep.* 888, 1–57. doi:10.1016/j.physrep.2020.08.004

Wang, X., Ding, G., Cheng, Z., Yuan, H., Wang, X. L., Yang, T., Khenata, W., and Wang, W. (2019). R3c-type LnNiO3(ln = La, Ce, Nd, Pm, Gd, Tb, Dy, Ho, Er, Lu) half-metals with multiple Dirac cones: A potential class of advanced spintronic materials. *Int. Union Crystallogr. J.* 6 (6), 990–995. doi:10.1107/s2052252519012570

Wang, X., Du, K., Fredrik Liu, Y. Y. F., Hu, P., Zhang, J., Zhang, Q., et al. (2016). Raman spectroscopy of atomically thin two-dimensional magnetic iron phosphorus trisulfide (FePS 3) crystals. *2D Mat.* 3 (3), 031009. doi:10.1088/2053-1583/3/3/031009

Wang, X. L. (2017). Dirac spin-gapless semiconductors: Promising platforms for massless and dissipationless spintronics and new (quantum) anomalous spin Hall effects. *Natl. Sci. Rev.* 4 (2), 252–257. doi:10.1093/nsr/nww069

Wang, X., Li, T., Cheng, Z., Wang, X. L., and Chen, H. (2018). Recent advances in Dirac spin-gapless semiconductors. *Appl. Phys. Rev.* 5 (4), 041103. doi:10.1063/1.5042604

Wang, X. L. (2008). Proposal for a new class of materials: Spin gapless semiconductors. *Phys. Rev. Lett.* 100 (15), 156404. doi:10.1103/physrevlett.100.156404

Wang, Z., Zhang, T., Ding, M., Dong, B., Li, Y., Chen, M., et al. (2018). Electric-field control of magnetism in a few-layered van der Waals ferromagnetic semiconductor. *Nat. Nanotech* 13 (7), 554–559. doi:10.1038/s41565-018-0186-z

Wu, X., Feng, Y., Li, S., Zhang, B., and Gao, G. (2020). 2D Mn2C6Se12 and Mn2C6S6Se6: Intrinsic room-temperature Dirac spin gapless semiconductors and perfect spin transport properties. *J. Phys. Chem. C* 124 (29), 16127–16135. doi:10.1021/acs.jpcc.0c04786

Wu, X., Feng, Y., Li, S., Zhang, B., and Gao, G. (2020). *2D Mn2C6Se12 and Mn2C6Se12: Intrinsic room-temperature Dirac spin gapless semiconductors and perfect spin transport properties.*

Xing, J., Jiang, X., Liu, Z., Qi, Y., and Zhao, J. (2022). Robust Dirac spin gapless semiconductors in a two-dimensional oxalate based organic honeycomb-kagome lattice. *Nanoscale* 14 (5), 2023–2029. doi:10.1039/d1nr07076b

Xu, J., Li, W., and Hou, Y. (2020). Two-dimensional magnetic nanostructures. *Trends Chem.* 2 (2), 163–173. doi:10.1016/j.trechm.2019.11.007

Yang, Q., Kou, L., Hu, X., Wang, Y., Lu, C., Krasheninnikov, A. V., et al. (2020). Strain robust spin gapless semiconductors/half-metals in transition metal embedded MoSe2 monolayer. *J. Phys. Condens. Matter* 32 (36), 365305. doi:10.1088/1361-648x/ab9052

Yang, S. A. (2016). Dirac and Weyl materials: Fundamental aspects and some spintronics applications. *Spin*, 6. World Scientific Publishing Company, 1640003. doi:10.1142/s2010324716400038

Yang, T., Cheng, Z., Surucu, G., and Wang, X. (2020). Coexistence of parabolic and linear band crossings and electron-doped spin-gapless properties in rhombohedral type YbBO3. *J. Alloys Compd.* 823, 153835. doi:10.1016/j.jallcom.2020.153835

Yang, T., Cheng, Z., Wang, X., and Wang, X. L. (2021). Nodal ring spin gapless semiconductor: New member of spintronic materials. *J. Adv. Res.* 28, 43–49. doi:10.1016/j.jare.2020.06.016

Yue, Z., Li, Z., Sang, L., and Wang, X. (2020). Spin-gapless semiconductors. *Small* 16 (31), 1905155. doi:10.1002/smll.201905155

Zhang, K., Chen, M., Wang, D., Lv, H., Wu, X., and Yang, J. (2021). Nodal-loop half metallicity in a two-dimensional Fe4N2 pentagon crystal with room-temperature ferromagnetism. *Nanoscale* 13 (46), 19493–19499. doi:10.1039/d1nr06033c

Zhang, L., Li, T., Li, J., Jiang, Y., Yuan, J., and Li, H. (2020). Perfect spin filtering effect on Fe3GeTe2-based van der Waals magnetic tunnel junctions. *J. Phys. Chem. C* 124 (50), 27429–27435. doi:10.1021/acs.jpcc.0c09432

Zhang, L., Zhang, S. F., Ji, W. X., Zhang, C. W., Li, P., Wang, P. J., et al. (2018). Discovery of a novel spin-polarized nodal ring in a two-dimensional HK lattice. *Nanoscale* 10 (44), 20748–20753. doi:10.1039/c8nr05383a

Zhang, R. W., Zhang, Z., Liu, C. C., and Yao, Y. (2020). Nodal line spin-gapless semimetals and high-quality candidate materials. *Phys. Rev. Lett.* 124 (1), 016402. doi:10.1103/physrevlett.124.016402

Zhang, S., Xu, R., Luo, N., and Zou, X. (2021). Two-dimensional magnetic materials: Structures, properties and external controls. *Nanoscale* 13 (3), 1398–1424. doi:10.1039/d0nr06813f

Zhang, X., Wang, A., and Zhao, M. (2015). Spin-gapless semiconducting graphitic carbon nitrides: A theoretical design from first principles. *Carbon* 84, 1–8. doi:10.1016/j.carbon.2014.11.049

Zhou, X. F., Oganov, A. R., Wang, Z., Popov, I. A., Boldyrev, A. I., and Wang, H. T. (2016). Two-dimensional magnetic boron. *Phys. Rev. B* 93 (8), 085406. doi:10.1103/physrevb.93.085406

Zhou, X., Hang, Y., Liu, L., Zhang, Z., and Guo, W. (2019). A large family of synthetic two-dimensional metal hydrides. *J. Am. Chem. Soc.* 141 (19), 7899–7905. doi:10.1021/jacs.9b02279

Zhu, S., and Li, T. (2016). Strain-induced programmable half-metal and spin-gapless semiconductor in an edge-doped boron nitride nanoribbon. *Phys. Rev. B* 93 (11), 115401. doi:10.1103/physrevb.93.115401

frontiers | Frontiers in Physics

TYPE Original Research
PUBLISHED 17 October 2022
DOI 10.3389/fphy.2022.1055981

OPEN ACCESS

EDITED BY
San-Dong Guo,
Xi'an University of Posts and Telecommunications, China

REVIEWED BY
Minquan Kuang,
Southwest University, China
Liying Wang,
Tianjin University, China

*CORRESPONDENCE
Ying Yang,
physicsyy@126.com

SPECIALTY SECTION
This article was submitted to Physical Chemistry and Chemical Physics, a section of the journal Frontiers in Physics

RECEIVED 28 September 2022
ACCEPTED 05 October 2022
PUBLISHED 17 October 2022

CITATION
Yang Y (2022), Ideal phononic charge-two nodal point and long nontrivial surface arcs in $Na_2Zn_2O_3$. *Front. Phys.* 10:1055981. doi: 10.3389/fphy.2022.1055981

Ideal phononic charge-two nodal point and long nontrivial surface arcs in $Na_2Zn_2O_3$

Ying Yang*

College of Physics and Electronic Engineering, Chongqing Normal University, Chongqing, China

Recently, there has been significant interest in exploring the chiral quasiparticles in phonons, which describe the atomic lattice vibrations in solids. In this work, using first-principle calculation, we select a realistic material $Na_2Zn_2O_3$ as an example to demonstrate that it is an ideal candidate with charge-two Dirac point phonons and charge-two Weyl point phonons at high-symmetry points A and Γ, respectively. The phononic charge-two nodal points in $Na_2Zn_2O_3$ are visible and almost ideal. That is, there are no other phonon bands nearby. Moreover, nontrivial phononic surface arcs span the whole surface Brillouin zone. Such clean and long nontrivial arc-shaped phononic surface states benefit the experimental detection. The current work is hoped to guide the investigations of chiral nodal points in phononic systems.

KEYWORDS

topological phonons, DFPT calculation, Dirac point, weyl point, phonons

Introduction

It is well known that the chiral quasiparticles could exist in spinless systems, such as the phononic system and classical elastic waves in macroscopic artificial phononic crystals. Recently, there has been great interest in exploring topological quasiparticles in phonons [1], which describe the atomic lattice vibrations in solids. So far, a number of materials hosting Weyl point phonons [2–10], Dirac point phonons [11, 12], triple degenerate nodal point phonons [13, 14], sixfold degenerate nodal point phonons [15, 16], nodal line phonons [17–30] and nodal surfaces phonons [31–33] have been discovered. Compared with chiral fermions in electronic systems, chiral phonons exist without spin-orbital coupling.

Let us come to review the recent advances in chiral nodal point phonons as follows: In 2018, Zhang *et al.* [2] identified a class of crystalline materials of MSi (M = Fe, Co, Mn, Re, Ru) exhibiting double Weyl phonons, and they named the topological points as 'spin-1 Weyl point' at the Brillouin zone (BZ) center and "charge-2 Dirac point" at the zone corner. Motivated by Zhang *et al.*'s recent theoretical work [2], Huang *et al.* [4] measured the phonon dispersion in parity-breaking FeSi using inelastic x-ray scattering and confirmed the double Weyl phonons in experiments. Moreover, based on first-principle calculation and symmetry analysis, Liu *et al.* [5] defined a new type of Weyl phonons with Chern numbers of ±4. They [5] also proposed that BiIrSe and Li_3CuS_2 are candidate materials with charge-four Weyl phonons. In 2020, Wang *et al.* [9] proposed a

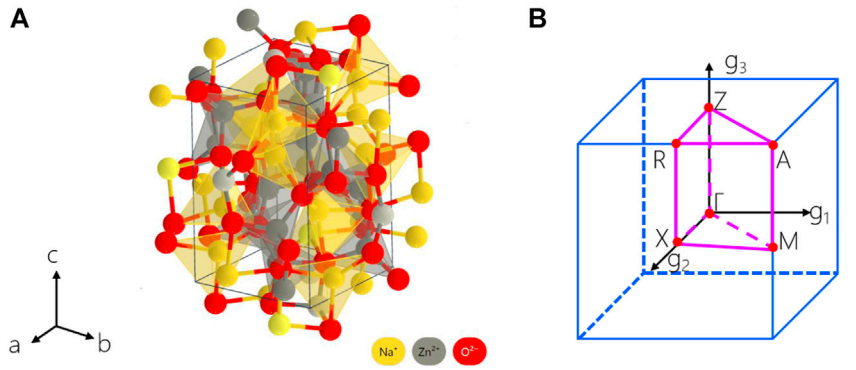

FIGURE 1
(A) Crystal structure of tetragonal $Na_2Zn_2O_3$ with $P4_32_12$ space group. **(B)** Three-dimensional BZ and selected symmetry paths.

symmetry-protected topological triangular Weyl complex composed of one double Weyl point and two single Weyl points. They [9] also stated that the unique triangular Weyl complex could be observed in the phonon dispersion of α–SiO_2. In 2022, Ding *et al.* [34] predicted that $BaZnO_2$ is an ideal material candidate with type-III charge-two Weyl point phonons. $BaZnO_2$ can support double-helicoid phonon surface states covering the entire Brillouin zone (001) surface. Besides trigonal $BaZnO_2$, they [34] stated that some other candidate materials, including tetragonal $MgTiO_4$, trigonal Li_2GeF_6, hexagonal $CaSO_4$, and cubic $Li_{10}B_{14}Cl_2O_{25}$, can host the type-III charge-two Weyl point phonons.

In this work, we propose a realistic material $Na_2Zn_2O_3$ [35] is an ideal system with chiral phonons, i.e., charge-two Dirac point phonons and charge-two Weyl point phonons at A and *Γ* high-symmetry points, respectively. More interestingly, the nontrivial phonon surface arcs are very long, clean, and span over the whole surface BZ. $Na_2Zn_2O_3$ phonons should be an excellent platform to investigate the coexistence of charge-two Dirac and Weyl points in spinless systems. Also, our results can be extended to other bosonic systems.

Approach

We perform the first-principle calculations based on the density functional theory (DFT) [36]. The generalized gradient approximation (GGA) [37] with Perdew–Burke–Ernzerhof (PBE) [38] realization was adopted for the exchanged correlation potential. The phonon spectra of $Na_2Zn_2O_3$ is calculated by using the 2 × 2×1 supercell as implemented in Phonopy code. The pre-process and post-process were performed in the PHONOPY package using density functional perturbation theory (DFPT) [39]. The cutoff energy for the plane wave was 600 eV, and the Brillouin zone is sampled using converged 5 × 5×3 *Γ*-centered

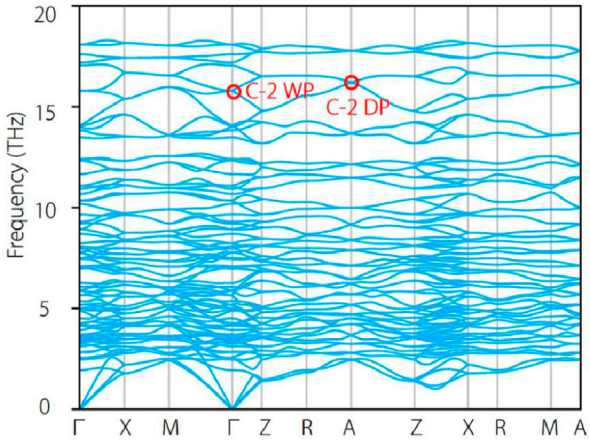

FIGURE 2
Phonon dispersion of tetragonal $Na_2Zn_2O_3$ with $P4_32_12$ along *Γ*-X-M-Γ-Z-R-A-Z-X-R-M-A high-symmetry paths. The charge-two Weyl point (C-2 WP) and charge-two Dirac point (C-2 DP) at high-symmetry points *Γ* and A, are highlighted by red circles.

k-mesh grids. To study the topological properties of nontrivial band crossings in the phonon spectrum, we calculate its corresponding surface states and constant frequency slices using the WANNIERTOOLS package [40].

Results and discussion

Figure 1A shows the crystal structure of tetragonal $Na_2Zn_2O_3$ with the $P4_32_12$ space group. Na^{1+} is bonded in a 4-coordinate geometry to four O^{2-} atoms. Zn^{2+} is bonded to four O^{2-} atoms to form a mixture of corner and edge-sharing ZnO_4 tetrahedra. There are two inequivalent O^{2-} sites. In the first O^{2-} site, O^{2-} is bonded in a 4-coordinate geometry to two equivalent Na^{1+} and two equivalent Zn^{2+} atoms. In the second O^{2-} site, O^{2-} is bonded

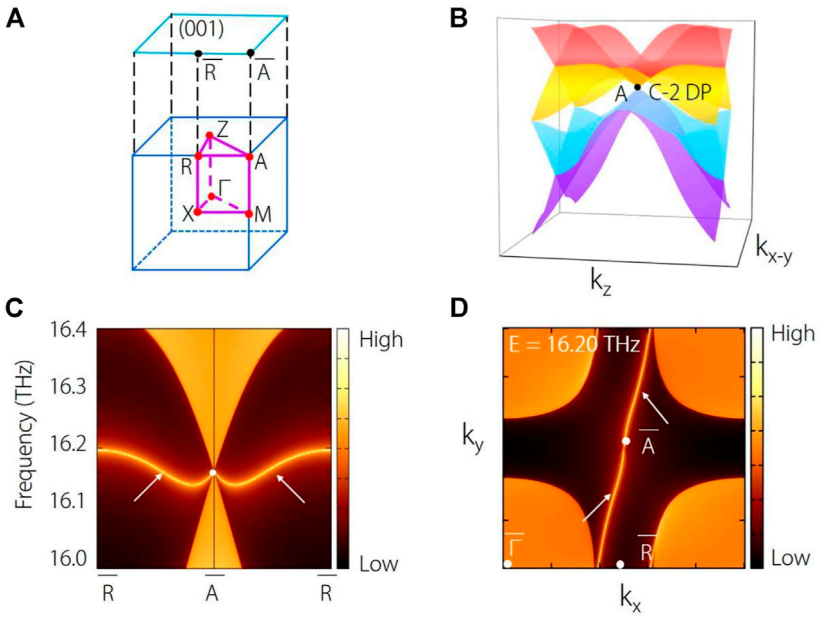

FIGURE 3
The bulk BZ and the corresponding (001) surface BZ. **(B)** Three-dimensional plot of the phonon bands around the charge-two Dirac point (C-2 DP) at **(A)**. **(C)** Projected spectrum on the (001) surface, and **(D)** the corresponding constant frequency slice at 16.20 THz.

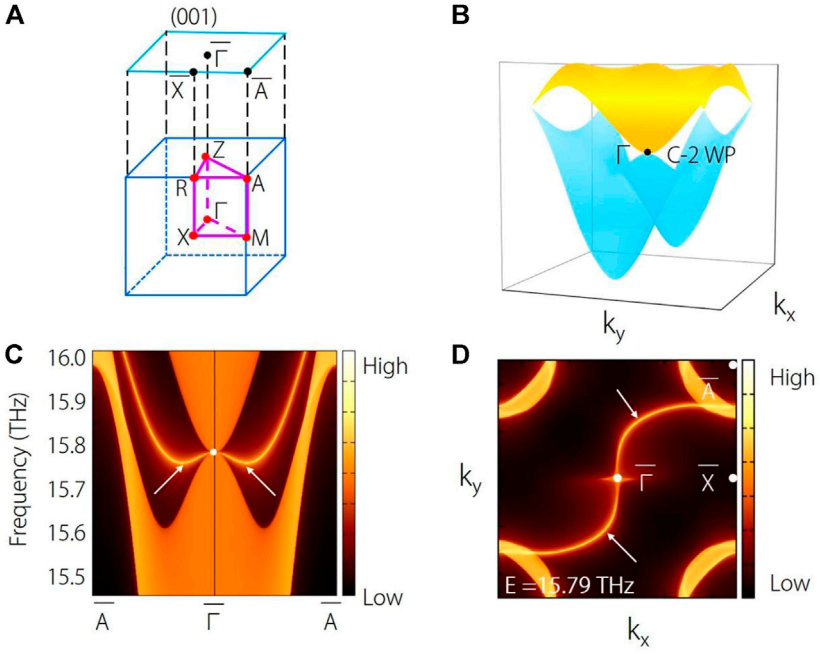

FIGURE 4
(A) The bulk BZ and the corresponding (001) surface BZ. **(B)** Three-dimensional plot of the phonon bands around the charge-two Weyl point (C-2 WP) at Γ. **(C)** Projected spectrum on the (001) surface, and **(D)** the corresponding constant frequency slice at 15.79 THz.

to three equivalent Na^{1+} and three equivalent Zn^{2+} atoms to form distorted edge-sharing ONa_3Zn_3 octahedra. The calculated lattice constants for tetragonal $Na_2Zn_2O_3$ are a = b = 6.262 Å, c = 9.507 Å, closing to the experimental data a = b = 6.181 Å, c = 9.447 Å. The Na atoms locate at 8b Wyckoff position, O atoms locate at 8b and 4a Wyckoff positions, and the Zn locates at 8b Wyckoff position.

Based the 3D BZ and the selected high-symmetry paths in Figure 1B, the phonon dispersion of $Na_2Zn_2O_3$ along Γ-X-M-Γ-Z-R-A-Z-X-R-M-A high-symmetry paths are shown in Figure 2. From Figure 2, one finds that there is no imaginary frequency, demonstrating the dynamical stability of material $Na_2Zn_2O_3$. Moreover, one finds that all the phonon bands along A-M-R-X-M and Z-R-A-Z paths are twofold degeneracy, and two twofold degenerate bands cross at A high-symmetry point, forming a fourfold degenerate Dirac point. Moreover, one finds that multiple Dirac points appear at high-symmetry point A with different frequencies, suggesting these Dirac points are symmetry-enforced and must appear at A high point. It is worth noting that the three-dimensional charge-two Dirac points may be hidden in rambling branches; thus, their topological features are invisible. We only focus on the Dirac point at about 16 THz (highlighted by the red circle). The three-dimensional plot of the phonon bands around the Dirac point are shown in Figure 3B. From Figure 3B, one finds that the Dirac point at A point has fourfold degeneracy. It should be noted that the Dirac point at A point is a charge-two Dirac point, which is a zero-dimensional fourfold band degeneracy with a topological charge $|C| = 2$. From Figure 3B, the charge-two Dirac point at A features a linear dispersion along any momentum-space direction. Dirac point can be considered as a combination of two charge-one Weyl points with opposite topological charge. Hence, the charge-two Dirac point contains two charge-one Weyl points with the same topological charge.

In Figure 3C, we show the projected spectrum on the (001) surface for $Na_2Zn_2O_3$. Obviously, clean phononic surface states can be found from the projection of the charge-two Dirac point. Moreover, the (001) surface states further display linear dispersions of the charge-two Dirac point, showing consistency with the three-dimensional plot of the phonon band in Figure 3B. Figure 3D shows the corresponding constant frequency slice at 16.20 THz. Indeed, one could observe that two arcs emanate from the projections of each Dirac point, indicating the charge of the Dirac point should equal 2. More interestingly, the surface arcs are nontrivial due to the chirality. The surface arcs (marked by white arrows) are very long and span over the whole surface BZ.

Next, we discuss the charge-two Weyl point at Γ high-symmetry point around 15.8 THz. From Figure 2, one finds that there exists a twofold degenerate Weyl point at Γ point. Such Weyl point is a charge-two Weyl point, a zero-dimensional twofold band degeneracy with a topological charge $|C| = 2$. As shown in Figure 4B, one finds that the charge-two Weyl point features a linear dispersion along k_z direction and a quadratic energy splitting in the plane (k_x-k_y plane) normal to the k_z direction. Here, the phonon spectrum is plotted in Figure 4C, in which one can observe the nontrivial surface states arising from the projections of the charge-two Weyl point at point. The isofrequency (001) surfaces at 15.79 THz are exhibited in Figure 4D. We can see that two branches of surface arcs start at $\bar{A}$. These long surface arcs exhibit a double-helicoid nature and span over the whole surface BZ. Note that all the arcs exhibited in Figure 4D are topological nontrivial, greatly facilitating the experimental detection and further applications.

Conclusion

In summary, we propose a realistic material, tetragonal $Na_2Zn_2O_3$ with $P4_32_12$ space group, which hosts symmetry-enforced charge-two Dirac point phonons and charge-two Weyl point phonons with unique long and nontrivial surface arcs. Our work uncovers the appearance of the chiral Dirac and Weyl points in the spinless system. In addition, we provide an ideal candidate who possesses chiral Dirac and Weyl points at high-symmetry points, leading to the formation of long and nontrivial surface arcs. Our work provides a good idea for detecting chiral phonons in realistic materials.

Data availability statement

The raw data supporting the conclusions of this article will be made available by the authors, without undue reservation.

Author contributions

YY - investigations and writing.

Funding

YY is grateful for support from the key project of education planning supported by Chongqing municipal education commission (No. 2021-GX-013), the National Natural Science Foundation of China (No. 12175027), and the Basic Research and Frontier Exploration Project of Chongqing Municipality (cstc2018jcyjAX0820).

Conflict of interest

The author declares that the research was conducted in the absence of any commercial or financial relationships that could be construed as a potential conflict of interest.

Publisher's note

References

1. Liu Y, Chen X, Xu Y. Topological phononics: From fundamental models to real materials. *Adv Funct Mater* (2020) 30(8):1904784. doi:10.1002/adfm.201904784

2. Zhang T, Song Z, Alexandradinata A, Weng H, Fang C, Lu L, et al. Double-Weyl phonons in transition-metal monosilicides. *Phys Rev Lett* (2018) 120(1): 016401. doi:10.1103/physrevlett.120.016401

3. Li J, Xie Q, Ullah S, Li R, Ma H, Li D, et al. Coexistent three-component and two-component Weyl phonons in TiS, ZrSe, and HfTe. *Phys Rev B* (2018) 97(5): 054305. doi:10.1103/physrevb.97.054305

4. Miao H, Zhang TT, Wang L, Meyers D, Said AH, Wang YL, et al. Observation of double Weyl phonons in parity-breaking FeSi. *Phys Rev Lett* (2018) 121(3): 035302. doi:10.1103/physrevlett.121.035302

5. Liu QB, Wang Z, Fu HH. Charge-four Weyl phonons. *Phys Rev B* (2021) 103(16):L161303. doi:10.1103/physrevb.103.l161303

6. Xia BW, Wang R, Chen ZJ, Zhao YJ, Xu H. Symmetry-protected ideal type-II Weyl phonons in CdTe. *Phys Rev Lett* (2019) 123(6):065501. doi:10.1103/physrevlett.123.065501

7. Liu QB, Qian Y, Fu HH, Wang Z. Symmetry-enforced Weyl phonons. *Npj Comput Mater* (2020) 6(1):95–6. doi:10.1038/s41524-020-00358-8

8. Liu J, Hou W, Wang E, Zhang S, Sun JT, Meng S. Ideal type-II Weyl phonons in wurtzite CuI. *Phys Rev B* (2019) 100(8):081204. doi:10.1103/physrevb.100.081204

9. Wang R, Xia BW, Chen ZJ, Zheng BB, Zhao YJ, Xu H. Symmetry-protected topological triangular Weyl complex. *Phys Rev Lett* (2020) 124(10):105303. doi:10.1103/physrevlett.124.105303

10. Jin YJ, Chen ZJ, Xiao XL, Xu H. Tunable double Weyl phonons driven by chiral point group symmetry. *Phys Rev B* (2021) 103(10):104101. doi:10.1103/physrevb.103.104101

11. Chen ZJ, Wang R, Xia BW, Zheng BB, Jin YJ, Zhao YJ, et al. Three-dimensional Dirac phonons with inversion symmetry. *Phys Rev Lett* (2021) 126(18):185301. doi:10.1103/physrevlett.126.185301

12. Wang J, Yuan H, Liu Y, Zhou F, Wang X, Zhang G. Hourglass Weyl and Dirac nodal line phonons, and drumhead-like and torus phonon surface states in orthorhombic-type KCuS. *Phys Chem Chem Phys* (2022) 24(5):2752–7. doi:10.1039/d1cp05217a

13. Singh S, Wu Q, Yue C, Romero AH, Soluyanov AA. Topological phonons and thermoelectricity in triple-point metals. *Phys Rev Mater* (2018) 2(11):114204. doi:10.1103/physrevmaterials.2.114204

14. Sreeparvathy PC, Mondal C, Barman CK, Alam A. Coexistence of multifold and multidimensional topological phonons in $KMgBO_3$. *Phys Rev B* (2022) 106(8): 085102. doi:10.1103/physrevb.106.085102

15. Xie C, Liu Y, Zhang Z, Zhou F, Yang T, Kuang M, et al. Sixfold degenerate nodal-point phonons: Symmetry analysis and materials realization. *Phys Rev B* (2021) 104(4):045148. doi:10.1103/physrevb.104.045148

16. Zhong M, Liu Y, Zhou F, Kuang M, Yang T, Wang X, et al. Coexistence of phononic sixfold, fourfold, and threefold excitations in the ternary antimonide $Zr_3Ni_3Sb_4$. *Phys Rev B* (2021) 104(8):085118. doi:10.1103/physrevb.104.085118

17. Liu G, Jin Y, Chen Z, Xu H. Symmetry-enforced straight nodal-line phonons. *Phys Rev B* (2021) 104(2):024304. doi:10.1103/physrevb.104.024304

18. Zhou F, Zhang Z, Chen H, Kuang M, Yang T, Wang X. Hybrid-type nodal ring phonons and coexistence of higher-order quadratic nodal line phonons in an AgZr alloy. *Phys Rev B* (2021) 104(17):174108. doi:10.1103/physrevb.104.174108

19. Ding G, Sun T, Surucu G, Surucu O, Gencer A, Wang X. Complex nodal structure phonons formed by open and closed nodal lines in CoAsS and Na_2CuP solids. *Phys Chem Chem Phys* (2022) 24(28):17210–6. doi:10.1039/d2cp01992b

20. Wang J, Yuan H, Yu ZM, Zhang Z, Wang X. Coexistence of symmetry-enforced phononic Dirac nodal-line net and three-nodal surfaces phonons in solid-state materials: Theory and materials realization. *Phys Rev Mater* (2021) 5(12): 124203. doi:10.1103/physrevmaterials.5.124203

21. Zhou F, Chen H, Yu ZM, Zhang Z, Wang X. Realistic cesium fluogermanate: An ideal platform to realize the topologically nodal-box and nodal-chain phonons. *Phys Rev B* (2021) 104(21):214310. doi:10.1103/physrevb.104.214310

22. Ding G, Sun T, Wang X. Ideal nodal-net, nodal-chain, and nodal-cage phonons in some realistic materials. *Phys Chem Chem Phys* (2022) 24(18): 11175–82. doi:10.1039/d2cp00731b

23. Wang X, Zhou F, Yang T, Kuang M, Yu ZM, Zhang G. Symmetry-enforced ideal lanternlike phonons in the ternary nitride Li6WN4. *Phys Rev B* (2021) 104(4): L041104. doi:10.1103/physrevb.104.l041104

24. Zheng B, Zhan F, Wu X, Wang R, Fan J. Hourglass phonons jointly protected by symmorphic and nonsymmorphic symmetries. *Phys Rev B* (2021) 104(6): L060301. doi:10.1103/physrevb.104.l060301

25. Liu QB, Fu HH, Wu R. Topological phononic nodal hexahedron net and nodal links in the high-pressure phase of the semiconductor CuCl. *Phys Rev B* (2021) 104(4):045409. doi:10.1103/physrevb.104.045409

26. Zhang TT, Miao H, Wang Q, Lin JQ, Cao Y, Fabbris G, et al. Phononic helical nodal lines with PT protection in MoB_2. *Phys Rev Lett* (2019) 123(24):245302. doi:10.1103/physrevlett.123.245302

27. Wang M, Wang Y, Yang Z, Fan J, Zheng B, Wang R, et al. Symmetry-enforced nodal cage phonons in Th_2BC_2. *Phys Rev B* (2022) 105(17):174309. doi:10.1103/physrevb.105.174309

28. Wang J, Yuan H, Kuang M, Yang T, Yu ZM, Zhang Z, et al. Coexistence of zero-one-and two-dimensional degeneracy in tetragonal SnO_2 phonons. *Phys Rev B* (2021) 104(4):L041107. doi:10.1103/physrevb.104.l041107

29. Liu Y, Zou N, Zhao S, Chen X, Xu Y, Duan W. Ubiquitous topological states of phonons in solids: Silicon as a model material. *Nano Lett* (2022) 22(5):2120–6. doi:10.1021/acs.nanolett.1c04299

30. Yang T, Gu Q, Wang P, Wu Z, Zhang Z. Phononic quadratic nodal lines of different types in Li_2NaN. *Appl Phys Lett* (2022) 121(5):053102. doi:10.1063/5.0102217

31. Liu QB, Wang ZQ, Fu HH. Ideal topological nodal-surface phonons in RbTeAu-family materials. *Phys Rev B* (2021) 104(4):L041405. doi:10.1103/physrevb.104.l041405

32. Xie C, Yuan H, Liu Y, Wang X. Two-nodal surface phonons in solid-state materials. *Phys Rev B* (2022) 105(5):054307. doi:10.1103/physrevb.105.054307

33. Xie C, Yuan H, Liu Y, Wang X, Zhang G. Three-nodal surface phonons in solid-state materials: Theory and material realization. *Phys Rev B* (2021) 104(13): 134303. doi:10.1103/physrevb.104.134303

34. Ding G, Zhou F, Zhang Z, Yu ZM, Wang X. Charge-two Weyl phonons with type-III dispersion. *Phys Rev B* (2022) 105(13):134303. doi:10.1103/physrevb.105.134303

35. Trinschek D, Jansen M. Eine neue modifikation von $Na_2Zn_2O_3$/A new modification of Na_2Zn2O_3. *Z für Naturforschung B* (1996) 51(7):917–21. doi:10.1515/znb-1996-0703

36. Parr RG. Density functional theory. *Annu Rev Phys Chem* (1983) 34(1): 631–56. doi:10.1146/annurev.pc.34.100183.003215

37. Perdew JP, Burke K, Ernzerhof M. Generalized gradient approximation made simple. *Phys Rev Lett* (1996) 77(18):3865–8. doi:10.1103/physrevlett.77.3865

38. Perdew JP, Burke K, Ernzerhof M. Perdew, burke, and ernzerhof reply. *Phys Rev Lett* (1998) 80(4):891. doi:10.1103/physrevlett.80.891

39. Baroni S, De Gironcoli S, Dal Corso A, Giannozzi P. Phonons and related crystal properties from density-functional perturbation theory. *Rev Mod Phys* (2001) 73(2):515–62. doi:10.1103/revmodphys.73.515

40. Wu Q, Zhang S, Song HF, Troyer M, Soluyanov AA. WannierTools: An open-source software package for novel topological materials. *Comput Phys Commun* (2018) 224:405–16. doi:10.1016/j.cpc.2017.09.033

frontiers | Frontiers in Chemistry

TYPE Mini Review
PUBLISHED 19 October 2022
DOI 10.3389/fchem.2022.1054337

OPEN ACCESS

EDITED BY
Guangzhao Wang,
Yangtze Normal University, China

REVIEWED BY
Xiaoming Zhang,
Hebei University of Technology, China
Tie Yang,
Southwest University, China

*CORRESPONDENCE
Ying Yang,
physicsyy@126.com

SPECIALTY SECTION
This article was submitted to Physical Chemistry and Chemical Physics, a section of the journal Frontiers in Chemistry

RECEIVED 26 September 2022
ACCEPTED 06 October 2022
PUBLISHED 19 October 2022

CITATION
Yang Y (2022), Mini-review of interesting properties in Mn_2CoAl bulk and films.
Front. Chem. 10:1054337.
doi: 10.3389/fchem.2022.1054337

Mini-review of interesting properties in Mn_2CoAl bulk and films

Ying Yang*

College of Physics and Electronic Engineering, Chongqing Normal University, Chongqing, China

Heusler compounds exhibit many interesting properties, such as high thermopower, magnetocaloric properties, and even topological insulator states. Heusler Mn_2CoAl alloy has been experimentally and theoretically proposed as a promising spin-gapless semiconductor with novel electronic, magnetic, spintronic, transport, and topological properties. Furthermore, the spin-gapless semiconducting-like behaviors are also predicted in Mn_2CoAl films by measuring the transport and magnetic properties. This mini-review systematically summarizes the interesting properties of Mn_2CoAl bulk and Mn_2CoAl-based films. This mini-review is hoped to guide further experimental investigations and applications in the particular scientific community.

KEYWORDS

Mn_2CoAl, spin-gapless materials, Heusler, DFT, density functional theory, film, substrate system

Introduction

On the one side, in 2008, Liu et al. (2008) investigated the structural, electronic, and magnetic properties of Mn_2CoZ (Z = Al, Si, Ge, Sn, and Sb) alloys with Hg_2CuTi-type structure with the help of first-principles calculations, and they stated that all the Mn_2CoZ alloys belong to ferrimagnetic half-metals (Fang et al., 2002; Dowben and Skomski, 2004; Müller et al., 2009; Ashton et al., 2017). It is noteworthy that the spin-gapless semiconducting state of Mn_2CoAl has not been mentioned by Liu et al. (2008). Moreover, Liu et al. (2008) stated that the Mn_2CoZ (Z = Al, Si, Ge, Sn, and Sb) alloys follow the Slater-Pauling rule $M_t = N_V - 24$ (M_t denotes the total magnetic moment and the N_V is the valence electrons in both spin channels). Then, Liu et al. (2008) successfully synthesized the Hg_2CuTi-type Mn_2CoZ alloys, in which the two Mn atoms exhibit different magnetic behaviors. In the same year, Xing et al. (2008) also proposed the half-metallic ferrimagnetism of the Heusler alloys Mn_2CoZ (Z = Al, Ga, Si, Ge) using the first-principles plane-wave pseudopotential method. Moreover, they (Xing et al., 2008) pointed out that the half-metallic states in Mn_2CoZ can maintain in a large range of lattice constants, reflecting robust half-metallic behaviors. In 2011, Meinert, Schmalhorst, and Reiss (Meinert et al., 2011) studied the complex magnetic interactions between the constituents and the Curie temperatures using first-principles calculations. Surprisingly, the Curie temperatures of $Mn_2CoAl/Ga/In$ are all above 800 K.

On the other side, in 2008, Wang, (2008) proposed the concept of a spin-gapless semiconductor. The spin-gapless semiconductor is a new class of zero-gap materials. Spin-gapless semiconductors for practical use should feature 1) completely spin polarized carriers; 2) high mobility of carriers; 3) zero or negligibly small excitation energy of electrons from the valence to the conduction band; 4) easy switching between electron and hole modes by tuning the Fermi level, owing to the ambipolar nature of the band gap (For type II spin-gapless semiconductors). Wang, (2008) proposed that by introducing magnetic ions into the parent nonmagnetic gapless compounds, such as $PbPdO_2$, the spin-gapless semiconducting state can appear. Based on his work, a series of spin-gapless semiconductors (Li et al., 2009; Gao et al., 2015; Wang et al., 2016a; Galanakis et al., 2016; Gao et al., 2016; He et al., 2017; Wang, 2017; Deng et al., 2018a; Huang et al., 2019a; Nadeem et al., 2020; Yue et al., 2020; Yang et al., 2021) with parabolic or linear dispersion between energy and momentum are proposed. More interestingly, topological signatures, such as Dirac point and nodal line states, can be found in spin-gapless semiconductors. For example, He et al. (2017) proposed that $NiCl_3$ monolayer is a near-room-temperature Dirac spin-gapless semiconductor when the spin-orbital coupling (SOC) is absent. When SOC is added, it becomes an intrinsic Chern insulator with a large non-trivial band gap of ~24 meV, at which the quantum anomalous Hall effect could be observed. In 2018, Zhang et al. (2018) proposed the nodal ring spin-gapless semiconducting state in a 2D HK lattice *via* first-principle calculations. In 2022, Ding et al. (2022) summarized almost all the predicted nodal ring/line spin-gapless semiconductors in 2D and 3D materials (Guan et al., 2013; Li and Yang, 2013; Ding and Wang, 2015; Wang et al., 2016b; Rasool et al., 2016; Wang et al., 2017c; Liu et al., 2017; Deng et al., 2018b; Wang et al., 2018; Huang et al., 2019b; Wu et al., 2020b; Guo et al., 2020; Li et al., 2021; Wang et al., 2021; Ji et al., 2022; Wu et al., 2022) in the past 3 years. Remarkably, they (Ding et al., 2022) also provided three valuable suggestions for the future theoretical design of nodal ring/line spin-gapless semiconductors. Moreover, some quaternary Heusler SGSs (Bainsla et al., 2015; Rani et al., 2019) have been prepared, and their interesting gapless behavior has been confirmed. For the verification of the spin-gapless semiconducting property, their specific transport behavior has been widely measured and accepted as strong evidence.

In 2013, the spin-gapless semiconducting state in Mn_2CoAl has been experimentally confirmed by Ouardi et al. (2013a) according to the transport behaviors. They reported that Mn_2CoAl with robust spin polarization is a promising material for room-temperature semiconductor spintronics. In this mini-review, the properties of Mn_2CoAl bulk, Mn_2CoAl [001] surface, Mn_2CoAl/GaAs heterostructures, Mn_2CoAl/Ag/Mn_2CoAl current-perpendicular-to-plane spin valves, MgO/Mn_2CoAl/Pd trilayers, and various types of Mn_2CoAl films are reviewed in details. This mini-review aims to provide an improved understanding of the properties for Mn_2CoAl that have been reported in the last 14 years.

Structural, electronic, elastic, and thermodynamic properties for Mn_2CoAl bulk

The crystal structure of the Heusler alloys can be viewed as a cubic structure with four interpenetrating f.c.c. Sublattices A, B, C, D (see Figure 1A). Normally, full-Heusler alloys X_2YZ can host two types of structures (XA and $L2_1$ type structures). As shown in Figure 1A, we exhibited the XA type and $L2_1$ type Mn_2CoAl. MnMnCoAl and MnCoMnAl represent the XA type Mn_2CoAl and $L2_1$ type Mn_2CoAl, respectively. As mentioned above, Liu et al. (2008) have determined that the crystal structure of Heusler Mn_2CoAl should be XA type (i.e., Hg_2CuTi) instead of $L2_1$. We would like to point out that other researchers have widely investigated the competition between XA and $L2_1$ atomic ordering in full Heusler alloys (Wang et al., 2017a; Wang et al., 2017b; Han et al., 2019a; Han et al., 2019b; Wu et al., 2019; Wu et al., 2020a) in recent years.

Based on the determined XA structure, the spin-polarized band structures for Mn_2CoAl are exhibited in Figure 1B. Obviously, in the minority-spin channel, a direct band gap can be found around the Fermi level, whereas, in the majority-spin channel, an indirect zero-band gap can be observed. Note that, such band structures allow for tunable spin transport. Mn_2CoAl hosts a high Curie temperature of ~720 K and a total M_t of 2 μ_B. In 2015, Chen et al. (2015) investigated the spin-gapless semiconducting states and the dynamical stability of Mn_2CoAl, and they found that the spin-gapless semiconducting states and the dynamical stability can maintain with a pressure less than 25 GPa. The calculated elastic modulus, shear modulus, Yong's modulus, and Pugh's ration for Mn_2CoAl under equilibrium lattice constants are 185.778, 77.782, 204.768 GPa, and 2.39, respectively. Moreover, with the help of the quasiharmonic Debye model, the pressure and temperature dependences of normalized volume V/V_0, bulk modulus B, thermal expansivity, Gruneisen parameter, heat capacity, and Debye temperature are evaluated by Chen et al. (2015) for Mn_2CoAl up to 25 GPa. The above-listed data can be viewed as a reference for the follow-up experimental studies.

Conditions for spin-gapless semiconducting behavior in Mn_2CoAl bulk

In 2014, Galanakis et al. (2014) examined the conditions for the spin-gapless semiconducting state in Mn_2CoAl *via* first-

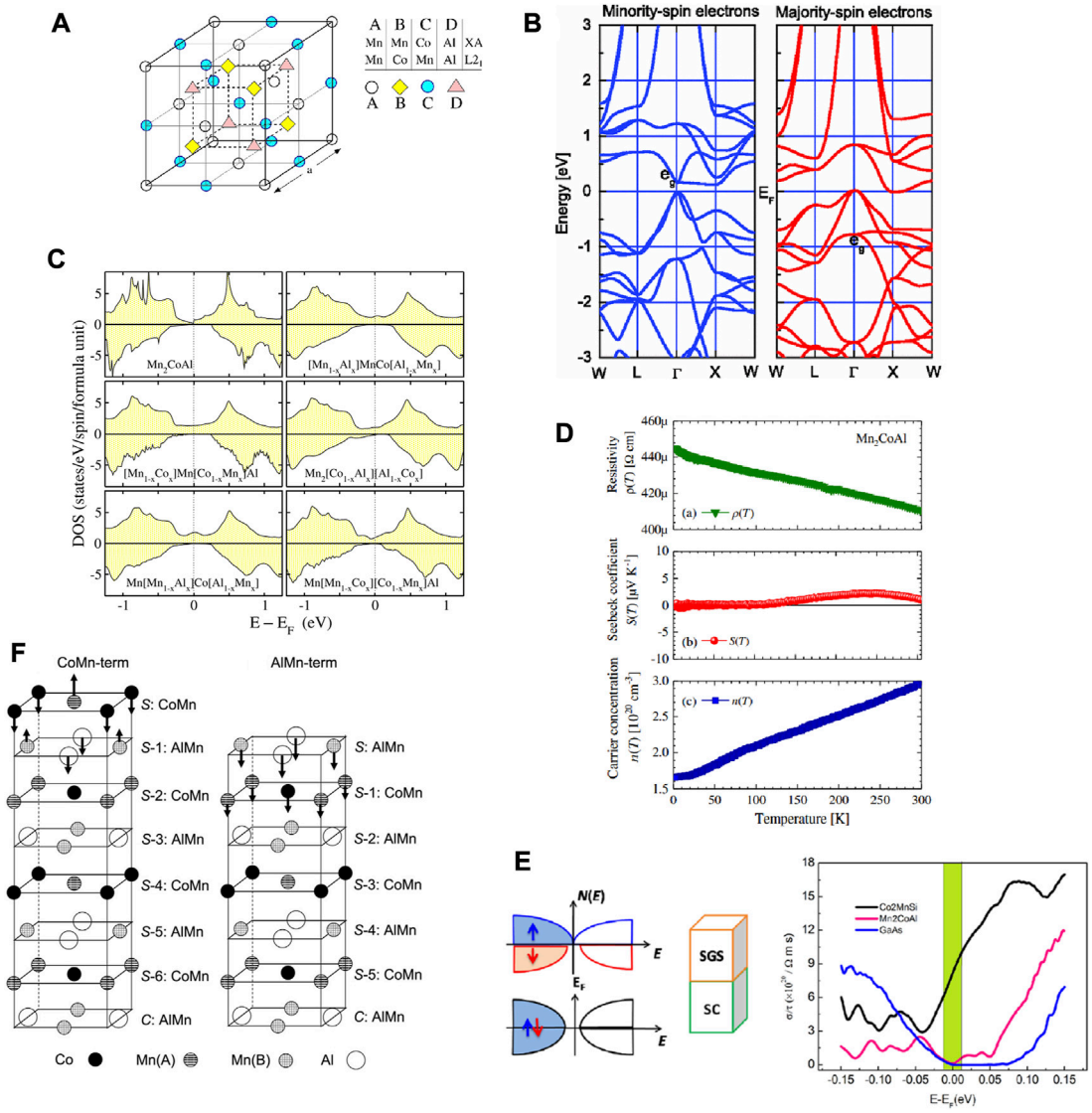

FIGURE 1
(A) Crystal structures of XA and L2$_1$ type Mn_2CoAl. **(B)** Band structures of XA Mn_2CoAl. **(C)** The density of states of Mn_2CoAl by considering atomic swaps. **(D)** Measured resistivity, S(T), and n for Mn_2CoAl sample under different temperatures. **(E)** Schematic diagrams of spin-gapless semiconductor (SGS)/semiconductor (SC) spin injection scheme and the calculated room temperature conductivities for half-metal Co2MnSi, spin-gapless semiconductor Mn_2CoAl, and semiconductor GaAs. **(F)** The (001) Mn_2CoAl surface with Co-Mn and Al-Mn terminated surfaces. Reproduced from Refs. (Ouardi et al., 2013a; Li and Jin, 2013; Galanakis et al., 2014; Xu et al., 2019) with permissions.

principle calculations. They (Galanakis et al., 2014) showed that the spin-gapless semiconducting states in Mn_2CoAl can be kept by applying the tetragonalization of the lattice. However, the spin-gapless semiconducting states in Mn_2CoAl are disappeared by considering the atomic swaps. Swapping the atoms induces a physics nature transition from a spin-gapless semiconducting state to a half-metallic state (as shown in Figure 1C). Furthermore, they (Galanakis et al., 2014) also pointed out that the appearance of Co-surplus will lead to half-metallic states.

Experimentally verified for the spin-gapless semiconducting behavior in Mn_2CoAl bulk

In 2013, the transport measurements of Mn_2CoAl bulk were performed by Ouardi *et al.* (Ouardi et al., 2013b; Ouardi et al., 2019) *via* a physical properties measurement system. They pointed out that Mn_2CoAl bulk hosts a nonmetallic resistivity (see Figure 1D). Note that the resistivity of Mn_2CoAl bulk is two orders of magnitude higher than that of Co_2FeSi metal. From

Figure 1D, one finds that the carrier concentration (n) is temperature independent, and the Seebeck coefficient ($S(T)$) is vanishing. The reason for the appearance of a vanishing $S(T)$ is the compensation of the electron and hole. Note that the temperature-independent n is a main feature for the gapless systems.

Combining the transport and magnetic properties, one can conclude that Mn_2CoAl bulk should be a spin-gapless semiconductor. Ouardi *et al.* (Ouardi et al., 2013b; Ouardi et al., 2019) also reported the magnetoresistance results and the anomalous Hall conductivity of Mn_2CoAl bulk, suggesting Mn_2CoAl is a novel spintronic material.

Note that the transport and magnetic properties cannot be viewed as the only criteria to judge the spin-gapless semiconducting states in Heusler alloys. The microstructure observations (Xu et al., 2019) should also be considered to validate the spin-gapless semiconducting states in Heusler alloys.

New spin injection scheme based on Mn_2CoAl

Spin injection efficiency based on conventional and/or half-metallic ferromagnets/semiconductors is greatly limited by the Schmidt barrier due to conductivity mismatch. In 2015, Xu et al. (2019) proposed that the spin-gapless semiconductor, such as Mn_2CoAl, can be used to replace the conventional and/or half-metallic ferromagnets and form a spin-gapless semiconductor/semiconductor heterostructure (as shown in Figure 1E).

From Figure 1E, we listed the calculated room temperature conductivities for half-metal Co_2MnSi, spin-gapless semiconductor Mn_2CoAl, and semiconductor GaAs. The figure shows that the conductivity of spin-gapless semiconductor Mn_2CoAl is much lower than that of half-metal Co_2MnSi. More importantly, the conductivity of spin-gapless semiconductor Mn_2CoAl is very close to that of semiconductor GaAs. Hence, using spin-gapless semiconductors as the magnetic injectors can reduce the conductive mismatch and enhance the spin injection efficiency.

We would like to point out that the thermodynamic stability, magnetism, and half metallicity of Mn_2CoAl/GaAs (0 0 1) interface have been studied by Feng *et al.* (Feng et al., 2015a) *via* first principle calculations in 2015. In this same year, Feng *et al.* (Feng et al., 2015b) studied the effect of disorder on the electronic and magnetic properties of Mn_2CoAl/GaAs heterostructures from theory.

Electronic structures, magnetism, and half-metallicity for [001] Mn_2CoAl surface

In 2013, Li and Jin (2013) studied the electronic, magnetic, and half-metallic properties of the Mn_2CoAl [001] surface by first-principles calculation. As shown in Figure 1F, two types of surface terminations, i.e., AlMn terminated and CoMn terminated surfaces, are considered by Li and Jin (2013). They Li and Jin (2013) reported that the AlMn-terminated Mn_2CoAl surface hosts half-metallic behavior, whereas the CoMn-terminated Mn_2CoAl surface does not have the half-metallic behavior.

In 2018, Meng *et al.* (Wei et al., 2018) investigated the interfacial electronic, magnetic, and spin transport properties of Mn_2CoAl/Ag/Mn_2CoAl current-perpendicular-to-plane spin valves. Interestingly, they (Wei et al., 2018) pointed out that the $MnCo^T$-terminated interface enjoys the largest interface spin polarization of 78% and magnetoresistance ratio of 2,886%.

Experimental Mn_2CoAl based films

To this date, some investigations are performed on Mn_2CoAl-based films in the experiment. Hence, this section reviews some interesting properties focusing on the Mn_2CoAl-based films. In 2018, Arima et al. (2018) studied the electronic structures and the anomalous Hall conductivity of Si-substituted Mn_2CoAl epitaxial films. Based on the calculated density of states in Figure 2A, one finds that the spin-gapless semiconducting-like behavior can be maintained in $Mn_2CoAl_{1-x}Si_x$ with $x < 0.2$. $Mn_2CoAl_{1-x}Si_x$ films ($0 \le x \le 0.3$) were grown on $MgAl_2O_4$ (100) substrates by molecular beam epitaxy. We collect the θ-2θ x-ray diffraction of the $Mn_2CoAl_{1-x}Si_x$ films in Figure 2B. Arima et al. (2018) stated that the electrical conductivity of $Mn_2CoAl_{0.8}Si_{0.2}$ film is 2340 S/cm, which is closes to that of Mn_2CoAl bulk (2440 S/cm).

In 2013, Jamer et al. (2013) prepared Mn_2CoAl films on GaAs (001) substrates using molecular beam epitaxy. From Figure 2C, one finds the low-temperature resistivity of a 69 nm thick Mn_2CoAl film is about 220 μΩcm, and a metallic-like behavior at low temperatures. They (Jamer et al., 2014) also reported that the Mn_2CoAl films on GaAs (001) substrates exhibited varying amounts of disorder under different annealing temperatures, resulting in the magnetism changing. As the annealing temperature increases, the M_t increases.

In 2014, Xu et al. (2014) prepared Mn_2CoAl films on the thermally oxidized Si substrates by magnetron sputtering deposition. They found that the films host a semiconducting-like resistivity and linear magnetoresistance in the whole region (see Figure 2D). Xu et al. (2014) also reported the unusually low anomalous Hall conductivity, saturation magnetization (1.94 μ_B at 5 K), and the Curie temperature (~550 K). Usually, the results mentioned above are the transport signatures of spin-gapless semiconductors. In 2018, Chen et al. (2018) prepared Mn_2CoAl films on MgO (001) substrates using molecular beam epitaxy. Their electro-

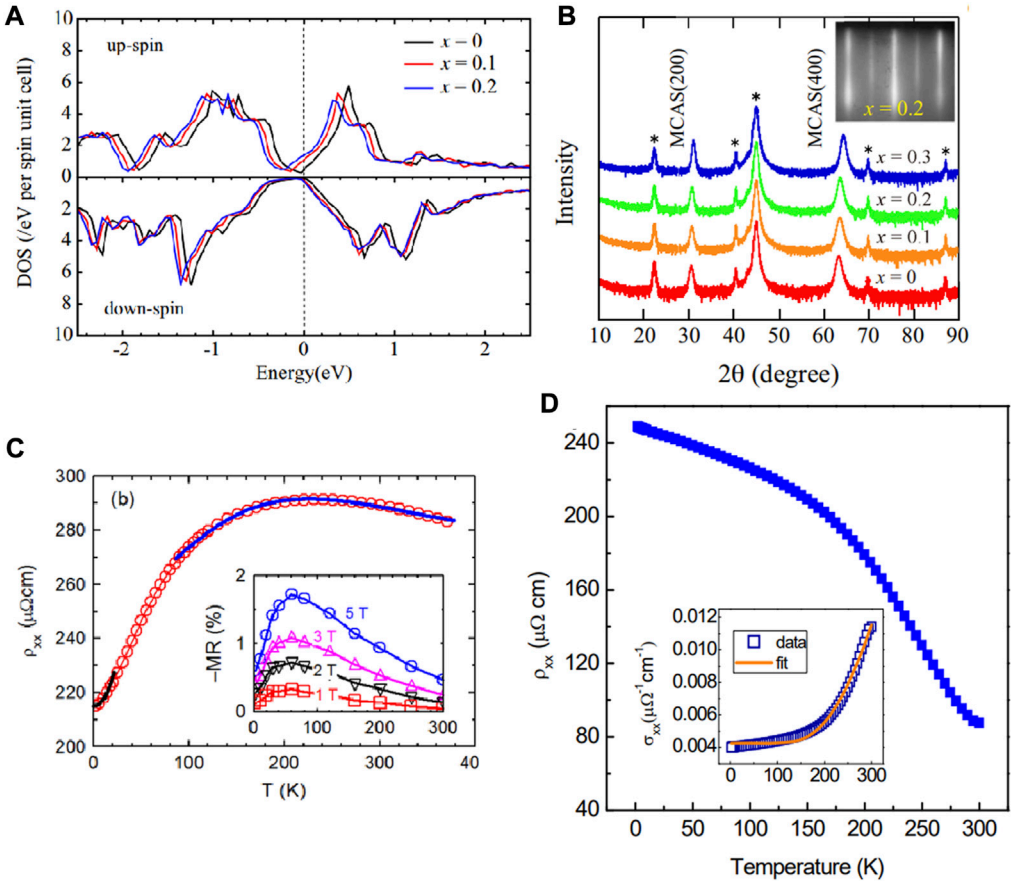

FIGURE 2
(A) Density of states for $Mn_2CoAl_{1-x}Si_x$ (x = 0, 0.1, and 0.2). **(B)** The θ-2θ x-ray diffraction of the $Mn_2CoAl_{1-x}Si_x$ films. **(C)** Resistivity *versus* temperature (red circles). Insert shows magnetoresistance at several magnetic fields. **(D)** The relationship between the resistivity and temperature was measured at zero magnetic fields. The inset shows the fitting of conductivity. Reproduced from Refs. (Jamer et al., 2013; Xu et al., 2014; Arima et al., 2018) with permissions.

and magneto-transport results showed that the Mn_2CoAl hosts spin gapless semiconducting mechanisms at low temperatures. In 2017, Ludbrook and the collaborators (Ludbrook et al., 2017) showed that the MgO/Mn_2CoAl/Pd trilayers could exhibit a novel topological Hall effect in temperatures between 3 K and 280 K. The topological Hall effect is evidence of skyrmions.

Summary

In this mini-review, the electronic, magnetic, and transport properties of Mn_2CoAl bulk, Mn_2CoAl [001] surface, Mn_2CoAl/GaAs heterostructures, Mn_2CoAl/Ag/Mn_2CoAl current-perpendicular-to-plane spin valves, MgO/Mn_2CoAl/Pd trilayers, and various types of Mn_2CoAl films (with $MgAl_2O_4$, GaAs, MgO, and thermally oxidized Si substrates) are reviewed in details. A new spin injection scheme based on Mn_2CoAl and normal semiconductors is also summarized in this mini-review.

Author contributions

The author confirms being the sole contributor of this work and has approved it for publication.

Acknowledgments

YY is grateful for support from the key project of education planning supported by the Chongqing municipal education commission (No. 2021-GX-013) and the Basic Research and

Frontier Exploration Project of Chongqing Municipality (cstc2018jcyjAX0820).

Conflict of interest

The author declares that the research was conducted in the absence of any commercial or financial relationships that could be construed as a potential conflict of interest.

Publisher's note

References

Arima, K., Kuroda, F., Yamada, S., Fukushima, T., Oguchi, T., and Hamaya, K. (2018). Anomalous Hall conductivity and electronic structures of Si-substituted Mn2CoAl epitaxial films. *Phys. Rev. B* 97 (5), 054427. doi:10.1103/physrevb.97.054427

Ashton, M., Gluhovic, D., Sinnott, S. B., Guo, J., Stewart, D. A., and Hennig, R. G. (2017). Two-dimensional intrinsic half-metals with large spin gaps. *Nano Lett.* 17 (9), 5251–5257. doi:10.1021/acs.nanolett.7b01367

Bainsla, L., Mallick, A., Raja, M., Nigam, A., Varaprasad, B., Takahashi, Y., et al. (2015). Spin gapless semiconducting behavior in equiatomic quaternary CoFeMnSi Heusler alloy. *Phys. Rev. B* 91, 104408. doi:10.1103/physrevb.91.104408

Chen, P., Gao, C., Chen, G., Mi, K., Liu, M., Zhang, P., et al. (2018). The low-temperature transport properties of Heusler alloy Mn2CoAl. *Appl. Phys. Lett.* 113 (12), 122402. doi:10.1063/1.5046396

Chen, X. R., Zhong, M. M., Feng, Y., Zhou, Y., Yuan, H. K., and Chen, H. (2015). Structural, electronic, elastic, and thermodynamic properties of the spin-gapless semiconducting Mn2CoAl inverse Heusler alloy under pressure. *Phys. Status Solidi B* 252 (12), 2830–2839. doi:10.1002/pssb.201552389

Deng, Y. X., Chen, S. Z., Zeng, Y., Feng, Y., Zhou, W. X., Tang, L. M., et al. (2018). Spin gapless semiconductor and half-metal properties in magnetic penta-hexa-graphene nanotubes. *Org. Electron.* 63, 310–317. doi:10.1016/j.orgel.2018.09.046

Deng, Y. X., Chen, S. Z., Zeng, Y., Feng, Y., Zhou, W. X., Tang, L. M., et al. (2018). Spin gapless semiconductor and half-metal properties in magnetic penta-hexa-graphene nanotubes. *Org. Electron.* 63, 310–317. doi:10.1016/j.orgel.2018.09.046

Ding, G., Wang, J., Chen, H., Zhang, X., and Wang, X. (2022). Investigation of nodal line spin-gapless semiconductors using first-principles calculations. *J. Mat. Chem. C Mat.* 10, 6530–6545. doi:10.1039/d2tc00305h

Ding, Y., and Wang, Y. (2015). Structural, electronic, and magnetic properties of adatom adsorptions on black and blue phosphorene: A first-principles study. *J. Phys. Chem. C* 119 (19), 10610–10622. doi:10.1021/jp5114152

Dowben, P. A., and Skomski, R. (2004). Are half-metallic ferromagnets half metals? *J. Appl. Phys.* 95 (11), 7453–7458. doi:10.1063/1.1682911

Fang, C. M., De Wijs, G. A., and De Groot, R. A. (2002). Spin-polarization in half-metals (invited). *J. Appl. Phys.* 91 (10), 8340–8344. doi:10.1063/1.1452238

Feng, Y., Tian, C. L., Yuan, H. K., Kuang, A. L., and Chen, H. (2015). The effect of disorder on the electronic and magnetic properties of Mn2CoAl/GaAs heterostructures. *J. Phys. D. Appl. Phys.* 48 (44), 445003. doi:10.1088/0022-3727/48/44/445003

Feng, Y., Zhou, T., Chen, X., Yuan, H., and Chen, H. (2015). Thermodynamic stability, magnetism and half metallicity of Mn2CoAl/GaAs (0 0 1) interface. *J. Phys. D. Appl. Phys.* 48 (28), 285302. doi:10.1088/0022-3727/48/28/285302

Galanakis, I., Özdoğan, K., Şaşıoğlu, E., and Blügel, S. (2014). Conditions for spin-gapless semiconducting behavior in Mn2CoAl inverse Heusler compound. *J. Appl. Phys.* 115 (9), 093908. doi:10.1063/1.4867917

Galanakis, I., Özdoğan, K., and Şaşıoğlu, E. (2016). Spin-filter and spin-gapless semiconductors: The case of Heusler compounds. *AIP Adv.* 6 (5), 055606. doi:10.1063/1.4943761

Gao, G., Ding, G., Li, J., Yao, K., Wu, M., and Qian, M. (2016). Monolayer MXenes: Promising half-metals and spin gapless semiconductors. *Nanoscale* 8 (16), 8986–8994. doi:10.1039/c6nr01333c

Gao, Q., Xie, H. H., Li, L., Lei, G., Deng, J. B., and Hu, X. R. (2015). First-principle study on some new spin-gapless semiconductors: The Zr-based quaternary Heusler alloys. *Superlattices Microstruct.* 85, 536–542. doi:10.1016/j.spmi.2015.05.049

Guan, J., Chen, W., Li, Y., Yu, G., Shi, Z., Huang, X., et al. (2013). An effective approach to achieve a spin gapless semiconductor–half-metal–metal transition in zigzag graphene nanoribbons: Attaching A floating induced dipole field via π–π interactions. *Adv. Funct. Mat.* 23 (12), 1507–1518. doi:10.1002/adfm.201201677

Guo, S. D., Mu, W. Q., Zhu, Y. T., and Chen, X. Q. (2020). Coexistence of intrinsic piezoelectricity and ferromagnetism induced by small biaxial strain in septuple-atomic-layer VSi 2 P 4. *Phys. Chem. Chem. Phys.* 22 (48), 28359–28364. doi:10.1039/d0cp05273f

Han, Y., Chen, Z., Kuang, M., Liu, Z., Wang, X., and Wang, X. (2019). 171 scandium-based full heusler compounds: A comprehensive study of competition between XA and L21 atomic ordering. *Results Phys.* 12, 435–446. doi:10.1016/j.rinp.2018.11.079

Han, Y., Wu, M., Feng, Y., Cheng, Z., Lin, T., Yang, T., et al. (2019). Competition between cubic and tetragonal phases in all-*d*-metal heusler alloys, $X_{2-x}Mn_{1+x}V$ (X = Pd, Ni, Pt, Ag, Au, Ir, Co; x = 1, 0): A new potential direction of the heusler family. *IUCrJ* 6 (3), 465–472. doi:10.1107/s2052252519004007

He, J., Li, X., Lyu, P., and Nachtigall, P. (2017). Near-room-temperature chern insulator and Dirac spin-gapless semiconductor: Nickel chloride monolayer. *Nanoscale* 9 (6), 2246–2252. doi:10.1039/c6nr08522a

Huang, H. M., Cao, M. L., Jiang, Z. Y., Xiong, Y. C., Zhang, X., Luo, S. J., et al. (2019). High spin polarization in formamidinium transition metal iodides: First principles prediction of novel half-metals and spin gapless semiconductors. *Phys. Chem. Chem. Phys.* 21 (29), 16213–16222. doi:10.1039/c9cp00958b

Huang, H. M., Cao, M. L., Jiang, Z. Y., Xiong, Y. C., Zhang, X., Luo, S. J., et al. (2019). High spin polarization in formamidinium transition metal iodides: First principles prediction of novel half-metals and spin gapless semiconductors. *Phys. Chem. Chem. Phys.* 21 (29), 16213–16222. doi:10.1039/c9cp00958b

Jamer, M. E., Assaf, B. A., Devakul, T., and Heiman, D. (2013). Magnetic and transport properties of Mn2CoAl oriented films. *Appl. Phys. Lett.* 103 (14), 142403. doi:10.1063/1.4823601

Jamer, M. E., Assaf, B. A., Sterbinsky, G. E., Arena, D. A., and Heiman, D. (2014). Atomic moments in Mn2CoAl thin films analyzed by X-ray magnetic circular dichroism. *J. Appl. Phys.* 116 (21), 213914. doi:10.1063/1.4903771

Ji, Y., Tan, X., Yue, X., Sun, Y., Wang, Y., Liang, H., et al. (2022). Strain-induced spin-gapless semiconductors and pure thermal spin-current in magnetic black arsenic-phosphorus monolayers. *Phys. Chem. Chem. Phys.* 24 (22), 13897–13904. doi:10.1039/d2cp01108e

Li, H., Hayashi, K., Nagashima, Y., Yoshioka, S., Dong, J., Li, J. F., et al. (2021). Effects of disorder on the electronic structure and thermoelectric properties of an inverse full-heusler Mn2CoAl alloy. *Chem. Mat.* 33 (7), 2543–2547. doi:10.1021/acs.chemmater.0c04902

Li, J., and Jin, Y. (2013). Half-metallicity of the inverse heusler alloy Mn2CoAl (0 0 1) surface: A first-principles study. *Appl. Surf. Sci.* 283, 876–880. doi:10.1016/j.apsusc.2013.07.036

Li, X., and Yang, J. (2013). Bipolar magnetic materials for electrical manipulation of spin-polarization orientation. *Phys. Chem. Chem. Phys.* 15 (38), 15793–15801. doi:10.1039/c3cp52623b

Li, Y., Zhou, Z., Shen, P., and Chen, Z. (2009). Spin gapless semiconductor–metal– half-metal properties in nitrogen-doped zigzag graphene nanoribbons. *ACS Nano* 3 (7), 1952–1958. doi:10.1021/nn9003428

Liu, G. D., Dai, X. F., Liu, H. Y., Chen, J. L., Li, Y. X., Xiao, G., et al. (2008). Mn2CoZ(Z=Al, Ga, In, Si, Ge, Sn, Sb)compounds: Structural, electronic, and magnetic properties. *Phys. Rev. B* 77 (1), 014424. doi:10.1103/physrevb.77.014424

Liu, J. H., Kan, X., Amin, B., Gan, L. Y., and Zhao, Y. (2017). Theoretical exploration of the potential applications of Sc-based MXenes. *Phys. Chem. Chem. Phys.* 19 (48), 32253–32261. doi:10.1039/c7cp06224a

Ludbrook, B. M., Dubuis, G., Puichaud, A. H., Ruck, B. J., and Granville, S. (2017). Nucleation and annihilation of skyrmions in Mn2CoAl observed through the topological Hall effect. *Sci. Rep.* 7 (1), 13620. doi:10.1038/s41598-017-13211-8

Meinert, M., Schmalhorst, J. M., and Reiss, G. (2011). Exchange interactions and Curie temperatures of Mn2CoZ compounds. *J. Phys. Condens. Matter* 23 (11), 116005. doi:10.1088/0953-8984/23/11/116005

Müller, G. M., Walowski, J., Djordjevic, M., Miao, G. X., Gupta, A., Ramos, A. V., et al. (2009). Spin polarization in half-metals probed by femtosecond spin excitation. *Nat. Mat.* 8 (1), 56–61. doi:10.1038/nmat2341

Nadeem, M., Hamilton, A. R., Fuhrer, M. S., and Wang, X. (2020). Quantum anomalous Hall effect in magnetic doped topological insulators and ferromagnetic spin-gapless semiconductors—a perspective review. *Small* 16 (42), 1904322. doi:10.1002/smll.201904322

Ouardi, S., Fecher, G. H., Felser, C., and Kübler, J. (2019). Erratum: Realization of spin gapless semiconductors: The heusler compound Mn2CoAl [phys. Rev. Lett. **110**, 100401 (2013)]. *Phys. Rev. Lett.* 122 (5), 059901. doi:10.1103/physrevlett.122.059901

Ouardi, S., Fecher, G. H., Felser, C., and Kübler, J. (2013). Realization of spin gapless semiconductors: The heusler CompoundMn2CoAl. *Phys. Rev. Lett.* 110 (10), 100401. doi:10.1103/physrevlett.110.100401

Ouardi, S., Fecher, G. H., Felser, C., and Kübler, J. (2013). Realization of spin gapless semiconductors: The heusler CompoundMn2CoAl. *Phys. Rev. Lett.* 110 (10), 100401. doi:10.1103/physrevlett.110.100401

Rani, D., EnamullahBainsla, L., Suresh, K., and Alam, A. (2019). Spin-gapless semiconducting nature of Co-rich Co1+xFe1−xCrGa. *Phys. Rev. B* 99, 104429. doi:10.1103/physrevb.99.104429

Rasool, M. N., Hussain, A., Javed, A., Khan, M. A., and Iqbal, F. (2016). Structural stability, electronic and magnetic behaviour of spin-polarized YCoVZ (Z= Si, Ge) and YCoTiZ (Z= Si, Ge) Heusler alloys. *Mater. Chem. Phys.* 183, 524–533. doi:10.1016/j.matchemphys.2016.09.011

Wang, A., Peng, J., Ren, N., Ding, L., Yu, X., Wang, Z., et al. (2021). Spin-gapless states in two-dimensional molecular ferromagnet Fe2 (TCNQ) 2. *J. Phys. Chem. Lett.* 12 (33), 7921–7927. doi:10.1021/acs.jpclett.1c01869

Wang, A., Zhang, X., Feng, Y., and Zhao, M. (2017). Chern insulator and Chern half-metal states in the two-dimensional spin-gapless semiconductor Mn2C6S12. *J. Phys. Chem. Lett.* 8 (16), 3770–3775. doi:10.1021/acs.jpclett.7b01187

Wang, X., Cheng, Z., Wang, J., and Liu, G. (2016). A full spectrum of spintronic properties demonstrated by a C1 b-type Heusler compound Mn 2 Sn subjected to strain engineering. *J. Mat. Chem. C Mat.* 4 (36), 8535–8544. doi:10.1039/c6tc02526a

Wang, X., Cheng, Z., Wang, J., Wang, X. L., and Liu, G. (2016). Recent advances in the Heusler based spin-gapless semiconductors. *J. Mat. Chem. C Mat.* 4 (30), 7176–7192. doi:10.1039/c6tc01343k

Wang, X., Cheng, Z., and Wang, W. (2017). L21 and XA ordering competition in hafnium-based full-heusler alloys Hf2VZ (Z= Al, Ga, In, Tl, Si, Ge, Sn, Pb). *Materials* 10 (10), 1200. doi:10.3390/ma10101200

Wang, X., Cheng, Z., Yuan, H., and Khenata, R. (2017). L2 1 and XA ordering competition in titanium-based full-Heusler alloys. *J. Mat. Chem. C Mat.* 5 (44), 11559–11564. doi:10.1039/c7tc03909c

Wang, X. H., Yang, A. J., Koratkar, N., Chu, J. F., Lv, P. L., Rong, M. Z., et al. (2018). Effects of adatom and gas molecule adsorption on the physical properties of tellurene: A first principles investigation. *Phys. Chem. Chem. Phys.* 20 (6), 4058–4066. doi:10.1039/c7cp07906k

Wang, X. L. (2017). Dirac spin-gapless semiconductors: Promising platforms for massless and dissipationless spintronics and new (quantum) anomalous spin Hall effects. *Natl. Sci. Rev.* 4 (2), 252–257. doi:10.1093/nsr/nww069

Wang, X. L. (2008). Proposal for a new class of materials: Spin gapless semiconductors. *Phys. Rev. Lett.* 100 (15), 156404. doi:10.1103/physrevlett.100.156404

Wei, M. S., Cui, Z., Ruan, X., Zhou, Q. W., Fu, X. Y., Liu, Z. Y., et al. (2018). Interface characterization of current-perpendicular-to-plane spin valves based on spin gapless semiconductor Mn2CoAl. *Appl. Sci.* 8 (8), 1348. doi:10.3390/app8081348

Wu, D. D., Ji, Y. T., Du, G. F., Yue, X. Y., Wang, Y. Y., Li, Q. J., et al. (2022). Spin-gapless semiconducting Cl-intercalated phosphorene bilayer: A perfect candidate material to identify its ferroelectric states by spin-seebeck currents. *J. Mat. Chem. C Mat.* 10 (8), 3188–3195. doi:10.1039/d1tc05932g

Wu, M., Han, Y., Bouhemadou, A., Cheng, Z., Khenata, R., Kuang, M., et al. (2019). Site preference and tetragonal distortion in palladium-rich Heusler alloys. *IUCrJ* 6 (2), 218–225. doi:10.1107/s2052252518017578

Wu, M., Zhou, F., Khenata, R., Kuang, M., and Wang, X. (2020). Phase transition and electronic structures of all-d-metal Heusler-type X2MnTi compounds (X= Pd, Pt, Ag, Au, Cu, and Ni). *Front. Chem.* 8, 546947. doi:10.3389/fchem.2020.546947

Wu, X., Feng, Y., Li, S., Zhang, B., and Gao, G. (2020). 2D Mn2C6Se12 and Mn2C6S6Se6: Intrinsic room-temperature Dirac spin gapless semiconductors and perfect spin transport properties. *J. Phys. Chem. C* 124 (29), 16127–16135. doi:10.1021/acs.jpcc.0c04786

Xing, N., Li, H., Dong, J., Long, R., and Zhang, C. (2008). First-principle prediction of half-metallic ferrimagnetism of the Heusler alloys Mn2CoZ (Z= Al, Ga, Si, Ge) with a high-ordered structure. *Comput. Mater. Sci.* 42 (4), 600–605. doi:10.1016/j.commatsci.2007.09.007

Xu, G. Z., Du, Y., Zhang, X. M., Zhang, H. G., Liu, E. K., Wang, W. H., et al. (2014). Magneto-transport properties of oriented Mn2CoAl films sputtered on thermally oxidized Si substrates. *Appl. Phys. Lett.* 104 (24), 242408. doi:10.1063/1.4884203

Xu, X. D., Chen, Z. X., Sakuraba, Y., Perumal, A., Masuda, K., Kumara, L. S. R., et al. (2019). Microstructure, magnetic and transport properties of a Mn2CoAl Heusler compound. *Acta Mater.* 176, 33–42. doi:10.1016/j.actamat.2019.06.047

Yang, T., Cheng, Z., Wang, X., and Wang, X. L. (2021). Nodal ring spin gapless semiconductor: New member of spintronic materials. *J. Adv. Res.* 28, 43–49. doi:10.1016/j.jare.2020.06.016

Yue, Z., Li, Z., Sang, L., and Wang, X. (2020). Spin-gapless semiconductors. *Small* 16 (31), 1905155. doi:10.1002/smll.201905155

Zhang, L., Zhang, S. F., Ji, W. X., Zhang, C. W., Li, P., Wang, P. J., et al. (2018). Discovery of a novel spin-polarized nodal ring in a two-dimensional HK lattice. *Nanoscale* 10 (44), 20748–20753. doi:10.1039/c8nr05383a

frontiers | Frontiers in Chemistry

TYPE Original Research
PUBLISHED 08 November 2022
DOI 10.3389/fchem.2022.1061703

OPEN ACCESS

EDITED BY
San-Dong Guo,
Xi'an University of Posts and Telecommunications, China

REVIEWED BY
Liang Qiao,
Changchun University, China
Zhi Wen Chen,
University of Toronto, Canada

*CORRESPONDENCE
Haihua Huang,
huanghaihua@lcu.edu.cn

SPECIALTY SECTION
This article was submitted to Physical Chemistry and Chemical Physics, a section of the journal Frontiers in Chemistry

RECEIVED 04 October 2022
ACCEPTED 28 October 2022
PUBLISHED 08 November 2022

CITATION
Li L, Huang Z, Xu J and Huang H (2022), Theoretical analysis of the thermoelectric properties of penta-PdX2 (X = Se, Te) monolayer. *Front. Chem.* 10:1061703. doi: 10.3389/fchem.2022.1061703

Theoretical analysis of the thermoelectric properties of penta-PdX2 (X = Se, Te) monolayer

Lei Li[1], Zhuqin Huang[2], Jinqi Xu[2] and Haihua Huang[2]*

[1]Key Laboratory of Extraordinary Bond Engineering and Advanced Materials Technology (EBEAM) of Chongqing, Yangtze Normal University, Chongqing, China, [2]School of Materials Science and Engineering, Liaocheng University, Liaocheng, China

Based on the successful fabrication of $PdSe_2$ monolayers, the electronic and thermoelectric properties of pentagonal PdX_2 (X = Se, Te) monolayers were investigated *via* first-principles calculations and the Boltzmann transport theory. The results showed that the PdX_2 monolayer exhibits an indirect bandgap at the Perdew–Burke–Ernzerhof level, as well as electronic and thermoelectric anisotropy in the transmission directions. In the $PdTe_2$ monolayer, P-doping owing to weak electron–phonon coupling is the main reason for the excellent electronic properties of the material. The low phonon velocity and short phonon lifetime decreased the thermal conductivity (κ_l) of penta-$PdTe_2$. In particular, the thermal conductivity of $PdTe_2$ along the x and y transmission directions was 0.41 and 0.83 $Wm^{-1}K^{-1}$, respectively. Owing to the anisotropy of κ_l and electronic structures along the transmission direction of PdX_2, an anisotropic thermoelectric quality factor *ZT* appeared in PdX_2. The excellent electronic properties and low lattice thermal conductivity (κ_l) achieved a high *ZT* of the penta-$PdTe_2$ monolayer, whereas the maximum *ZT* of the p- and n-type $PdTe_2$ reached 6.6 and 4.4, respectively. Thus, the results indicate $PdTe_2$ as a promising thermoelectric candidate.

KEYWORDS

two-dimensional material, thermoelectric material, transport property, first-principles calculation, electronic structure

1 Introduction

Currently, the energy crisis is the greatest challenge facing the world today, and requires the rapid acquisition of technological alternatives to traditional energy sources (Tan et al., 2016; Yang et al., 2018). Based on the Seebeck and Peltier effects, thermoelectric materials can convert thermal and electrical energy, thereby providing an initial solution to address this problem (He and Tritt, 2017). We use the thermoelectric quality factor *ZT* (Zhao et al., 2016; Snyder and Snyder, 2017) to measure the conversion efficiency of a thermoelectric material, expressed as:

$$ZT = \frac{S^2 \sigma T}{\kappa}, \quad (1)$$

where S, σ, T, and κ are the Seebeck coefficient, electrical conductivity, absolute temperature, and thermal conductivity, respectively. The overall thermal conductivity (κ) is generated by the combined effect of the lattice (κ_l) and electronic (κ_e) thermal conductivity. Thus, a material with excellent electrical heating should achieve exceptional electrical properties [high Seebeck coefficient S, electronic conductivity σ, and power factor (PF) = $S^2\sigma$] and thermal properties (low thermal conductivity κ). In addition, electrical conductivity is counter-correlated to S and directly proportional to κ_e (Jonson and Mahan, 1980), demonstrating the tradeoff in thermoelectric materials with a good ZT.

Low-dimensional materials can achieve local quantum pegging and polarization owing to the changes in their coordination environment and, thus, work well as thermoelectric materials (Dresselhaus et al., 2007). In particular, two-dimensional (2D) materials (Buscema et al., 2013; Kumar and Schwingenschlogl, 2015; Hong et al., 2016a; Gu et al., 2016; Yoshida et al., 2016; Hippalgaonkar et al., 2017; Hu et al., 2017; Huang et al., 2019; Zhu et al., 2019), especially transition metal dichalcogenides (TMDs) (Hippalgaonkar et al., 2017; Marfoua and Hong, 2019; Ding et al., 2020; Patel et al., 2020; Tao et al., 2020; Bilc et al., 2021; Wang et al., 2021), have garnered extensive attention owing to their thermoelectric properties. TMDs exhibit various crystal structures, mainly the H (p-6 $m2$) and T (p-3$m1$) phases, which are experimentally found to have good thermal conductivity and low ZT (Yan et al., 2014; Hong et al., 2016b; Ma et al., 2016; Zhang et al., 2017). After the discovery of pentagonal graphene (Zhang et al., 2015), the low symmetry of the pentagonal composition has elevated the study of 2D electrothermal materials, such as pentagonal Y_2N_4 (Y = Pd, Ni or Pt), pentagonal Y_2C (Y = Sb, As, P) and pentasilene (Tian et al., 2016; Liu et al., 2018a; Naseri et al., 2018; Gao et al., 2019; Gao and Wang, 2020; Liu et al., 2020; Liu et al., 2021). The discovery of the good structural stability and high carrier mobility of monoclinic pentagonal PdS_2 by Wang et al. (2015) led researchers to conduct extensive studies on the various properties and potential applications of pentaco-MY_2 (M = Pd, Pt; Y = Te, Se) (Oyedele et al., 2017; Sun et al., 2018; Lan et al., 2019; Zhao et al., 2020; Raval et al., 2021; Tao et al., 2021). Lan et al. (2019) demonstrated that the κ_l along the x-(y-) transport direction for $PdTe_2$, $PdSe_2$, and PdS_2 are 1.42 (5.90), 2.91 (6.62), and 4.34 (12.48) $Wm^{-1}K^{-1}$, respectively. The maximum p-type ZT of penta-PdX_2 (X = S, Se, Te) along the x-direction are 0.85, 1.18, and 2.42, respectively, demonstrating the potential of penta-PdX_2 monolayers as thermoelectric materials. However, penta-$PdTe_2$ monolayers have not yet been synthesized experimentally. In particular, although several studies have investigated the thermoelectric properties of pristine penta-PdX_2, the conclusion are conflicting, and the principal discussions are controversial. Therefore, a systematic and detailed investigation should be conducted on the electronic and thermoelectric properties of pristine penta-PdX_2 (X = Se, Te).

In this study, we systematically investigated the electronic and thermoelectric transport properties of monolayer pentagonal $PdSe_2$ and $PdTe_2$ by combining first-principles calculations and the Boltzmann transport theory. PdX_2 exhibited the characteristics of an indirect bandgap semiconductor. The results show that the thermoelectric performance parameters of the penta-PdX_2 (X = Se, Te) monolayers, such as thermal conductivity, relaxation time, carrier mobility, and ZT, show strong anisotropy in the x and y directions due to their specific structural characteristics. Compared with $PdSe_2$, the heavier atomic mass and weaker chemical bonds of $PdTe_2$ achieved a lower κ_l and higher ZT.

2 Computational details

All calculations were performed based on the density functional theory with the projector-augmented plane wave method used in the Vienna *ab initio* simulation package (VASP) (Blöchl, 1994; Kresse and Furthmüller, 1996). The electron exchange-correlation energy was described by GGA-PBE (Perdew et al., 1996) and the cut-off energy was set to 500 eV (Monkhorst and Pack, 1976). The structural optimization was performed until the energy change per atom was less than 10^{-5} eV, the forces on atoms were less than 10^{-4} eV Å^{-1}, all the stress components were less than 0.02 GPa, and there was a maximum displacement of 5.0×10^{-4} Å. The k-point meshes were set as $12 \times 11 \times 1$ to ensure the energy convergence. We took a 20 Å thick vacuum slab insertion to model the periodic structure of the monolayers. We used the Boltzmann transport equation based on the relaxation time approximation to calculate the thermoelectric transport coefficients (Madsen and Singh, 2006).

κ_l is mainly dominated by anharmonic phonon–phonon scattering. According to the Boltzmann–Peierls theory and the relaxation time approximation, κ_l is computed by (Yue et al., 2022):

$$\kappa_L^{\alpha\beta}(T) = \frac{1}{N_q \Omega} \sum_{q,j} C_{q,j}(T) v_{q,j}^{\alpha} v_{q,j}^{\beta} \tau_{q,j}(T) \quad (2)$$

where N_q is the number of wave vectors, Ω is the unit cell volume, α and β are Cartesian coordinate directions, $C_{q,j}$ is the specific heat capacity of the jth phonon branch at the crystal momentum q, $v_{q,j}$ is the phonon group velocity obtained from the harmonic phonon frequency, and $\tau_{q,j}$ is the phonon lifetime. The harmonic phonon frequency was calculated by constructing a $4 \times 4 \times 1$ supercell based on the finite displacement method, as implemented in the Phonopy package (Togo et al., 2008). The

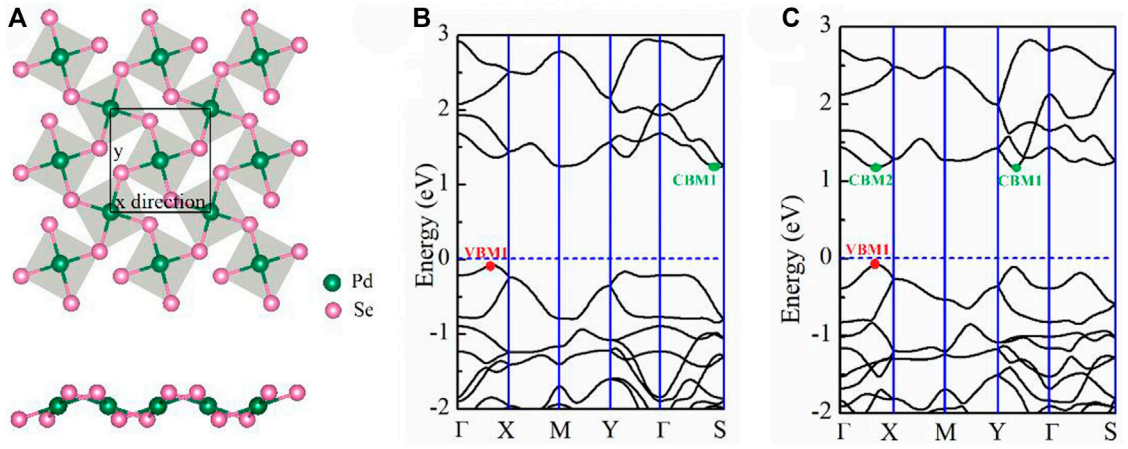

FIGURE 1
(A) Schematic of the top and side view of the penta-$PdSe_2$ monolayer; the unit cells are marked by the black line. **(B)** Band structure of the $PdSe_2$ and **(C)** $PdTe_2$ monolayers. The horizontal line indicates the Fermi level. The high symmetry *k* points are: Γ(0 0 0), X (0.5 0 0), M (0.5 0.5 0), Y (0 0.5 0), and S (0.39 0.5 0).

TABLE 1 Lattice parameters (a ,b), the thickness of monolayer materials (h), and bandgap (Eg) at the PBE level.

Materials	a (Å)	b (Å)	h (Å)	PdSe(Te) (Å)	Eg (eV)
$PdSe_2$	5.71	5.90	1.52	2.46	1.31
$PdTe_2$	6.14	6.44	1.70	2.63	1.26

anharmonic third-order interatomic force constants (3^{rd}-IFCs) were computed by constructing a 4 × 4 × 1 supercell with the cutoff value of the fifth nearest neighbor. By combining the 2^{nd}-IFCs and 3^{rd}-IFCs, κ_l was obtained through the ShengBTE code (Li et al., 2014).

3 Results and discussion

3.1 Structural models and electronic properties

The penta-PdX_2 monolayer with the $P2_1/c$ space group (No. 14) consists entirely of pentagons. The schematic crystal structures of pentagonal PdX_2 (X = Se, Te) are shown in Figure 1A. The diagram shows that the Pd atom is linked to four X-atoms, and that the adjacent X-atoms are connected to each other to form an anisotropic pentagonal structure. The anisotropy of pentagonal structure determines the anisotropy of the electron and transport properties. After structural optimization, the lattice parameter *a* (*b*) of penta-$PdSe_2$ and penta-$PdTe_2$ are 5.71 (5.90) and 6.14 (6.44) Å, respectively, which are consistent with previous theoretical calculations (Bardeen and Shockley, 1950) (see Table 1).

To determine the electronic properties of the $PdSe_2$ and $PdTe_2$ monolayers, we calculated the respective energy band structures and electronic density of states (DOS), as shown in Figure 1, Supplementary Figure S1 of the Supporting Information (SI). All materials exhibited semiconducting band structures with indirect bandgaps for the penta-$PdSe_2$ (1.31 eV) and $PdTe_2$ (1.26 eV) monolayers. Combined with the partial DOS (Supplementary Figure S1 of SI), the conduction and valence bands were mainly composed of Pd_d and X_p orbitals. In penta-$PdSe_2$, the valence band maximum (VBM) and conduction band minimum (CBM) occurred in the Γ-X and Γ-S paths, respectively, as shown in Figure 1B. In penta-$PdTe_2$, the CBM values were close to the degenerate minima in the Γ-Y and Γ-X paths with a difference of 2 meV only.

3.2 Electronic transport properties

The carrier mobility can be calculated using the deformation potential theory, which is based on the electron–acoustic phonon scattering mechanism, and can be expressed as follows (Bardeen and Shockley, 1950):

$$\mu_{2D} = \frac{e\hbar^3 C_{2D}}{k_B T m^* m_d E_l^2} \quad (3)$$

where $\hbar$, k_B, T, and m^* are the reduced Planck constant, Boltzmann constant, temperature, and effective mass along the transport direction, respectively. m_d is the average effective mass, decided by the effective masses along the x and y transport

TABLE 2 Calculated deformation potential (E_l), elastic constant (C_{2D}), effective mass of carrier (m*), average effective mass (m_d), carrier mobility (μ), relaxation time (τ) of the electron (e) and hole (h) along different directions (D) at 300 K, and average Debye temperatureθ_D (K).

	Carrier	D	C_{2D}	E_l	m*	m_d	μ	τ(fs)	θ_D
$PdSe_2$	h	x	2.34	1.22	0.81	1.07	619.88	285.86	63
		y	3.83	0.84	1.41	1.07	1229.46	986.97	
	e	x	2.34	3.32	14.68	2.74	1.80	15.07	
		y	3.83	3.73	0.51	2.74	67.32	19.55	
$PdTe_2$	h	x	1.44	1.01	0.54	0.84	1063.47	326.95	45
		y	3.18	0.74	1.30	0.84	1817.26	1345.03	
	e	x	1.44	2.09	0.87	1.12	115.61	57.27	
		y	3.18	1.80	1.44	1.12	207.96	170.49	

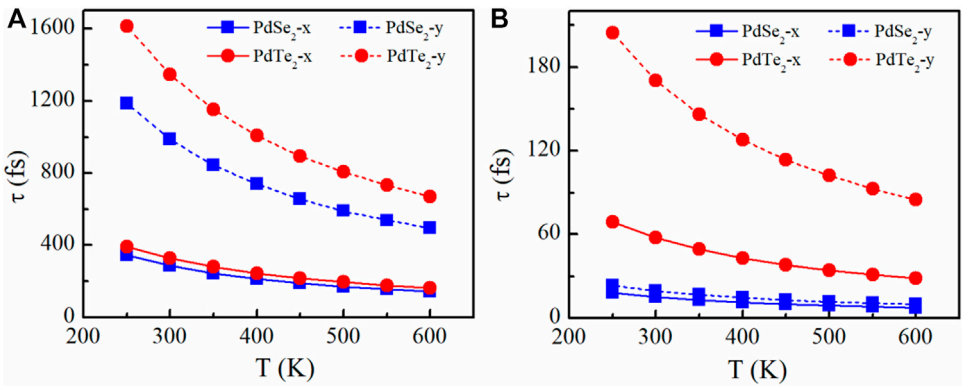

FIGURE 2
Relaxation time of the **(A)** holes and **(B)** electrons of the $PdSe_2$ and $PdTe_2$ monolayer along the x and y transport directions.

directions. C_{2D} represent the elastic modulus, which can be expressed as $C_{2D} = \frac{1}{S_0}\frac{\partial^2 E}{\partial(\frac{l}{l_0})^2}$, where E, l, l_0, and S_0 are the total energy, lattice constant after and before deformation, and area of the unit cell, respectively. By fitting the band-edge curve, we can obtained the deformation potential constant E_l.

The parameters calculated at 300 K are listed in Table 2 and include the effective mass neutrality, the elastic modulus, the deformation potential and the carrier mobility. As Table 2 shows, the anisotropy of the $PdSe_2$ and $PdTe_2$ structures causes them to exhibit anisotropy in all of the above parameters. In the *x*-direction, the effective mass of the holes was smaller than that of the electrons, particularly for the $PdSe_2$ monolayers, which is in good agreement with their dispersive band structures (Figure 1). In the *y*-direction, the effective mass of the electrons (0.51) of $PdSe_2$ was smaller than that of the holes (1.41), whereas the opposite results were found in the $PdTe_2$ monolayers. The deformation potential of the holes in the monolayer materials was smaller than that of the electrons in both directions, which reflects the lower scattering rate due to the hole–acoustic phonon interaction and larger carrier mobility. As listed in Table 1, the penta-PdX_2 monolayer exhibited high hole mobility at 300 K. For p-type doping, the small potential constant along the y transport direction indicates high hole mobility. The hole mobilities along the x(y) directions were 620 (1230) and 1063 (1817) $cm^2\ V^{-1}\ s^{-1}$ for the $PdSe_2$ and $PdTe_2$ monolayers, respectively which mark them as showing a great advantage in electron transport.

The relaxation time can be obtained using the following equation:

$$\tau = \frac{m^* \mu}{e} \tag{4}$$

The temperature-dependent relaxation times of electrons and holes along the x and y transport directions is shown in Figure 2. In agreement with our predictions, the relaxation times also exhibit significant anisotropy, and the holes lifetime (Figure 2A) was significantly longer than that of the electrons because of the weaker hole phonon scattering (Figure 2B). The results demonstrated that the individual anisotropy of the

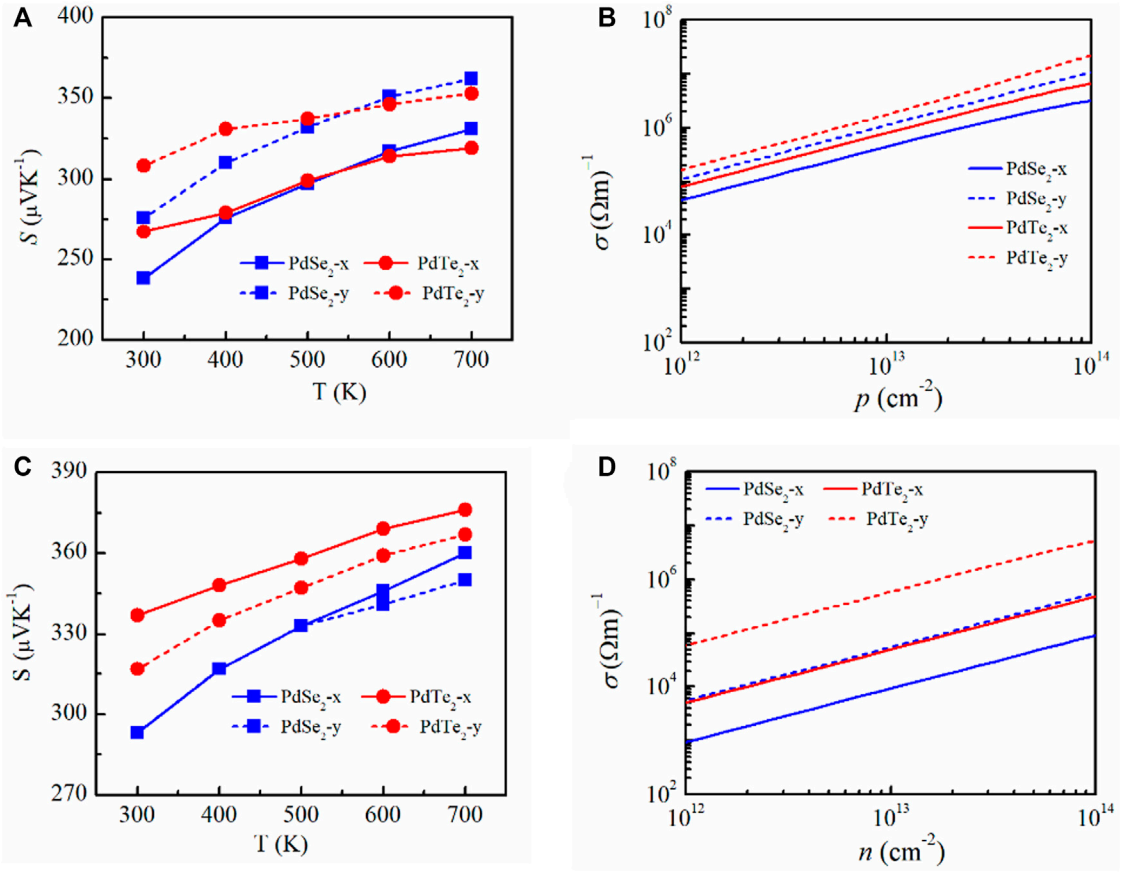

FIGURE 3
(A,C) Calculated Seebeck coefficient of penta-$PdSe_2$ and penta-$PdTe_2$ as a function of temperature and electrical conductivity. **(B,D)** Function of the carrier concentration at 300 K along the *x* and *y* directions under *p*-type (top panels) and *n*-type (bottom panels) doping.

relaxation times was mainly due to differences in the effective masses in x and y transport directions. Among all *p*-type candidates, The $PbTe_2$ monolayer had the largest amount of relaxation time variation with temperature along the *y*-direction, which is mainly due to the smallest potential constant E_l and average effective mass m^* at the VBM.

The calculated *S* and σ/τ along the x and y transport directions at 300 K as functions of the carrier concentration (n) of the $PdSe_2$ and $PdTe_2$ monolayer are plotted in Supplementary Figures S2, S3 of SI, respectively. With increasing n, *S* decreased while σ/τ increased. The transmission coefficients S and σ can be treated with the degenerate-doped single parabolic model, where S and σ were expressed as:

$$S_{2D} = \frac{2\pi^3 k_B^2 T}{3eh^2 n} m^* \quad (5)$$

$$\sigma = \frac{ne^2\tau}{m^*} \quad (6)$$

In the single parabolic band, *S* decreased as n increased, whereas σ linearly increased with n. Compared with p-type doping (Figure 3A), the *S* of *n*-type doping was higher for a fixed n (10^{13} cm^{-2}). This is because the electron effective mass lies at the edge of conduction band. The isoenergy surfaces enabled analysis of the shape of the electron band. The isoenergy surfaces of the PdX_2 monolayer were plotted (Figure 4), and the results suggested that a single pocket appear only in the Γ-X path for p-type doping, whereas multiple degenerate isoenergy pockets occurs for n-type doping. These results are consistent with previous reports on the significant enhancement of *S* owing to multiple degenerate bands at the band extrema (Xing et al., 2016; Huang et al., 2021). In *p*-type doping, the two-pocket properties (Figure 1C) increased *S* for $PdTe_2$ in penta-PdX_2 at room temperature. *S* decreased from $PdSe_2$ to $PdTe_2$ at temperatures above 600 K, which can be ascribed to the dual polarization effect caused by the reduced bandgap. Meanwhile, a larger hole's effective mass increased *S* along the *y*-direction for the $PdSe_2$ and $PdTe_2$ monolayers. The electrical conductivity during the relaxation time is inversely proportional to *S*, (as shown in Figure 3A and C) of the SI. In addition, the higher carrier pocket degeneracy and effective mass favor a higher *S* for

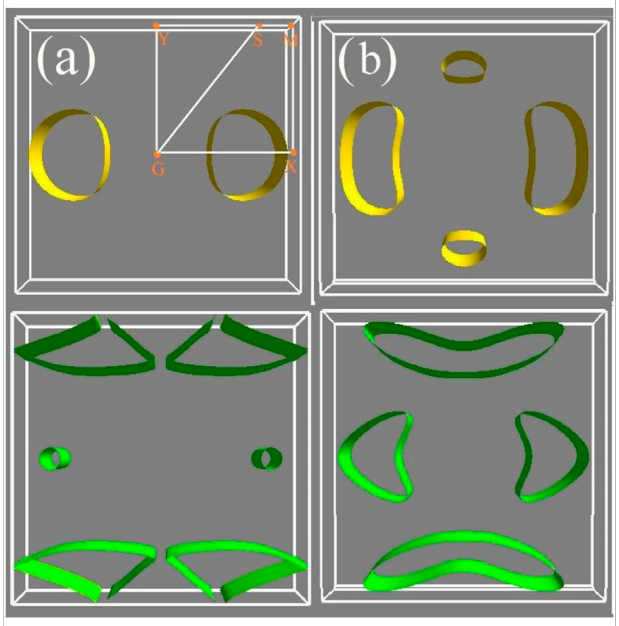

FIGURE 4
Constant energy surface of **(A)** penta-$PdSe_2$ and **(B)** penta-$PdTe_2$. The top images denote the highest valence with the energy of 0.1 eV less than the VBM, and the bottom images denote the lowest conduction band with the energy of 0.1 eV more than the CBM.

n-type doping. Among them, *n*-type doped $PdTe_2$ obtained the largest *S* in the x- or *y*-direction.

Electrical conductivity was determined based on the relaxation time τ. Figures 3B,D show the electrical conductivities of the $PdSe_2$ and $PdTe_2$ monolayers at 300 K in *p*-type and *n*-type doping. The *p*-type electrical conductivity was higher than the *n*-type electrical conductivity because of the higher carrier mobility and longer carrier lifetime. In *p*-type doping, the electrical conductivity along the *y*-direction was larger than that along the *x*-direction, although the effective mass of the holes in the *y*-direction was higher. Similar behavior was observed for n-type doping. This trend is mainly attributed to the significantly larger elastic constant in the *y*-direction, which increased τ in all temperature ranges.

PF is used to evaluate the ability of a material to convert electrical energy. The determined PF in this study is plotted in Figure 5. A higher electrical conductivity combined with a suitable *S* achieved a higher PF for p-type doping. In particular, for $PdTe_2$, the highest PF during p-type and n-type doping at 300 K reached 300 $mWmK^{-2}$ along the *y*-direction (Figure 5A) and 90 $mW\ mK^{-2}$ (Figure 5B), respectively.

3.3 Thermal transport properties

We analyzed the thermal transport properties of the PdX_2 (X = Se, Te) monolayer based on the harmonic and anharmonic effects. Phonon spectra were obtained from the harmonic interatomic force constants, as shown in Supplementary Figure S4 of SI. Heavier elements and a small force constant have lower vibration frequency. The maximum phonon vibrational frequency gradually decreased from the $PdSe_2$ to $PdTe_2$ monolayers, indicating the suppressed phonon vibrations and shift of the optical branches toward lower energies, thereby achieving strong interactions between the phonon modes and decreasing κ_l. Using the harmonic (2^{nd}) and anharmonic (3^{rd}) interatomic force constants, κ_l of the $PdSe_2$ and $PdTe_2$ monolayers were obtained, as shown in Figure 6A. In general, κ_l decreased with increasing temperature owing to the low-frequency phonons (Figure 6B) and demonstrate

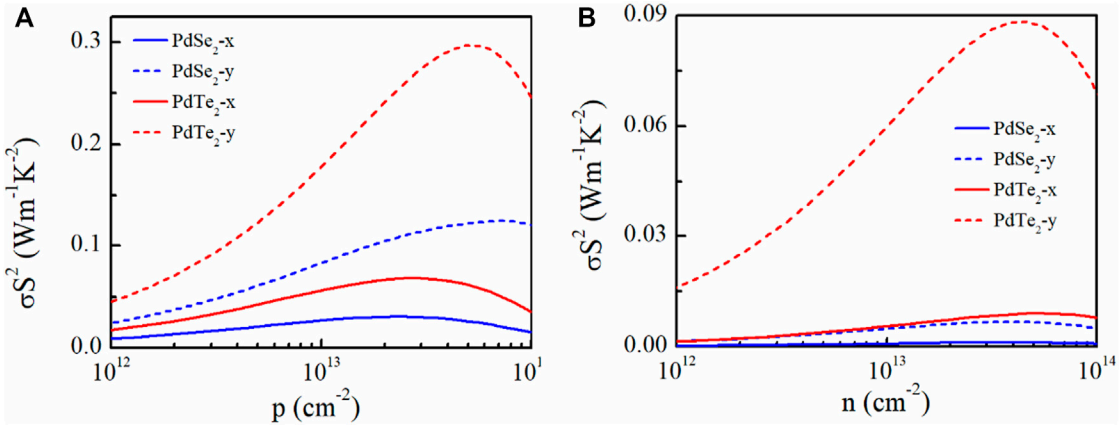

FIGURE 5
Calculated **(A)** *p*-type and **(B)** *n*-type power factor (σS^2) of penta-$PdSe_2$ and penta-$PdTe_2$ as a function of the carrier concentration at 300 K along the *x*- (solid lines) and *y*- (dotted lines) directions.

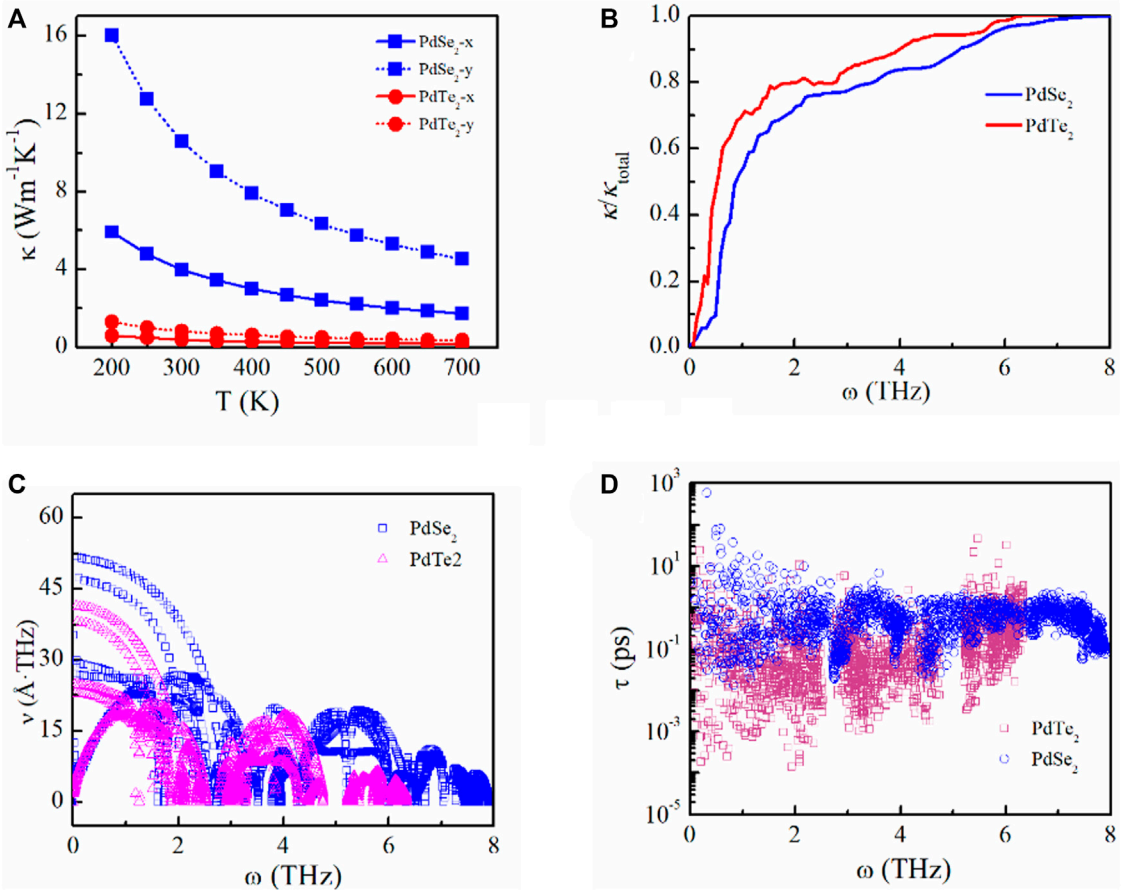

FIGURE 6
(A) Lattice thermal conductivity as a function of temperature, **(B)** phonon contributions toward the total lattice thermal conductivity, **(C)** phonon velocity, and **(D)** phonon lifetime of the penta-$PdSe_2$ and penta-$PdTe_2$ monolayers.

anisotropy along different directions. At 300 K, the calculated κ_l was 3.99 (10.58) and 0.41 (0.83) $W\,m^{-1}K^{-1}$ for $PdSe_2$ and $PdTe_2$, respectively, along the x(y) transport directions. These results are comparable to other thermoelectric materials with superior thermoelectric properties, such as monolayer SnSe (3 $Wm^{-1}K^{-1}$) (Zhang et al., 2016), bulk SnSe (0.62 $Wm^{-1}K^{-1}$) (Xiao et al., 2016), Ge_4Se_3Te (1.6 $Wm^{-1}K^{-1}$) (Huang et al., 2021), silicene (2.86 $Wm^{-1}K^{-1}$) (Peng et al., 2016), germanene (2.4 $Wm^{-1}K^{-1}$) (Peng et al., 2017), and GeSe (2.63 $Wm^{-1}K^{-1}$) (Liu et al., 2018b). Therefore, κ_e is a vital factor in the *ZT* evaluation owing to the low κ_l.

To analyze κ_l, we obtained the phonon group velocity and lifetime. The lower thermal conductivity is mainly attributed to the decreasing phonon velocity from $PdSe_2$ to $PdTe_2$, as shown in Figure 6C. Compared to the $PdSe_2$ monolayer, the $PdTe_2$ monolayer exhibited a shorter phonon lifetime, as shown in Figure 6D, indicating that the $PdTe_2$ monolayer exhibits a considerably higher scattering rate and anharmonic feature, which can also be obtained from the phonon spectra. The scattering probability of the emission and absorption processes can be described by the frequency-dependent scattering phase space. The scattering phase spaces of the emission and absorption processes at 300 K are shown in Supplementary Figure S5 in the SI. The suppressed phonons increased the scattering phase space and enhanced the anharmonic feature, resulting in decreased thermal conductivity from $PdSe_2$ to $PdTe_2$ in the low-frequency region.

To further analyze the anharmonic feature, the difference in the charge density was computed as:

$$\Delta\boldsymbol{\rho} = \boldsymbol{\rho}_{\boldsymbol{MX2}} - \boldsymbol{\rho}_{\boldsymbol{M}} - \boldsymbol{\rho}_{\boldsymbol{X2}} \tag{7}$$

where ρ_{MX2}, ρ_M, and ρ_{X2} are the total charge density, charge density of the metal atoms, and chalcogen atoms, respectively. Lower charge density was accumulated on the Pd–Te bonds of $PdTe_2$, compared to $PdSe_2$, suggesting that penta-$PdTe_2$ was significantly softer than $PdSe_2$ with a strong anharmonic effect, as shown in Figure 7. Furthermore, the average acoustic Debye temperature (θ_D) was evaluated using the formula:

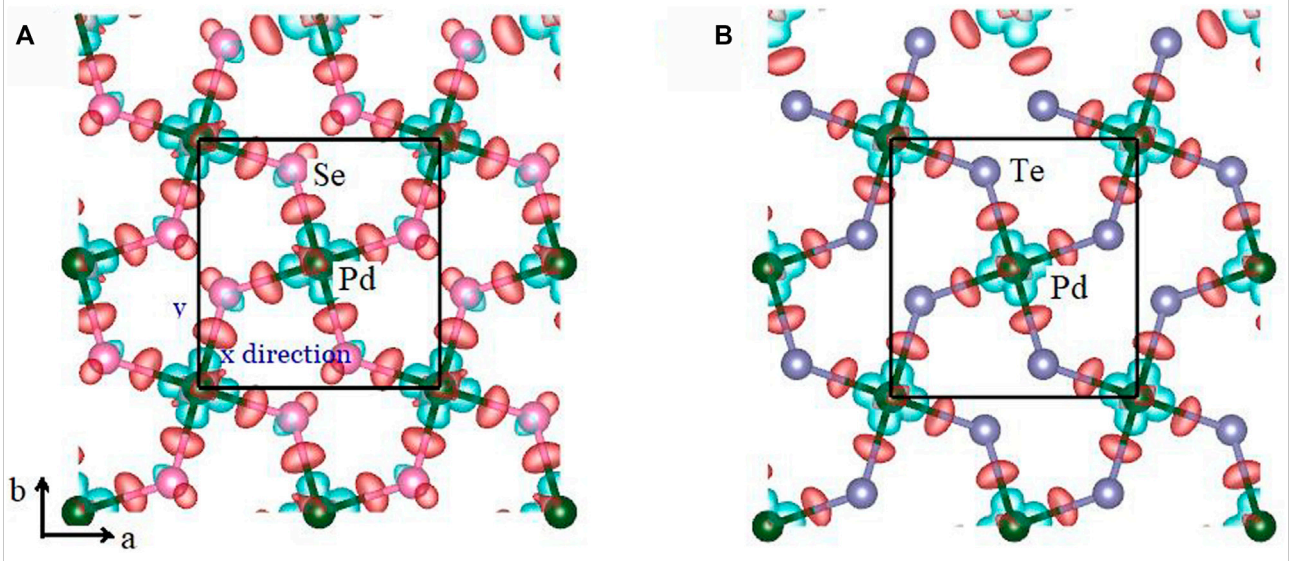

FIGURE 7
Difference of the charge density of the **(A)** penta-$PdSe_2$ and **(B)** penta-$PdTe_2$ monolayers, respectively. The red and green regions denote the charge accumulation and depletion, respectively. The charge density isosurfaces were set to 0.05 eÅ^{-3}.

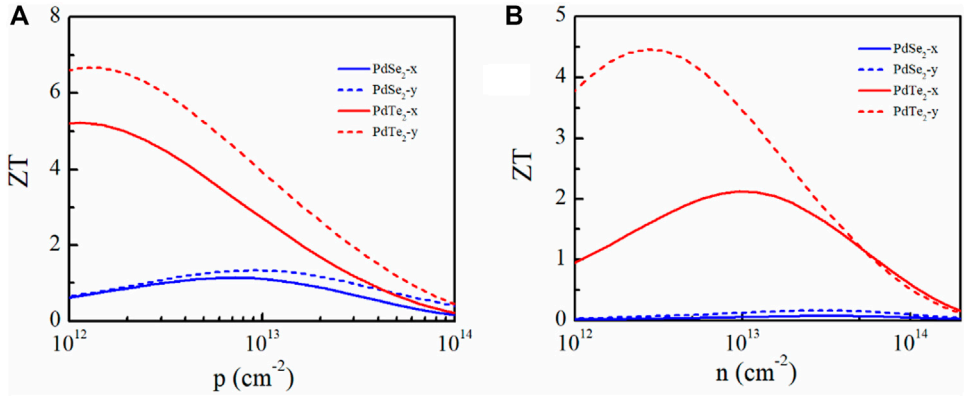

FIGURE 8
Figure of merit *ZT* of the penta-$PdSe_2$ and penta-$PdTe_2$ monolayers under **(A)** *p*-type and **(B)** *n*-type doping as a function of the carrier concentration at 300 K along the *x* and *y* directions.

$$\frac{1}{\theta_D^3} = \frac{1}{3}\left(\frac{1}{\theta_{ZA}^3} + \frac{1}{\theta_{TA}^3} + \frac{1}{\theta_{LA}^3}\right) \tag{8}$$

where θ_i (i = ZA, TA, LA) is obtained by $\theta_i = h\nu_{i,max}/k_B$, where h, k_B, and $\nu_{i,max}$ are the Planck constant, Boltzmann constant, and the maximal phonon frequency of the ith acoustic phonon mode, respectively. The θ_D values of the $PdSe_2$ and $PdTe_2$ monolayers were 63 and 45 K, respectively. The low Debye temperature is due to the weak interatomic bonding of the $PdTe_2$ monolayer, which suggested more phonons could participate in the scattering process, thereby reducing κ_l.

3.4 Quality factor

The dimensionless thermoelectric *ZT* was analyzed. κ_e was calculated using the Wiedemann–Franz law (Jonson and Mahan, 1980):

$$\kappa_e = L\sigma T \quad (9)$$

where L is the Lorenza number ($L = 2.45 \times 10^{-8}$ WΩK^{-2}). κ_e of the $PdSe_2$ and $PdTe_2$ monolayers at 300 K are shown in Supplementary Figure S6 of the SI, which was similar to κ_l. κ_e in the *y*-direction was larger than that in the *x*-direction owing to the high electronic conductivity in the *y*-direction. The larger κ_e and κ_l in the *y*-direction also prove that the thermoelectric properties were worse along the *y*-direction than along the *x*-direction.

The *ZT* values for *p*- and *n*-type doping of the monolayer materials at 300 K along the *x* and *y* directions are plotted in Figure 8. The *ZT* values of the p-type-doped $PdSe_2$ and $PdTe_2$ monolayers were larger than those with n-type doping because of the higher electronic conductivity. Owing to the smaller κ_l and higher PF, the $PdTe_2$ monolayer obtained the largest *ZT* values, regardless of the doping type. In particular, the calculated *ZT* of the p-type- and n-type-doped $PdTe_2$ monolayers along the x- (y-) direction were 5.2 (6.6) and 2.1 (4.4), demonstrating $PdTe_2$ as a promising thermoelectric candidate.

4 Conclusion

In this study, we systematically investigated the electronic structures, electronic transport, and thermal transport properties of pentagonal PdX_2 (X = Se, Te) monolayers using first-principles calculations and with Boltzmann transport theory. The $PdSe_2$ and $PdTe_2$ monolayer semiconductors had bandgaps of 1.31 and 1.26 eV, respectively. The anisotropic crystal structure of penta-PdX_2 (X = Se, Te) achieved anisotropic transport properties. At the optimized doping concentration, the $PdSe_2$ and $PdTe_2$ monolayers with p-type and n-type doping along the x- (y-) directions obtained PF of up to 30 (120) and 70 (300) mW m^{-1} K^{-2}, and 1 (7) and 9 (88) mW m^{-1} K^{-2}, respectively. The shorter phonon lifetime of penta- PdX_2 decreased κ_l. In particular, the κ_l values were 3.99 (10.58) and 0.41 (0.83) Wm^{-1}K^{-1} for $PdSe_2$ and $PdTe_2$ along the x- (y-) direction at 300 K, respectively. Owing to its smaller phonon group velocity and larger scattering space, $PdTe_2$ exhibited lower thermal conductivity. The reasonable PF and low κ_l imply that the optimal *ZT* values of *p*-type and *n*-type-doped $PdTe_2$ along the *y*-direction at the optimal doping concentrations of 6.6 and 4.4, respectively, indicating that the $PdTe_2$ monolayer is a thermoelectric material with excellent properties.

Data availability statement

The original contributions presented in the study are included in the article/Supplementary Material, further inquiries can be directed to the corresponding author.

Author contributions

LL and HH: Conceptualization, methodology, software; LL and HH: Writing—original draft preparation. LL, ZH, JX, and HH: Investigation; HH: Supervision; LL: Writing—review and editing.

Funding

Financial support was received from the National Natural Science Foundation of China (11904033 and 12204215), the Advanced Research Projects of Chongqing Municipal Science and Technology Commission (cstc2019jcyj-msxmX0674), and the Natural Science Foundation of Shandong Province of China (ZR2021QA026).

Conflict of interest

The authors declare that the research was conducted in the absence of any commercial or financial relationships that could be construed as a potential conflict of interest.

Publisher's note

Supplementary material

The Supplementary Material for this article can be found online at: https://www.frontiersin.org/articles/10.3389/fchem.2022.1061703/full#supplementary-material

References

Bardeen, J., and Shockley, W. (1950). Deformation potentials and mobilities in non-polar crystals. *Phys. Rev.* 80, 72–80. doi:10.1103/physrev.80.72

Bilc, D. I., Benea, D., Pop, V., Ghosez, P., and Verstraete, M. J. (2021). Electronic and thermoelectric properties of transition-metal dichalcogenides. *J. Phys. Chem. C* 125, 27084–27097. doi:10.1021/acs.jpcc.1c07088

Blöchl, P. E. (1994). Projector augmented-wave method. *Phys. Rev. B* 50, 17953–17979. doi:10.1103/physrevb.50.17953

Buscema, M., Barkelid, M., Zwiller, V., van der Zant, H. S., Steele, G. A., and Castellanos-Gomez, A. (2013). Large and tunable photothermoelectric effect in single-layer MoS_2. *Nano Lett.* 13, 358–363. doi:10.1021/nl303321g

Ding, W., Li, X., Jiang, F., Liu, P., Liu, P., Zhu, S., et al. (2020). Defect modification engineering on a laminar MoS_2 film for optimizing thermoelectric properties. *J. Mat. Chem. C* 8, 1909–1914. doi:10.1039/c9tc06012j

Dresselhaus, M. S., Chen, G., Tang, M. Y., Yang, R., Lee, H., Wang, D., et al. (2007). New directions for low-dimensional thermoelectric materials. *Adv. Mat.* 19, 1043–1053. doi:10.1002/adma.200600527

Gao, Z., and Wang, J.-S. (2020). Thermoelectric penta-silicene with a high room-temperature figure of merit. *ACS Appl. Mat. Interfaces* 12, 14298–14307. doi:10.1021/acsami.9b21076

Gao, Z., Zhang, Z., Liu, G., and Wang, J.-S. (2019). Ultra-low lattice thermal conductivity of monolayer penta-silicene and penta-germanene. *Phys. Chem. Chem. Phys.* 21, 26033–26040. doi:10.1039/c9cp05246a

Gu, X., Li, B., and Yang, R. (2016). Layer thickness-dependent phonon properties and thermal conductivity of MoS_2. *J. Appl. Phys.* 119, 085106. doi:10.1063/1.4942827

He, J., and Tritt, T. M. (2017). Advances in thermoelectric materials research: Looking back and moving forward. *Science* 357, eaak9997. doi:10.1126/science.aak9997

Hippalgaonkar, K., Wang, Y., Ye, Y., Qiu, D. Y., Zhu, H., Wang, Y., et al. (2017). High thermoelectric power factor in two-dimensional crystals of MoS_2. *Phys. Rev. B* 95, 115407. doi:10.1103/physrevb.95.115407

Hong, J., Lee, C., Park, J.-S., and Shim, J. H. (2016). Control of valley degeneracy in MoS_2 by layer thickness and electric field and its effect on thermoelectric properties. *Phys. Rev. B* 93, 035445. doi:10.1103/physrevb.93.035445

Hong, Y., Zhang, J., and Zeng, X. C. (2016). Thermal conductivity of monolayer $MoSe_2$ and MoS_2. *J. Phys. Chem. C* 120, 26067–26075. doi:10.1021/acs.jpcc.6b07262

Hu, Z.-Y., Li, K.-Y., Lu, Y., Huang, Y., and Shao, X.-H. (2017). High thermoelectric performances of monolayer SnSe allotropes. *Nanoscale* 9, 16093–16100. doi:10.1039/c7nr04766e

Huang, H., Fan, X., Zheng, W., and Singh, D. J. (2021). Improved thermoelectric transport properties of Ge_4Se_3 Te through dimensionality reduction. *J. Mat. Chem. C* 9, 1804–1813. doi:10.1039/d0tc04537c

Huang, S., Wang, Z., Xiong, R., Yu, H., and Shi, J. (2019). Significant enhancement in thermoelectric performance of Mg_3Sb_2 from bulk to two-dimensional mono layer. *Nano Energy* 62, 212–219. doi:10.1016/j.nanoen.2019.05.028

Jonson, M., and Mahan, G. (1980). Mott's formula for the thermopower and the Wiedemann-Franz law. *Phys. Rev. B* 21, 4223–4229. doi:10.1103/physrevb.21.4223

Kresse, G., and Furthmüller, J. (1996). Efficiency of *ab-initio* total energy calculations for metals and semiconductors using a plane-wave basis set. *Comput. Mat. Sci.* 6, 15–50. doi:10.1016/0927-0256(96)00008-0

Kumar, S., and Schwingenschlogl, U. (2015). Thermoelectric response of bulk and monolayer $MoSe_2$ and WSe_2. *Chem. Mat.* 27, 1278–1284. doi:10.1021/cm504244b

Lan, Y.-S., Chen, X.-R., Hu, C.-E., Cheng, Y., and Chen, Q.-F. (2019). Penta-PdX_2 (X= S, Se, Te) monolayers: Promising anisotropic thermoelectric materials. *J. Mat. Chem. A* 7, 11134–11142. doi:10.1039/c9ta02138h

Li, W., Carrete, J., Katcho, N. A., and Mingo, N. (2014). ShengBTE: A solver of the Boltzmann transport equation for phonons. *Comput. Phys. Commun.* 185, 1747–1758. doi:10.1016/j.cpc.2014.02.015

Liu, P.-F., Bo, T., Xu, J., Yin, W., Zhang, J., Wang, F., et al. (2018). First-principles calculations of the ultralow thermal conductivity in two-dimensional group-IV selenides. *Phys. Rev. B* 98, 235426. doi:10.1103/physrevb.98.235426

Liu, X., Ouyang, T., Zhang, D., Huang, H., Wang, H., Wang, H., et al. (2020). First-principles calculations of phonon transport in two-dimensional penta-X_2C family. *J. Appl. Phys.* 127, 205106. doi:10.1063/5.0004904

Liu, X., Zhang, D., Wang, H., Chen, Y., Wang, H., and Ni, Y. (2021). Ultralow lattice thermal conductivity and high thermoelectric performance of penta-Sb_2C monolayer: A first principles study. *J. Appl. Phys.* 130, 185104. doi:10.1063/5.0065330

Liu, Z., Wang, H., Sun, J., Sun, R., Wang, Z., and Yang, J. (2018). Penta-Pt_2N_4: An ideal two-dimensional material for nanoelectronics. *Nanoscale* 10, 16169–16177. doi:10.1039/c8nr05561k

Ma, J., Chen, Y., Han, Z., and Li, W. (2016). Strong anisotropic thermal conductivity of monolayer WTe_2. *2D Mat.* 3, 045010. doi:10.1088/2053-1583/3/4/045010

Madsen, G. K., and Singh, D. J. (2006). BoltzTraP. A code for calculating band-structure dependent quantities. *Comput. Phys. Commun.* 175, 67–71. doi:10.1016/j.cpc.2006.03.007

Marfoua, B., and Hong, J. (2019). High thermoelectric performance in hexagonal 2D $PdTe_2$ monolayer at room temperature. *ACS Appl. Mat. Interfaces* 11, 38819–38827. doi:10.1021/acsami.9b14277

Monkhorst, H. J., and Pack, J. D. (1976). Special points for Brillouin-zone integrations. *Phys. Rev. B* 13, 5188–5192. doi:10.1103/physrevb.13.5188

Naseri, M., Lin, S., Jalilian, J., Gu, J., and Chen, Z. (2018). Penta-P_2X (X= C, Si) monolayers as wide-bandgap semiconductors: A first principles prediction. *Front. Phys.* 13, 138102–138109. doi:10.1007/s11467-018-0758-2

Oyedele, A. D., Yang, S., Liang, L., Puretzky, A. A., Wang, K., Zhang, J., et al. (2017). $PdSe_2$: Pentagonal two-dimensional layers with high air stability for electronics. *J. Am. Chem. Soc.* 139, 14090–14097. doi:10.1021/jacs.7b04865

Patel, A., Singh, D., Sonvane, Y., Thakor, P., and Ahuja, R. (2020). High thermoelectric performance in two-dimensional Janus monolayer material WS-X (X= Se and Te). *ACS Appl. Mat. Interfaces* 12, 46212–46219. doi:10.1021/acsami.0c13960

Peng, B., Zhang, D., Zhang, H., Shao, H., Ni, G., Zhu, Y., et al. (2017). The conflicting role of buckled structure in phonon transport of 2D group-IV and group-V materials. *Nanoscale* 9, 7397–7407. doi:10.1039/c7nr00838d

Peng, B., Zhang, H., Shao, H., Xu, Y., Zhang, R., Lu, H., et al. (2016). First-principles prediction of ultralow lattice thermal conductivity of dumbbell silicene: A comparison with low-buckled silicene. *ACS Appl. Mat. Interfaces* 8, 20977–20985. doi:10.1021/acsami.6b04211

Perdew, J. P., Burke, K., and Ernzerhof, M. (1996). Generalized gradient approximation made simple. *Phys. Rev. Lett.* 77, 3865–3868. doi:10.1103/physrevlett.77.3865

Raval, D., Babariya, B., Gupta, S. K., Gajjar, P., and Ahuja, R. (2021). Ultrahigh carrier mobility and light-harvesting performance of 2D penta-PdX_2 monolayer. *J. Mat. Sci.* 56, 3846–3860. doi:10.1007/s10853-020-05501-w

Snyder, G. J., and Snyder, A. H. (2017). Figure of merit ZT of a thermoelectric device defined from materials properties. *Energy Environ. Sci.* 10, 2280–2283. doi:10.1039/c7ee02007d

Sun, M., Chou, J.-P., Shi, L., Gao, J., Hu, A., Tang, W., et al. (2018). Few-layer $PdSe_2$ sheets: Promising thermoelectric materials driven by high valley convergence. *ACS omega* 3, 5971–5979. doi:10.1021/acsomega.8b00485

Tan, G., Zhao, L.-D., and Kanatzidis, M. G. (2016). Rationally designing high-performance bulk thermoelectric materials. *Chem. Rev.* 116, 12123–12149. doi:10.1021/acs.chemrev.6b00255

Tao, W.-L., Lan, J.-Q., Hu, C.-E., Cheng, Y., Zhu, J., and Geng, H.-Y. (2020). Thermoelectric properties of Janus MXY (M= Pd, Pt; X, Y= S, Se, Te) transition-metal dichalcogenide monolayers from first principles. *J. Appl. Phys.* 127, 035101. doi:10.1063/1.5130741

Tao, W.-L., Zhao, Y.-Q., Zeng, Z.-Y., Chen, X.-R., and Geng, H.-Y. (2021). Anisotropic thermoelectric materials: Pentagonal PtM_2 (M = S, Se, Te). *ACS Appl. Mat. Interfaces* 13, 8700–8709. doi:10.1021/acsami.0c19460

Tian, H., Tice, J., Fei, R., Tran, V., Yan, X., Yang, L., et al. (2016). Low-symmetry two-dimensional materials for electronic and photonic applications. *Nano Today* 11, 763–777. doi:10.1016/j.nantod.2016.10.003

Togo, A., Oba, F., and Tanaka, I. (2008). First-principles calculations of the ferroelastic transition between rutile-type and $CaCl_2$-type SiO_2 at high pressures. *Phys. Rev. B* 78, 134106. doi:10.1103/physrevb.78.134106

Wang, N., Gong, H., Sun, Z., Shen, C., Li, B., Xiao, H., et al. (2021). Boosting thermoelectric performance of 2D transition-metal dichalcogenides by complex cluster substitution: The role of octahedral Au6 clusters. *ACS Appl. Energy Mat.* 4, 12163–12176. doi:10.1021/acsaem.1c01777

Wang, Y., Li, Y., and Chen, Z. (2015). Not your familiar two dimensional transition metal disulfide: Structural and electronic properties of the PdS_2 monolayer. *J. Mat. Chem. C* 3, 9603–9608. doi:10.1039/c5tc01345c

Xiao, Y., Chang, C., Pei, Y., Wu, D., Peng, K., Zhou, X., et al. (2016). Origin of low thermal conductivity in SnSe. *Phys. Rev. B* 94, 125203. doi:10.1103/physrevb.94.125203

Xing, G., Sun, J., Ong, K. P., Fan, X., Zheng, W., and Singh, D. J. (2016). Perspective: n-Type oxide thermoelectrics via visual search strategies. *Apl. Mat.* 4, 053201. doi:10.1063/1.4941711

Yan, R., Simpson, J. R., Bertolazzi, S., Brivio, J., Watson, M., Wu, X., et al. (2014). Thermal conductivity of monolayer molybdenum disulfide obtained from temperature-dependent Raman spectroscopy. *ACS Nano* 8, 986–993. doi:10.1021/nn405826k

Yang, L., Chen, Z. G., Dargusch, M. S., and Zou, J. (2018). High performance thermoelectric materials: Progress and their applications. *Adv. Energy Mat.* 8, 1701797. doi:10.1002/aenm.201701797

Yoshida, M., Iizuka, T., Saito, Y., Onga, M., Suzuki, R., Zhang, Y., et al. (2016). Gate-optimized thermoelectric power factor in ultrathin WSe_2 single crystals. *Nano Lett.* 16, 2061–2065. doi:10.1021/acs.nanolett.6b00075

Yue, T., Sun, Y., Zhao, Y., Meng, S., and Dai, Z. (2022). Thermoelectric performance in the binary semiconductor compound A_2Se_2 (A= K, Rb) with host-guest structure. *Phys. Rev. B* 105, 054305. doi:10.1103/physrevb.105.054305

Zhang, J., Liu, X., Wen, Y., Shi, L., Chen, R., Liu, H., et al. (2017). Titanium trisulfide monolayer as a potential thermoelectric material: A first-principles-based Boltzmann transport study. *ACS Appl. Mat. Interfaces* 9, 2509–2515. doi:10.1021/acsami.6b14134

Zhang, L.-C., Qin, G., Fang, W.-Z., Cui, H.-J., Zheng, Q.-R., Yan, Q.-B., et al. (2016). Tinselenidene: A two-dimensional auxetic material with ultralow lattice thermal conductivity and ultrahigh hole mobility. *Sci. Rep.* 6, 19830. doi:10.1038/srep19830

Zhang, S., Zhou, J., Wang, Q., Chen, X., Kawazoe, Y., and Jena, P. (2015). Penta-graphene: A new carbon allotrope. *Proc. Natl. Acad. Sci. U. S. A.* 112, 2372–2377. doi:10.1073/pnas.1416591112

Zhao, L.-D., Tan, G., Hao, S., He, J., Pei, Y., Chi, H., et al. (2016). Ultrahigh power factor and thermoelectric performance in hole-doped single-crystal SnSe. *Science* 351, 141–144. doi:10.1126/science.aad3749

Zhao, Y., Yu, P., Zhang, G., Sun, M., Chi, D., Hippalgaonkar, K., et al. (2020). Low-symmetry $PdSe_2$ for high performance thermoelectric applications. *Adv. Funct. Mat.* 30, 2004896. doi:10.1002/adfm.202004896

Zhu, X.-L., Hou, C.-H., Zhang, P., Liu, P.-F., Xie, G., and Wang, B.-T. (2019). High thermoelectric performance of new two-dimensional IV–VI compounds: A first-principles study. *J. Phys. Chem. C* 124, 1812–1819. doi:10.1021/acs.jpcc.9b09787

frontiers | Frontiers in Physics

TYPE Mini Review
PUBLISHED 11 November 2022
DOI 10.3389/fphy.2022.1078202

OPEN ACCESS

EDITED BY
Guangzhao Wang,
Yangtze Normal University, China

REVIEWED BY
Shan Guan,
Institute of semiconductors, China
Dongbao Luo,
University at Buffalo, United States

*CORRESPONDENCE
Xiuyun Zhang,
xyzhang@yzu.edu.cn
Bing Wang,
wb@henu.edu.cn

†These authors have contributed equally to this work

SPECIALTY SECTION
This article was submitted to Physical Chemistry and Chemical Physics, a section of the journal Frontiers in Physics

RECEIVED 24 October 2022
ACCEPTED 27 October 2022
PUBLISHED 11 November 2022

CITATION
Tu Y, Liu Q, Hou L, Shi P, Jia C, Su J, Zhang J, Zhang X and Wang B (2022), Two-dimensional Cr-based ferromagnetic semiconductor: Theoretical simulations and design. *Front. Phys.* 10:1078202. doi: 10.3389/fphy.2022.1078202

Two-dimensional Cr-based ferromagnetic semiconductor: Theoretical simulations and design

Yufei Tu[1,2†], Qingquan Liu[3†], Lipeng Hou[2], Puyuan Shi[2], Chaobin Jia[2], Jingjuan Su[2], Jiawen Zhang[2], Xiuyun Zhang[4*] and Bing Wang[2*]

[1]School of Electronics and Information Engineering, Sias University, Xinzheng, China, [2]Institute for Computational Materials Science, School of Physics and Electronics, Henan University, Kaifeng, China, [3]Patent Examination Cooperation (Henan) Center of the Patent Office, China National Intellectual Property Administration, Zhengzhou, China, [4]College of Physics Science and Technology, Yangzhou University, Yangzhou, China

Two-dimensional (2D) material is the promising for next-generation information technology. The recently discovered intrinsic magnetic crystals have simulated a renaissance in 2D spintronics, which provides an ideal platform for exploring novel physical phenomena. However, current experimental trial-and-error methods in discovering new spintronic material are still very expensive and challenging. In contrast, based on well-developed first-principles calculations, computationally designing the spintronic materials provides a more efficient way for exploring new ferromagnetic (FM) materials and understanding the nature of magnetic properties. Several predictions, such as CrI_3 monolayer, $CrGeTe_3$ bilayer, CrSBr monolayer, $FeCl_2$ monolayer, and Fe_3GeTe_2 monolayer have been confirmed by experiments, showing the great performance of computational approaches. This minireview article attempts to give a brief of discovering intrinsic 2D spintronics from theoretical aspect, and in particular, we emphasize roles played by calculation based on first-principles methods in designing 2D FM materials and devices. The current challenges and proposals on future developments of 2D spintronics are also discussed.

KEYWORDS

two-dimensional, ferromaganetism, semiconductor, first-principal calculations, 2D spintronics

1 Introduction

Due to non-volatility, lower energy consumption, and faster information operation compared to controlling a charge current, spintronic devices that use the spin of an electron for information processing have attracted worldwide interest [1–7]. Just as graphene, TMS_2 (TM = Mo, W), and black P revolutionized condensed matter, the introduction of 2D van der Waals (vdW) magnetic materials promises to open new

horizons in materials science and enable the potential development of spintrons [8–11]. In fact, 2D magnetism has been studied for decades but only recently they have been experimentally verified. The recent exciting 2D ferromagnetic breakthroughs, such as CrI_3 monolayer, Fe_3GeTe_2 monolayer, $CrGeTe_3$ bilayer, and CrSBr monolayer exfoliated from their vdW bulk, have promoted research into new magnetic properties and creative concepts [1,2,11–17].

Traditional trial and error experiments have no clear goals and guidelines, and face the fundamental challenges of long time and high cost. Computational simulations are an important first step in exploring possible applications of new materials. It not only can predict new 2D materials, but also suggest possible routes for their synthesis. Many interesting cases have been confirmed by experiment, such as the growth of borophene, ferroelectricity in SnTe. Compared to other computational methods, the first-principles approach, which is an effective method to study new materials, is the most widely used tool in designing new materials, requiring very few fundamental physical constants and atomic position coordinates. In fact, the rapid development of 2D FM materials benefits from theoretical simulation. From the theoretical point of view, magnetic anisotropy, which can improve the stability of magnetic information, can break the Mermin-Wagner theoryopening the door for 2D long-range FM materials. Firstly, ultra-thin VSe_2 had been predicted to be intrinsic ferromagnetism theoretically in 2012, and has been confirmed by recent experiment [18–21]. The recent star ferromagnetic $CrGeTe_3$ bilayer, CrI_3 monolayer, CrSBr monolayer, $FeCl_2$ monolayer, and Fe_3GeTe_2 monolayer were also first predicted theoretically [22–26], and they have recently been experimentally made [1,2,11,14,15], which show the strong power of first-principles calculations in designing these spintronics materials.

This minireview will summarize recent progress of 2D intrinsic FMSs in theoretical side and show the importance of first-principles calculations in designing new materials. Firstly, we give the reason why ferromagnetic order exists in 2D space theoretically. Then, we summarized the discovery processes and magnetic properties of recent landscape of several 2D ferromagnetic semiconductors, using 2D CrI_3, CrSBr, and $CrGeTe_3$ as the examples, respectively. Finally, we highlight the problems existing in the designed 2D FM materials and suggest possible directions for further development of computational simulations.

2 Results and discussion

2.1 Importance of MAE in low dimensional magnetic materials

Theoretically, spontaneous FM order takes place in three-dimensional (3D) system for isotropic Heisenberg model at finite temperatures, but is completely prohibited by the thermal fluctuations in 2D isotropic Heisenberg model according to the Mermin–Wagner (M-W) theorem. For 2D isotropic Heisenberg ferromagnet, due to the absence of a spin wave excitation gap, the diverging Bose-Einstein statistics at zero energy, and the abrupt onset of magnon density of states (DOS), there will be plenty of excitations of magnons at nonzero temperatures, which would cause the long-range spin ordering to collapse and giant magnon excitations (Figure 1A). However, the presence of uniaxial magnetocrystalline anisotropy (UMA) can open up the magnon excitation gap, which resists the thermal agitations (Figure 1B). This removes the M-W restriction by breaking the continuous rotational symmetry of the Hamiltonian and leads to the finite Curie temperature (T_C) [6]. As the materials evolves from 2D to 3D, the density of states (DOS) spectrum of magnon has changed from a step function to a gradually increasing function with zero DOS at the threshold of excitation (Figures 1C,D). As a result, in 3D system, UMA is not the prerequisite for the existence of long-range FM order at finite temperature. As a result, MA is important in 2D magnets, which not only effects magnetic properties, but also is necessary to stabilize magnetic order in the 2D space limit.

The previous works show that the sizable MAE mainly arises from the strong SOC [27–30]. In addition to the SOC contribution, the shape anisotropy caused by the dipolar interaction also contributes to the MAE [24,31]. It is worth mentioning that the quantitative microscopic origin of MA is still an open question and the 2D magnetic materials usually possess small MAE (below meV), which is difficult to be measured directly. Therefore, it is in longing need of careful examination and more theoretical efforts will be spent to discover effective strategy to enhancing the MAE or searching new 2D FM materials with sizeable MAE.

2.2 Prediction of 2D magnetism

Magnetism usually originates from the spin of unpaired electrons in partially filled *d* or *f* orbitals. According to characteristics of electronic structures, the FM materials can be clearly classified into three types: ferromagnetic semiconductors (FMS), ferromagnetic metals (FMM) (Figure 1G), and ferromagnetic half-metals (FHM) (Figure 1F). Based on the easy magnetization directions, there are three forms of Heisenberg, XY, and Ising ferromagnet, respectively, as shown in Figure 1H. The Heisenberg ferromagnet has no MA; the XY ferromagnet possesses an easy magnetization plane, in which spin can rotate freely in the whole plane; and the Ising ferromagnet exhibits an out-of-plane easy axis.

FMS (Figure 1E), both spin-up and spin-down channels with semiconducting gaps, combines the advantages and properties of both semiconductors and magnets, which can be applied for spin injection, spin manipulation, and spin detection [32]. The history

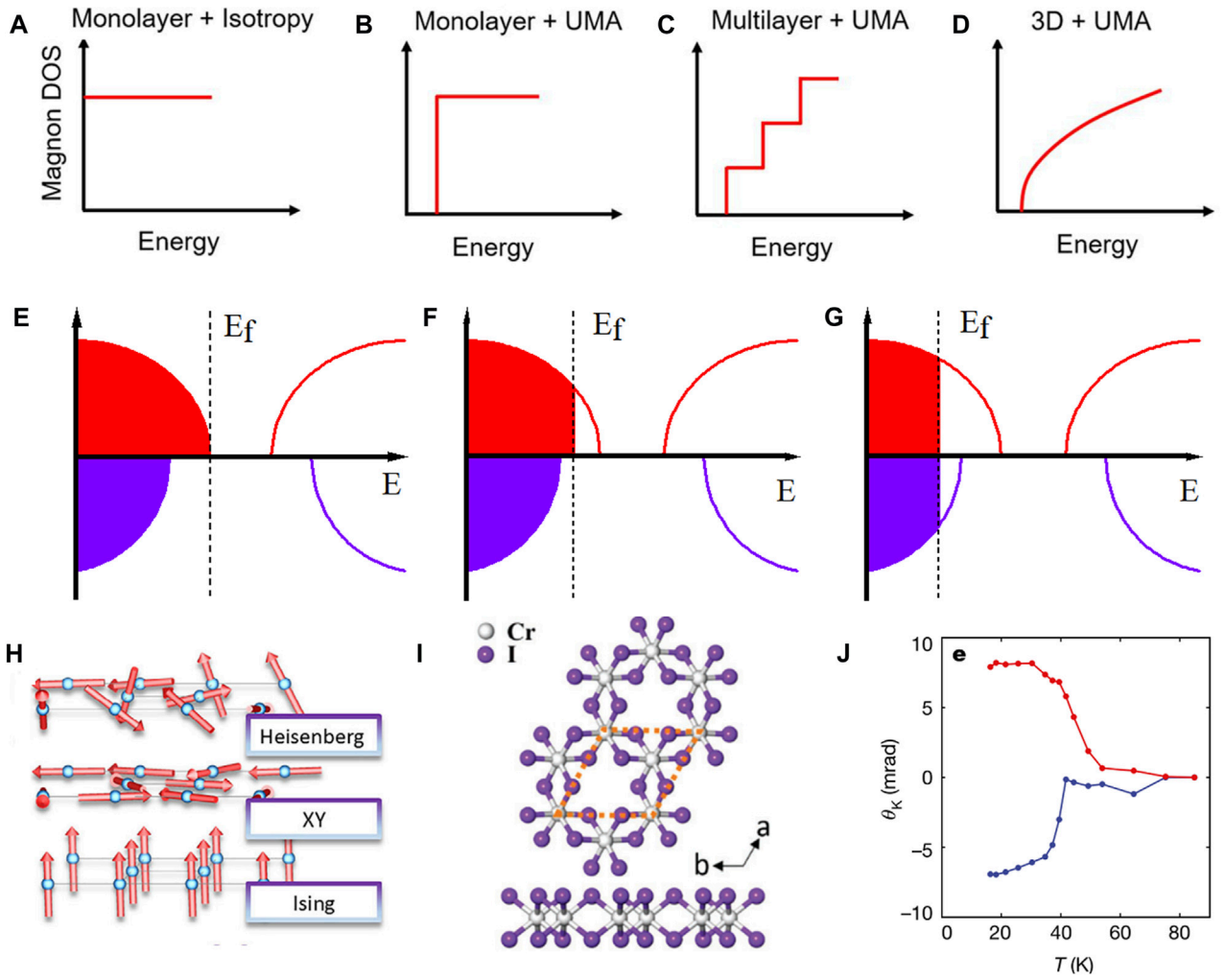

FIGURE 1
(A–D) Spin wave excitations in ferromagnets of different dimensionalities Reproduced with permission [6]. Copyright©2019 American Association for the Advancement of Science (AAAS). **(E–G)** Schematic DOS for three types of ferromagnetic semiconductor, half-metal, and metal materials. **(H)** Spin symmetries of MA for Heisenberg model, XY model, and Ising model, respectively. Reproduced with permission. Copyright©2020 John Wiley and Sons Australia. **(I)** The structure of CrI_3 monolayer. **(J)** Polar MOKE signal for a CrI_3 monolayer. Reproduced with permission [1]. Copyright©2017 Springer Nature.

of the discovery of the typical 2D FMS, CrI_3 monolayer (Figure 1I), illustrates the power of first-principles calculations, and shows the intimate interaction between experiment and theory, which greatly accelerates the discovery of new materials. The layered vdW bulk CrI_3 possesses Ising ferromagnetism below the T_C of 61 K with strong UMA [33]. Its monolayer was first predicted to be intrinsic FMS with T_C of 95 K by using Monte Carlo (MC) simulations and large MAE (685 μeV/Cr), and could be easily exfoliated from the bulk crystals [34]. The other theoretical work showed the its T_C was 107 K and can be further increased to 293 K by hole doping [22]. By lithium atom adsorption, the CrI_3 monolayer can be switched from semiconducting to half-metallicity, which can further enhance the ferromagnetism of CrI_3 sheets [35]. Excitingly, 2 years later, this CrI_3 monolayer was exfoliated from its layered bulk successfully, and its intrinsic long-range ferromagnetic order was also confirmed by scanning magneto-optic Kerr microscopy with the T_C of 45 K (Figure 1J) [1], which provides an ideal platform for the application of 2D spintronics. For CrI_3 bilayer, the first-principles calculations show that it is interlayer antiferromagnetically coupled [36], and further theoretical study shows that the stacking order defines the antiferromagnetic (AFM) coupling, [37]. This result was confirmed by recent experiment [38], and the magnetic order of CrI_3 bilayers can further transfer from AFM to FM order by electric fields [39] and pressure [40]. In

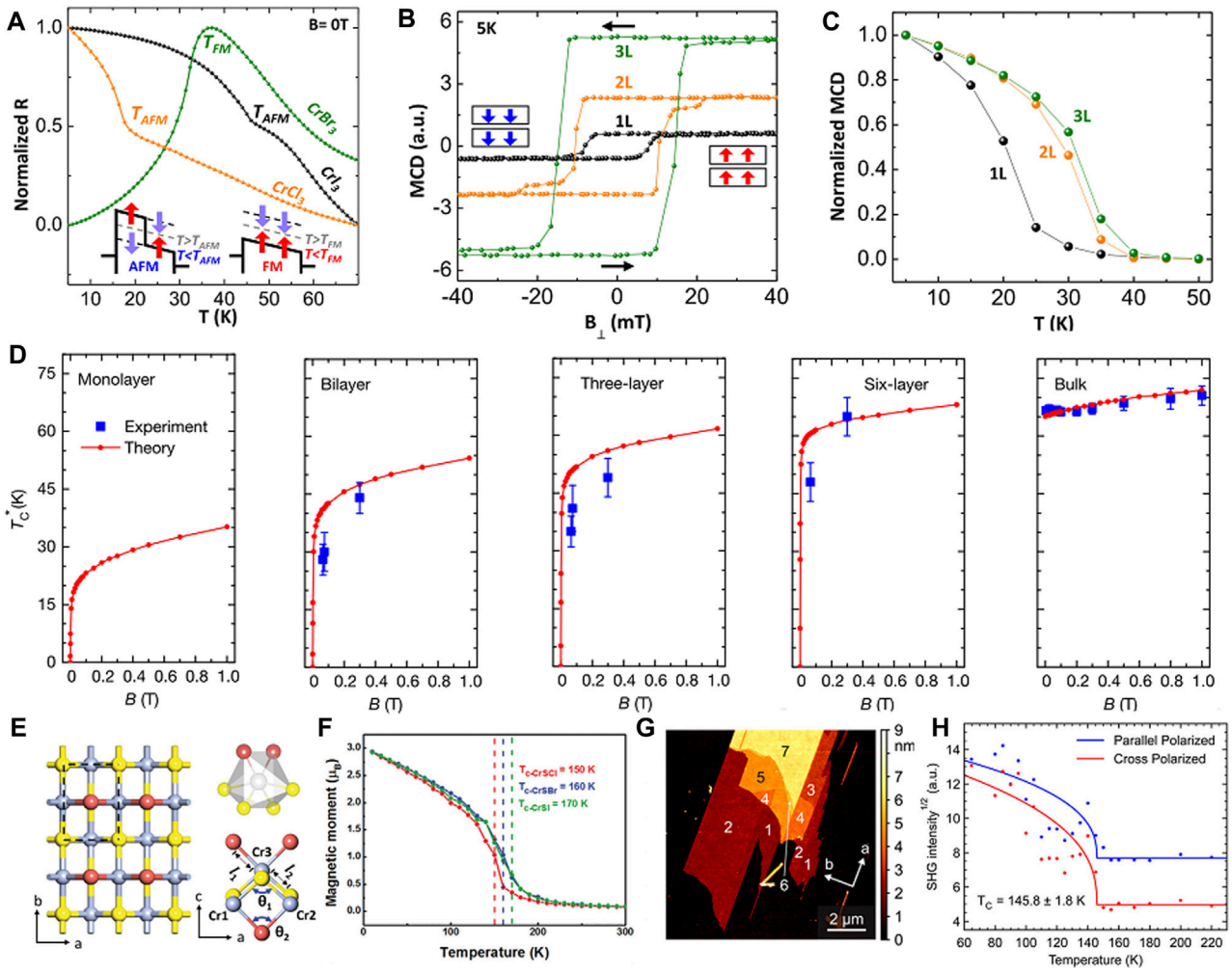

FIGURE 2
(A) Normalized temperature-dependent dc resistance of CrX_3 (X = I, Br, and Cl) at constant current of 0.1 nA. Insets show schematics of the spin-dependent tunnel barrier for AFM and FM interlayer coupling. MCD measurements on $CrBr_3$. **(B)** Low-temperature MCD vs B⊥ and **(C)** temperature-dependent normalized MCD at zero field ($MCD_{\uparrow(\downarrow)}(T) = MCD_{\uparrow(\downarrow),5K}$)for 1L, 2L, and 3L $CrBr_3$. Reproduced with permission [41]. Copyright©2018 National Academy of Sciences. **(D)** Experimental (blue squares) and theoretical (red circles) field dependence of T_C in samples of various thickness. Reproduced with permission [2]. Copyright©2017 Springer Nature. **(E)** The structure of CrSBr monolayer and **(F)** evolution of spin magnetic moment with respect to temperature of CrSX (X = Cr, S, and Br) monolayers. Reproduced with permission [25], Copyright©2018 Royal Society of Chemistry. **(G)** Atomic force microscopy image of an exfoliated flake of varying thicknesses from one to seven layers for CrSBr and **(H)** square roots of the average SHG intensities of monolayer CrSBr as a function of temperature. Reproduced with permission [11]. Copyright©2018 American Chemical Society.

addition, the isostructure vdW layered $CrBr_3$ and $CrCl_3$ also have FM ordering, and the previous predicted $CrBr_3$ monolayer and $CrCl_3$ bilayer has been confirmed by recent experiments (Figures 2A–C) [12,13,41], showing the accuracy and efficiency of computational predictions.

Another typical 2D FMS is $CrXY_3$ (X = Si, Ge, and Sn; Y = S, Se, and Te). In 2014, Yang's group demonstrates the possibility of 2D intrinsic FMSs by exfoliating layered crystals of $CrMTe_3$ (M = Si, Ge) through first-principles calculations, and the 2D FM order can persist up to 35.7 K ($CrSiTe_3$) or 57.2 K ($CrGeTe_3$) based on classical Heisenberg model in MC simulations [23]. Then, Sivadas *et al.* show that $CrSiTe_3$ monolayer is an antiferromagnet (AFM) with a zigzag spin texture contrary to other studies, whereas $CrGeTe_3$ is a FMS with a T_C of 106 K based on Heisenberg model. Zhuang *et al.* have performed accurate hybrid density functional methods to predict that $CrSnTe_3$ monolayer is a FMS and the calculated T_C is about 170 K, which is higher than those of $CrGeTe_3$ (130 K) and $CrSiTe_3$ (90 K) monolayers based on Ising model [42, 43]. After that, Gong *et al.* confirmed the intrinsic long-range FM order in pristine 2D $CrGeTe_3$ bilayer *via* scanning magneto-optic Kerr microscopy and the measured T_C is about 30 K (Figure 2D)

[2]. Although the value of calculated T_C for $CrGeTe_3$ is higher than that of experiment, the first-principles method is still an important tool to fuel the discovery of novel 2D FM materials and guide experimental understanding. Unfortunately, $CrGeTe_3$ monolayer was not still confirmed, and the nature of magnetism in this monolayer needs more effort to be paid.

A class of 2D magnetic materials, CrMN (M = O, S, Se, and Te; N = Cl, Br, and I) will crystakize in the space group *Pmmn*, which has a vdW layered structure in the *z*-axis direction. As early as in 2018, our group shows that the FMS CrSX (X = Cl, Br, and I) monolayers possess high hole mobilities (10^3 $cm^2V^{-1}s^{-1}$) and T_C (150–170 K) (Figures 2E,F), which are competitive candidates for next-generation spintronics and electronics [25]. Then, Wang *et al.* have extensively explored the ferromagnetic properties of CrCX (C = S, Se, and Te; X = Cl, Br, and I) monolayers and found that they show extremely large anisotropy [26]. Recently, Millimeter-size CrSBr single crystals were grown by chemical vapor transport from Cr and S_2Br_2 [11] and was confirmed to be a layered vdW A-type AFM with a bulk Néel temperature (T_N) of 132 K [25,26,44]. Interestingly, CrSBr monolayer was easily exfoliated from its bulk and the experiment value of T_C is about 146 K (Figures 2G,H) [11], which is in good agreement with what we predicted. Besides, several other 2D Cr-based semiconductors such as CrOCl, CrOBr [45], CrOF [46], $Cr_2I_3X_3$ (X = Br, and Cl) [47], Cr_2O_3 [48], were also predicted to possess robust FM order. Although the rapid development of theoretical work has generated a lot of very important results, the presently demonstrated 2D FMSs are still rare and more efforts should be paid to searching or designing interesting materials.

3 Conclusion and outlook

2D FM materials have received widespread attention and form the basis for next-generation nanoscale spintronics. Based on the first-principles simulations, plenty of theoretical efforts have been devoted to designing low-dimensional FM materials, and some of them have been confirmed later by experiment, which has promoted the rapid development of 2D magnetism field. Several interesting cases including 2D ferromagnetic semiconductors have been discussed in this minireview, showing the strong power of first-principles methods. The comparison between simulation and experiment proves the accuracy and efficiency of the calculation and prediction. As an important tool, first-principles calculations will remain a key component of designing materials, providing guidance for the development of spintronics. It should be emphasized that although great recent successes have been made, the study of 2D magnetism is still in its infancy, and searching for high 2D T_C intrinsic ferromagnetism is still a current hotspot. Several key challenges are still needed to be overcome in the future as follow:

(1). Designing new members of 2D FM materials with high T_C, large out-of-plane MAE, and easy experimental accessibility. On one hand, the types of 2D FM materials confirmed experimentally are rather limited, and should be enriched further. On the other hand, the present 2D FM materials suffer the problem of low T_C and small MAE, greatly limit their application scope. One need to investigate the factors that affect Curie temperature (such as the exchange interaction and the magnetic anisotropy), and then find appropriate strategies to increase T_C. Synthesizable 2D FM materials with high temperature T_C and sizable MAE are still highly desirable.

(2). Improving the accuracy of theoretical prediction. Due to limitations of standard DFT theory, close cooperation between theory and experiment is needed to combine the advantages of both to accelerate the discovery and synthesis of 2D FM materials. For example, the predicted T_C with the Ising model and mean field theory are usually overestimated compared with experiment values [49]. MC simulation based on Heisenberg model appears to be more reliable in the accurate prediction of T_C, which is also very important to model new systems for practical applications.

(3). Making full use of rapid development of the 2D database. To take the advantage of the established database, high-throughput method [50–53] and machine learning [54–56] models need to be developed to reduce the number of required objective function evaluations (first-principles calculations) and avoid the amount of computational cost. These methods offer new tools for designing new 2D FM materials to overcome the challenges in the practical application of information technologies.

Author contributions

YT: Data curation, Investigation, Validation, Writing original draft; QL: Data curation, Investigation, Validation, Writing original draft; LH: Data curation, Investigation; PS: Conceptualization, Methodology; CJ: Methodology; JS: Data Curation; JZ: Formal analysis; XZ: Validation, Writing—Review and Editing, Supervision; Bing Wang: Writing—Review and Editing, Supervision, Funding acquisition.

Funding

This work was financially supported by the National Natural Science Foundation of China (Nos 12047517 and 12104130), and the China Postdoctoral Science Foundation (Nos 2020M682274 and 2020TQ0089). Innovative experimental training program for college students of Henan University (No. 20221011005), Open-ended research projects for

undergraduates in the Scientific Research Laboratory (Platform) of Henan University.

Conflict of interest

The authors declare that the research was conducted in the absence of any commercial or financial relationships that could be construed as a potential conflict of interest.

Publisher's note

References

1. Huang B, Clark G, Navarro-Moratalla E, Klein DR, Cheng R, Seyler KL, et al. Layer-dependent ferromagnetism in a van der Waals crystal down to the monolayer limit. *Nature* (2017) 546:270–3. doi:10.1038/nature22391

2. Gong C, Li L, Li Z, Ji H, Stern A, Xia Y, et al. Discovery of intrinsic ferromagnetism in two-dimensional van der Waals crystals. *Nature* (2017) 546: 265–9. doi:10.1038/nature22060

3. Huang C, Feng J, Wu F, Ahmed D, Huang B, Xiang H, et al. Toward intrinsic room-temperature ferromagnetism in two-dimensional semiconductors. *J Am Chem Soc* (2018) 140:11519–25. doi:10.1021/jacs.8b07879

4. Burch KS. Electric switching of magnetism in 2D. *Nat Nanotechnol* (2018) 13: 532. doi:10.1038/s41565-018-0165-4

5. Zhang Y, Chu J, Yin L, Shifa TA, Cheng Z, Cheng R, et al. Ultrathin magnetic 2D single-crystal CrSe. *Adv Mater* (2019) 31:e1900056. doi:10.1002/adma.201900056

6. Gong C, Zhang X. Two-dimensional magnetic crystals and emergent heterostructure devices. *Science* (2019) 363:eaav4450. doi:10.1126/science.aav4450

7. Wu Y, Sun W, Liu S, Wang B, Liu C, Yin H, et al. Ni(NCS)2 monolayer: A robust bipolar magnetic semiconductor. *Nanoscale* (2021) 13:16564–70. doi:10.1039/d1nr04816c

8. Mak KF, Lee C, Hone J, Shan J, Heinz TF. Atomically ThinMoS2: A new direct-gap semiconductor. *Phys Rev Lett* (2010) 105:136805. doi:10.1103/physrevlett.105.136805

9. Novoselov KS, Jiang D, Schedin F, Booth TJ, Khotkevich VV, Morozov SV, et al. Two-dimensional atomic crystals. *Proc Natl Acad Sci U S A* (2005) 102: 10451–3. doi:10.1073/pnas.0502848102

10. Li L, Yu Y, Ye GJ, Ge Q, Ou X, Wu H, et al. Black phosphorus field-effect transistors. *Nat Nanotechnol* (2014) 9:372–7. doi:10.1038/nnano.2014.35

11. Lee K, Dismukes AH, Telford EJ, Wiscons RA, Wang J, Xu X, et al. Magnetic order and symmetry in the 2D semiconductor CrSBr. *Nano Lett* (2021) 21:3511–7. doi:10.1021/acs.nanolett.1c00219

12. Cai X, Song T, Wilson NP, Clark G, He M, Zhang X, et al. Atomically thin CrCl3: An in-plane layered antiferromagnetic insulator. *Nano Lett* (2019) 19: 3993–8. doi:10.1021/acs.nanolett.9b01317

13. Zhang ZS, Jiang J, Rasmita C, Gao A, Yu WT. Direct photoluminescence probing of ferromagnetism in monolayer two-dimensional CrBr3. *Nano Lett* (2019) 19:3138–42. doi:10.1021/acs.nanolett.9b00553

14. Fei Z, Huang B, Malinowski P, Wang W, Song T, Sanchez J, et al. Two-dimensional itinerant ferromagnetism in atomically thin Fe3GeTe2. *Nat Mater* (2018) 17:778–82. doi:10.1038/s41563-018-0149-7

15. Deng Y, Yu Y, Song Y, Zhang J, Wang NZ, Sun Z, et al. Gate-tunable room-temperature ferromagnetism in two-dimensional Fe3GeTe2. *Nature* (2018) 563: 94–9. doi:10.1038/s41586-018-0626-9

16. Guo S-D, Guo X-S, Zhu Y-T, Ang Y-SJAPL. Predicted ferromagnetic monolayer CrSCl with large vertical piezoelectric response: A first-principles study. *Appl Phys Lett* (2022) 121:062403. doi:10.1063/5.0109033

17. Hu J, Wang P, Zhao J, Wu R. Engineering magnetic anisotropy in two-dimensional magnetic materials. *Adv Phys X* (2018) 3:1432415. doi:10.1080/23746149.2018.1432415

18. Ma Y, Dai Y, Guo M, Niu C, Zhu Y, Huang B. Evidence of the existence of magnetism in pristine VX(2) monolayers (X = S, Se) and their strain-induced tunable magnetic properties. *ACS Nano* (2012) 6:1695–701. doi:10.1021/nn204667z

19. Zhuang HL, Hennig RG. Stability and magnetism of strongly correlated single-layerVS2. *Phys Rev B* (2016) 93:054429. doi:10.1103/physrevb.93.054429

20. Guo Y, Deng H, Sun X, Li X, Zhao J, Wu J, et al. Modulation of metal and insulator states in 2D ferromagnetic VS2 by van der Waals interaction engineering. *Adv Mater* (2017) 29:1700715. doi:10.1002/adma.201700715

21. Bonilla M, Kolekar S, Ma Y, Diaz HC, Kalappattil V, Das R, et al. Strong room-temperature ferromagnetism in VSe2 monolayers on van der Waals substrates. *Nat Nanotechnol* (2018) 13:289–93. doi:10.1038/s41565-018-0063-9

22. Liu J, Sun Q, Kawazoe Y, Jena P. Exfoliating biocompatible ferromagnetic Cr-trihalide monolayers. *Phys Chem Chem Phys* (2016) 18:8777–84. doi:10.1039/c5cp04835d

23. Li X, Yang J. CrXTe3 (X=Si, Ge) nanosheets: Two dimensional intrinsic ferromagnetic semiconductors. *J Mater Chem C Mater* (2014) 2:7071. doi:10.1039/c4tc01193g

24. Zhuang HL, Kent PRC, Hennig RG. Strong anisotropy and magnetostriction in the two-dimensional Stoner ferromagnetFe3GeTe2. *Phys Rev B* (2016) 93: 134407. doi:10.1103/physrevb.93.134407

25. Guo Y, Zhang Y, Yuan S, Wang B, Wang J. Chromium sulfide halide monolayers: Intrinsic ferromagnetic semiconductors with large spin polarization and high carrier mobility. *Nanoscale* (2018) 10:18036–42. doi:10.1039/c8nr06368k

26. Wang C, Zhou X, Zhou L, Tong N-H, Lu Z-Y, Ji W. A family of high-temperature ferromagnetic monolayers with locked spin-dichroism-mobility anisotropy: MnNX and CrCX (X = Cl, Br, I; C = S, Se, Te). *Sci Bull (Beijing)* (2019) 64:293–300. doi:10.1016/j.scib.2019.02.011

27. Guo Y, Wang B, Zhang X, Yuan S, Ma L, Wang J. Magnetic two-dimensional layered crystals meet with ferromagnetic semiconductors. *InfoMat* (2020) 2:639–55. doi:10.1002/inf2.12096

28. Mermin ND, Wagner H. Absence of ferromagnetism or antiferromagnetism in one- or two-dimensional isotropic Heisenberg models. *Phys Rev Lett* (1966) 17: 1307–136. doi:10.1103/physrevlett.17.1307

29. Wang B, Zhang Y, Ma L, Wu Q, Guo Y, Zhang X, et al. MnX (X = P, as) monolayers: A new type of two-dimensional intrinsic room temperature ferromagnetic half-metallic material with large magnetic anisotropy. *Nanoscale* (2019) 11:4204–9. doi:10.1039/c8nr09734h

30. Wang X, Wu R, Wang D-S, Freeman AJ. Torque method for the theoretical determination of magnetocrystalline anisotropy. *Phys Rev B* (1966) 54:61–4. doi:10.1103/physrevb.54.61

31. Fang Y, Wu S, Zhu Z-Z, Guo G-Y. Large magneto-optical effects and magnetic anisotropy energy in two-dimensional Cr2Ge2Te6. *Phys Rev B* (2018) 98:125416. doi:10.1103/physrevb.98.125416

32. Li X, Yang J. First-principles design of spintronics materials. *Natl Sci Rev* (2016) 3:365–81. doi:10.1093/nsr/nww026

33. Mcguire MA, Dixit H, Cooper VR, Sales BC. Coupling of crystal structure and magnetism in the layered, ferromagnetic insulator CrI3. *Chem Mater* (2015) 27: 612–20. doi:10.1021/cm504242t

34. Zhang W-B, Qu Q, Zhu P, Lam C-H. Robust intrinsic ferromagnetism and half semiconductivity in stable two-dimensional single-layer chromium trihalides. *J Mater Chem C Mater* (2015) 3:12457–68. doi:10.1039/c5tc02840j

35. Guo Y, Yuan S, Wang B, Shi L, Wang J. Half-metallicity and enhanced ferromagnetism in Li-adsorbed ultrathin chromium triiodide. *J Mater Chem C Mater* (2018) 6:5716–20. doi:10.1039/c8tc01302k

36. Sivadas N, Okamoto S, Xu X, Fennie CJ, Xiao D. Stacking-dependent magnetism in bilayer CrI3. *Nano Lett* (2018) 18:7658–64. doi:10.1021/acs.nanolett.8b03321

37. Jiang P, Wang C, Chen D, Zhong Z, Yuan Z, Lu Z-Y, et al. Stacking tunable interlayer magnetism in bilayer CrI3. *Phys Rev B* (2019) 99:144401. doi:10.1103/physrevb.99.144401

38. Huang B, Clark G, Klein DR, Macneill D, Navarro-Moratalla E, Seyler KL, et al. Electrical control of 2D magnetism in bilayer CrI 3. *Nat Nanotechnol* (2018) 13:544–8. doi:10.1038/s41565-018-0121-3

39. Jiang S, Shan J, Mak KF. Electric-field switching of two-dimensional van der Waals magnets. *Nat Mater* (2018) 17:406–10. doi:10.1038/s41563-018-0040-6

40. Song T, Fei Z, Yankowitz M, Lin Z, Jiang Q, Hwangbo K, et al. Switching 2D magnetic states via pressure tuning of layer stacking. *Nat Mater* (2019) 18:1298–302. doi:10.1038/s41563-019-0505-2

41. Kim HH, Yang B, Li S, Jiang S, Jin C, Tao Z, et al. Evolution of interlayer and intralayer magnetism in three atomically thin chromium trihalides. *Proc Natl Acad Sci U S A* (2019) 116:11131–6. doi:10.1073/pnas.1902100116

42. Sivadas N, Daniels MW, Swendsen RH, Okamoto S, Xiao D. Magnetic ground state of semiconducting transition-metal trichalcogenide monolayers. *Phys Rev B* (2015) 91:235425. doi:10.1103/physrevb.91.235425

43. Zhuang HL, Xie Y, Kent PRC, Ganesh P. Computational discovery of ferromagnetic semiconducting single-layerCrSnTe3. *Phys Rev B* (2015) 92:035407. doi:10.1103/physrevb.92.035407

44. Xu B, Li S, Jiang K, Yin J, Liu Z, Cheng Y, et al. Switching of the magnetic anisotropy via strain in two dimensional multiferroic materials: CrSX (X = Cl, Br, I). *Appl Phys Lett* (2020) 116:052403. doi:10.1063/1.5140644

45. Miao N, Xu B, Zhu L, Zhou J, Sun Z. 2D intrinsic ferromagnets from van der Waals antiferromagnets. *J Am Chem Soc* (2018) 140:2417–20. doi:10.1021/jacs.7b12976

46. Xiao T, Wang G, Liao Y. Theoretical prediction of two-dimensional CrOF sheet as a ferromagnetic semiconductor or a half-metal. *Chem Phys* (2018) 513:182–7. doi:10.1016/j.chemphys.2018.08.007

47. Zhang F, Mi W, Wang X. Spin-dependent electronic structure and magnetic anisotropy of 2D ferromagnetic janus Cr2I3X3 (X = Br, Cl) monolayers. *Adv Electron Mater* (2019a1900778) 6:1900778. doi:10.1002/aelm.201900778

48. Chen JY, Li XX, Zhou WZ, Yang JL, Ouyang FP, Xiong X. Large-spin-gap nodal-line half-metal and high-temperature ferromagnetic semiconductor in Cr2X3 (X=O, S, Se) monolayers. *Adv Electron Mater* (2020) 6:1900490. doi:10.1002/aelm.201900490

49. Sun Y, Zhuo Z, Wu X, Yang J. Room-temperature ferromagnetism in two-dimensional Fe2Si nanosheet with enhanced spin-polarization ratio. *Nano Lett* (2017) 17:2771–7. doi:10.1021/acs.nanolett.6b04884

50. Zhang X, Chen A, Zhou Z. *High-throughput computational screening of layered and two-dimensional materials*. WIREs Comput Mol Sci. (2018). p. e1385. doi:10.1002/wcms.1385

51. Mounet N, Gibertini M, Schwaller P, Campi D, Merkys A, Marrazzo A, et al. Two-dimensional materials from high-throughput computational exfoliation of experimentally known compounds. *Nat Nanotechnol* (2018) 13:246–52. doi:10.1038/s41565-017-0035-5

52. Ashton M, Paul J, Sinnott SB, Hennig RG. Topology-scaling identification of layered solids and stable exfoliated 2D materials. *Phys Rev Lett* (2017) 118:106101. doi:10.1103/physrevlett.118.106101

53. Paul JT, Singh AK, Dong Z, Zhuang H, Revard BC, Rijal B, et al. Computational methods for 2D materials: Discovery, property characterization, and application design. *J Phys : Condens Matter* (2017) 29:473001. doi:10.1088/1361-648x/aa9305

54. Correa-Baena J-P, Hippalgaonkar K, van Duren J, Jaffer S, Chandrasekhar VR, Stevanovic V, et al. Accelerating materials development via automation, machine learning, and high-performance computing. *Joule* (2018) 2:1410–20. doi:10.1016/j.joule.2018.05.009

55. Lu S, Zhou Q, Guo Y, Zhang Y, Wu Y, Wang J. Coupling a crystal graph multilayer descriptor to active learning for rapid discovery of 2D ferromagnetic semiconductors/half-metals/metals. *Adv Mater* (2020) 32:2002658. doi:10.1002/adma.202002658

56. Court CJ, Cole JM. Magnetic and superconducting phase diagrams and transition temperatures predicted using text mining and machine learning. *Npj Comput Mater* (2020) 6:18–9. doi:10.1038/s41524-020-0287-8

frontiers | Frontiers in Physics

TYPE Original Research
PUBLISHED 25 November 2022
DOI 10.3389/fphy.2022.1085367

OPEN ACCESS

EDITED BY
Guangzhao Wang,
Yangtze Normal University, China

REVIEWED BY
Chengyong Zhong,
Chongqing Normal University, China
Tang Yong,
Huanghuai University, China

*CORRESPONDENCE
Jianping Li,
szyljp0170@szpt.edu.cn

SPECIALTY SECTION
This article was submitted to Physical Chemistry and Chemical Physics, a section of the journal Frontiers in Physics

RECEIVED 31 October 2022
ACCEPTED 14 November 2022
PUBLISHED 25 November 2022

CITATION
Cui Q, Ren K, Zheng R, Zhang Q, Yu L and Li J (2022), Tunable thermal properties of the biphenylene and the lateral heterostructure formed with graphene: A molecular dynamics investigation. *Front. Phys.* 10:1085367. doi: 10.3389/fphy.2022.1085367

Tunable thermal properties of the biphenylene and the lateral heterostructure formed with graphene: A molecular dynamics investigation

Qiang Cui[1], Kai Ren[2], Ruxing Zheng[3], Qiuhua Zhang[4], Luxin Yu[5] and Jianping Li[6]*

[1]School of Mechanical Engineering, Anhui Technical College of Mechanical and Electrical Engineering, Wuhu, China, [2]School of Mechanical and Electronic Engineering, Nanjing Forestry University, Nanjing, Jiangsu, China, [3]School of Mechanical Engineering, Southeast University, Nanjing, Jiangsu, China, [4]School of Automobile and Aviation, Wuhu Institute of Technology, Wuhu, China, [5]School of Automotive and Traffic Engineering, Hefei University of Technology, Hefei, China, [6]School of Automotive and Transportation Engineering, Shenzhen Polytechnic, Shenzhen, Guangdong, China

Recently, biphenylene was successfully synthesized as a novel allotrope of carbon. In this investigation, non-equilibrium molecular dynamics calculations are conducted to explore the intrinsic thermal properties of biphenylene. The isotropic thermal conductivity of biphenylene is obtained, which is also sensitive to size and temperature. Furthermore, the graphene/biphenylene lateral heterostructure is constructed to possess an interfacial thermal conductance of about 2.84×10^9 W K^{-1} m^{-2}. The external tensile strain can induce a redshift of the vibrational density of states of pristine graphene and biphenylene, and the improved overlap also results in an enhanced heat flux in the biphenylene/graphene heterostructure. Our approach can provide theoretical guidance to design a thermal management device based on graphene and biphenylene.

KEYWORDS

biphenylene, thermal conductivity, biphenylene/graphene heterostructure, interfacial thermal conductance, strain effect

Introduction

After the graphene was prepared by the Geim using a mechanical stripping method [1]; two-dimensional (2D) materials attract extensive attention because of their novel performance and promising applications [2–8]. Specifically, transition metal dichalcogenides (TMDs) and transition metal carbides or carbonitrides (MXene) have also been proposed to rise rapidly [9–12]. Their unique layered structure endows unusual physical and chemical properties, such as high mechanical strength [13] and excellent thermal [14], magnetic [4], and optical performance [15]. For example, when GeC changes from an indirect band gap to a direct band gap, it can maintain structural stability under high pressure [16]. Interestingly, the band gap of arsenene can be changed under

the effect of stress. Research studies found a novel phenomenon, especially for folded arsenene: when 6% stress is applied, the gap of arsenene will be closed [17].

Thermal behaviors of 2D materials act as critical factors in heat dissipation when used as nano-devices, and the heat transport will directly determine the efficiency [18, 19]. Thus, research on the thermal properties of 2D materials has become a hotspot. For example, Balandin et al. measured the thermal conductivity of a suspended graphene monolayer in a room-temperature environment for the first time using the Raman method [20]. The measurement results show that its thermal conductivity is much higher than that of diamond and graphite block, reaching about 4,840–5,300 W m^{-1} K^{-1}. Cai et al. obtained the thermal conductivity of the suspended graphene monolayer using the same method and simultaneously measured the Raman laser absorption of graphene using a laser power meter [21]. The results demonstrate that the thermal conductivity of the graphene monolayer grown by chemical vapor deposition (CVD) was about 2,500–3,100 W m^{-1} K^{-1} and 1,200–1,400 W m^{-1} K^{-1}, at the temperatures 350 K and 500 K, respectively. Interestingly, when two different layered materials form a lateral heterostructure, the phonons can scatter when passing through the interface, resulting in interfacial thermal conductance [22]. For example, topological defects can improve the interfacial thermal conductance of graphene/h-BN from 6.42×10^9 W K^{-1} m^{-2} to 7.09×10^9 W K^{-1} m^{-2} [23]. The interfacial thermal conductance of the black phosphorene heterostructure can be reduced using a nanophononic structure [24]. In addition, the covalent interface of the lateral heterostructure can evidently induce a temperature drop, which is a critical factor for interfacial thermal conductance [25]. Recently, a novel non-benzenoid carbon allotrope was prepared [26], named biphenylene, which shows metallic characteristics [26]. It is an anti-aromatic compound and possesses tunable magnetic properties [27]. In addition, the maximum Young's modulus of biphenylene is obtained as 259.7 N/m, and its ultra-high melting point is up to 4,500 K, showing strong mechanical and high stability performance [28]. In addition, biphenylene has been reported to be a candidate material for fuel cells [29].

In this work, the thermal conductivity of biphenylene is addressed using molecular dynamics calculations. Then, the size and temperature dependence of the thermal conductivity of biphenylene are addressed. Importantly, the biphenylene/graphene heterostructure is constructed, and interfacial thermal conductance is investigated. In addition, the stain-tunable interfacial thermal conductance of the biphenylene/graphene heterostructure is studied, and the vibrational density of states is further explored.

Computational methods

In our simulations, the LAMMPS package was used for all the molecular dynamics (MD) calculations [30]. The interaction between the C atoms was described by the Tersoff potential [3]. The time step was set as 0.5 fs and NPT (isothermal and isobaric), NVT, and NVE (isovolumetric and isoenergetic) ensembles were conducted for 500 ps in the MD simulations to obtain an equilibrium state for the system. Moreover, Newton's equations were reflected in the integrated velocity. The Verlet algorithm was used to show the atomic motion. The temperature and energy of the studied system were monitored, and they also present a convergence, further showing a steady state. In the calculations for the phonon spectra of the system, the density functional perturbation theory (DFPT) within the PHONOPY code was used [31, 32].

Results and discussion

In order to investigate the heat transfer characteristics along the x direction, the nanoribbon of the biphenylene monolayer is constructed along x, as shown in Figure 1. Two ends of biphenylene are fixed and hot and cold baths are used by Nosé–Hoover reservoirs next to the two ends. Thus, the heat current induced by such a temperature gradient is obtained along the x direction. The size dependence of thermal conductivity was considered by setting the width (in the y direction) of the biphenylene nanoribbon to about 50 Å, while the length (L, in the x direction) is variable by 411.1, 616.5, 822.8, 1,027.8, and 1,233.4 Å. Similarly, the thermal conductivity of the biphenylene monolayer along the y direction is also calculated using the nanoribbon with the width (in the x direction) of the biphenylene nanoribbon about 50 Å, while the length (in the y direction) is variable by 409.1, 614.0, 818.3, 1,022.8, and 1,227.0 Å.

The thermal conductivity κ of pure biphenylene is obtained by Fourier's calculation of

$$\kappa = \frac{J}{S \cdot dT/dL}, \tag{1}$$

where J is the heat flux and T and S are the temperature and the cross-sectional area of the heat flux, respectively [33]. Importantly, dT/dL is obtained by the fitting of the linear region. In addition, we calculate the heat flux (J) using the non-equilibrium molecular dynamics (NEMD) method [30]:

$$J = \frac{1}{V}\left[\sum_i^N \varepsilon_i v_i + \frac{1}{2}\sum_{ij,i\neq j}^N \left(F_{ij}\cdot v_i\right)\mathrm{r}_{ij} + \frac{1}{6}\sum_{ijk,i\neq j\neq k}^N \left(F_{ijk}\cdot v_i\right)\left(\mathrm{r}_{ij}+\mathrm{r}_{jk}\right)\right], \tag{2}$$

where ε_i is the energy of the atoms I, while v_i represents the velocity of the atom. r_{ij} is used to decide the distance between i and j. F_{ij} and F_{ijk} are the two-body and three-body forces, respectively. V is the volume of the studied system. The thermal conductivity of the biphenylene monolayer is shown

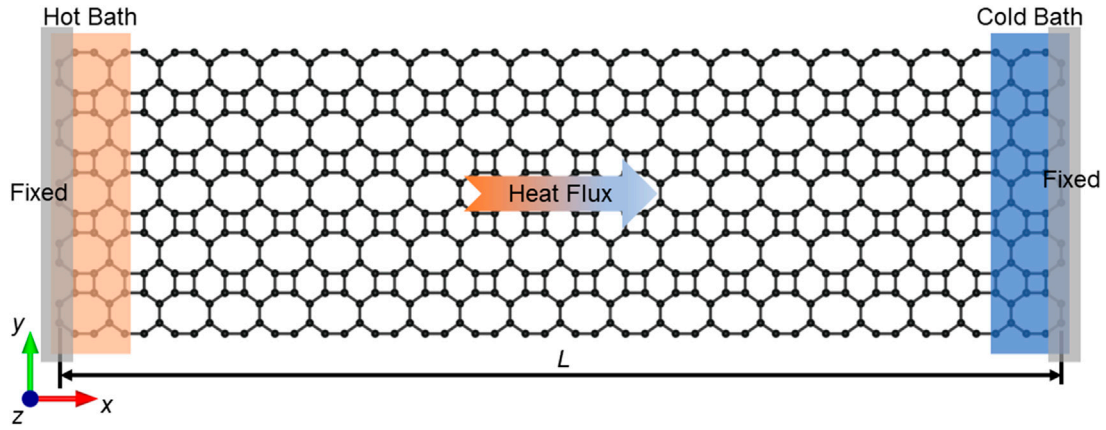

FIGURE 1
Schematic diagram of heat transfer in the biphenylene monolayer.

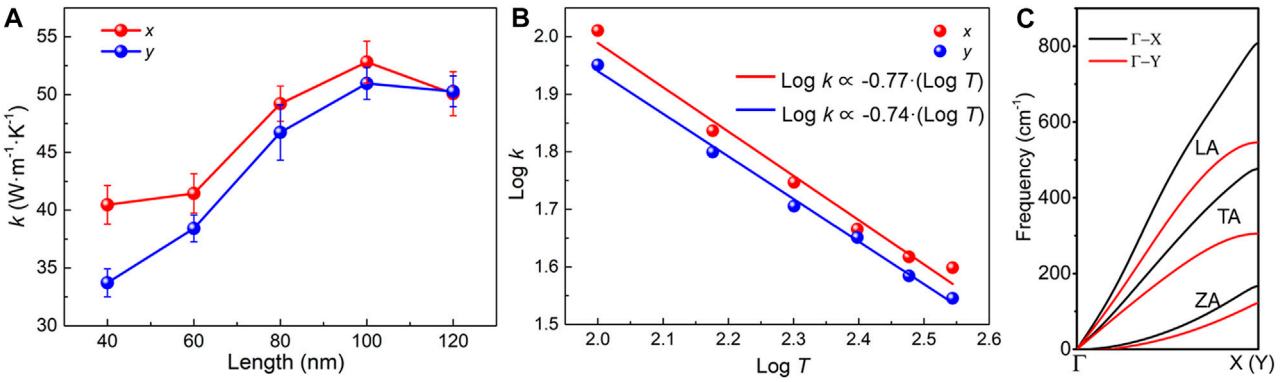

FIGURE 2
Thermal conductivity of the biphenylene monolayer by different **(A)** lengths and **(B)** temperatures; **(C)** phonon scattering spectrum of the biphenylene monolayer along the *x* and *y* directions.

in Figure 2A with the length ranging from 40 nm to 120 nm at 300 K in the *x* and *y* directions. One can see that the biphenylene monolayer reveals isotropic thermal conductivity, which is enhanced as the length increases, but it will not increase at a certain length of about 100 nm. In addition, we obtain the maximum thermal conductivity of about 52.82 W m^{-1} K^{-1} and 50.97 W m^{-1} K^{-1} in the *x* and *y* directions, respectively. In contrast, the thermal conductivity of the biphenylene monolayer can be decreased by increasing the temperature, as shown in Figure 2B, in both *x* and *y* directions. In addition, there is a decent linear relationship between temperature and thermal conductivity. It is worth noting that the thermal conductivity of biphenylene in the *x* direction is higher than that in the *y* direction, which is contributed by the higher group velocity in the *x* direction because the acoustic branches in the *x* direction are steeper than those in the *y* direction, as shown in Figure 2C.

Then, we construct the lateral heterostructure by biphenylene and graphene with the length and width as 613.7 and 47.5 Å, respectively, as shown in Figure 3A, where the interface is denoted by the blue dashed line. To investigate the interface properties of biphenylene and graphene, the potential drop (ΔV) is calculated as shown in Figure 3B. The obtained potential drop of the biphenylene/graphene interface is 0.326 eV, which is important to induce a built-in electric field enhancing the migration of the charges [10]. Then, the stability of the biphenylene/graphene lateral heterostructure is calculated by the phonon spectrum, as shown in Figure 3C. One can see that an imaginary frequency exists in the phonon spectrum of the biphenylene/graphene lateral heterostructure, suggesting the stability of the structure. To explore the thermal performance of the biphenylene/graphene lateral heterostructure, the NEMD method is also used to obtain the heat flux of the calculated

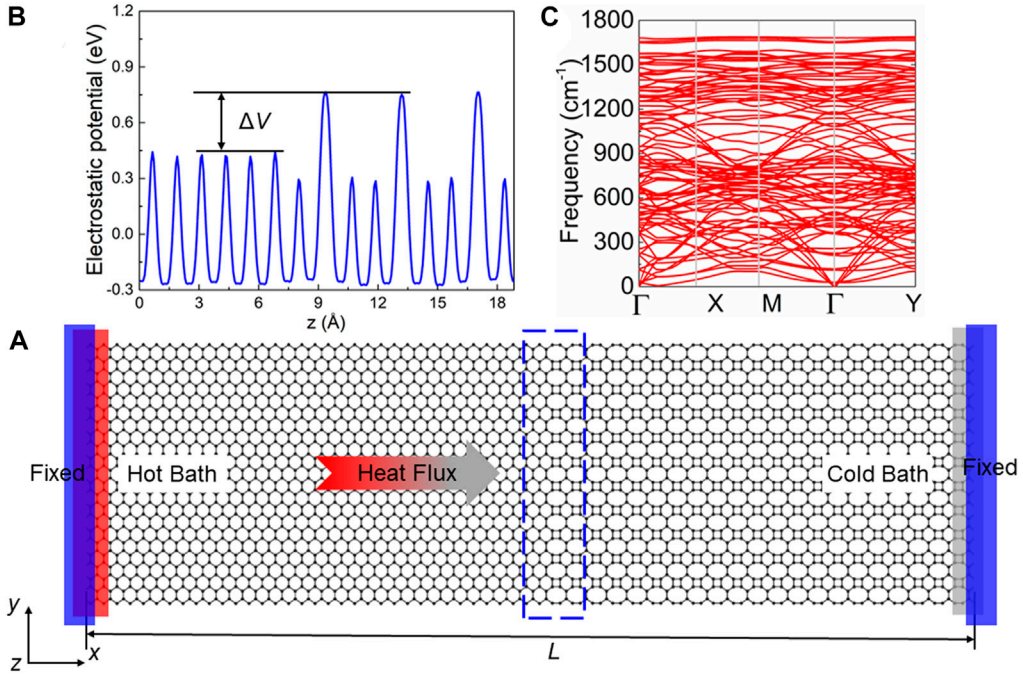

FIGURE 3
(A) Schematic of heat transfer in the biphenylene/graphene lateral heterostructure; **(B)** potential drop and **(C)** phonon scattering spectrum of the interface.

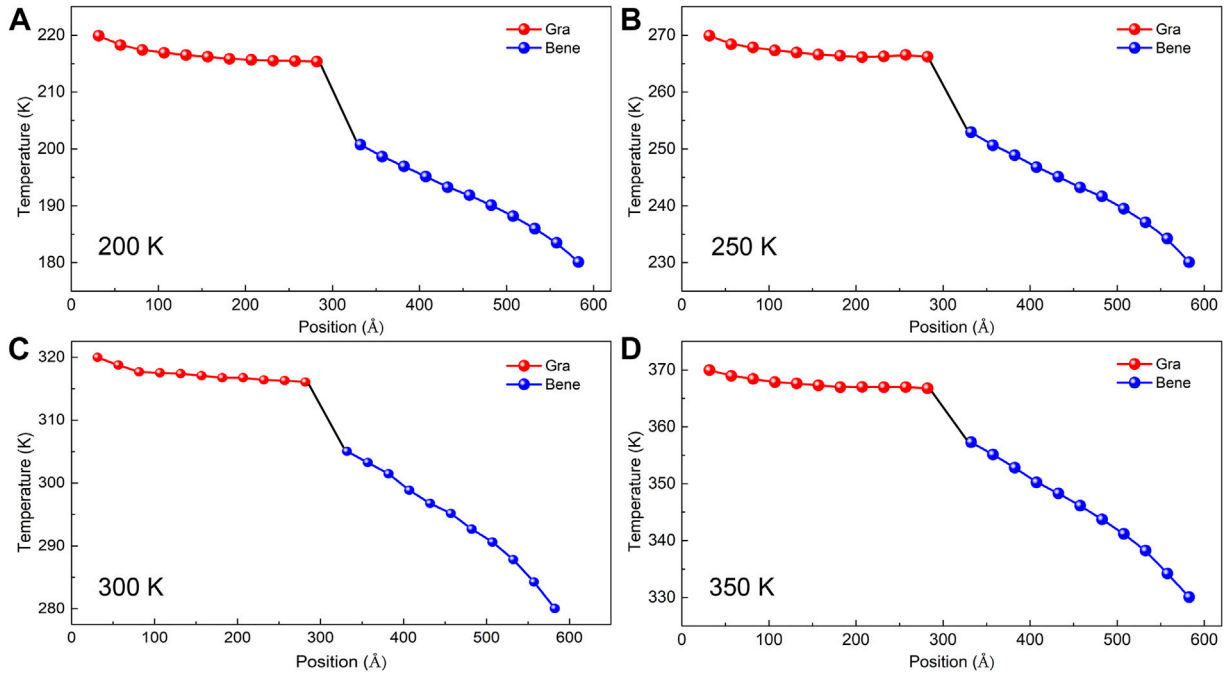

FIGURE 4
Temperature distribution of the biphenylene/graphene lateral heterostructure at **(A)** 200 K, **(B)** 250 K, **(C)** 300 K, and **(D)** 350 K.

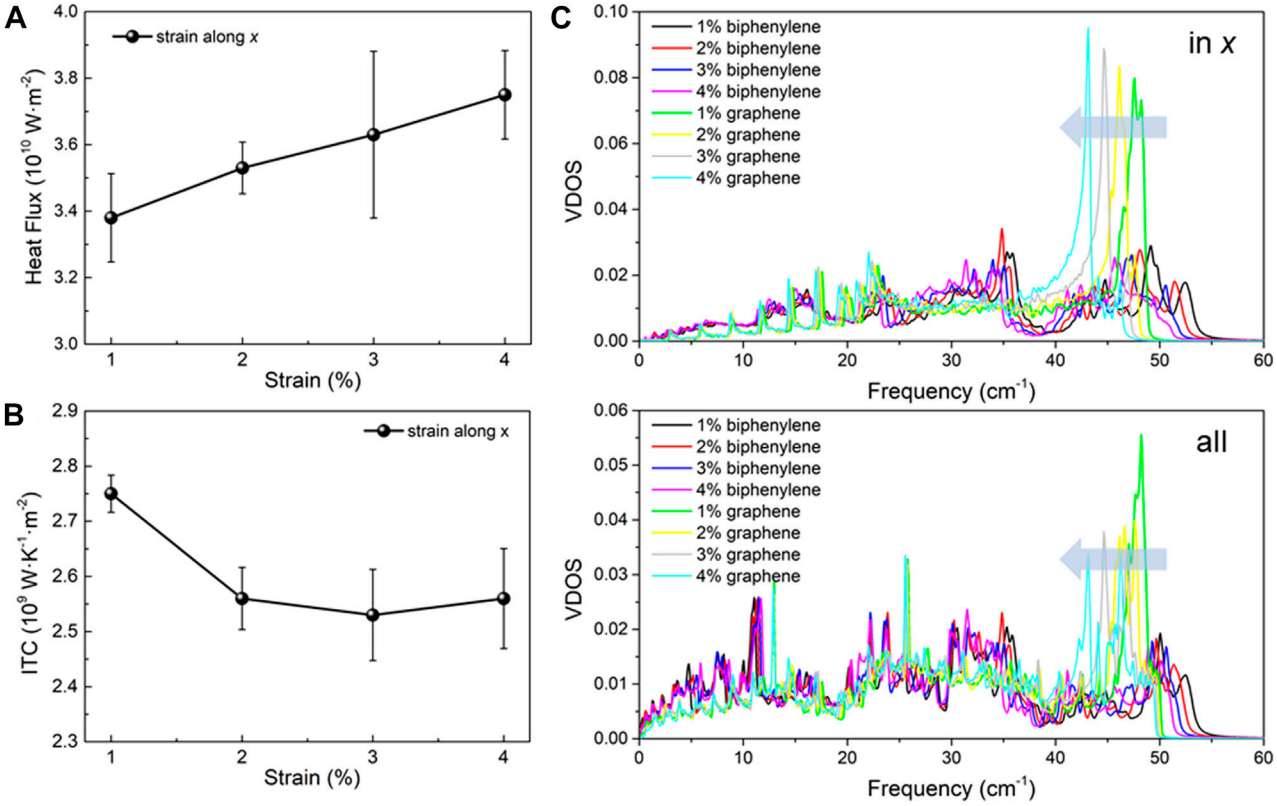

FIGURE 5
(A) Heat flux, **(B)** interfacial thermal conductance, and **(C)** VDOS of the biphenylene/graphene lateral heterostructure under external strain along the *x* direction.

system. Similarly, hot and cold baths are fixed on biphenylene and graphene, respectively, by Nosé–Hoover reservoirs as shown in Figure 3A. Thus, the heat flux is transferred from graphene to biphenylene. After crossing the interface, the interfacial thermal conductance of the biphenylene/graphene lateral heterostructure is further explored by

$$\lambda = \frac{J}{\Delta T}, \tag{3}$$

where ΔT is the temperature difference across the biphenylene/graphene interface. In addition, a free boundary condition was set in the *y*-direction and *z*-direction to build such a nanoribbon structure for the biphenylene/graphene lateral heterostructure. The system temperature is decided by the average temperature of the hot and cold baths.

The temperature difference of the biphenylene/graphene lateral heterostructure under different temperatures is shown in Figure 4. Evidently, a large temperature difference is induced across the interface. The obtained temperature difference of the biphenylene/graphene lateral heterostructure at 300 K is about 11.02 K. In addition, the heat flux is calculated as 3.13×10^{10} W m^{-2}; thus, the interfacial thermal conductance of the biphenylene/graphene lateral heterostructure is about 2.84×10^{9} W K^{-1} m^{-2}. Such a pronounced temperature drop resulted in phonon scattering across the interface. In addition, the calculated interfacial thermal conductance of the biphenylene/graphene heterostructure is higher than that of other graphene-based lateral heterostructures such as graphene/BN (about 1.2×10^{9} W K^{-1} m^{-2}) [34], graphene/metal (about 2.50×10^{8} W K^{-1} m^{-2}) [35], graphene/phosphorene (about 2.49×10^{8} W K^{-1} m^{-2}) [36], and graphene/MoS_2 (about 2.49×10^{8} W K^{-1} m^{-2}) [37].

Strain engineering is a popular method to tune the properties of the 2D materials, such as electronic [38], thermal [39], and thermoelectric [40] performances. In general, the thermal conductivity of 2D materials can be reduced because of the suppressed phonon group velocity and the improved anharmonicity under external tensile strain, which is reported by graphene [41, 42]. Thus, we further investigate the response of the thermal transport of the biphenylene/graphene lateral heterostructure on external tensile stress along the *x* direction. We can see that the heat flux of the biphenylene/graphene heterostructure is increased while the interfacial thermal conductance is decreased by the strain, as shown in Figure 5A and Figure 5B, respectively. To

clarify the intrinsic mechanism of the strain-dependent thermal transport in the biphenylene/graphene heterostructure, the vibrational density of states (VDOS) of pristine graphene and biphenylene is calculated, which is defined as follows [43]:

$$\mathrm{VDOS}(\omega) = \frac{1}{\sqrt{2\pi}} \int_0^{\infty} e^{i\omega t} \mathrm{C}(t) dt, \tag{4}$$

where ω and $\mathrm{C}(t)$ demonstrate the angular frequency and the velocity auto-correlation function, respectively. In the calculations of the total VDOS, $\mathrm{C}(t)$ is obtained by

$$\mathrm{C}(t) = \left\langle \sum_{j=1}^{N} \vec{\mathbf{v}}_j(0) \cdot \vec{\mathbf{v}}_j(t) \right\rangle, \tag{5}$$

where $\vec{\mathbf{v}}_j(t)$ represents the velocity of atom j, and the ensemble average is described by $\langle\ \rangle$. The obtained VDOS in the x direction and the total VDOS are shown in Figures 5C,D, respectively. It is worth emphasizing that the increase in strain can result in a redshift for both graphene and biphenylene. In addition, the calculated value of the overlap (S) of the total VDOS for graphene and biphenylene increases from 0.7062 to 0.8392 with strain from 1% to 4% along the x direction, which also explains the enhanced heat flow by the strain in the biphenylene/graphene heterostructure.

Conclusion

In conclusion, the non-equilibrium molecular dynamics calculations in this work demonstrate that biphenylene possesses isotropic thermal transport characteristics. The thermal conductivity of biphenylene can be improved by length along the heat flux but reduced by increasing the temperature. The graphene/biphenylene heterostructure presents interfacial thermal conductance of about $2.84 \times 10^9\ \mathrm{W\,K^{-1}\,m^{-2}}$. In addition, the interfacial thermal conductance of the biphenylene/graphene heterostructure is found to be dependent on strain, and the enhanced heat flux by the strain results from the larger overlap of the VDOS between graphene and biphenylene.

Data availability statement

The original contributions presented in the study are included in the article/Supplementary Material; further inquiries can be directed to the corresponding author.

Author contributions

Conceptualization, QC; methodology, KR and RZ; software, JL; validation, KR; investigation, JL; writing—original draft preparation, QC, KR and RZ; writing—review and editing, JL; funding acquisition, QC and KR. All authors have read and agreed to the published version of the manuscript.

Funding

This research is supported by the Key projects of natural science research in Colleges and Universities of Anhui Province (KJ2021A1520, KJ2018A0698, and KJ2020A0909) and the Natural Science Foundation of Jiangsu (No. BK20220407).

Conflict of interest

The authors declare that the research was conducted in the absence of any commercial or financial relationships that could be construed as a potential conflict of interest.

Publisher's note

All claims expressed in this article are solely those of the authors and do not necessarily represent those of their affiliated organizations, or those of the publisher, the editors, and the reviewers. Any product that may be evaluated in this article, or claim that may be made by its manufacturer, is not guaranteed or endorsed by the publisher.

References

1. Geim AK, Novoselov KS. The rise of graphene. *Nat Mater* (2007) 6:183–91. doi:10.1038/nmat1849

2. Zhang L, Ren K, Li J, Cui Z, Cheng H. The first-principles study of external strain tuning the electronic and optical properties of the 2D $MoTe_2/PtS_2$ van der Waals heterostructure. *Front Chem* (2022) 10:934048. doi:10.3389/fchem.2022.934048

3. Ren K, Chen Y, Qin H, Feng W, Zhang G. Graphene/biphenylene heterostructure: Interfacial thermal conduction and thermal rectification. *Appl Phys Lett* (2022) 121:082203. doi:10.1063/5.0100391

4. Zhang J, Zhang C, Ren K, Lin X, Cui Z. Tunable electronic and magnetic properties of $Cr_2Ge_2Te_6$ monolayer by organic molecular adsorption. *Nanotechnology* (2022) 33:345705. doi:10.1088/1361-6528/ac715d

5. Wang G, Zhi Y, Bo M, Xiao S, Li Y, Zhao W, et al. 2D hexagonal boron nitride/cadmium sulfide heterostructure as a promising water-splitting photocatalyst. *Phys Status Solidi B* (2020) 257:1900431. doi:10.1002/pssb.201900431

6. Wang G, Zhang L, Li Y, Zhao W, Kuang A, Li Y, et al. Biaxial strain tunable photocatalytic properties of 2D ZnO/GeC heterostructure. *J Phys D Appl Phys* (2020) 53:015104. doi:10.1088/1361-6463/ab440e

7. Wang G, Gong L, Li Z, Wang B, Zhang W, Yuan B, et al. A two-dimensional CdO/CdS heterostructure used for visible light photocatalysis. *Phys Chem Chem Phys* (2020) 22:9587–92. doi:10.1039/d0cp00876a

8. Ren K, Wang K, Zhang G. Atomic adsorption-controlled magnetic properties of a two-dimensional (2D) janus monolayer. *ACS Appl Electron Mater* (2022) 4:4507–13. doi:10.1021/acsaelm.2c00740

9. Zhang H, Chhowalla M, Liu Z. 2D nanomaterials: Graphene and transition metal dichalcogenides. *Chem Soc Rev* (2018) 47:3015–7. doi:10.1039/c8cs90048e

10. Ren K, Sun M, Luo Y, Wang S, Yu J, Tang W. First-principle study of electronic and optical properties of two-dimensional materials-based heterostructures based on transition metal dichalcogenides and boron phosphide. *Appl Surf Sci* (2019) 476:70–5. doi:10.1016/j.apsusc.2019.01.005

11. Ren K, Zheng R, Xu P, Cheng D, Huo W, Yu J, et al. Electronic and optical properties of atomic-scale heterostructure based on MXene and mn (M = Al, Ga): A dft investigation. *Nanomaterials* (2021) 11:2236. doi:10.3390/nano11092236

12. Sun M, Re Fiorentin M, Schwingenschlögl U, Palummo M. Excitons and light-emission in semiconducting $MoSi_2X_4$ two-dimensional materials. *Npj 2d Mater Appl* (2022) 6:81. doi:10.1038/s41699-022-00355-z

13. Ren K, Ma X, Liu X, Xu Y, Huo W, Li W, et al. Prediction of 2D IV–VI semiconductors: Auxetic materials with direct bandgap and strong optical absorption. *Nanoscale* (2022) 14:8463–73. doi:10.1039/d2nr00818a

14. Ren K, Qin H, Liu H, Chen Y, Liu X, Zhang G. Manipulating interfacial thermal conduction of 2D janus heterostructure via a thermo-mechanical coupling. *Adv Funct Mater* (2022) 32:2110846. doi:10.1002/adfm.202110846

15. Ren K, Shu H, Huo W, Cui Z, Yu J, Xu Y. Mechanical, electronic and optical properties of a novel B_2P_6 monolayer: Ultrahigh carrier mobility and strong optical absorption. *Phys Chem Chem Phys* (2021) 23:24915–21. doi:10.1039/d1cp03838a

16. Pandey R, Rérat M, Darrigan C, Causà M. A theoretical study of stability, electronic, and optical properties of GeC and SnC. *J Appl Phys* (2000) 88:6462–6. doi:10.1063/1.1287225

17. Kamal C, Ezawa M. Arsenene: Two-dimensional buckled and puckered honeycomb arsenic systems. *Phys Rev B* (2015) 91:085423. doi:10.1103/physrevb.91.085423

18. Wang K, Ren K, Zhang D, Cheng Y, Zhang G. Phonon properties of biphenylene monolayer by first-principles calculations. *Appl Phys Lett* (2022) 121:042203. doi:10.1063/5.0102085

19. Qin H, Ren K, Zhang G, Dai Y, Zhang G. Lattice thermal conductivity of Janus MoSSe and WSSe monolayers. *Phys Chem Chem Phys* (2022) 24:20437–44. doi:10.1039/d2cp01692c

20. Balandin AA, Ghosh S, Bao W, Calizo I, Teweldebrhan D, Miao F, et al. Superior thermal conductivity of single-layer graphene. *Nano Lett* (2008) 8:902–7. doi:10.1021/nl0731872

21. Cai W, Moore AL, Zhu Y, Li X, Chen S, Shi L, et al. Thermal transport in suspended and supported monolayer graphene grown by chemical vapor deposition. *Nano Lett* (2010) 10:1645–51. doi:10.1021/nl9041966

22. Liu B, Baimova JA, Reddy CD, Law AW, Dmitriev SV, Wu H, et al. Interfacial thermal conductance of a silicene/graphene bilayer heterostructure and the effect of hydrogenation. *ACS Appl Mater Inter* (2014) 6:18180–8. doi:10.1021/am505173s

23. Liu X, Zhang G, Zhang YW. Topological defects at the graphene/h-BN interface abnormally enhance its thermal conductance. *Nano Lett* (2016) 16:4954–9. doi:10.1021/acs.nanolett.6b01565

24. Ren K, Liu X, Chen S, Cheng Y, Tang W, Zhang G. Remarkable reduction of interfacial thermal resistance in nanophononic heterostructures. *Adv Funct Mater* (2020) 30:2004003. doi:10.1002/adfm.202004003

25. Qin H, Pei QX, Liu Y, Zhang YW. The mechanical and thermal properties of MoS_2-WSe_2 lateral heterostructures. *Phys Chem Chem Phys* (2019) 21:15845–53. doi:10.1039/c9cp02499a

26. Fan Q, Yan L, Tripp MW, Krejčí O, Dimosthenous S, Kachel SR, et al. Biphenylene network: A nonbenzenoid carbon allotrope. *Science* (2021) 372:852–6. doi:10.1126/science.abg4509

27. Ren K, Shu H, Huo W, Cui Z, Xu Y. Tuning electronic, magnetic and catalytic behaviors of biphenylene network by atomic doping. *Nanotechnology* (2022) 33:345701. doi:10.1088/1361-6528/ac6f64

28. Luo Y, Ren C, Xu Y, Yu J, Wang S, Sun M. A first principles investigation on the structural, mechanical, electronic, and catalytic properties of biphenylene. *Sci Rep* (2021) 11:19008–6. doi:10.1038/s41598-021-98261-9

29. Liu T, Jing Y, Li Y. Two-dimensional biphenylene: A graphene allotrope with superior activity toward electrochemical oxygen reduction reaction. *J Phys Chem Lett* (2021) 12:12230–4. doi:10.1021/acs.jpclett.1c03851

30. Plimpton S. Fast parallel algorithms for short-range molecular dynamics. *J Comput Phys* (1995) 117:1–19. doi:10.1006/jcph.1995.1039

31. Togo A, Tanaka I. First principles phonon calculations in materials science. *Scripta Materialia* (2015) 108:1–5. doi:10.1016/j.scriptamat.2015.07.021

32. Togo A, Oba F, Tanaka IJPRB. First-principles calculations of the ferroelastic transition between rutile-type and $CaCl_2$-type SiO_2 at high pressures. *Phys Rev B* (2008) 78:134106. doi:10.1103/physrevb.78.134106

33. Qin H, Chen Y, Wu Y, Li M, Liu Y, Pei Q-X. Defect-engineered thermal transport in wrinkled graphene: A comprehensive molecular dynamics study. *J Phys Chem C* (2022) 126:5759–66. doi:10.1021/acs.jpcc.2c00324

34. Mao R, Kong B, Gong C, Xu S, Jayasekera T, Cho K, et al. First-principles calculation of thermal transport in metal/graphene systems. *Phys Rev B* (2013) 87:165410. doi:10.1103/physrevb.87.165410

35. Jiang J-W, Wang J-S. Manipulation of heat current by the interface between graphene and white graphene. *Europhysics Lett* (2011) 96:16003. doi:10.1209/0295-5075/96/16003

36. Liu X, Gao J, Zhang G, Zhang YW. Design of phosphorene/graphene heterojunctions for high and tunable interfacial thermal conductance. *Nanoscale* (2018) 10:19854–62. doi:10.1039/c8nr06110f

37. Liu X, Gao J, Zhang G, Zhang Y-W. MoS_2-graphene in-plane contact for high interfacial thermal conduction. *Nano Res* (2017) 10:2944–53. doi:10.1007/s12274-017-1504-8

38. Desai SB, Seol G, Kang JS, Fang H, Battaglia C, Kapadia R, et al. Strain-induced indirect to direct bandgap transition in multilayer WSe_2. *Nano Lett* (2014) 14:4592–7. doi:10.1021/nl501638a

39. Yu C, Zhang G, Zhang Y-W, Peng L-M. Strain engineering on the thermal conductivity and heat flux of thermoelectric Bi_2Te_3 nanofilm. *Nano Energy* (2015) 17:104–10. doi:10.1016/j.nanoen.2015.08.003

40. Zhang G, Zhang Y-W. Strain effects on thermoelectric properties of two-dimensional materials. *Mech Mater* (2015) 91:382–98. doi:10.1016/j.mechmat.2015.03.009

41. Guo Z, Zhang D, Gong X-G. Thermal conductivity of graphene nanoribbons. *Appl Phys Lett* (2009) 95:163103. doi:10.1063/1.3246155

42. Wei N, Xu L, Wang H-Q, Zheng J-C. Strain engineering of thermal conductivity in graphene sheets and nanoribbons: A demonstration of magic flexibility. *Nanotechnology* (2011) 22:105705. doi:10.1088/0957-4484/22/10/105705

43. Grest G, Nagel S, Rahman A, Witten T, Jr. Density of states and the velocity autocorrelation function derived from quench studies. *J Chem Phys* (1981) 74:3532–4. doi:10.1063/1.441508

frontiers | Frontiers in Chemistry

TYPE Original Research
PUBLISHED 08 December 2022
DOI 10.3389/fchem.2022.1103704

OPEN ACCESS

EDITED BY
Guangzhao Wang,
Yangtze Normal University, China

REVIEWED BY
Xiaoming Zhang,
Hebei University of Technology, China
Weikang Wu,
Shandong University, China

*CORRESPONDENCE
Jiaren Yuan,
jryuan@ncu.edu.cn

SPECIALTY SECTION
This article was submitted to Physical Chemistry and Chemical Physics, a section of the journal Frontiers in Chemistry

RECEIVED 20 November 2022
ACCEPTED 28 November 2022
PUBLISHED 08 December 2022

CITATION
Chen D, Jiang Z, Tang Y, Zhou J, Gu Y, He J-J and Yuan J (2022), Electrical and magnetic properties of antiferromagnetic semiconductor $MnSi_2N_4$ monolayer.
Front. Chem. 10:1103704.
doi: 10.3389/fchem.2022.1103704

Electrical and magnetic properties of antiferromagnetic semiconductor $MnSi_2N_4$ monolayer

Dongke Chen[1,2], Zhengyu Jiang[2], Ying Tang[2], Junlei Zhou[2], Yuzhou Gu[2], Jing-Jing He[3] and Jiaren Yuan[1]*

[1]School of Physics and Materials Science Nanchang University, Nanchang, China, [2]School of Physics and Electronic Engineering, Jiangsu University, Zhenjiang, China, [3]College of Information Science and Technology, Nanjing Forestry University, Nanjing, China

Two-dimensional antiferromagnetic semiconductors have triggered significant attention due to their unique physical properties and broad application. Based on first-principles calculations, a novel two-dimensional (2D) antiferromagnetic material $MnSi_2N_4$ monolayer is predicted. The calculation results show that the two-dimensional $MnSi_2N_4$ prefers an antiferromagnetic state with a small band gap of 0.26 eV. $MnSi_2N_4$ has strong antiferromagnetic coupling which can be effectively tuned under strain. Interestingly, the $MnSi_2N_4$ monolayer exhibits a half-metallic ferromagnetic properties under an external magnetic field, in which the spin-up electronic state displays a metallic property, while the spin-down electronic state exhibits a semiconducting characteristic. Therefore, 100% spin polarization can be achieved. Two-dimensional $MnSi_2N_4$ monolayer has potential application in the field of high-density information storage and spintronic devices.

KEYWORDS

two-dimensional materials, antiferromagnetic semiconductor, half metals, electronic properties, biaxial strain

Introduction

In 2004, the successfully prepared graphene opened a new era of two-dimensional materials (Novoselov et al., 2004). Subsequently, numerous new systems have already been discovered, greatly promoting the development of the two-dimensional material family. Two-dimensional materials have a wide variety of electronic properties, including metallic, semi-metallic, semiconducting and insulating properties. For example, 1H-MoS_2 is a semiconductor with a direct band gap, 1T phase MoS_2 is a metal, while 1T' phase MoS_2 is semimetal (Hung et al., 2018). In addition, hexagonal boron nitride (h-BN) shows insulating properties (Liu et al., 2003), and graphene is semimetal (Sheng et al., 2019). However, many 2D materials lack intrinsic magnetism, such as graphene and MoS_2, which motivates researchers to induce magnetism through defect engineering, adsorption or insertion of magnetic atoms. However, these schemes are difficult to construct stable

long-range magnetic order. Therefore, two-dimensional intrinsic ferromagnetic materials have aroused tremendous attention.

According to Mermin-Wagner theory, the long-range magnetic order is predicted to be unstable in 2D material and can be easily destroyed by thermal fluctuations (Mermin and Wagner, 1966). Until 2017, the magnetism in the two-dimensional material CrI_3 at the monolayer limit was observed experimentally (Gong et al., 2017; Huang et al., 2017). Hereafter, more 2D magnetic materials have been found, such as Fe_3GeTe_2 (Xian et al., 2022), $FePS_3$ (Lee et al., 2016) and VSe_2 (Bonilla et al., 2018). Two-dimensional magnetic materials possess a wide variety of excellent physical properties. For instance, monolayer magnetic metal materials have been widely used as electrodes in electronic devices, such as Fe_3GeTe_2 based van der Waals tunnel junctions (O'Hara et al., 2018). Furthermore, magnetic tunnel junction with antimagnetic semiconductor CrI_3 tunnel barrier has been reported to possess a giant magnetoresistance effect due to the significant difference of energy band in the ferromagnetic and antiferromagnetic states (Song et al., 2018), which has achieved a huge breakthrough in spintronic devices. Hence antiferromagnetic semiconductor materials have become a hot research topic because of their novel band characteristics. However, such materials are very rare, the prediction of new antiferromagnetic semiconductor materials becomes the key to the development of spintronic devices.

In this paper, the electronic structure and magnetic properties of monolayer $MnSi_2N_4$ are explored based on first-principles calculations. The results demonstrate that 2D $MnSi_2N_4$ is a stable antiferromagnetic semiconductor in which the ground state is an antiferromagnetic state. The large magnetic exchange parameter indicates a strong antiferromagnetic coupling between the magnetic Mn atoms. When an external magnetic field is applied, the $MnSi_2N_4$ monolayer turns into a half-metal with a magnetic state transition from an antiferromagnetic state to a ferromagnetic state. In which the spin-up electronic state displays a metallic nature, while the spin-down electronic state exhibits a semiconducting feature. Therefore, the $MnSi_2N_4$ monolayer has great application prospects in spintronics and nanosensors.

Computational details

All calculations were conducted using the Vienna *ab initio* simulation package (VASP) (Kresse and Furthmuller, 1996; Kresse and Joubert, 1999). The projection plane wave (PAW) method was adopted to describe the interaction between ions and electrons (Blöchl, 1994). The cutoff energy is set as 500 eV. The generalized gradient approximation (GGA) of the form Perdew–Burke–Ernzerhof (PBE) was employed to describe the exchange correlation (Perdew et al., 1996). The convergence criteria for electronic iteration and ionic relaxation were 10^{-6} eV and 0.001 eV/Å, respectively. An 18 Å vacuum layer was added in the out plane direction of the monolayer $MnSi_2N_4$ to eliminate interlayer interactions. The Brillouin zone was sampled with a 13 × 13 × 1 k-point mesh. Due to the strong correlation effect of Mn atoms, the DFT + U method proposed by Dudarev et al. (Dudarev et al., 1998) was adopted, and the effective parameter U_{eff} was set to 3.9 eV (Wang et al., 2006; Jain et al., 2011; Ling and Mizuno, 2012; Togo and Tanaka, 2015). The phonon spectrum of monolayer $MnSi_2N_4$ was calculated by the PHONONPY software (Togoet al., 2015) using a 5 × 5 supercell.

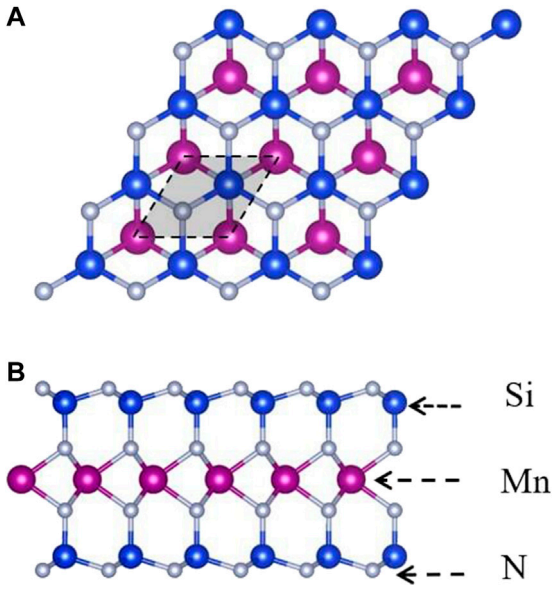

FIGURE 1
Top **(A)** and side **(B)** views of $MnSi_2N_4$. The balls are highlighted with blue (Si atom), purple (Mn atom) and silvery (N atom). The rhombic unit cells are marked with black dashed lines.

Results and discussion

Similar to the two-dimensional $MoSi_2N_4$, the monolayer $MnSi_2N_4$ is a two-dimensional material with a hexagonal lattice structure and D_{3h} point group as shown in Figure 1. $MnSi_2N_4$ monolayer consists of seven atomic layers stacked with the order N-Si-N-Mn-N-Si-N, which can be regarded as a 1H-phase MnN_2 triple-layer sandwiched between two buckled N-Si layers. The lattice constant of unit cell is 2.88Å, the bond length between Mn and N atoms is 2.02 Å and the bond length between Si and N atoms is 1.74 Å.

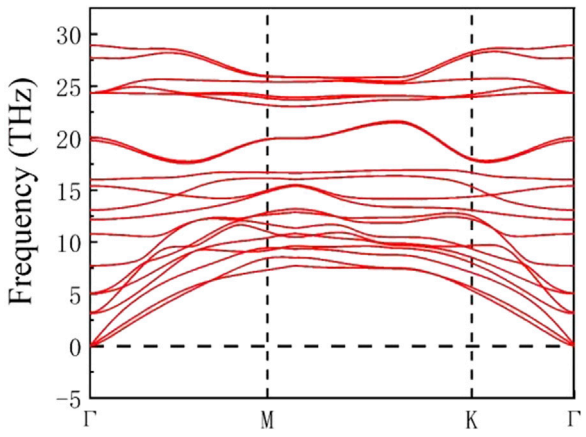

FIGURE 2
Phonon spectrum of monolayer $MnSi_2N_4$.

The cohesive energy of the monolayer $MnSi_2N_4$ was evaluated to confirm the stability of monolayer $MnSi_2N_4$ using the equation:

$$E_{coh} = \left(E_{MnSi_2N_4} - E_{Mn} - 2E_{Si} - 4E_N\right)/7 \quad (1)$$

Where $E_{MnSi_2N_4}$ represents the energy of $MnSi_2N_4$, E_{Mn} , E_{Si} and E_N represent the energy of isolated single Mn, Si and N atoms, respectively. The calculated results show that the cohesive energy of $MnSi_2N_4$ is -5.03 eV/atom which is comparable to the value of MoS_2 monolayer (−5.12 eV/atom) (Canton-Vitoria et al., 2020) and $MoSi_2N_4$ (−8.46 eV/atom) (Bafekry et al., 2021). We also calculated the phonon spectrum to check the stability, and there is no imaginary phonon frequency throughout the Brillouin zone, indicating that the structure is dynamically stable. Consequently, the $MnSi_2N_4$ monolayer has excellent stability and thus may be experimentally prepared in Figure 2.

The magnetic properties of monolayer $MnSi_2N_4$ were investigated. We first determined the ground-state magnetic ordering with two possible magnetic order ferromagnetic (FM) and antiferromagnetic (AFM) states. The total energies of the AFM and FM phases of $MnSi_2N_4$ are -218.650eV and -217.658 eV, respectively. The energy of the AFM state is lower than that of the FM state, hence $MnSi_2N_4$ has an AFM ground state. The AFM order in monolayer $MnSi_2N_4$ sourced from the superexchange interactions between two magnetic atoms bridged by nonmetal atoms, following the Goodenough-Kanamori rules (Goodenough, 1955; Kanamori, 1959). In this case, the net magnetic moment is zero and the four Mn atoms in the supercell have an antiparallel magnetic state along with the same value of magnetic moments (3.05 μ_B). The spin-polarized charge density and the schematic diagram for FM and AFM order are plotted in Figure 3. The spin-polarized charge density map shows that Mn atoms possess an high spin-polarized charge density, while spin-polariztion of N atoms is tiny with small magnetic moments (0.05 μ_B).

The electronic properties of AFM states are investigated to further explore potential applications of $MnSi_2N_4$. The electronic band structure and density of states (TDOS) are calculated as

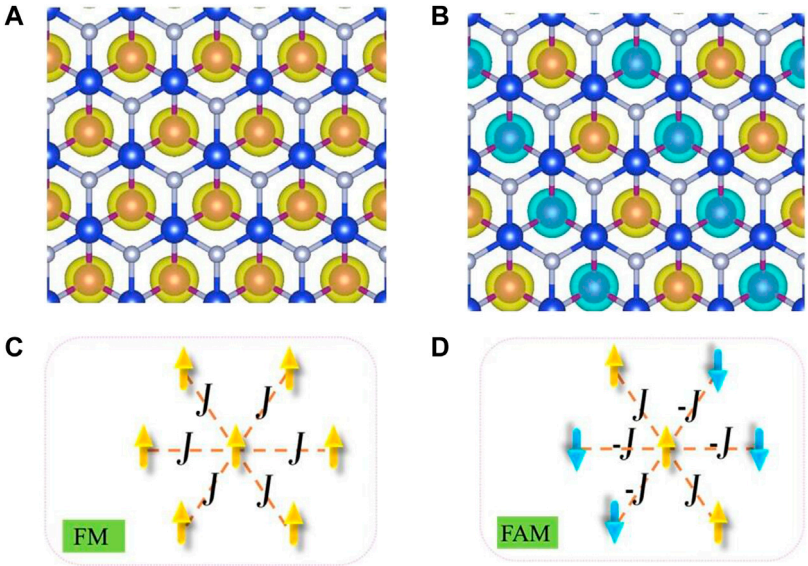

FIGURE 3
(A,B) spin-polarized charge densities of the FM and AFM case for $MnSi_2N_4$. The yellow and light blue isosurface with an isosurface value of 0.05 e/Bohr^3 represent the spin-up and spin-down charge densities, respectively. **(C,D)** The scheme represents spin orientation of Mn atoms in FM and AFM case.

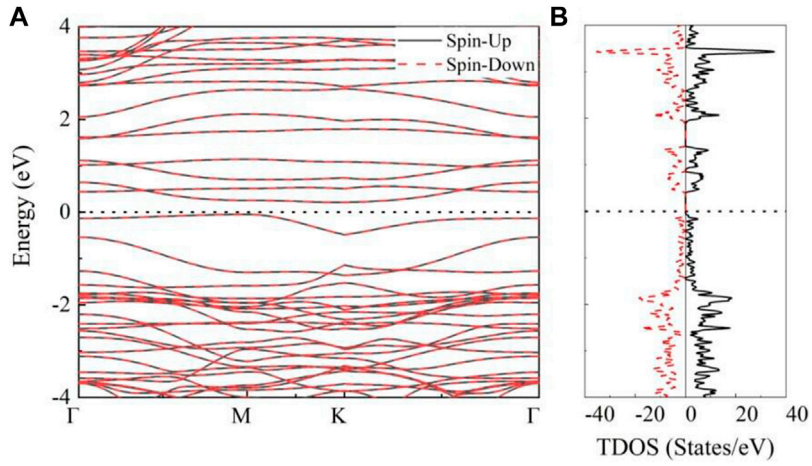

FIGURE 4
(A) The band structures and **(B)** total density of states (TDOS) of $MnSi_2N_4$ monolayer in the AFM states, the spin-up states and spin-down states are represented by the black lines and red dotted lines, respectively.

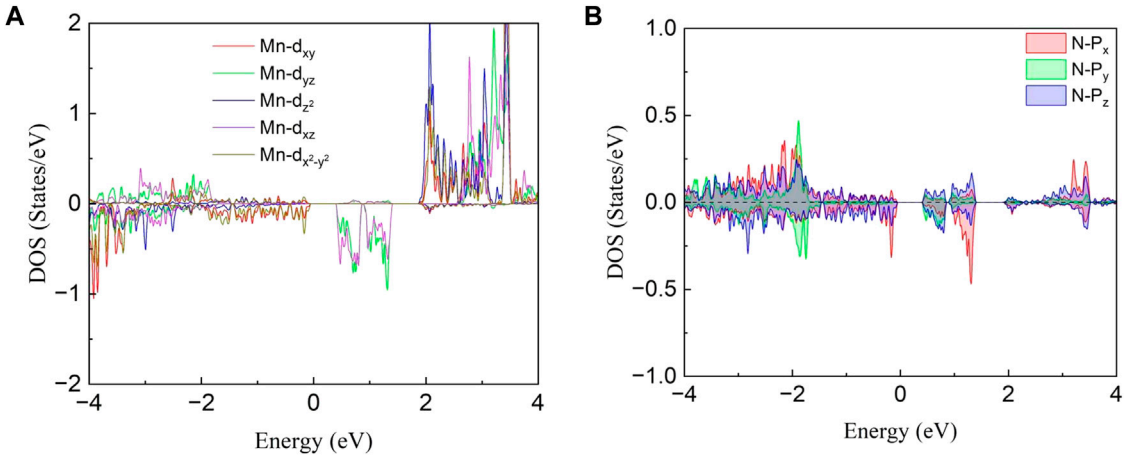

FIGURE 5
Projected density of states (PDOS) for **(A)** Mn-*d* orbital and **(B)** N-*p* orbital.

illustrated in Figure 4. It is clear that $MnSi_2N_4$ exhibits indirect semiconducting property without band cross Fermi level, which is different from nonmagnetic direct bandgap semiconductor $MoSi_2N_4$ monolayer (Yuan et al., 2022). The conduction band minimum (CBM) and the valence band maximum (VBM) are located at K point and M point, respectively. The band gap is small (0.26 eV). The bands are degenerate and the TDOS is symmetrical for spin-up and spin-down states. Furthermore, no states exist near the Fermi level along with a small energy gap.

The projected density of states (PDOS) for Mn atom and the nearest neighbor N atom are depicted in Figure 5 to better analyze orbit contribution for electron structure and magnetic properties. One can notice that the density of states for the five 3*d* orbitals are all asymmetric as shown in Figure 5A, indicating the large spin splitting for an isolated Mn atom. The magnetic moment (3.04 μ_B/Mn) is mainly dominated by the spin-up (majority-spin) states of *d* orbitals which is much more than the spin-down electron. For the N atom, the difference in PDOS between the spin-up and spin-down states is not obvious, resulting in a smaller magnetic moment. In addition, the DOS mainly comes from Mn-*d* and N-*p* in the energy range from 0.5 to 1.5 eV indicating that the hybridizations between the N-*p* and Mn-*d* orbitals are strong.

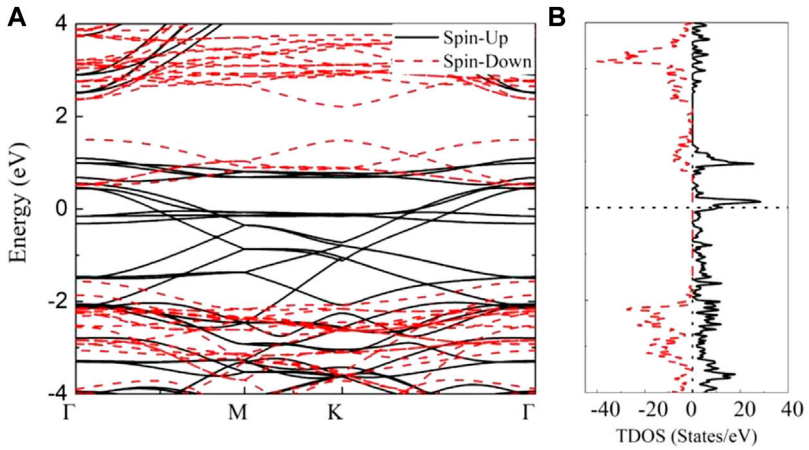

FIGURE 6
(A) The band structures and **(B)** total density of states (TDOS) of $MnSi_2N_4$ in the FM states, the spin-up states and spin-down states are represented by the black lines and red dotted lines, respectively.

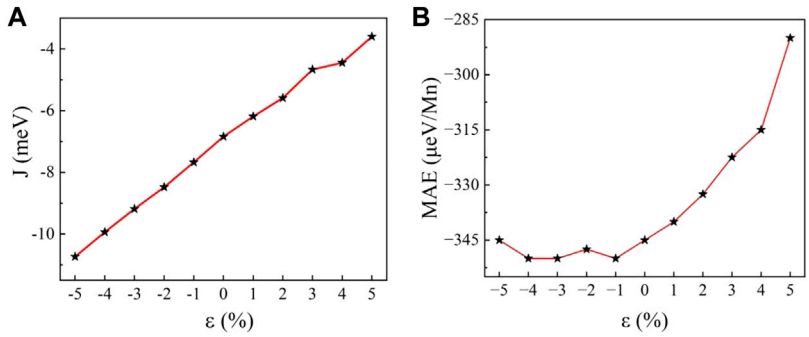

FIGURE 7
(A) Magnetic exchange parameter J and **(B)** magnetocrystalline anisotropy energy E_{MAE} as a function of strain.

Furthermore, the ground antiferromagnetic states will transition to ferromagnetic states under an external magnetic field. The band structure and density of states for FM state are depicted in Figure 6. It is clear that the spin-up and spin-down energy bands are not degenerate. The spin-polarized states can be noticed around the Fermi level. In the spin-up channel, several flat bands near the Fermi level existe and the others band display dispersion along Γ–M and K–Γ, which behave as a metal. But for the spin-down channel, a direct bandgap of 2.07 eV is observed with the VBM and CBM located at Γ point. Hence, $MnSi_2N_4$ monolayer behaves half-metallic properties in the FM case. The spin polarization is obvious with an asymmetric density of states distribution for spin-up and spin-down states as depicted in Figure 6B. One can find that a peak of spin-up states can be seen near the Fermi level and a large bandgap exists in the spin-down states, which further confirms the metallic behavior for the spin-up states and semiconducting property for spin-down states, respectively. Therefore, the 2D $MnSi_2N_4$ in FM state is a half-metal with 100% spin polarization.

Strain is an effective means of manipulating electronic structure and magnetic properties which is widely utilized to modulate the electronic structure and magnetic properties of monolayer system. In this paper, the strain is defined as $\varepsilon = (a - a_0)/a_0$, where a_0 is the relaxed lattice constant in the equilibrium state. The magnetic moment of the Mn atom remains about 3 μ_B per unit cell under strain. The effective spin Hamiltonian based on the Heisenberg model can be expressed as

$$H = -\sum_{<i,j>} J_{ij}\mu_i\mu_j \quad (2)$$

where J_{ij} is the magnetic exchange parameter, and μ_i/μ_j is the magnetic moment at nearest neighbor sites i and j, respectively (Kan et al., 2013). The magnetic exchange parameter J is a significant parameter, which can be evaluated by calculating the total energy of the system in different magnetic states. For the FM case, the total energy can be written as $E_{FM} = E_0 - 3J|\mu|^2$, where E_0 represents the total energy without spin polarization. For the AFM case, the total energy can be expressed as $E_{AFM} = E_0 + J|\mu|^2$. Thus, the exchange parameter can be extracted by $J = (E_{AFM} - E_{FM})/4|\mu|^2$. According to Figure 7A, although the value of J increases nearly linearly with biaxial strain, the energy difference between AFM case and FM case remains positive over the range of applied biaxial strain, indicating that $MnSi_2N_4$ behaves as AFM phase and no transition from AFM to FM phase is observed. Furthermore, the magnetic exchange parameter J increases with tensile strain and decreases with compressive strain. According to this trend, an extremely large tensile strain may be needed to turn the AFM to the FM ordering.

To identify the easy axis of $MnSi_2N_4$, we computed the magnetic anisotropy energy (MAE). The MAE of the magnetic crystal is defined as $E_{MAE} = E_{in}$-E_{out} (Webster and Yan, 2018), that is, the energy difference between the in-plane (E_{in}) and out-of-plane (E_{out}) of $MnSi_2N_4$. For the strain-free monolayer $MnSi_2N_4$, the MAE is −345 μeV/Mn atom, indicating that the easy axis of $MnSi_2N_4$ prefers in-plane and the spin of the Mn atoms is arranged parallel to the basal plane. The MAE of monolayer $MnSi_2N_4$ is mainly derived from Mn atoms since Mn atoms have relatively stronger spin-orbit coupling than other atoms. The MAE is depicted as a function of strain in Figure 7B. When the structure is compressed, this value fluctuates around −350 μeV/Mn, hence the effect of compressive strain on MAE is not obvious. While MAE increases significantly with increasing tensile strain. MAE changes from -345 μeV/Mn to −290 μeV/Mn under the 5% tensile strain.

Conclusion

The electronic and magnetic properties of monolayer $MnSi_2N_4$ are explored based on first-principles calculations. Monolayer $MnSi_2N_4$ is an intrinsic antiferromagnetic semiconductor with a small indirect band gap (0.26 eV). The $MnSi_2N_4$ has strong antiferromagnetic coupling along with strong in-plane magnetocrystalline anisotropy energy (−345 μeV/Mn). Furthermore, the $MnSi_2N_4$ monolayer exhibits half-metallic properties with a metallic spin-up state and a semiconducting spin-down state. The effect of biaxial strain on magnetism is also investigated. The magnetic exchange parameter J and MAE increase with biaxial tensile strain. The tunable magnetic properties may enrich the 2D antiferromagnets community and stimulate potential applications in spintronic devices.

Data availability statement

The original contributions presented in the study are included in the article/Supplementary Material, further inquiries can be directed to the corresponding author.

Author contributions

DC and ZJ: Conceptualization, methodology, software; JY and J-JH: Investigation, Formal analysis, Visualization; JZ and YG: Formal analysis, Data Curation; DC and YT: Writing—original draft preparation; JY: Supervision, Writing—review and editing.

Funding

Financial support was received from the National Natural Science Foundation of China (NSFC12004142 and NSFC12264026), and Natural Science Funds for Colleges and Universities in Jiangsu Province (20KJB140017).

Conflict of interest

The authors declare that the research was conducted in the absence of any commercial or financial relationships that could be construed as a potential conflict of interest.

Publisher's note

References

Bafekry, A., Faraji, M., Stampfl, C., Abdolhosseini Sarsari, I., Abdollahzadeh Ziabari, A., Hieu, N. N., et al. (2021). Band-gap engineering, magnetic behavior and Dirac-semimetal character in the $MoSi_2N_4$ nanoribbon with armchair and zigzag edges. *J. Phys. D. Appl. Phys.* 55 (3), 035301. doi:10.1088/1361-6463/ac2cab

Blöchl, P. E. (1994). Projector augmented-wave method. *Phys. Rev. B* 50 (24), 17953–17979. doi:10.1103/PhysRevB.50.17953

Bonilla, M., Kolekar, S., Ma, Y., Diaz, H. C., Kalappattil, V., Das, R., et al. (2018). Strong room-temperature ferromagnetism in VSe_2 monolayers on van der Waals substrates. *Nat. Nanotechnol.* 13, 289–293. doi:10.1038/s41565-018-0063-9

Canton-Vitoria, R., Sayed-Ahmad-Baraza, Y., Humbert, B., Arenal, R., Ewels, C., and Tagmatarchis, N. (2020). Pyrene coating transition metal disulfides as protection from photooxidation and environmental aging. *Nanomaterials* 10 (2), 363. doi:10.3390/nano10020363

Dudarev, S. L., Botton, G. A., Savrasov, S. Y., Humphreys, C. J., and Sutton, A. P. (1998). Electron-energy-loss spectra and the structural stability of nickel oxide: An LSDA+ U study. *Phys. Rev. B* 57 (3), 1505–1509. doi:10.1103/PhysRevB.57.1505

Gong, C., Li, L., Li, Z., Ji, H., Stern, A., Xia, Y., et al. (2017). Discovery of intrinsic ferromagnetism in two-dimensional van der Waals crystals. *Nature* 546 (7657), 265–269. doi:10.1038/nature22060

Goodenough, J. B. (1955). Theory of the role of covalence in the perovskite-type manganites [La, M (II)] MnO_3. *Phys. Rev.* 100 (2), 564–573. doi:10.1103/PhysRev.100.564

Huang, B., Clark, G., Navarro-Moratalla, E., Klein, D. R., Cheng, R., Seyler, K. L., et al. (2017). Layer-dependent ferromagnetism in a van der Waals crystal down to the monolayer limit. *Nature* 546 (7657), 270–273. doi:10.1038/nature22391

Hung, N. T., Nugraha, A. R. T., and Saito, R. (2018). Two-dimensional MoS_2 electromechanical actuators. *J. Phys. D. Appl. Phys.* 51 (7), 075306. doi:10.1088/1361-6463/aaa68f

Jain, A., Hautier, G., Moore, C. J., Ping Ong, S., Fischer, C. C., Mueller, T., et al. (2011). A high-throughput infrastructure for density functional theory calculations. *Comput. Mat. Sci.* 50 (8), 2295–2310. doi:10.1016/j.commatsci.2011.02.023

Kan, M., Zhou, J., Sun, Q., Kawazoe, Y., and Jena, P. (2013). The intrinsic ferromagnetism in a MnO2 monolayer. *J. Phys. Chem. Lett.* 4 (20), 3382–3386. doi:10.1021/jz4017848

Kanamori, J. (1959). Superexchange interaction and symmetry properties of electron orbitals. *J. Phys. Chem. Solids* 10 (2-3), 87–98. doi:10.1016/0022-3697(59)90061-7

Kresse, G., and Furthmüller, J. (1996). Efficient iterative schemes for *ab initio* total-energy calculations using a plane-wave basis set. *Phys. Rev. B* 54 (16), 11169–11186. doi:10.1103/PhysRevB.54.11169

Kresse, G., and Joubert, D. (1999). From ultrasoft pseudopotentials to the projector augmented-wave method. *Phys. Rev. B* 59 (3), 1758–1775. doi:10.1103/PhysRevB.59.1758

Lee, J. U., Lee, S., Ryoo, J. H., Kang, S., Kim, T. Y., Kim, P., et al. (2016). Ising-type magnetic ordering in atomically thin $FePS_3$. *Nano Lett.* 16 (12), 7433–7438. doi:10.1021/acs.nanolett.6b03052

Ling, C., and Mizuno, F. (2012). Capture lithium in αMnO_2: Insights from first principles. *Chem. Mat.* 24 (20), 3943–3951. doi:10.1021/cm302347j

Liu, L., Feng, Y. P., and Shen, Z. X. (2003). Structural and electronic properties of h-BN. *Phys. Rev. B* 68 (10), 104102. doi:10.1103/PhysRevB.68.104102

Mermin, N. D., and Wagner, H. (1966). Absence of ferromagnetism or antiferromagnetism in one-or two-dimensional isotropic Heisenberg models. *Phys. Rev. Lett.* 17 (22), 1133–1136. doi:10.1103/PhysRevLett.17.1133

Novoselov, K. S., Geim, A. K., Morozov, S. V., Jiang, D., Zhang, Y., Dubonos, S. V., et al. (2004). Electric field effect in atomically thin carbon films. *Science* 306 (5696), 666–669. doi:10.1126/science.1102896

O'Hara, D. J., Zhu, T., Trout, A. H., Ahmed, A. S., Luo, Y. K., Lee, C. H., et al. (2018). Room temperature intrinsic ferromagnetism in epitaxial manganese selenide films in the monolayer limit. *Nano Lett.* 18 (5), 3125–3131. doi:10.1021/acs.nanolett.8b00683

Perdew, J. P., Burke, K., and Ernzerhof, M. (1996). Generalized gradient approximation made simple. *Phys. Rev. Lett.* 77 (18), 3865–3868. doi:10.1103/PhysRevLett.77.3865

Sheng, X. L., Chen, C., Liu, H., Chen, Z., Yu, Z. M., Zhao, Y., et al. (2019). Two-dimensional second-order topological insulator in graphdiyne. *Phys. Rev. Lett.* 123 (25), 256402. doi:10.1103/PhysRevLett.123.256402

Song, T. C., Cai, X., Tu, M. W. Y., Zhang, X., Huang, B., Wilson, N. P., et al. (2018). Giant tunneling magnetoresistance in spin-filter van der Waals heterostructures. *Science* 360, 1214–1218. doi:10.1126/science.aar4851

Togo, A., and Tanaka, I. (2015). First principles phonon calculations in materials science. *Scr. Mat.* 108, 1–5. doi:10.1016/j.scriptamat.2015.07.021

Wang, L., Maxisch, T., and Ceder, G. (2006). Oxidation energies of transition metal oxides within theGGA+Uframework. *Phys. Rev. B* 73 (19), 195107. doi:10.1103/PhysRevB.73.195107

Webster, L., and Yan, J. A. (2018). Strain-tunable magnetic anisotropy in monolayer CrCl3, CrBr3, and CrI3. *Phys. Rev. B* 98 (14), 144411. doi:10.1103/PhysRevB.98.144411

Xian, J. J., Wang, C., Nie, J. H., Li, R., Han, M., Lin, J., et al. (2022). Spin mapping of intralayer antiferromagnetism and field-induced spin reorientation in monolayer $CrTe_2$. *Nat. Commun.* 13, 257. doi:10.1038/s41467-021-27834-z

Yuan, J., Wei, Q., Sun, M., Yan, X., Cai, Y., Shen, L., et al. (2022). Protected valley states and generation of valley-and spin-polarized current in monolayer MA_2Z_4. *Phys. Rev. B* 105 (19), 195151. doi:10.1103/PhysRevB.105.195151

frontiers | Frontiers in Physics

TYPE Original Research
PUBLISHED 17 January 2023
DOI 10.3389/fphy.2022.1128983

OPEN ACCESS

EDITED BY
Guangzhao Wang,
Yangtze Normal University, China

REVIEWED BY
Wei Sun,
University of Jinan, China
Zhaobo Zhou,
University of Bremen, Germany

*CORRESPONDENCE
Qianshuai Cheng,
hndxcqs@163.com
Yungeng Zhang,
20130016@vip.henu.edu.cn

SPECIALTY SECTION
This article was submitted to Physical Chemistry and Chemical Physics, a section of the journal Frontiers in Physics

RECEIVED 21 December 2022
ACCEPTED 30 December 2022
PUBLISHED 17 January 2023

CITATION
Wang R, Hou L, Shi P, Cheng Q and Zhang Y (2023), Ultrathin high-temperature ferromagnetic rare-earth films: GdScGe and GdScSi monolayers. *Front. Phys.* 10:1128983. doi: 10.3389/fphy.2022.1128983

Ultrathin high-temperature ferromagnetic rare-earth films: GdScGe and GdScSi monolayers

Rui Wang[1], Lipeng Hou[2], Puyuan Shi[2], Qianshuai Cheng[1]* and Yungeng Zhang[1,2]*

[1]School of Computer and Information Engineering, Henan University, Kaifeng, Henan, China, [2]School of Physics and Electronics, Henan University, Kaifeng, Henan, China

Two-dimensional (2D) ferromagnetism with robust room-temperature ferromagnetism has sparked intense interest for future miniature information storage devices. However, most 2D ferromagnetic materials have a low Curie temperature. Here, by using density functional theory, two rare-earth monolayers, the GdScSi monolayer and the GdScGe monolayer, were predicted, in which these two monolayers exhibit ferromagnetic orders with large magnetic moments of approximately 7 μ_B/Gd. Monte Carlo simulations predict Curie temperatures of approximately 470 K and 495 K for the 2D GdScSi monolayer and the GdScGe monolayer, respectively. The spin band calculations show that they are metal. In addition, these two monolayers exhibit dynamical, mechanical, and thermal stabilities. The combination of these novel magnetic properties makes these 2D ferromagnetic crystals promising candidates for high-efficiency spintronic applications.

KEYWORDS

high-temperature ferromagnetic materials, rare-earth films, two-dimensional material, density functional theory, large magnetic moments

1 Introduction

Since the successful synthesis of graphene, two-dimensional (2D) materials have attracted a great deal of attention [1–11]. First, the 'star material' graphene possesses excellent mechanical and electronic properties, but it has zero band gap. Then, a MoS_2 monolayer was successfully prepared, but it has relatively low electron and hole mobilities. In 2014, black phosphorus with a direct band gap and high carrier mobility was confirmed in an experiment, but it has poor stability when exposed to air. In addition, most synthesized 2D materials are non-magnetic, which has prevented their application in advanced spintronics. Although many efforts have been made in designing 2D ferromagnetism by introducing defects [12,13], strains [11,14–17], doping[18–22], and surface functionalization[19,23–26], it is still very challenging to obtain robust magnetism.

In 2017, an ultrathin ferromagnetic CrI_3 monolayer and a $CrGeTe_3$ bilayer were discovered [7,8], which disturb the limitation to the Mermin–Wagner (M–W) theorem[27]. The Mermin–Wagner theorem shows that the magnetic order is prohibited in the 2D isotropic Heisenberg model at finite temperatures. Recent studies have shown that magnetic anisotropy is the fundamental cause of 2D long-range magnetism [28–36]. Almost all synthetic and predicted 2D ferromagnetic materials have relatively low Curie temperatures (T_C) and small magnetic anisotropy energies (MAEs), for example, 45 K for the CrI_3 monolayer [8], 30 K for the $CrGeTe_3$ bilayer [7], 146 K for the CrSBr monolayer [37], 185 K for the ScCl monolayer [22], and 24 L K for the GdI_2 monolayer [38]. Therefore, it is highly desirable to search for new

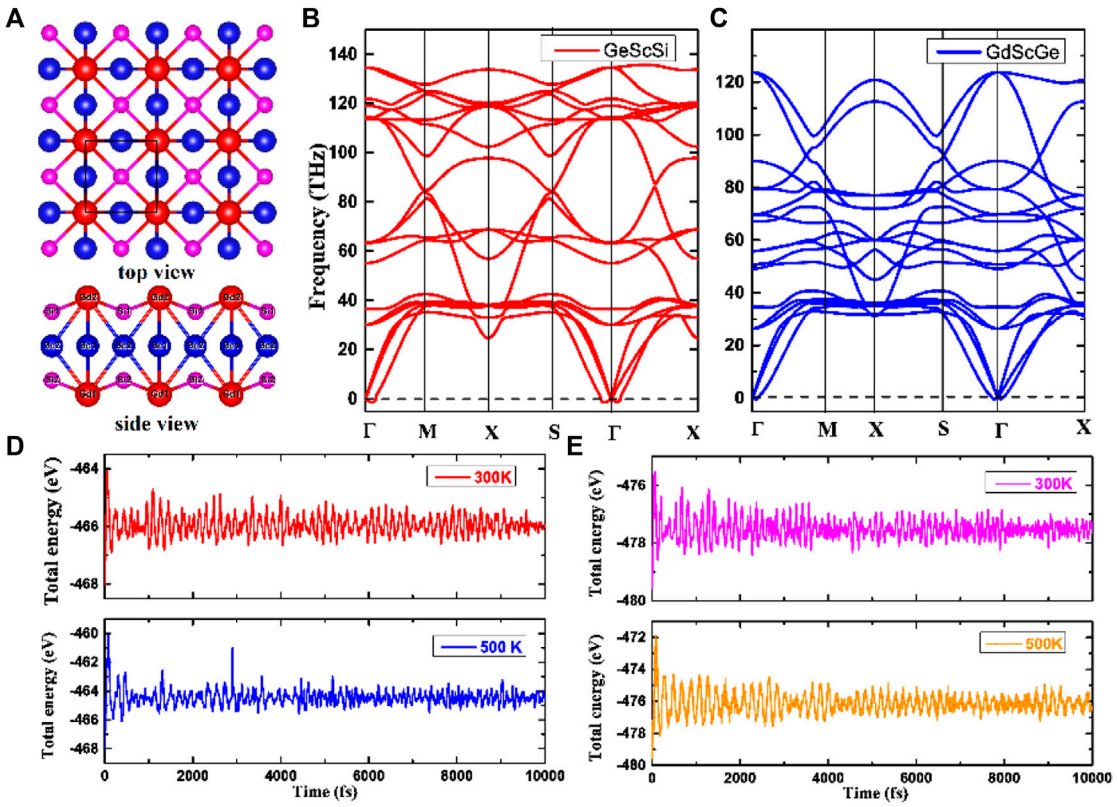

FIGURE 1
(A) Structures of GdScX (*X* = Si, Ge) monolayers. The Gd atom is located at 2 *g* (0, 0, 0.3633), Sc at 2e (1/2, 0, 1/2), and Si at 2 h (1/2, 1/2, 0.5971) for the GdScSi monolayer. The Gd atom is located at 2 *g* (0, 0, 0.3628), Sc at 2e (1/2, 0, 1/2), and Ge at 2 h (1/2, 1/2, 0.5988) for the GdScGe monolayer. **(B, C)** Phonon dispersion spectra of the GdScX (*X* = Si, Ge) monolayers. **(D, E)** Evolution of the total energy from the 10 ps AIMD simulations at 300 K and 500 K.

intrinsically 2D ferromagnetic materials with high T_C. Rare-earth elements usually have large magnetic moments and high T_C. With the increasing demand for device miniaturization, 2D rare-earth magnetic materials will be highly sought after for future spintronics. Gd-based compounds usually possess a long-range ferromagnetic order with a high T_C. We predicted the 2D GdI_2 monolayer to be a ferromagnetic semiconductor with a high T_C of 241 K and a large magnetization [38]. GdX_2 (*X* = Cl, Br, and I) monolayers were also ferromagnetic semiconductors and underwent spontaneous valley polarization [39,40]. $GdGe_2$ was predicted to be a ferromagnetic half-semiconductor with a large magnetic moment and an indirect band gap [41]. Gd_2C was predicted to be a time-reversal-symmetry-breaking Weyl semimetal phase [42]. The CeI_2 monolayer was predicted to be an intrinsic room-temperature ferrovalley semiconductor [43]. Dong et al., introduced the importance of 4f and 5d orbitals in 2D Gd halides [44,45]. Topological, nodal-line semimetals were also predicted in ferromagnetic rare-earth-metal monohalides [46]. As a result, 2D Gd-based compounds exhibit excellent ferromagnetism.

In this work, two rare-earth compounds of GdScX (*X* = Si and Ge) monolayers were predicted by using first-principles calculation. The result shows that they both are ferromagnetic with a large magnetization (7 μ_B/Gd). Monte Carlo simulations show that they possess a high Tc: 470 K for the GdScSi monolayer and 495 K for the GdScGe monolayer. Analysis of electronic band properties shows that they both are metals. In addition, their thermal, dynamical, and mechanical stabilities were confirmed by *ab initio* molecular dynamics, phonon dispersions, and elastic constants, respectively. Our results certainly boost the study of 2D Gd-based magnetism.

2 Computational methods

The optimized structures were simulated by density functional theory (DFT), as implemented in the Vienna *ab initio* simulation package (VASP) [47]. The ion–electron interaction was described by using the projector-augmented plane wave (PAW) approach [48], and the exchange and correlation interactions of the electrons were calculated using the Perdew–Burke–Ernzerhof (PBE) functional within the generalized gradient approximation (GGA) [49]. In addition, to consider the Coulomb and exchange interactions of *f* electrons, the GGA + U method was adopted with *U* = 6.6 eV, according to previous studies [50], and 500 eV was used as the energy cutoff of the plane wave. The convergence criteria for the energy and ionic force were set to 10^{-8} eV and 0.01 eV/Å, respectively. To avoid interaction between the layers, the vacuum length was set to 20 Å along the *z*-axis.

Density functional perturbation theory was used to calculate the phonon dispersions, as embedded in phonopy software [51]. The *ab initio* molecular dynamics (AIMD) simulations were carried out to evaluate the thermal stabilities of GdScX (X = Si, Ge) monolayers. At 300 K and 500 K, AIMD simulations were performed in the NVT

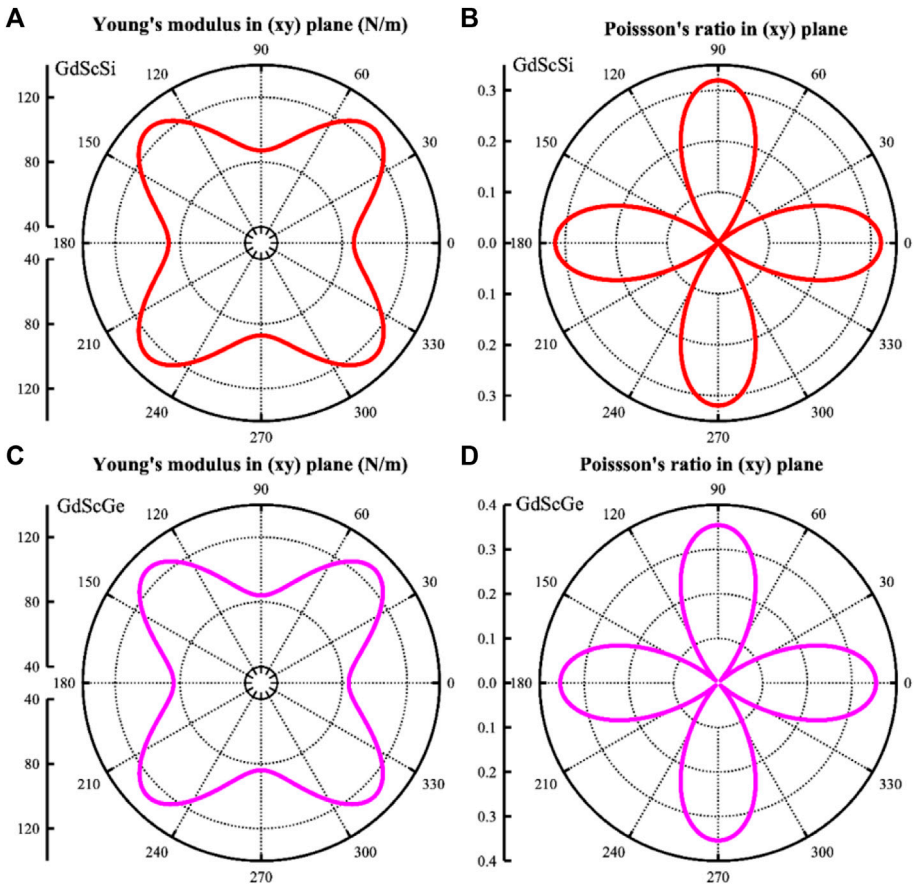

FIGURE 2
Calculated orientation-dependent **(A)** Poisson's ratios and **(B)** Young's moduli of the GdScSi monolayer **(A, B)** and the GdScGe **(C, D)** monolayer.

ensemble. The temperature was controlled by using the Nosé–Hoover method [52], and the simulation lasted for 10 *ps* with a time step of 1 *fs* at 300 K and 500 K. The orientation-dependent Young's modulus $E(\alpha)$ and Poisson's ratio $\nu(\alpha)$ were calculated as follows [30,33,53]:

$$E(\alpha) = \frac{C_{11}C_{22} - C_{12}^2}{C_{11}s^4 + C_{22}c^4 + \left(\frac{C_{11}C_{22}-C_{12}^2}{C_{44}} - 2C_{12}\right)c^2s^2}, \quad (1)$$

$$\nu(\alpha) = \frac{\left(C_{11} + C_{22} - \frac{C_{11}C_{12}-C_{12}^2}{C_{44}}\right)c^2s^2 - C_{12}\left(c^4 + s^4\right)}{C_{11}s^4 + C_{22}c^4 + \left(\frac{C_{11}C_{22}-C_{12}^2}{C_{44}} - 2C_{12}\right)c^2s^2}, \quad (2)$$

where $c = \cos\alpha$ and $s = \sin\alpha$.

3 Results and discussion

3.1 Structures and stabilities of GdScX monolayers

The structures present the P4/MMM group (No. 123) with a tetrahedron structure. The optimized lattice constants are a = 4.08 Å and b = 4.12 Å for GdScX (*X* = Si and Ge) monolayers as shown in Figure 1A; Figures 1B, C show the calculated phonon dispersion spectra of the GdScSi monolayer and the GdScGe monolayer, respectively. Notably, the absence of imaginary modes along the entire Brillouin zone indicates their dynamical stability. The corresponding fluctuations of the total potential energy for GdScX (*X* = Si and Ge) monolayers at 300 K and 500 K are shown in Figures 1D, E, respectively, which last for 10 *ps* in the *ab initio* molecular dynamics. The result shows that the average values of the total potential energy oscillate with a very narrow range, confirming their thermal stabilities. As a result, the GdScX (*X* = Si, Ge) monolayers are both dynamically and thermally stable at high-temperatures.

Mechanical stability is also necessary for materials. The elastic constants are $C_{11} = C_{22} = 97$ N/m, $C_{12} = 31$ N/m, and $C_{66} = 65$ N/m for the GdScSi monolayer, and $C_{11} = C_{22} = 96$ N/m, $C_{12} = 34$ N/m, and $C_{66} = 64$ N/m for the GdScGe monolayer. Their elastic constants meet the Born criteria for a tetrahedron 2D system ($C_{11} > 0$; $C_{44} > 0$; $C_{11} > |C_{12}|$; $C_{11} + 2C_{12} > 0$), indicating their good mechanical stabilities. According to Eqs 1, 2, Young's moduli and Poisson's ratios, as functions of the arbitrary direction α in the 2D polar representation curve, were also calculated (Figures 2, 3), where α is the angle relative to the positive *x*-direction in these monolayers. Figures 2A, C show that the Young's moduli for GdScX monolayers first increase to a maximum value of approximately 125 N/m at $\alpha = 45^\circ$ from $\alpha = 0^\circ$ (*x*-direction) and decrease to a minimum value of approximately 100 N/m at $\alpha = 90^\circ$ (*y*-direction). The maximum value (125 N/m) is comparable to that of a MoS_2 monolayer

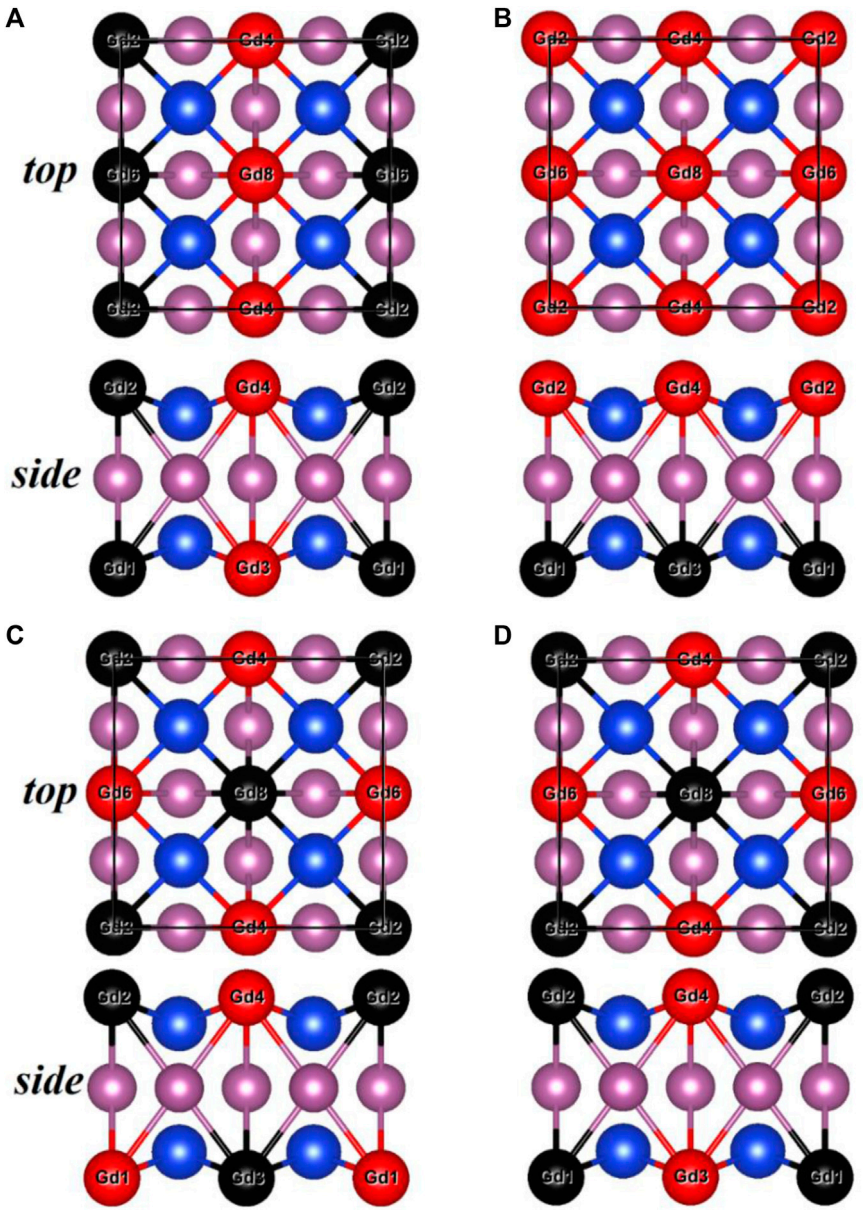

FIGURE 3
Top and side views of four AFM structures [**(A)**, AFM1; **(B)**, AFM2; **(C)**, AFM3; **(D)**, AFM4] for the GdScSi and GdScGe monolyers.

(123 N/m) [54]. Figures 2B, D show that the Poisson's ratios also strongly depend on the direction α. This shows their anisotropic mechanical properties.

3.2 Electronic band structures of GdScX monolayers

After confirming the stabilities of the GdScX monolayers, their magnetic ground states were investigated. One ferromagnetic (FM) state and four antiferromagnetic (AFM) states were considered, and the FM configuration is energetically lower than all the AFM orders (Figure 4), indicating that GdScX monolayers prefer FM coupling. Their spin band structures were also calculated by using the PBE + U method, which are shown in Figures 4A, C. The result shows that these two monolayers are metal, in which the spin up and spin down bands cross the Fermi level. Because of the relatively heavy element Gd, the spin–orbit coupling (SOC) interactions were also considered for the electronic band structures of GdScX monolayers (Figures 4C, D). The figures show that SOC has a negligible influence on the band structure.

3.3 MAEs of GdScX monolayers

Due to the M–W theorem, [27] no long-range FM state exists if a 2D material lacks magnetic anisotropy. Therefore, magnetic anisotropy, which can be scaled by MAE, is an important property in 2D ferromagnetic systems [55]. In addition, MAE is of importance

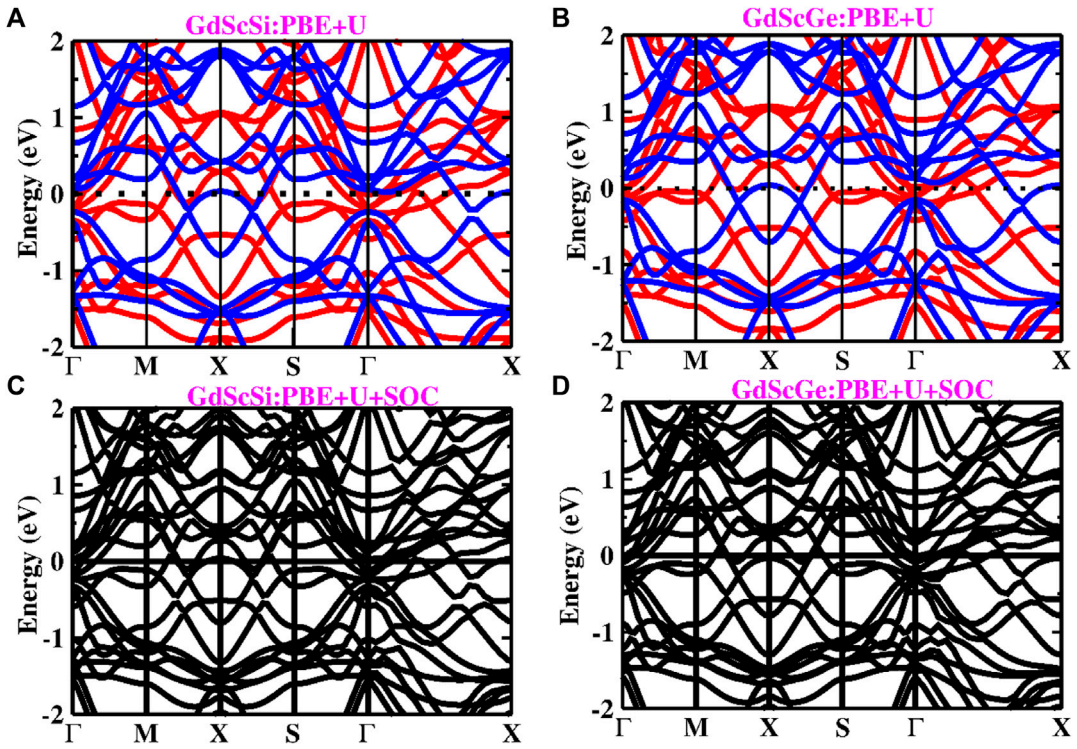

FIGURE 4
Band structures of the GdScSi monolayer **(A, B)** and GdScGe **(C, D)** monolayer determined using PBE + U and PBE + U + SOC methods.

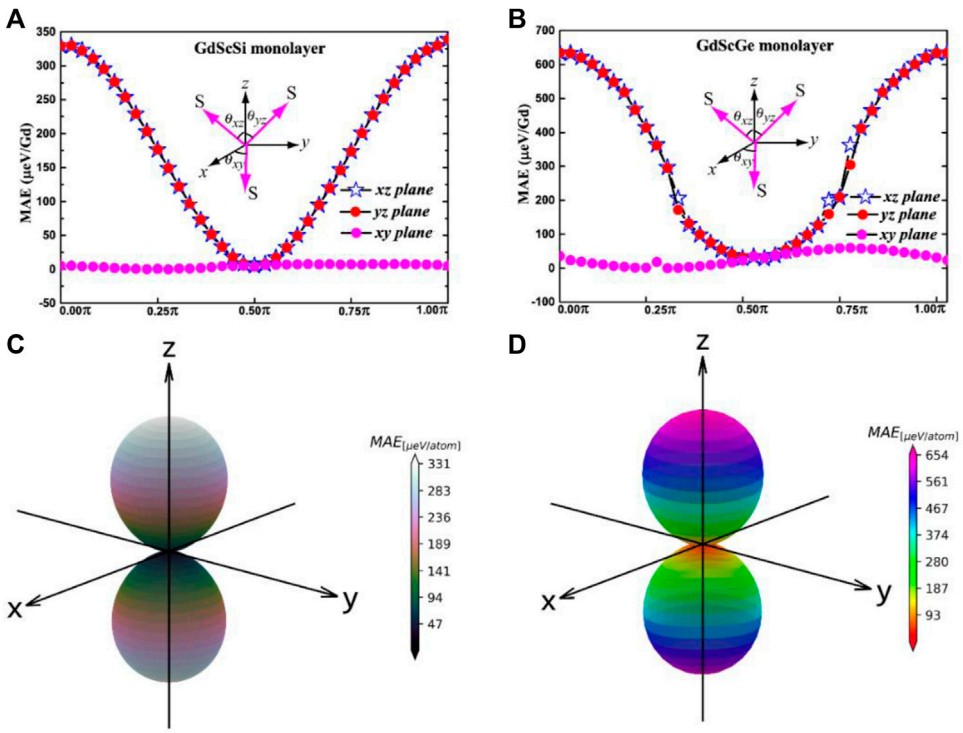

FIGURE 5
Angular dependence of the magnetic anisotropic energy (MAE) with the direction of magnetization lying on three different planes and the whole space for the GdScSi monolayer **(A, B)** and the GdScGe **(C, D)** monolayer.

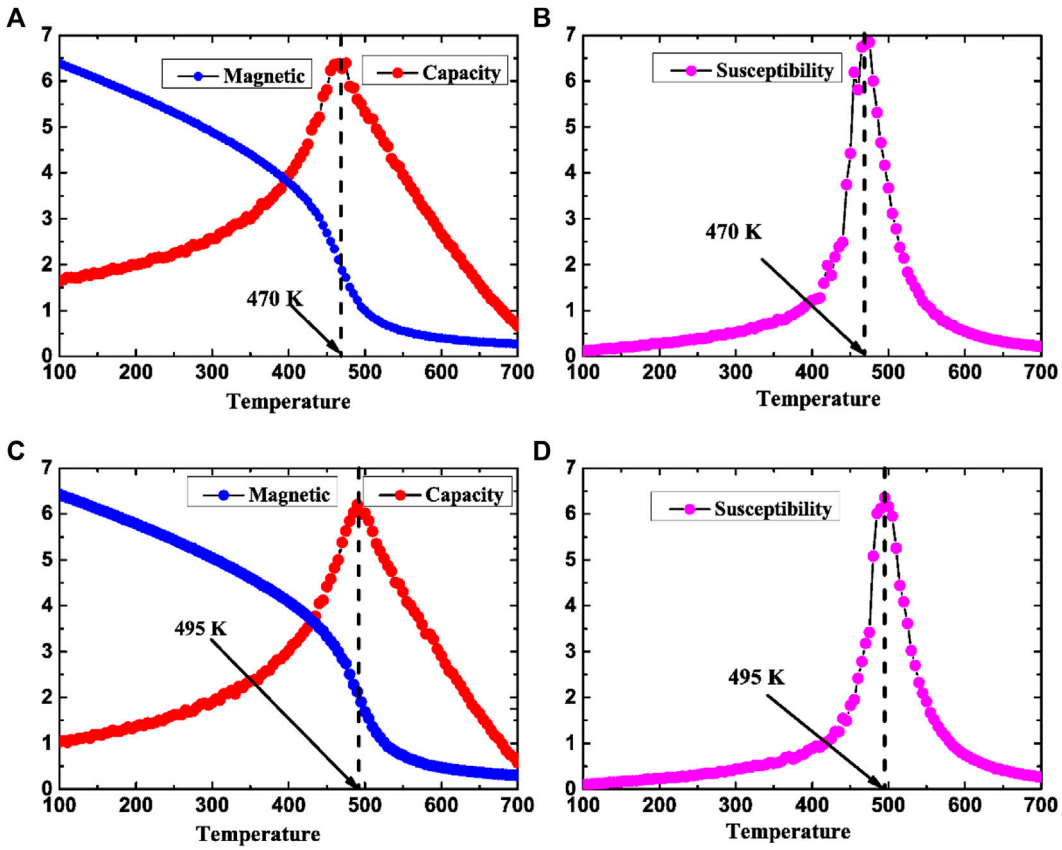

FIGURE 6
Magnetic moment (blue line), capacity (red), and magnetic susceptibility (magenta) as functions of temperature for the GdScSi monolayer **(A, B)** and the GdScGe **(C, D)** monolayer.

for the thermal stability of magnetic storage. SOC calculations were performed on the GdScX monolayers to obtain the values of MAE. Figures 5A, B show the MAEs of xy, yz, and xz planes for the GdScSi monolayer and the GdScGe monolayer, respectively. These figures clearly show that the MAE is almost a straight line in the xy plane, and that it strongly depends on the angular dependence of magnetization. In addition, the MAE of the xy plane is lower than that of the xz and yz planes, which indicates that these two monolayers belong to the family of 2D XY magnets. In other words, they possess an easy magnetization plane. The corresponding MAE through the whole space is also plotted in Figures 5C, D, which confirms again the strong magnetic anisotropy in these monolayers.

3.4 Curie temperatures of GdScX monolayers

Tc is an important parameter for ferromagnetic materials. To get an accurate estimate of the Tc for GdScX monolayers, Monte Carlo simulations based on the Heisenberg model were used. The Hamiltonian is defined as follows:

$$H = -\sum_{ij} J_1 S_i S_j - \sum_{ik} J_2 S_i S_k - \sum_{ik} J_3 S_i S_k - A S_i^Z S_i^Z,$$

where J_1, J_2, and J_3 are the first, second, and third nearest-neighboring exchange parameters, respectively. Using the energy differences of the FM and AFM orders, the exchange parameters J_1, J_2, and J_3 are calculated to be 4.82 meV (4.81 meV), −.0106 meV (−0.038 meV), and 0.163 meV (0.102 meV) for the GdScSi monolayer and the GdScGe monolayer, respectively. The magnetic moments, capacities, and susceptibilities of the GdScX monolayers with respect to temperature (Figure 6) show that the T_C of the GdScSi monolayer and the GdScGe monolayer are approximately 470 K and 495 K, respectively, which are significantly higher than room temperature.

4 Conclusion

In summary, two 2D intrinsic ferromagnetic rare-earth monolayers, the GdScSi monolayer and the GdScGe monolayer, were predicted using first-principles calculation. Interestingly, these 2D GdScX (X = Si, Ge) monolayers exhibit high Tc (470 K for the GdScSi monolayer and 495 K for the GdScGe monolayer), which are above room temperature. In addition, they possess excellent dynamical, thermal, and mechanical stabilities. Our findings on the intrinsic room-temperature ferromagnetic rare-earth material GdScX (X = Si, Ge) monolayers open up new possibilities for spintronic applications at the nanoscale.

Data availability statement

The original contributions presented in the study are included in the article/supplementary material; further inquiries can be directed to the corresponding authors.

Author contributions

RW: data curation, investigation, validation, and writing—original draft; PS: data curation, investigation, and validation; LH: data curation, investigation, and validation; QC: validation, writing—review and editing, and supervision; YZ: writing—review and editing, supervision, and funding acquisition.

Funding

This work was financially supported by the Scientific Research Key Project Fund of Henan Provincial Education Department (No. 23B140005) and the Innovative experimental training program for college students of Henan University (No. 20221011005).

Conflict of interest

The authors declare that the research was conducted in the absence of any commercial or financial relationships that could be construed as a potential conflict of interest.

Publisher's note

All claims expressed in this article are solely those of the authors and do not necessarily represent those of their affiliated organizations, or those of the publisher, the editors, and the reviewers. Any product that may be evaluated in this article, or claim that may be made by its manufacturer, is not guaranteed or endorsed by the publisher.

References

1. Novoselov KS, Geim AK, Morozov SV, Jiang D, Zhang Y, Dubonos SV, et al. Electric field effect in atomically thin carbon films. *science* (2004) 306:666–9. doi:10.1126/science.1102896

2. Novoselov KS, Jiang D, Schedin F, Booth TJ, Khotkevich VV, Morozov SV, et al. Two-dimensional atomic crystals. *P Natl Acad Sci USA* (2005) 102:10451–3. doi:10.1073/pnas.0502848102

3. Geim AK, Novoselov KS. The rise of graphene. *Nat Mater* (2007) 6:183–91. doi:10.1038/nmat1849

4. Mak KF, Lee C, Hone J, Shan J, Heinz TF. Atomically ThinMoS2: A new direct-gap semiconductor. *Phys Rev Lett* (2010) 105:136805. doi:10.1103/physrevlett.105.136805

5. Radisavljevic B, Radenovic A, Brivio J, Giacometti V, Kis A. Single-layer MoS2 transistors. *Nat Nanotechnol* (2011) 6:147–50. doi:10.1038/nnano.2010.279

6. Li L, Yu Y, Ye GJ, Ge Q, Ou X, Wu H, et al. Black phosphorus field-effect transistors. *Nat Nanotechnol* (2014) 9:372–7. doi:10.1038/nnano.2014.35

7. Gong C, Li L, Li Z, Ji H, Stern A, Xia Y, et al. Discovery of intrinsic ferromagnetism in two-dimensional van der Waals crystals. *Nature* (2017) 546:265–9. doi:10.1038/nature22060

8. Huang B, Clark G, Navarro-Moratalla E, Klein DR, Cheng R, Seyler KL, et al. Layer-dependent ferromagnetism in a van der Waals crystal down to the monolayer limit. *Nature* (2017) 546:270–3. doi:10.1038/nature22391

9. Liu S, Yin H, Singh DJ, Liu P-F. Ta4SiTe4: A possible one-dimensional topological insulator. *Phys Rev B* (2022) 105:195419. doi:10.1103/physrevb.105.195419

10. Liu P, Liu S, Jia M, Yin H, Zhang G, Ren F, et al. Strain-driven valley states and phase transitions in Janus VSiGeN4 monolayer. *Appl Phys Lett* (2022) 121:063103. doi:10.1063/5.0104477

11. Guo S-D, Mu W-Q, Wang J-H, Yang Y-X, Wang B, Ang Y-S. Strain effects on the topological and valley properties of the Janus monolayer VSiGeN4. *Phys Rev B* (2022) 106:064416. doi:10.1103/physrevb.106.064416

12. Wang R, Su Y, Yang G, Zhang J, Zhang S. Bipolar doping by intrinsic defects and magnetic phase instability in monolayer CrI3. *Chem Mater* (2020) 32:1545–52. doi:10.1021/acs.chemmater.9b04645

13. Lima Fernandes I, Bouhassoune M, Lounis S. Defect-implantation for the all-electrical detection of non-collinear spin-textures. *Nat Commun* (2020) 11:1602. doi:10.1038/s41467-020-15379-6

14. Chittari BL, Lee D, Banerjee N, Macdonald AH, Hwang E, Jung J. Carrier- and strain-tunable intrinsic magnetism in two-dimensional MAX3 transition metal chalcogenides. *Phys Rev B* (2020) 101:085415. doi:10.1103/physrevb.101.085415

15. Liu P, Zhang G, Yan Y, Jia G, Liu C, Wang B, et al. Strain-tunable phase transition and doping-induced magnetism in iodinene. *Appl Phys Lett* (2021) 119:102403. doi:10.1063/5.0063802

16. Yang K, Wang G, Liu L, Lu D, Wu H. Triaxial magnetic anisotropy in the two-dimensional ferromagnetic semiconductor CrSBr. *Phys Rev B* (2021) 104:144416. doi:10.1103/physrevb.104.144416

17. Cenker J, Sivakumar S, Xie K, Miller A, Thijssen P, Liu Z, et al. Reversible strain-induced magnetic phase transition in a van der Waals magnet. *Nat Nanotechnol* (2022) 17:256–61. doi:10.1038/s41565-021-01052-6

18. Gerber E, Yao Y, Arias TA, Kim EA. *Ab initio*<i/> mismatched interface theory of graphene on α−RuCl3: Doping and magnetism. *Phys Rev Lett* (2020) 124:106804. doi:10.1103/physrevlett.124.106804

19. Luo P, Zhuge F, Zhang Q, Chen Y, Lv L, Huang Y, et al. Doping engineering and functionalization of two-dimensional metal chalcogenides. *Nanoscale Horiz* (2019) 4:26–51. doi:10.1039/c8nh00150b

20. Park SY, Kim DS, Liu Y, Hwang J, Kim Y, Kim W, et al. Controlling the magnetic anisotropy of the van der Waals ferromagnet Fe3GeTe2 through hole doping. *Nano Lett* (2019) 20:95–100. doi:10.1021/acs.nanolett.9b03316

21. Wang C, Zhou X, Pan Y, Qiao J, Kong X, Kaun C-C, et al. Layer and doping tunable ferromagnetic order in two-dimensional CrS2 layers. *Phys Rev B* (2018) 97:245409. doi:10.1103/physrevb.97.245409

22. Wang B, Wu Q, Zhang Y, Guo Y, Zhang X, Zhou Q, et al. High Curie-temperature intrinsic ferromagnetism and hole doping-induced half-metallicity in two-dimensional scandium chlorine monolayers. *Nanoscale Horiz* (2018) 3:551–5. doi:10.1039/c8nh00101d

23. Hartman T, Sturala J, Luxa J, Sofer Z. Chemistry of germanene: Surface modification of germanane using alkyl halides. *ACS Nano* (2020) 14:7319–27. doi:10.1021/acsnano.0c02635

24. Jiang Z, Wang P, Jiang X, Zhao J. MBene (MnB): A new type of 2D metallic ferromagnet with high Curie temperature. *Nanoscale Horiz* (2018) 3:335–41. doi:10.1039/c7nh00197e

25. Zhao Y, Lin L, Zhou Q, Li Y, Yuan S, Chen Q, et al. Surface vacancy-induced switchable electric polarization and enhanced ferromagnetism in monolayer metal trihalides. *Nano Lett* (2018) 18:2943–9. doi:10.1021/acs.nanolett.8b00314

26. Song C, Xiao W, Li L, Lu Y, Jiang P, Li C, et al. Tunable band gap and enhanced ferromagnetism by surface adsorption in monolayer Cr2Ge2Te6. *Phys Rev B* (2019) 99:214435. doi:10.1103/physrevb.99.214435

27. Mermin ND, Wagner H. Absence of ferromagnetism or antiferromagnetism in one- or two-dimensional isotropic Heisenberg models. *Phys Rev Lett* (1966) 17:1133–6. doi:10.1103/physrevlett.17.1133

28. Wang B, Zhang Y, Ma L, Wu Q, Guo Y, Zhang X, et al. MnX (X = P, as) monolayers: A new type of two-dimensional intrinsic room temperature ferromagnetic half-metallic material with large magnetic anisotropy. *Nanoscale* (2019) 11:4204–9. doi:10.1039/c8nr09734h

29. Wu Q, Zhang Y, Zhou Q, Wang J, Zeng XC. Transition metal dihydride monolayers: A new family of two-dimensional ferromagnetic materials with intrinsic room-temperature half-metallicity. *J Phys Chem Lett* (2018) 9:4260–6. doi:10.1021/acs.jpclett.8b01976

30. Bai Y, Shi R, Wu Y, Wang B, Zhang X. Cr2XTe4 (X = Si, Ge) monolayers: A new type of two-dimensional high-TC ising ferromagnetic semiconductors with a large magnetic anisotropy. *J Phys Condens Matter* (2022) 34:384001. doi:10.1088/1361-648x/ac7f16

31. Zhang Y, Wu Y, Jin C, Ren F, Wang B. B2S3 monolayer: A two-dimensional direct-gap semiconductor with tunable band-gap and high carrier mobility. *Nanotechnology* (2021) 32:475709. doi:10.1088/1361-6528/ac1d07

32. Zhang Y, Wang B, Guo Y, Li Q, Wang J. A universal framework for metropolis Monte Carlo simulation of magnetic Curie temperature. *Comput Mater Sci* (2021) 197: 110638. doi:10.1016/j.commatsci.2021.110638

33. Wu Y, Sun W, Liu S, Wang B, Liu C, Yin H, et al. Ni(NCS)2 monolayer: A robust bipolar magnetic semiconductor. *Nanoscale* (2021) 13:16564–70. doi:10.1039/d1nr04816c

34. Gong C, Zhang X. Two-dimensional magnetic crystals and emergent heterostructure devices. *Science* (2019) 363:eaav4450. doi:10.1126/science.aav4450

35. Sun Y, Wang L, Li X, Yao X, Xu X, Guo T, et al. TM2B3 monolayers: Intrinsic anti-ferromagnetism and Dirac nodal line semimetal. *Appli Phys Lett* (2022) 121:183103. doi:10.1063/5.0113408

36. Yao X, Ji J, Lin Y, Sun Y, Wang L, He A, et al. TMB2C (TM= Ti, V): 2D transition metal borocarbide monolayer with intriguing electronic, magnetic and electrochemical properties. *Appli Sur Sci* (2022) 605:154692. doi:10.1016/j.apsusc.2022.154692

37. Lee K, Dismukes AH, Telford EJ, Wiscons RA, Wang J, Xu X, et al. Magnetic order and symmetry in the 2D semiconductor CrSBr. *Nano Lett* (2021) 21:3511–7. doi:10.1021/acs.nanolett.1c00219

38. Wang B, Zhang X, Zhang Y, Yuan S, Guo Y, Dong S, et al. Prediction of a two-dimensional high-TC f-electron ferromagnetic semiconductor. *Mater Horiz* (2020) 7: 1623–30. doi:10.1039/d0mh00183j

39. Liu W, Tong J, Deng L, Yang B, Xie G, Qin G, et al. Two-dimensional ferromagnetic semiconductors of rare-earth monolayer GdX2 (X = Cl, Br, I) with large perpendicular magnetic anisotropy and high Curie temperature. *Mater Today Phys* (2021) 21:100514. doi:10.1016/j.mtphys.2021.100514

40. Sheng K, Yuan HK, Wang ZY. Monolayer gadolinium halides, GdX(2) (X = F, Cl, Br): Intrinsic ferrovalley materials with spontaneous spin and valley polarizations. *Phys Chem Chem Phys* (2022) 24:3865–74. doi:10.1039/d1cp05097d

41. Wang Y, Cui Z, Zeng H, Wang Z, Zhang X, Shi J, et al. Tunable magnetic order in two-dimensional layered GdGe2. *J Mate Chem C* (2022) 10:1259–69. doi:10.1039/d1tc05350g

42. Liu S, Wang C, Liu L, Choi JH, Kim HJ, Jia Y, et al. Ferromagnetic Weyl fermions in two-dimensional layered electride Gd2C. *Phys Rev Lett* (2020) 125:187203. doi:10.1103/physrevlett.125.187203

43. Sheng K, Chen Q, Yuan H-K, Wang Z-Y. Monolayer CeI2: An intrinsic room-temperature ferrovalley semiconductor. *Phys Rev B* (2022) 105:075304. doi:10.1103/physrevb.105.075304

44. You H, Ding N, Chen J, Yao X, Dong S. Gadolinium halide monolayers: A fertile family of two-dimensional 4f magnets. *ACS Appl Electron Mater* (2022) 4:3168–76. doi:10.1021/acsaelm.2c00384

45. You HP, Chen J, Zhang JJ, Ding N, Zhang XW, Yao XY, et al. Structural reconstruction and anisotropic conductance in 4f-ferromagnetic monolayer. *Mater Today Phys* (2022) 24:100693. doi:10.1016/j.mtphys.2022.100693

46. Nie S, Weng H, Prinz FB. Topological nodal-line semimetals in ferromagnetic rare-earth-metal monohalides. *Phys Rev B* (2019) 99:035125. doi:10.1103/physrevb.99.035125

47. Kresse G, FurthmüLLER J. Efficient iterative schemes for *ab initio* total-energy calculations using a plane-wave basis set. *Phys Rev B* (1996) 54:11169–86. doi:10.1103/physrevb.54.11169

48. BlöCHL PE. Projector augmented-wave method. *Phys Rev B* (1994) 50:17953–79. doi:10.1103/physrevb.50.17953

49. Perdew JP, Burke K, Ernzerhof M. Generalized gradient approximation made simple. *Phys Rev Lett* (1996) 77:3865–8. doi:10.1103/physrevlett.77.3865

50. Jain A, Hautier G, Ong SP, Moore CJ, Fischer CC, Persson KA, et al. Formation enthalpies by mixing GGA and GGA+Ucalculations. *Phys Rev B* (2011) 84:045115. doi:10.1103/physrevb.84.045115

51. Togo A, Oba F, Tanaka I. First-principles calculations of the ferroelastic transition between rutile-type andCaCl2-typeSiO2at high pressures. *Phys Rev B* (2008) 78:134106. doi:10.1103/physrevb.78.134106

52. Martyna GJ, Klein ML, Tuckerman M. Nosé–Hoover chains: The canonical ensemble via continuous dynamics. *J Chem Phys* (1992) 97:2635–43. doi:10.1063/1.463940

53. Peng R, Ma Y, He Z, Huang B, Kou L, Dai Y. Single-Layer Ag2S: A two-dimensional bidirectional auxetic semiconductor. *Nano Lett* (2019) 19:1227–33. doi:10.1021/acs.nanolett.8b04761

54. Wang B, Wu Q, Zhang Y, Ma L, Wang J. Auxetic B4N monolayer: A promising 2D material with in-plane negative Poisson's ratio and large anisotropic mechanics. *ACS Appl Mater Inter* (2019) 11:33231–7. doi:10.1021/acsami.9b10472

55. Tu Y, Liu Q, Hou L, Shi P, Jia C, Su J, et al. Two-dimensional Cr-based ferromagnetic semiconductor: Theoretical simulations and design. *Front Phys* (2022) 10:1078202. doi:10.3389/fphy.2022.1078202

frontiers | Frontiers in Physics

TYPE Original Research
PUBLISHED 31 March 2023
DOI 10.3389/fphy.2023.1159064

OPEN ACCESS

EDITED BY
Guangzhao Wang,
Yangtze Normal University, China

REVIEWED BY
Longfei Yang,
Nanjing University of Science and Technology, China
Yi Luo,
Jiangsu Ocean University, China

*CORRESPONDENCE
Wencheng Tang,
101000185@seu.edu.cn

SPECIALTY SECTION
This article was submitted to Physical Chemistry and Chemical Physics, a section of the journal Frontiers in Physics

RECEIVED 05 February 2023
ACCEPTED 02 March 2023
PUBLISHED 31 March 2023

CITATION
Ren K, Leng B, Zhang C, Sun Q and Tang W (2023), The dynamic investigation of intrinsic vibration characteristics of a stranding machine by the finite element method.
Front. Phys. 11:1159064.
doi: 10.3389/fphy.2023.1159064

The dynamic investigation of intrinsic vibration characteristics of a stranding machine by the finite element method

Kai Ren[1], Bo Leng[1], Chang Zhang[2], Qingyun Sun[1] and Wencheng Tang[2]*

[1]School of Mechanical and Electronic Engineering, Nanjing Forestry University, Nanjing, China, [2]School of Mechanical Engineering, Southeast University, Nanjing, China

In response to the design problems of violent vibration and noise when a stranding machine is running at high speed, this project completed a motion simulation and vibration analysis based on the prototype FB-650C-2 bow-type stranding machine produced by Fuchuan Mechanical and Electrical Technology Co. The modal analysis was carried out in ANSYS to obtain the first eight orders of inherent frequencies and vibration patterns, combined with excitation force analysis to verify whether the rotating parts could avoid the resonant frequency when operating. Harmonic response analysis was carried out based on the modal state to calculate the steady-state forced vibration of the structure, and the variation curve of response value (usual deformation) with frequency and the cloud diagrams of stress distribution of each component at the rotation frequency were obtained. Suggestions for improving vibration and reducing noise were made based on the experimental and analytical results.

KEYWORDS

stranding machine, modal analysis, harmonic response analysis, vibration, structure

1 Introduction

Wire and cable play a very big role in promoting the economic development of China and are a basic auxiliary industry for various other industries [1]. With the rapid development of the economy and the popularity of electric vehicles, the power shortage has continued to expand, which also increases the need for wire and cable production in China. In the fabrication of wire and cable, the stranding equipment occupies a critical position [2–4] and the vibration and noise of the machine not only adversely affects the workers' environment but also contributes to metal fatigue that reduces the performance and life of the machine components [5–7]. In the past three decades, with the continuous updating of stranding technology, domestic stranding equipment has been greatly improved; nevertheless, there is still much work to be carried out before domestic stranding machines reach leading international levels.

For modal analysis and experimental modal analysis of stranding machines, the current trend is to combine finite element methods and experimental modal analysis techniques in an organic way [8–11]. To understand the dynamic performance of the stranding machine, modal analysis of each key component as well as the whole machine is required to obtain accurate modal parameters. However, since the modal analysis alone does not reflect the influence of external excitation on the instrument under normal operation, the harmonic

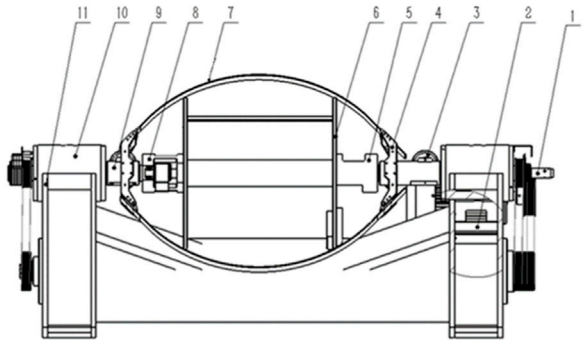

FIGURE 1
Schematic diagram of the structure of the bow-type stranding machine. (1) Incoming spindle, (2) motor base, (3) spindle guide wheel, (4) bow arm, (5) incoming disc bearing seat, (6) disc, (7) carbon fiber bow belt, (8) threading disc bearing seat, (9) outgoing spindle, (10) bearing box, and (11) base.

response analysis of the whole machine is very important [12, 13]. Modal analysis is an essential method for studying the vibration of components under working conditions. For example, the theoretical working of the buffer block was explored to investigate vibration and its effect on fatigue and performance, and the predictions showed good agreement with the experimental results [14]. Even at a nanometer scale, atomic vibration has a large influence on the overall performance of materials [15].

In this paper, a modal analysis and vibration test of the FB-650C-2 bow-type stranding machine produced by Fuchuan Mechanical and Electrical Co., Ltd were carried out to simulate the actual working condition of the machine and to determine the causes of vibration and noise. The results provide a theoretical basis for future research on ways to reduce vibration and noise without compromising productivity.

2 Materials and methods

2.1 Modal analysis theory

The bow-type stranding machine is generally used to produce small cross-section strands for making a cable. It operates at a high speed, up to 2800 rpm, and the output can reach 3–4.5 times that of a tubular stranding machine or frame stranding machine. However, the high speed of rotation of the spindle in the cantilever mechanism can easily generate strong vibration. Figure 1 provides a schematic diagram of the structure of the bow-type stranding machine.

In the bow-type stranding machine, the whole rotating part is driven by a motor, accelerated by a synchronous pulley, up to 2000 rpm. Multi-strand copper wire from the feed spindle passes through a small hole, guided by the spindle guide wheel, bow arm, and carbon fiber bow belt. The wire is then twisted together in a certain order and at a specific distance by the circular movement of the bow and the forward movement of the machine. Then, it is passed through the relay wheel, tensioning mechanism, wire arrangement mechanism, and is finally wound on the wire tray to complete the stranding. The wire feed spindle delivers the wire to the stranding machine, and the wire enters the system through the wire feed hole at the right end of the shaft. Supported by four bearings on the bearing box, this usually suffers from violent vibration and serious heat generation during the extended high-speed rotation. The outgoing spindle, whose operating principle is roughly the same as the incoming spindle, is structurally smaller in length but larger in radius, with improved cantilevering. An electromagnetic relay is provided at one end of the spindle so that the machine can stop in time if the wire is broken to prevent ineffective stranding. The FB-650C-2 bow-type stranding machine studied in this project has a high output with lower power usage compared with domestic and foreign machines of the same specification. However, according to feedback from the cable manufacturers, the violent vibration and noise generated during operation of the machine seriously hinder development of the enterprise.

The bow-type stranding machine is a linear system with multiple degrees of freedom, and based on the principles of mechanical vibration, the differential equation of motion for a deterministic system is:

$$[K]^e\{\delta\}^e + [M]^e\left\{\ddot{\delta}\right\}^e + [C]^e\left\{\dot{\delta}\right\} = \{F(t)\}^e \tag{1}$$

Eq. 1 is the basic equation of dynamic finite element analysis. In undamped modal analysis, the damping term in (1) can be neglected and a new differential equation of motion can be written with the external forces equal to zero, as shown in Eq. 2:

$$[M]\left\{\ddot{\delta}\right\} + [K]\{\delta\} = 0 \tag{2}$$

For a linear system, the solution of Eq. 2 takes the form:

$$\{\delta\} = \{\varnothing\}_i \cos \omega_i t \tag{3}$$

where $\{\varnothing\}_i$ is the ith order mode corresponding to the eigenvector of the vibration mode and ω_i is the ith order modal corresponding to the intrinsic frequency (in rad/s). Substituting Equation 3 into Equation 2, we obtain:

$$\left([K] - \omega_i^2[M]\right)\{\varnothing\}_i = 0 \tag{4}$$

When the structure vibrates freely, the amplitude $\{\varnothing\}_i$ cannot be 0. Therefore, from the aforementioned equation, the coefficient determinant of the characteristic equation is 0:

$$\det\left|\left([K] - \omega_i^2[M]\right)\right| = 0 \tag{5}$$

Eq. 5 represents a system of N algebraic equations about ω^2, and assuming that Equation 5 has no repeated roots, we obtain N mutually exclusive positive roots, ω_i. Arranging them in order of magnitude, we have $0 < \omega_1 < \omega_2 < \ldots < \omega_n$. ω_i is the ith order modal frequency, and the modal oscillation of the response is φ_i. For φ_i, where i ranges from 1 to N, we can transform the physical coordinates into modal coordinates [16–19].

2.2 Harmonic response analysis theory

In the stranding machine vibration test system, the external force generated in the operation of the system can be considered as a

TABLE 1 Summary of material parameters.

Serial number	Name	Material	Modulus of elasticity (GPa)	Poisson's ratio	Density (kg/m^3)
1	Incoming spindle	45 gauge steel	210	0.269	7850
2	Outgoing spindle	45 gauge steel	210	0.269	7850
3	Bow belt	Carbon fiber	0.21	0.307	1750
4	Cantilever	Q235-A	200	0.3	7800
5	Base	HT150	130	0.3	7210
6	Motor base plate	Q235-A	200	0.3	7800
7	Disc	Q235-A	200	0.3	7800
8	Steel belt guard	Q235-A	200	0.3	7800

periodic load. The structure is loaded with a simple harmonic force consistent with the operating conditions, and the load force is brought into Formula (1) as follows:

$$[M]\{\ddot{\delta}\} + [K]\{\delta\} + [C]\{\dot{\delta}\} = \{F^a\} \tag{6}$$

where $\{F^a\}$ is external load vector on the structure.

For a general mechanical model, the damping at each node in the structure is different, resulting in each unit node in the structure moving at the same frequency but in different phases. The displacement expression of the structure is:

$$\{\delta\} = \{\delta_{max} e^{i\phi}\} e^{i\Omega t} \tag{7}$$

where δ_{max} is the maximum displacement; i is the unit negative and Ω is the forced circular frequency (rad/s), $\Omega = 2\pi f$; f is the forced vibration frequency (week-s/unit time, in Hz); t is the time (s); and ϕ is the displacement phase shift (rad).

All the calculations in this work, including the fundamental harmonic response equations, were performed using ANSYS Workbench with three basic solution methods: the full method, the reduced method, and the modal superposition method [20–22]. The ANSYS Workbench is based on the finite element method (FEM), which is a numerical technique for solving approximate solutions of boundary value problems of partial differential equations. It uses the variational method to make the error function reach the minimum value and produce a stable solution. All the mesh types were hexahedrons in our calculations.

2.3 Generation of the finite element model of the stranding machine

The main working part of the stranding machine contains complex structures such as the incoming spindle and the outgoing spindle. First, the 3D model of the bow-shaped stranding machine was simplified, and a common node was used between the base side plate and the barrel, between the tendon plate and the bearing box, and between the supporting tendon and the barrel to convey the nodal forces and deformation displacement. The material parameters of the simplified model of the stranding machine are shown in Table 1.

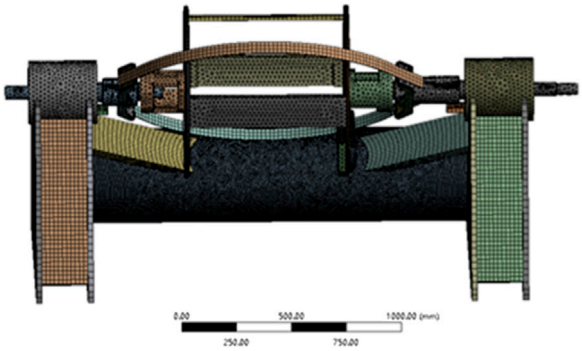

FIGURE 2
Stranding machine mesh division.

2.4 Body meshing

In our structural model, a quadrilateral mapping division was used to control the number of meshes by taking the length of the shortest line as the reference and to minimize the calculation volume within the specified range by ensuring the calculation error. To choose a suitable degree of refinement and avoid meshes with excessive angles and deformations, the base cylinder was locally encrypted at the connection with the side plate, and the mesh was divided as shown in Figure 2, while the main shaft was separately separated for meshing, as shown in Supplementary Figure S1 in Supporting Information.

3 Results and discussion

3.1 Modal analysis results

Using the finite element model of the bow-type stranding machine that was constructed, the solution mode was set to modal analysis, the block method was adopted, and the order was set to 8. After 40,530 s of calculation, the first eight steps of the machine's inherent frequencies and the corresponding vibration patterns were obtained. The inherent frequencies are shown in

TABLE 2 Stranding machine first eighth order inherent frequency.

Number of steps	Frequency (Hz)	Number of steps	Frequency (Hz)
1	10.982	5	37.455
2	12.668	6	49.733
3	32.283	7	50.603
4	32.336	8	52.812

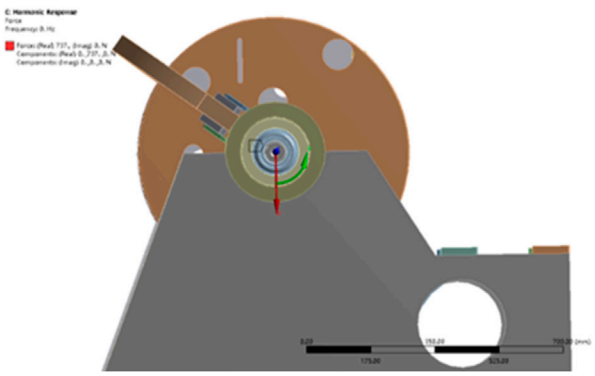

FIGURE 3
Schematic diagram of incentive addition.

Table 2, and the corresponding vibration patterns are shown in Supplementary Figure S2.

As can be seen in Table 2, the first eight orders of the stranding machine's inherent frequency are concentrated between 32 and 53 Hz. Under normal operation, the stranding machine rotating part has a rotation frequency of 33.33 Hz, between the fourth- and fifth-order inherent frequencies. When the machine is in normal operation, the rotation frequency is 1 Hz different from the fourth-order inherent frequency; the motor frequency is 50 Hz, located between the sixth and seventh orders, and the sixth-order inherent frequency difference is 0.27 Hz. Thus, in normal operation at the given excitation frequency, the machine is likely to resonate.

3.2 Harmonic response analysis results

In this paper, the harmonic response analysis of the structural model of the aforementioned bow-type stranding machine was carried out using the modal superposition method to find the displacement response of the stranding machine under the action of excitation frequencies from 0 to 100 Hz. With a motor power of 11 kW and a synchronous belt acceleration system transmission ratio $i = 1.37$, a motor speed of 1460 rad/min can be obtained from the motor with an incoming spindle and outgoing spindle input torque of 49.42 Nm. With a spindle drive pulley of 134 mm diameter, a torsional force of 737 N can be obtained by adding the shaft's circumferential direction as shown in Figure 3.

Figures 4A, B show the deformation curves of the carbon fiber bow belt in turn. It can be seen that the deformation curves of the carbon fiber bow belt in the vertical y and horizontal z directions are approximately the same. In the vertical direction, a sharp increase in deformation occurs at frequencies between 34 Hz and 38 Hz and reaches a maximum of 2.38 mm at 38 Hz; in the horizontal direction, the bow belt reaches a maximum deflection of 1.705 mm at 38 Hz. The stranding machine studied in this paper operates normally at 2000 rpm (33.33 Hz) with a motor frequency of 50 Hz. From the shape of the curve, it can be seen that the horizontal and vertical displacements are relatively large at this frequency, so resonance will occur at the normal operating frequency. Figures 4C, D show the deformation of the incoming spindle in the y and z directions. The shape of the curve is similar to that of the bow belt, the deformation of the incoming spindle in the y-direction reaches its maximum at 38 Hz and the deformation amplitude is up to 0.017 mm. Smaller peaks of deformation occur at both 32 Hz and 50 Hz (Fig. 4). Figures 4E, F show the related curves of deformation and frequency of the outgoing spindles, respectively. In the vertical direction, when the excitation frequency is 38 Hz, the deformation amplitude reaches 0.019 mm and 0.093 mm in the horizontal direction. The peak value is more prominent at 32 Hz in the horizontal direction, and it can be seen that there is a large deformation of the outgoing spindle in the horizontal direction, which is most obvious when the structure resonates. In summary, it can be seen that each component resonates at 32 Hz, 38 Hz, and 50 Hz and that the deformation reaches a maximum at 38 Hz; however, the rotation frequency of this model is 33.33 Hz under normal working conditions. To combine the peak point and modal analysis, we chose to solve the stress distribution of each component at 32 Hz.

Figure 5 shows that the stress distribution on the incoming and outgoing spindles is maximum at the incoming disc bearing installation at 30.123 MPa, with a minimum at the end of the shaft of 200 Pa. At the bearing connection in the bearing box, the shaft also has a large stress concentration, with a value of 10.041 MPa or more; thus, it is necessary to strengthen the bearing assembly to prevent the machine from resonating.

3.3 Vibration damping solutions

From the overall results of the vibration analysis to determine the maximum resonance point and identify the root cause of the axial vibration, we found that the resonance appears at the right end of the bearing seat position. The center of gravity of the bearing force deviates from the geometric center of the bearing seat. The projection point of the excitation force does not coincide with the collection center of the bearing seat so that the bearing seat

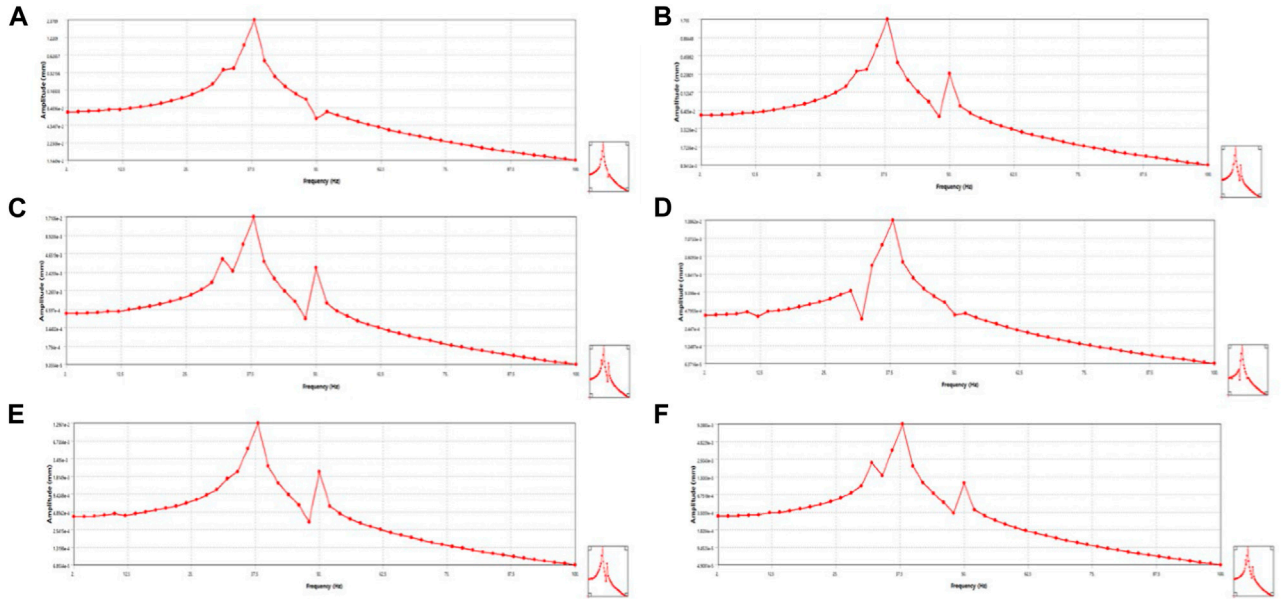

FIGURE 4
Calculated deformation curve of carbon fiber bow belt in **(A)** *y*-direction and **(B)** *z*-direction; deformation curve of incoming spindle in **(C)** *y*-direction and **(D)** *z*-direction; and deformation curve of outgoing spindle in **(E)** *y*-direction and **(F)** *z*-direction.

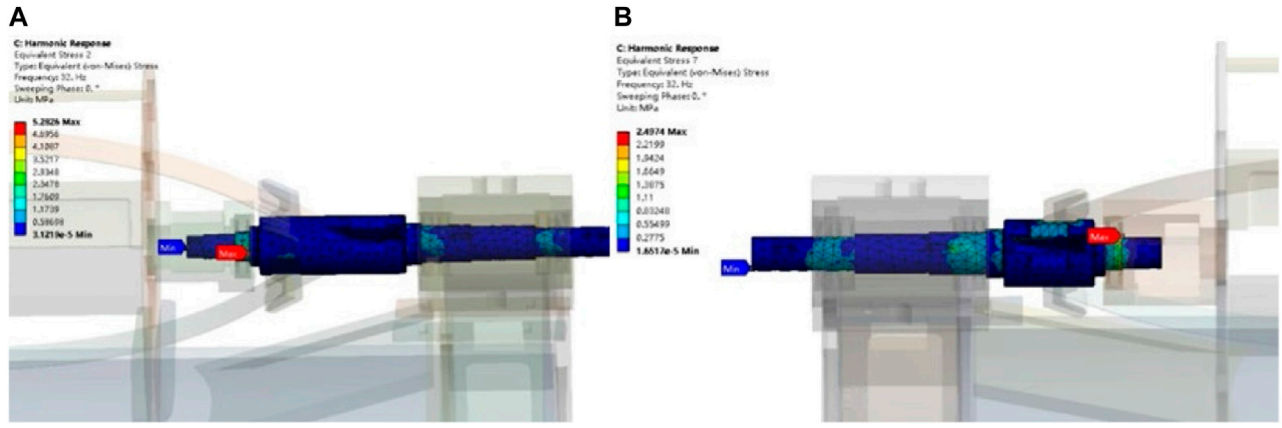

FIGURE 5
Stress nephogram of **(A)** incoming and **(B)** outgoing spindle with excitation force at 32 Hz.

connection stiffness is low and the bearing seat produces axial sway, although the base of the machine has minimal impact. The rotating assembly was separated, some simplification operations were carried out, and the simplified model is shown in Figure 6A.

From consideration of the structural vibration results, the resonant frequency could be avoided and vibration reduced by changing the wall thickness of the right end bearing seat. As the model has many holes on both sides of the disc, and the shortest distance of the holes from the bearing seat is 4 mm, the inner wall must also be thickened to avoid stress concentration in the holes on the incoming disc after thickening the outer wall. The clearance between the inner wall of the bearing seat and the rotor is 6.25 mm, but because of bearing wear, the wall thickness of the bearing seat cannot increase beyond the maximum range of 4 mm. The thickening position is shown in Figure 6B (yellow area of symmetric thickening). There is also a gap between the bearing seat and the rotor assembly, and over time, the bearing seat will wear and the gap will increase; thus, it is difficult to avoid the resonant frequency. Wear can be reduced to some extent by using a sleeve and improving the lubrication system. After considering all the aforementioned factors, the wall thickness of the bearing seat was tested by increasing it 1 mm and 3 mm, and reducing it by 1 mm, and analyzing the modalities of the spindle. The results of the analysis using the ANSYS Workbench are shown in Table 3.

From the results of modal analysis of the bearing seat improvement, it can be seen that reducing the bearing wall thickness by 1 mm did not have much effect on the modal values

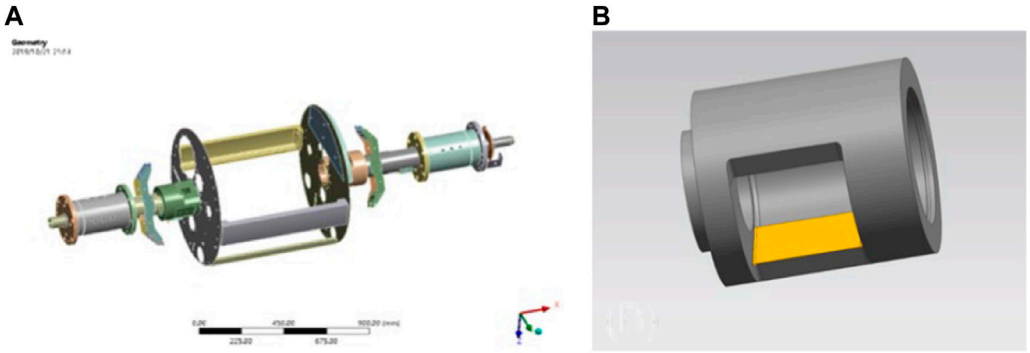

FIGURE 6
(A) Simplified spindle model and diagram of bearing thickening position and **(B)** the thickening position.

TABLE 3 First eighth order modal analysis of spindle (Hz).

Number of steps	Original state (before improvement)	Bearing wall reduction by 1 mm (after improvement)	Bearing seat thickened by 1 mm (after improvement)	Bearing seat thickened by 3 mm (after improvement)
1	60.55	60.29	62.55	62.84
2	68.09	68.06	70.31	70.37
3	74.53	74.38	77.62	77.79
4	82.87	82.650	85.94	86.26
5	103.36	102.88	104.22	104.44
6	103.31	103.23	105.49	105.51
7	105.59	105.58	108.60	108.70
8	112.86	112.74	114.13	114.22

of the spindle and did not achieve avoidance of the resonant frequency. However, an appropriate increase in the wall thickness of the bearing seat did effectively avoid the resonant frequency, thus achieving vibration and noise reduction. Considering the structural machining and the friction between bearing and shaft, the maximum wall thickness of the bearing seat should be increased by 3 mm. By doing that, the original resonant frequency can be avoided at all vibration orders, which provides a good reference point for optimization of the structure.

4 Conclusion

In this study, a modal analysis of a structural model of a stranding machine was carried out, and the first eight orders of inherent frequencies and vibration patterns were obtained. The analysis of the inherent frequencies and vibration patterns of each order showed that when the machine was in normal operation, the operating frequency was located between the fourth- and fifth-order inherent frequencies, and the motor frequency was located between the sixth and seventh orders; thus, the machine was likely to resonate under normal operation at the given excitation frequency. The modal analysis of the key elements of the rotating part shows that the first-order inherent frequency of the bow belt was close to the motor frequency (50 Hz) under normal operating conditions and is the part that causes the resonance. It was found that the response patterns of the incoming spindle, outgoing spindle, and carbon fiber bow belt were basically the same, and resonance would occur at 32 Hz, 38 Hz, and 50 Hz in each. By analyzing the stress nephogram of the structure under the effect of a 32 Hz excitation frequency, we found that the stress values of the incoming spindle and outgoing spindle were larger at the bearing installation and smaller at the shaft end. The stress value of the bow belt was greatest at the bolt fixation and least at both ends, which indicates the parts to be optimized. Through modal analysis, we found that increasing the wall thickness of the bearing seat could effectively avoid the resonant frequency and achieve vibration reduction, providing the basis for design improvements and structural optimization in the future.

Data availability statement

The raw data supporting the conclusions of this article will be made available by the authors, without undue reservation.

Author contributions

Conceptualization, BL; methodology, KR; software, WT; validation, KR; investigation, QS; writing—original draft preparation, BL, KR, and CZ; writing—review and editing, KR;

funding acquisition, KR. All authors have read and agreed to the submitted version of the manuscript.

Funding

The authors would like to thank the support of the Natural Science Foundation of Jiangsu (No. BK20220407).

Conflict of interest

The authors declare that the research was conducted in the absence of any commercial or financial relationships that could be construed as a potential conflict of interest.

Publisher's note

Supplementary material

The Supplementary Material for this article can be found online at: https://www.frontiersin.org/articles/10.3389/fphy.2023.1159064/full#supplementary-material

References

1. Lv Y, Sui Z, Li LJ. *Online monitoring system of cable based on microchip 51*. 2020 IEEE Conference on telecommunications, Optics and computer science (TOCS) (2020). p. 72–5.

2. Cui XZ, Yuan LL, Chen X, Chen B. Research on development of smart grid in regional electricity market. *AER-Advances Eng Res* (2015) 12:1419–22.

3. Yong JY, Ramachandaramurthy VK, Tan KM, Mithulananthan N A review on the state-of-the-art technologies of electric vehicle, its impacts and prospects. *Renew Sustain Energ Rev*. 2015, 49, 365–85. doi:10.1016/j.rser.2015.04.130

4. Li H, Liu L, Luo WB, Zhang XB, Luo MY. Research on optimization method of wire and cable extrusion control system. *Chin Automation Congress* (2019) 1703–8.

5. Chen YD, Tai YP, Xu J, Xu XM, Chen N. Vibration analysis of a 1-DOF system coupled with a nonlinear energy sink with a fractional order inerter. *Sensors*. 2022, 22, 6408. doi:10.3390/s22176408

6. Qin XD, Lu C, Wang Q, Li H, Gui LJ. Modal analysis of helical milling unit. *Adv Mater Res* (2012) 482-484:2454–9. doi:10.4028/www.scientific.net/amr.482-484.2454

7. Zhong YH, Sun GH. Experimental investigation of the vibration and noise and structural optimization of motor. *AER-Advances Eng Res* (2015) 27:2201–6.

8. Wu S, Su T, Wang Z. Research on optimization design of cantilever beam for cantilever crane based on improved GA. *Inf Technol J* (2013) 12(14):2883–7. doi:10.3923/itj.2013.2883.2887

9. Zhang JJ, Zhong JT, He LL, Gao RZ. Modal analysis of the cable-stayed space truss combining ANSYS and MSC.ADAMS. *Adv Mater Res* (2010) 121-122:832–7. doi:10.4028/www.scientific.net/amr.121-122.832

10. Nygards T, Berbyuk V. Multibody modeling and vibration dynamics analysis of washing machines. *Multibody Syst Dyn* (2012) 27(2):197–238. doi:10.1007/s11044-011-9292-5

11. Zhang ZP, Liu HW, He WT, Gao YH. Vibration modal analysis and structural optimal design of car rear-view mirror based on ANSYS. *Adv Mater Res*. 2012, 549, 848–51. doi:10.4028/www.scientific.net/amr.549.848

12. Zheng ZC, Gao Y, Liu N, Zhang KJ, Chen HO, Huang XB, et al. The harmonic response analysis of engine block based on modal analysis. *Appl Mech Mater* (2012) 138-139:246–51. doi:10.4028/www.scientific.net/amm.138-139.246

13. Arbain A, Mazlan AZA, Zawawi MH, Radzi MRM. Modal and harmonic response analyses of the kenyir dam intake section. *Lecture Notes Civil Eng* (2020) 53: 1055–63.

14. Kai R, WenCheng T, Jian W, Hui L, Fatigue reliability analysis and life bench test of buffer block in car damper, in: *IEEE international conference on engineering, technology and innovation (ICE/ITMC)*, IEEE, 2018, pp. 1–6.

15. Wang K, Ren K, Zhang D, Cheng Y, Zhang G. Phonon properties of biphenylene monolayer by first-principles calculations. *Appl Phys Lett* (2022) 121:042203. doi:10.1063/5.0102085

16. Zhou J, Xu LY, Zhang AQ, Hang XC. Finite element explicit dynamics simulation of motion and shedding of jujube fruits under forced vibration. *Comput Electron Agric* (2022) 198:107009. doi:10.1016/j.compag.2022.107009

17. Zhou J, Xu LY, Zhao JW, Hang XC, Zhou HP. Effective excitation conditions for the intense motion of the ginkgo seed-stem system during mechanical vibration harvesting. *Biosyst Eng* (2022) 215:239–48. doi:10.1016/j.biosystemseng.2022.01.014

18. Wang YB, Zhao CC, Li XL. Vibration and noise analysis of flux-modulation double stator electrical-excitation synchronous machine. *IEEE Trans Energ Convers* (2021) 36(4):3395–404. doi:10.1109/tec.2021.3084607

19. Wang JW, Xu CS, Xu YA, Wang JF, Zhou WQ, Wang Q, et al. Resonance analysis and vibration reduction optimization of agricultural machinery frame-taking vegetable precision seeder as an example. *Processes* (2021) 9(11):1979. doi:10.3390/pr9111979

20. Bhore CV, Andhare AB, Padole PM, Chavan CR, Gawande VS, Prashanth VS, et al. Harmonic response analysis of photovoltaic module using finite element method. *Machines, Mechanism and Robotics* (2022) 1219–26.

21. Kurbet R, Doddaswamy V, Amruth CM, Kerur MH, Ghanaraja S. Frequency response analysis of spur gear pair using FEA. *Mater Today- Proc* 2022, 52, 2327–38. doi:10.1016/j.matpr.2021.12.517

22. Patel J, Panchal D, Patel H, Pandya DH. Harmonic analysis of single point cutting tool with multi-layer passive damping (MLPD) technique. *Mater Today- Proc* (2021) 44: 625–8. doi:10.1016/j.matpr.2020.10.601

frontiers | Frontiers in Physics

TYPE Original Research
PUBLISHED 03 April 2023
DOI 10.3389/fphy.2023.1172989

OPEN ACCESS

EDITED BY
San-Dong Guo,
Xi'an University of Posts and Telecommunications, China

REVIEWED BY
Zhang Tian,
Sichuan Normal University, China
Jun Li,
Southwest University, China

*CORRESPONDENCE
Bing Lv,
lvbing@gznu.edu.cn

†These authors have contributed equally to this work and share first authorship

SPECIALTY SECTION
This article was submitted to Physical Chemistry and Chemical Physics, a section of the journal Frontiers in Physics

RECEIVED 24 February 2023
ACCEPTED 17 March 2023
PUBLISHED 03 April 2023

CITATION
Yin X, Zhou L, Wang Q, Liao Y and Lv B (2023), High thermoelectric performance of $TlInSe_3$ with ultra-low lattice thermal conductivity.
Front. Phys. 11:1172989.
doi: 10.3389/fphy.2023.1172989

High thermoelectric performance of $TlInSe_3$ with ultra-low lattice thermal conductivity

Xixi Yin[1,2†], Lang Zhou[1,2†], Qi Wang[1,2], Yangfang Liao[1,2] and Bing Lv[1,2*]

[1]School of Physics and Electronic Science, Guizhou Normal University, Guiyang, China, [2]Key Laboratory of Low Dimensional Condensed Matter Physics of Higher Educational Institution of Guizhou Province, Guizhou Normal University, Guiyang, China

Thermoelectric (TE) materials with an excellent thermoelectric figure of merit (*ZT*) provide an effective way to alleviate energy pressure and protect the environment. By applying the first-principles method, this paper makes a systematic study of the electronic and phonon transport properties of two-dimensional (2D) novel $TlInSe_3$ utilizing the Boltzmann transport theory (BTE). The calculation results reveal that 2D $TlInSe_3$ has an excellent power factor (0.81×10^{-2} W/mK^2) and ultra-low lattice thermal conductivity (0.46 W/mK) at 300 K. We find that the low phonon group velocity and strong anharmonicity are the main factors leading to the ultra-low lattice thermal conductivity of $TlInSe_3$. Meanwhile, by discussing the acoustic-optical scattering, we attribute low phonon group velocity and strong anharmonicity to the increase of scattering rates between acoustic mode and optical mode, which further suppresses the lattice thermal conductivity. In the analysis of electron and phonon transport properties, 2D $TlInSe_3$, as a novel TE material, exhibits a *ZT* value as high as 4.15 at 500 K. Our research results show that $TlInSe_3$ is a potential TE material, and the relevant analysis is significant in exploring new TE materials.

KEYWORDS

first-principles calculation, ultra-low lattice thermal conductivity, phonon anharmonicity, 2D $TlInSe_3$, high thermoelectric performance

1 Introduction

The thermoelectric effect enables the conversion of waste heat to electrical energy, while the conversion efficiency of thermoelectric (TE) materials can be evaluated by the thermoelectric figure of merit (*ZT*) value, demonstrated in the formula: $ZT = \frac{S^2\sigma T}{k_l + k_e}$, where *S* is the Seebeck coefficient; σ represents electrical conductivity,; k_l; k_e are lattice and electronic thermal conductivity, respectively [1]. In recent years, in order to increase the *ZT* value, researchers have employed phonon or electronic engineering techniques to reduce k_l or increase the power factor ($PF = S^2\sigma$) [2–4]. However, due to the mutual coupling between the TE parameters (S; σ; k_e) [5, 6], it achieved a negligible boost of *ZT* [7]. Therefore, a new material with intrinsic ultra-low k_l may offer exciting prospects to achieve higher *ZT* and thus realize its own potential utilization in TE fields.

Recent research has shown that thallium (Tl) compounds possess intrinsically ultra-low lattice thermal conductivity (k_l) [8–11]. For example, in Kurosaki's research, the binary and ternary thallium compounds demonstrated ultra-low k_l, in which the approximate value of k_l of $TlInTe_2$ is 0.5 W/mK at room temperature, almost one-third that of Bi_2Te_3 (~1.4 Wm/K) [8, 11, 12]. In addition, three-dimensional (3D) thallium selenide (TlSe) was synthesized

by Dutta, displaying its intrinsic ultra-low k_l of 0.62–0.4 W/mK [10]. However, the *ZT* of bulk Tl compounds (*ZT* value of $TlInTe_2$ is 1.78, Tl_9BiTe_6 is about 1, and Tl_4ZrTe_4 is only 0.16) is low compared to other TE materials because of the low power factor (*PF*) [7, 13–19]. Therefore, an ultra-low k_l and a high *PF* is necessary to obtain a high *ZT* value. Fortunately, two-dimensional (2D) materials can provide excellent *PF* values, especially 2D selenium compounds, such as Bi_2Se_3, Ag_2Se, SnSe, InSe, *etc.*, where the PF value of InSe is 0.049 W/mK^2 at 300 K, which is six times more than its bulk material [16, 20–24]. Moreover, experimentally synthesized Group III monolayer metal sulfides, such as In_2Se_3, GaSe, *etc.*, have been widely studied because of their distinctive TE properties [15, 20, 25, 26]. Considering that Tl is in the same group as Ga and In elements, and the high electronegativity and the lone pair electrons in Tl, it is feasible to design a new type of thallium chalcogenide semiconductor. Indeed, many ternary and binary thallium chalcogenides have been studied for their TE properties [9–11, 16, 27]. However, it is worth noting that previous investigations into Tl compounds were mainly laboratory work, while the inherent physical mechanism of the ultra-low k_l remains unclear. In addition, the ternary compounds formed by substituting the same group of elements have also attracted the attention of researchers due to their unique thermoelectric properties [28–32]. Therefore, inspired by these factors, it is urgent to design a novel 2D ternary compound material containing thallium, thallium congeners, and selenium elements to verify whether this can become a new and effective way to obtain materials with high thermoelectric performance.

This work employs the Boltzmann transport theory (BTE), taking $TlInSe_3$ as a typical example, to study its electron and phonon transport properties combined first principles. Our research shows that, at room temperature, $TlInSe_3$ has a *ZT* value of up to 4.15 at 500 K and an ultra-low k_l of 0.46 W/mK. In addition, we find that the lower phonon group velocity and the large phonon anharmonicity are the main factors leading to the extremely low k_l of $TlInSe_3$. Meanwhile, by discussing the phonon scattering channels, we find that the increase of the A + O/A→O ("A" is acoustic mode, "O" for optical mode) scattering channel leads to low phonon group velocity, which further suppresses the lattice thermal conductivity.

2 Computational and theoretical methods

We perform density functional theory (DFT) calculations using the QUANTUM ESPRESSO (QE) code [33, 34]. To obtain the relaxation structure and energy band structure, we use the kinetic energy of 70 Ry, the k-points of 16 × 16 × 1; and the energy convergence standard is 10^{-9} Ry, while the force convergence standard is 10^{-8} Ry. 16 × 16 × 1 k-points and 8 × 8×1 q-points are set to calculate phonon dispersion based on density functional perturbation theory (DFPT) [35, 36]. Meanwhile, based on periodic boundary conditions, in the 2D $TlInSe_3$ *z*-direction, we set a vacuum layer of 35 Å to prevent out-of-plane interactions. By working out the phonon Boltzmann transport equation, the k_l of 2D $TlInSe_3$ is obtained in the ShengBTE code [37]. A scaling parameter of 1.0 and a q-point grid of 60 × 60 × 1 are set. 3 × 3 × 1 supercell, together with a 4 × 4 × 1 k-mesh, is used to get the third-order interatomic force constants (IFCs). Supplementary Figure S1 shows the convergence of k_l with different cutoff radii of third-order, the k_l converges when the cutoff radius takes into account the 10th nearest neighbor. The electron transport properties considering electron-acoustic interactions are further studied by the PERTURBO software [38–41]. The maximum local Wannier function is built, through which the s, p orbitals of Tl atoms, the s, p orbitals of In atoms, and the p orbitals of Se atoms were selected by projecting the density of states.

In addition, to determine convergence, we tested the mobility using dense k-points, as demonstrated in Supplementary Figure S2A,B, which show that holes using 160 × 160 × 1 k-points and q-points can achieve convergence, while for electrons, it is necessary to use 480 × 480 × 1 k-points and a q point of 160 × 160 × 1 to ensure convergence.

In PERTURBO, $\tau_{nk} = \Gamma_{nk}^{-1}$ is employed to calculate the relaxation time, where Γ_{nk} is the scattering rate defined as

$$\Gamma_{nk} = \frac{1}{N_q}\sum_{m,vq} W_{nk,mk+q}^{vq}, \tag{1}$$

In the above equation, $W_{nk,mk+q}^{vq}$ is the scattering probability. The conductivity is computed as

$$\sigma_{\alpha\beta} = e^2 \int dE\left(-\frac{\partial f^0}{\partial E}\right)\sum_{\alpha\beta}(E), \tag{2}$$

where $\sum_{\alpha\beta}(E)$ is the transport distribution function at energy *E*, while *a* and *β* are Cartesian directions. The Seebeck coefficient (*S*) is computed from the $\sum_{\alpha\beta}(E)$ using the formula

$$S_{\alpha\beta} = \frac{e}{T}\int dE\left(-\partial f^0/\partial E\right)(E-\mu)\sum_{\alpha\beta}(E), \tag{3}$$

where μ is the chemical potential and *T* is the temperature. The electronic thermal conductivity is obtained by the formula

$$K_{\alpha\beta} = \frac{1}{T}\left\{\frac{\left(\int \sum_{\alpha\beta}(E)(E-\varepsilon_F)\left[-\frac{\partial f^0}{\partial E}\right]\right)^2 dE}{\int \sum_{\alpha\beta}(E)\left[-\frac{\partial f^0}{\partial E}\right]dE} - \int \sum_{\alpha\beta}(E)(E-\varepsilon_F)^2\left[-\frac{\partial f^0}{\partial E}\right]dE\right\}, \tag{4}$$

where ε_F is the Fermi level of a certain doping.

3 Results and discussions

The top and side drawings of the novel 2D $TlInSe_3$ are plotted in Figure 1A. The 2D $TlInSe_3$ is a hexagonal structure and is the P-3m1 space group. The optimized lattice constant is 4.17 Å, which is in agreement with the results in the literature [20, 42, 43]. Figure 1B shows the phonon spectrum of the novel 2D $TlInSe_3$. Since 2D $TlInSe_3$ has no imaginary frequency, its structure is dynamically stable. Meanwhile, we have tested the energy with different k-points, and compared the phonon dispersion by using the q points of 7 × 7 × 1 and 9 × 9 × 1, and found no difference, indicating that the phonon spectrum is convergent, as shown is Supplementary Figure S3A,B. At the same time, It is noteworthy that near the Γ point, the coupling exists between acoustic and optical phonons, suggesting that there is acoustic-optic scattering interaction. In addition, the

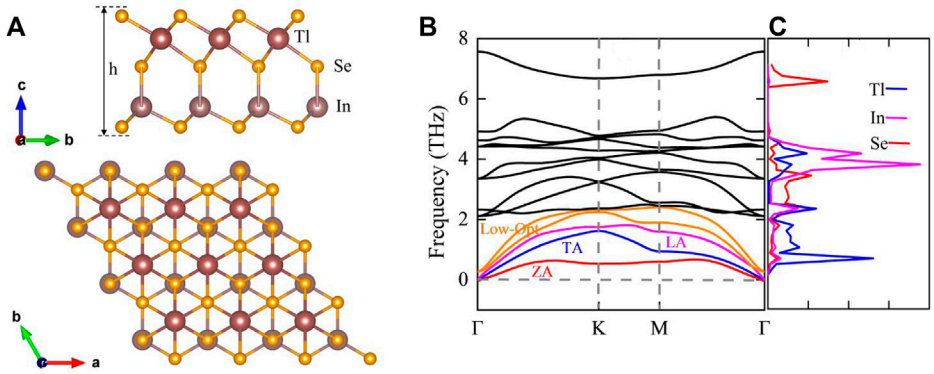

FIGURE 1
(A) Relaxed structure of 2D $TlInSe_3$, h is effective thickness, **(B)** phonon band plots where the red line represents the ZA mode, the blue line the TA mode, the magenta line the LA mode, the orange line the low-frequency optical mode, and the black line the high-frequency optical mode, and **(C)** DOS for 2D $TlInSe_3$.

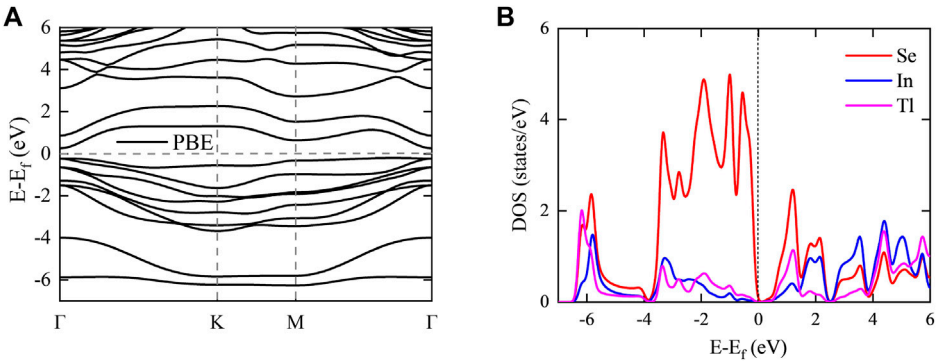

FIGURE 2
(A) The band structures without SOC, and **(B)** projected density of states of 2D $TlInSe_3$, respectively.

ZA and TA modes have an apparent concave, indicating the softening of acoustic phonons, which is beneficial to reduce the lattice thermal conductivity. In addition, the ZA mode is relatively smooth, suggesting that the ZA mode has a smaller phonon group velocity. The phonon density of states (DOS) of 2D $TlInSe_3$ is presented in Figure 1C. Since the atomic mass of thallium (Tl) is larger than that of In atoms and selenium (Se) atoms, it controls the acoustic branch and part of the low-frequency optical branch, while the optical branch is mostly dominated by the vibration of Indium (In) atoms.

Moreover, we study further the cohesive energy (E_{coh}) of $TlInSe_3$, whose formula is as follows:

$$E_{coh} = \frac{N_{Tl}E_{Tl} + N_{In}E_{In} + N_{Se}E_{Se} - E_{TlInSe3}}{N_{Tl} + N_{In} + N_{Se}}, \quad (1a)$$

Among them, N represents the number of atoms of each element, E is the energy of a single atom of each element, and $E_{TlInSe3}$ is the total energy of 2D $TlInSe_3$. The calculated E_{coh} is 0.32 eV, indicating that its structure is energetically favorable.

The *ab initio* molecular dynamics (AIMD) has been simulated using a 3 × 3 supercell at different temperatures with a time setting of 5 ps and a time step of 1 fs. Due to the small fluctuation in the total energy, the atomic structure exhibits only a small deviation from its equilibrium position at 300 and 500 K. These studies show that 2D $TlInSe_3$ is stable at 300 and 500 K. However, at 700 K, as shown in Supplementary Figure S4, there is significant distortion with large fluctuations in energy, and the $TlInSe_3$ monolayer is unstable.

Figure 2A shows the electronic energy bands of $TlInSe_3$ without considering the w-SOC (with the spin-orbit coupling). Meanwhile, it shows that the energy band structure of $TlInSe_3$ has a double degeneracy at the Γ point, which is beneficial for obtaining a high power factor. In Supplementary Figures S3A,B, the energy band structures considering the w-SOC and without considering the spin-orbit coupling are basically the same. Moreover, our study of the electronic band structure also reveals 2D $TlInSe_3$ as an indirect-band-gap material, which is also in line with previous studies [20, 43]. The projected density of states (DOS)in Figure 2B reveals that Se atoms are predominant near the valence band maximum (VBM), as

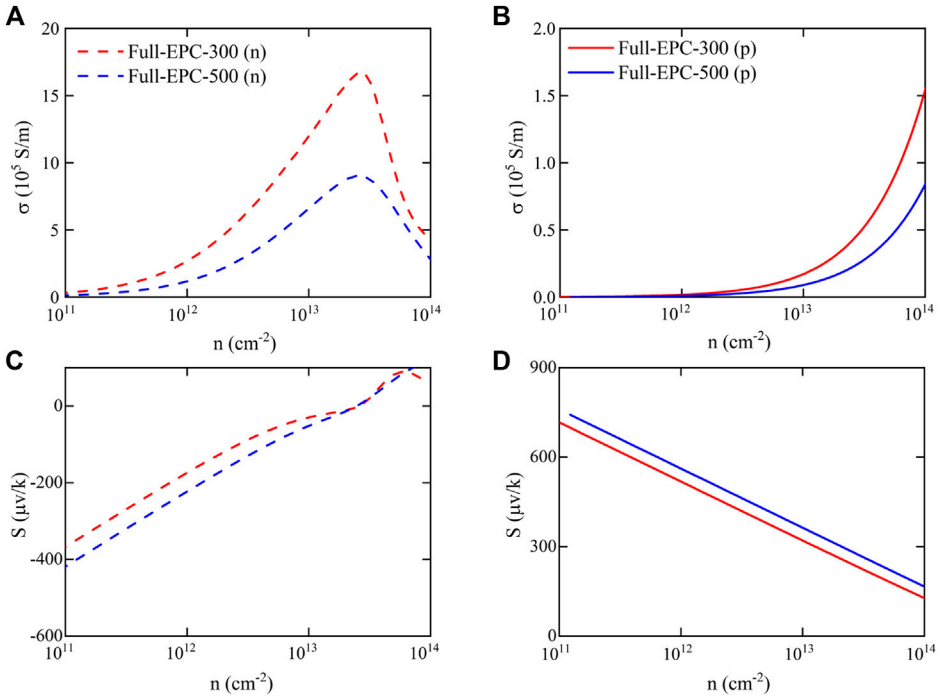

FIGURE 3
(A,B) Conductivity σ and **(C,D)** Seebeck coefficient S as a function of electrons and holes at 300, and 500 K, respectively.

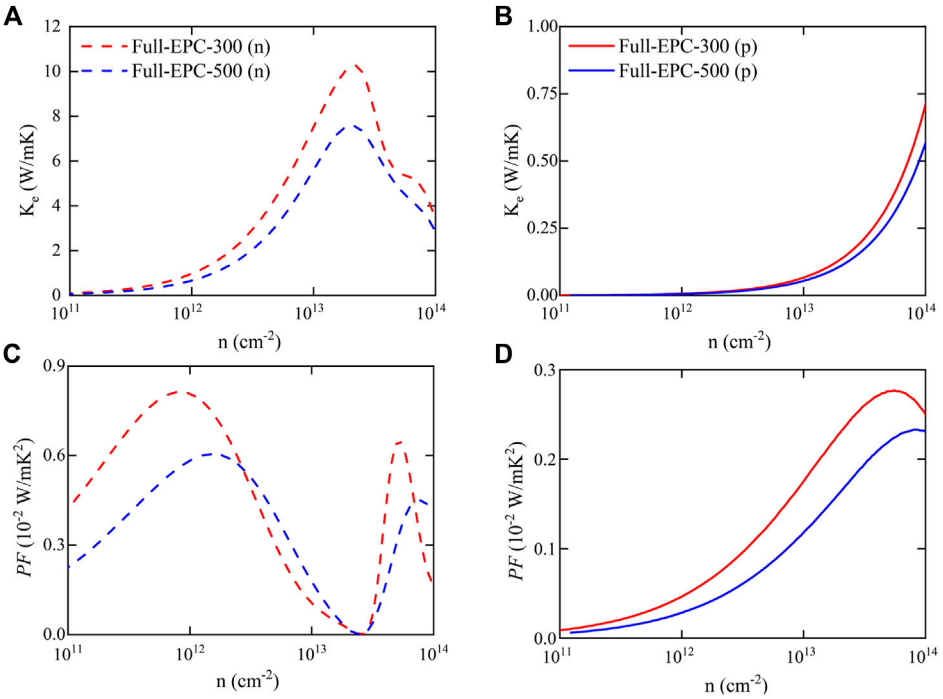

FIGURE 4
(A) and **(B)** are k_e, **(C)** and **(D)** are $S^2\sigma$ (PF) for 2D $TlInSe_3$ at 300 K and 500 K, respectively.

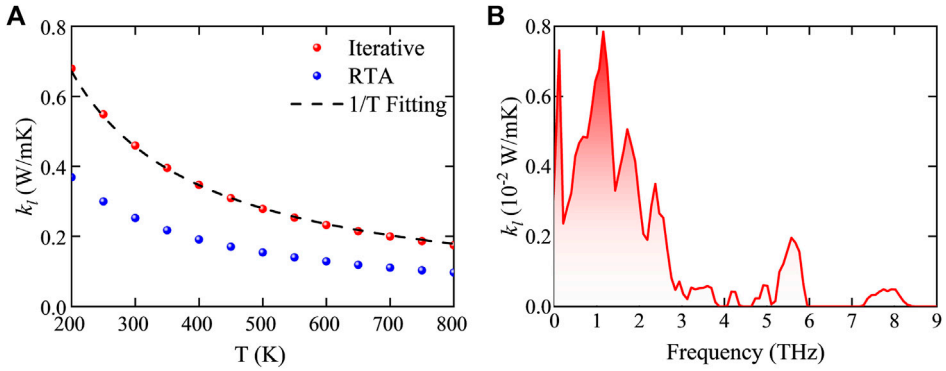

FIGURE 5
(A) The k_l of novel 2D $TlInSe_3$ at different temperatures. **(B)** Cumulative plot of k_l at different frequencies.

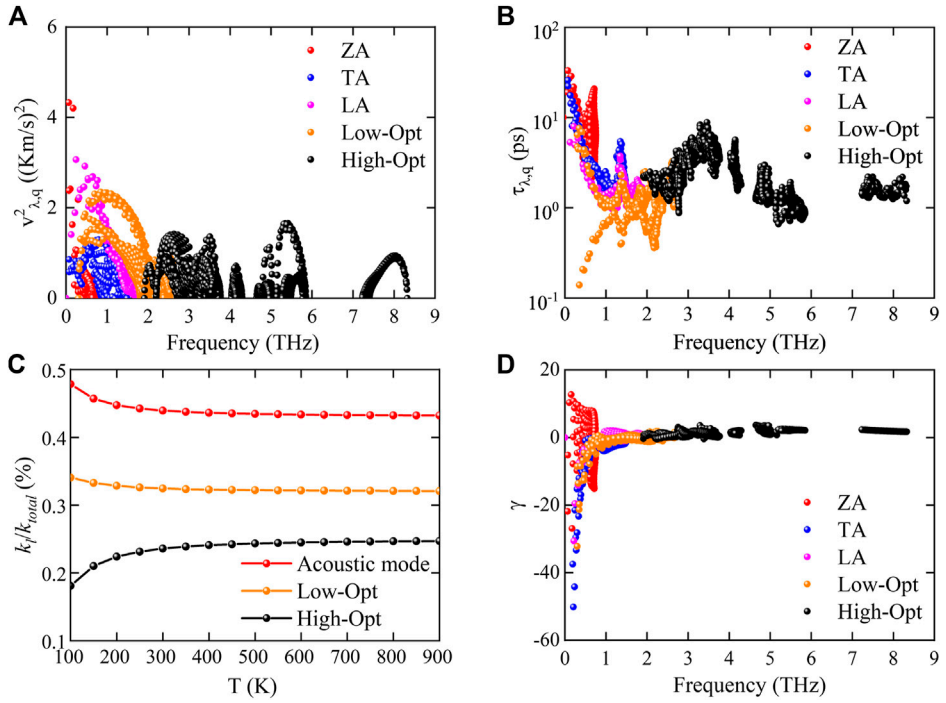

FIGURE 6
(A) The $v_{\lambda,q}$, **(B)** $\tau_{\lambda,q}$, **(C)** contribution of different phonon modes to the total k_l (percentage), **(D)** γ parameter of 2D $TlInSe_3$ at room temperature, respectively.

well as the conduction band minimum (CBM). Supplementary Figure S6 displays that the PBE band is in good agreement with those constructed by Wannier 90. Since performing QE and Perturbo software to calculate electron transport properties under electron-phonon interactions does not support HSE, therefore, we use the PBE function to carry out these calculations.

The electron transport coefficients of $TlInSe_3$ are obtained by solving the Boltzmann transport equation (BTE). The electron conductivity (σ) and the Seebeck coefficient (S) as a function of the carrier concentration from 300–500 K are demonstrated in Figures 3A–D. The calculation results clearly show that the σ of n-type doping is an order of magnitude, that is, higher than that of p-type doping, as presented in Figures 3A, B. For n-type doping, σ first arises and then goes down with carrier concentration because of the sudden drop in mobility at high concentrations when considering electron-phonon (el-ph) coupling, which was also reported in previous literature [44–47]. The $TlInSe_3$ monolayer shows a large S (absolute value) under n-type and p-type doping, as displayed in Figures 3C, D. Moreover, the S (absolute value) of 2D p-type $TlInSe_3$ is all higher than that of n-type due to the smoother

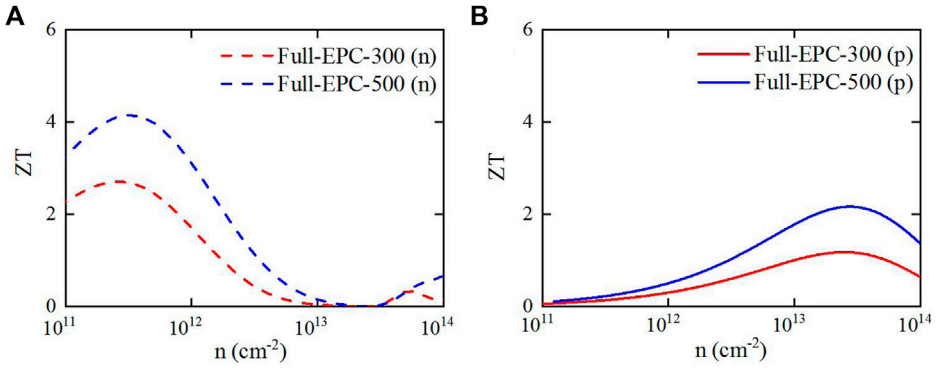

FIGURE 7
(A,B) The ZT values of novel 2D $TlInSe_3$ at 300, and 500 K, respectively.

VBM relative to CBM, resulting in a larger effective carrier mass. Moreover, according to the band convergence strategy, the band degeneracy can further enhance S ($S \propto m^* = N_V^{2/3} m_b^*$). Interestingly, at 300 K, 2D $TlInSe_3$ exhibits a high value of 704 μV/K, compared to TE materials with excellent properties such as PbTe (185 μV/K), Bi_2Te_3 (215 μV/K) and SnSe (~510 μV/K) [45].

Figure 4 displays the calculated results of the electronic thermal conductivity (k_e) and power factor ($S^2\sigma$) at 300 and 500 K, respectively. Since the k_e is dependent on the electrical conductivity, the k_e and σ have similar trends, as exhibited in Figures 4A, B. Furthermore, the calculation reveals that compared with p-type doping, n-type doping of 2D $TlInSe_3$ demonstrates higher conductivity, which leads to larger k_e of n-type. The power factor (*PF*) can be calculated *via* $PF = S^2\sigma$. Figures 4C, D shows the fluctuation of *PF* values of the p-type and n-type doping with the increase of the carrier concentration. Compared with p-type doping, the better conductivity and higher Seebeck coefficient of n-type doping lead to higher PF values. At 300 and 500 K, the maximum values of *PF* are 0.81/0.605 (10^{-2} W/mK^2) for n-type and 0.27/0.23 (10^{-2} W/mK^2) for p-type, respectively. Such a *PF* value is superior to conventional thermoelectric materials such as Bi_2Te_3 [48]and PbTe [49].

Phonons are considered chief carriers for heat transportation in semiconductors and insulators. Here, the k_l can be obtained by summing the contributions of all phonon modes λ and the wave vector q:

$$k_{\alpha\beta} = \frac{1}{V} \sum_{\lambda,q} C_{\lambda,q} \left(v_{\lambda,q}^{\alpha}\right)^2 \tau_{\lambda,q}^{\alpha}, \tag{2a}$$

where V stands for the primitive cell volume, $C_{\lambda,q}$ the specific heat capacity, $v_{\lambda,q}^{\alpha}$ the phonon group velocity, and $\tau_{\lambda,q}^{\alpha}$ the relaxation time. By summing up the radius of Se atoms on the outermost surface together with the van der Waals radius [50, 51], the effective thickness (h) is obtained as 11.2 Å. By employing the iterative method (ITA) and single-mode relaxation time approximation (RTA), and working out the Boltzmann transport equation, the k_l of 2D $TlInSe_3$ was calculated and displayed in Figure 5A. Apparently, at room temperature, the k_l value obtained by the RTA method is 0.25 W/mK, which is much lower than the k_l value (0.46 W/mK) obtained by the ITA method, because the RTA method is more suitable for relatively large samples or slow heating experiment conditions. Moreover, Umklapp scattering controls the heat transport of novel 2D $TlInSe_3$, because the k_l can be fitted well as the function $k_l \propto 1/T$ (the black dashed curve in Figure 5A). Meanwhile, Figure 5B shows that k_l is dominated by phonon and optical branches at a frequency below 3 THz, which indicates that acoustic and low-frequency optical modes contribute significantly to k_l. In addition, a large peak suddenly appears in the frequency range from 5 to 6 THz, indicating that the contribution of the high-frequency optical branch cannot be ignored.

According to Eq. 5, it can be known that the phonon group velocity ($v_{\lambda,q}^2$) and the phonon relaxation time ($\tau_{\lambda,q}$) are the key factors in determining k_l, and these main factors are shown in Figure 6. In Figure 6A, the acoustic phonons in the low-frequency range (frequency <2 THz) are usually considered as the main contributors to the lattice thermal conductivity because of the lager phonon group velocity of the LA mode and ZA mode. Meanwhile, Figure 6A also reveals that the Low-Opt branch possesses a non-negligible phonon group velocity, which indicates that its contribution to the lattice thermal conductivity cannot be ignored. Furthermore, In the frequency range from 5 to 6 THz, the phonon group velocity of the high-frequency optical branch is higher than that of the high-frequency optical branch in other frequency ranges, causing its contribution to the rise of k_l, which is in agreement with the data in Figure 5B. However, for the acoustic branch and the low-frequency optical branch, the phonon group velocity differs little in the low-frequency range (frequency <2 THz), and the main advantage of the acoustic branch comes from $\tau_{\lambda,q}$, as shown in Figure 6B. Figure 6B shows the $\tau_{\lambda,q}$ as a function of frequency. Compared to the optical branch, the acoustic mode clearly dominates. It is worth noting that the rapidly decreasing $\tau_{\lambda,q}$ of the Low-Opt and acoustic branch is beneficial to further reduce the k_l. The total contributions of acoustic modes (ZA, TA, and LA), the Low-Opt branch, and the High-Opt branch to the k_l at different temperatures are shown in Figure 6C. Notably, each phonon mode changes very little, particularly after 300 K, which can be considered as being independent of temperature. The results show that the contribution ratio does not change with temperature after 300 K due to the small change in heat capacity and phonon lifetime with

the increase of temperature. The proportion of the total contribution of acoustic modes to the k_l is about 45% at 300 K, compared to 32% for Low-Opt phonons. Moreover, we also analyze the Güneisen (γ) parameter because it can provide important information about heat transport, which enables the measurement of the anharmonicity of phonons. Figure 6D shows the relationship between the frequency and the γ parameter, with γ ranging from −55 to 10. Such a large value of γ (maximum γ (absolute value) of 55) reflects the strong anharmonicity of phonons, indicating the existence of strong phonon-phonon scattering. Significantly, in the low-frequency range, the acoustic and optical phonons are mixed, dedicating strong acoustic-optic scattering which is consistent with Figure 1B. Based on the above analysis, the strong phonon anharmonicity, especially the ZA and TA modes, as well as the strong acoustic-optic scattering, lead to ultra-low intrinsic lattice thermal conductivity [52, 53].

According to the phonon and electron transport properties, the thermoelectric conversion efficiency (*ZT*) of the new 2D $TlInSe_3$ is obtained, as plotted in Figure 7. In Figure 7A, n-type $TlInSe_3$ has an outstanding ZT value of up to 4.15 at 500 K. The *ZT* values of $TlInSe_3$ are more advantageous than the related materials reported from the literature, such as In_2Se_3 (2.8), TlSe (1.94), and $TlInTe_2$ (2.6). Compared with the ZT of p-type $TlInSe_3$ at 500 K (2.16), the ZT of n-type $TlInSe_3$ at 300 K is more promising. Such high thermoelectric conversion efficiency benefits from ultra-low k_l and outstanding *PF*. Meanwhile, this research demonstrated the novel 2D $TlInSe_3$ as a promising n-type TE material, further expanding the family of TE materials.

4 Conclusion

Overall, we investigate the TE performance of novel two-dimensional $TlInSe_3$ by the first-principles method. By working out the BTE (Boltzmann transport equation), the study reveals that the 2D $TlInSe_3$ possesses an ultra-low k_l of 0.46 W/mK at 300 K, and the analysis of the energy bands suggests that the high Seebeck coefficient is derived from the smooth energy band and band degeneracy. In addition, the performance of the phonon group velocity, phonon anharmonicity, and scattering channel shows that the ultra-low k_l of the novel 2D $TlInSe_3$ is attributed to the stronger phonon anharmonicity, lower phonon group velocity, and the scattering interaction of ZA + O→O, TA + O→O, and LA + O→O process. In addition, the weak Tl-Se chemical bond is also one of the reasons for the low phonon group velocity. Based on studies of electron and phonon transport properties, the ZT values of 2D TlInSe3 are as high as 4.15 at 500 K for n-type and 2.16 for p-type, which suggests that 2D TlInSe3 is a promising thermoelectric material.

Data availability statement

The original contributions presented in the study are included in the article/Supplementary Material, further inquiries can be directed to the corresponding author.

Author contributions

XY: calculation, writing—original draft, visualization. LZ: calculation, writing—original draft, visualization. QW: formal analysis, suggestion, visualization. YL: suggestion, visualization. BL: writing—review and editing, suggestion, software, visualization. All authors contributed to the article and approved the submitted version.

Funding

This work is supported by the Guizhou Provincial Science and Technology Foundation [Grant no. (2019) 1225].

Conflict of interest

The authors declare that the research was conducted in the absence of any commercial or financial relationships that could be construed as a potential conflict of interest.

Publisher's note

All claims expressed in this article are solely those of the authors and do not necessarily represent those of their affiliated organizations, or those of the publisher, the editors and the reviewers. Any product that may be evaluated in this article, or claim that may be made by its manufacturer, is not guaranteed or endorsed by the publisher.

Supplementary material

The Supplementary Material for this article can be found online at: https://www.frontiersin.org/articles/10.3389/fphy.2023.1172989/full#supplementary-material

References

1. Gao Z, Wang J-S. Thermoelectric penta-silicene with a high room-temperature figure of merit. *ACS Appl Mater.Interfaces* (2020) 12:14298–307. doi:10.1021/acsami.9b21076

2. Pei Y, Wang H, Snyder GJ. Band engineering of thermoelectric materials. *Adv Mater* (2012) 24:6125–35. doi:10.1002/adma.201202919

3. Kim J, Shim W, Lee W Bismuth nanowire thermoelectrics. *J Mater Chem C* (2015) 3(46), 11999–2013. doi:10.1039/c5tc02886h

4. Pei Y, Shi X, LaLonde A, Wang H, Chen L, Snyder GJ. Convergence of electronic bands for high performance bulk thermoelectrics. *Nature* (2011) 66-69:66–9. doi:10.1038/nature09996

5. Gao Z, Tao F, Ren J Unusually low thermal conductivity of atomically thin 2D tellurium. *Nanoscale* (2018) 10, 12997–3003. doi:10.1039/c8nr01649f

6. Madsen GK, Singh DJ. BoltzTraP. A code for calculating band-structure dependent quantities. *Comput Phys Commun* (2006) 175:67–71. doi:10.1016/j.cpc.2006.03.007

7. Ding G, He J, Cheng Z, Wang X, Li S. Low lattice thermal conductivity and promising thermoelectric figure of merit of zintl type $TlInTe_2$. *J Mater Chem C* (2018) 6: 13269–74. doi:10.1039/c8tc03492c

8. Matsumoto H, Kurosaki K, Muta H, Yamanaka S. Systematic investigation of the thermoelectric properties of $TlMTe_2$ (M= Ga, in, or Tl). *J Appl Phys* (2008) 104:073705. doi:10.1063/1.2987471

9. Jana MK, Pal K, Warankar A, Mandal P, Waghmare UV, Biswas K. Intrinsic rattler-induced low thermal conductivity in zintl type $TlInTe_2$. *J Am Chem Soc* (2017) 139: 4350–3. doi:10.1021/jacs.7b01434

10. Dutta M, Matteppanavar S, Prasad MV, Pandey J, Warankar A, Mandal P, Soni A, Waghmare UV, Biswas K. Ultralow thermal conductivity in chain-like TlSe due to inherent Tl+ rattling. *J Am Chem Soc* (2019) 141:20293–9. doi:10.1021/jacs.9b10551

11. Qiu B, Ruan X. Thermal conductivity prediction and analysis of few-quintuple Bi_2Te_3 thin films: A molecular dynamics study. *Appl Phys Lett* (2010) 97:183107. doi:10.1063/1.3514252

12. Kurosaki K, Yamanaka S. Low-thermal-conductivity group 13 chalcogenides as high-efficiency thermoelectric materials. *Wiley Online Libr* (2013) 210:82–8. doi:10.1002/pssa.201228680

13. Guo Q, Chan M, Kuropatwa B, Kleinke H. Enhanced thermoelectric properties of variants of Tl_9SbTe_6 and Tl_9BiTe_6. *Chem Mater* (2013) 25:4097–104. doi:10.1021/cm402593f

14. Sankar CR, Bangarigadu-Sanasy S, Assoud A, Kleinke H. Syntheses, crystal structures and thermoelectric properties of two new thallium tellurides: Tl_4ZrTe_4 and Tl_4HfTe_4. *J Mater Chem* (2010) 20:7485–90. doi:10.1039/c0jm01363c

15. Patel A, Singh D, Sonvane Y, Thakor P, Ahuja R. High thermoelectric performance in two-dimensional janus monolayer material WS-X (X= Se and Te). *ACS Appl Mater Inter* (2020) 12:46212–9. doi:10.1021/acsami.0c13960

16. Minhas H, Das S, Pathak B. Ultralow thermal conductivity and high thermoelectric performance of γ-GeSe: Effects of dimensionality and thickness. *ACS Appl Energ Mater* (2022) 5:9914–28. doi:10.1021/acsaem.2c01600

17. Ning S, Huang S, Zhang T, Zhang Z, Qi N, Chen Z. Two-dimensional β-PdX_2 (X= S, Se, and Te) monolayers with promising potential for thermoelectric applications. *J Phys Chem C* (2022) 126:17885–93. doi:10.1021/acs.jpcc.2c06186

18. Majumdar A, Chowdhury S, Ahuja R. Drastic reduction of thermal conductivity in hexagonal AX (A= Ga, in and Tl, X= S, Se and Te) monolayers due to alternative atomic configuration. *Nano Energy* (2021) 88:106248. doi:10.1016/j.nanoen.2021.106248

19. Majumdar A, Chowdhury S, Ahuja R. Ultralow thermal conductivity and high thermoelectric figure of merit in two-dimensional thallium selenide. *ACS Appl Energ Mater* (2020) 3:9315–25. doi:10.1021/acsaem.0c01658

20. Nian T, Wang Z, Dong B. Thermoelectric properties of α-in_2Se_3 monolayer. *Appl Phys Lett* (2021) 118(2021):033103. doi:10.1063/5.0036316

21. Zhao L-D, Lo S-H, Zhang Y, Sun H, Tan G, Uher C, Wolverton C, Dravid VP, Kanatzidis MG. Ultralow thermal conductivity and high thermoelectric figure of merit in SnSe crystals. *Nature* (2014) 508:373–7. doi:10.1038/nature13184

22. Sun G, Qin X, Li D, Zhang J, Ren B, Zou T, Xin H, Paschen SB, Yan X. Enhanced thermoelectric performance of n-type Bi_2Se_3 doped with Cu. *J Alloy Compd* (2015) 639: 9–14. doi:10.1016/j.jallcom.2015.03.124

23. Mi W, Qiu P, Zhang T, Lv Y, Shi X, Chen L. Thermoelectric transport of Se-rich Ag_2Se in normal phases and phase transitions. *Appl Phys Lett* (2014) 104:133903. doi:10.1063/1.4870509

24. Wickramaratne D, Zahid F, Lake RK. Electronic and thermoelectric properties of van der Waals materials with ring-shaped valence bands. *J Appl Phys* (2015) 118:075101. doi:10.1063/1.4928559

25. Zheng Y, Tang X, Wang W, Jin L, Li G Large-size ultrathinα-Ga_2S_3 nanosheets toward high-performance photodetection. *Adv Funct Mater* , 2008307,31(2021). doi:10.1002/adfm.202008307

26. Jeengar C, Tomar M, Jindal K, Sharma A, Jha PK. Influence of post deposition annealing on thermoelectric properties of In_2Se_3 thin films. *Mater Sci Semicond Process* (2023) 153(2023):107127. doi:10.1016/j.mssp.2022.107127

27. Li B, Zhang C, Sun Z, Han T, Zhang X, Du J, Wang J, Xiao X, Wang N. The potential thermoelectric material Tl_3XSe_4 (X= V, Ta, Nb): A first-principles study. *Phys Chem Chem Phys* (2022) 24:24447–56. doi:10.1039/d2cp00358a

28. Yang J, Li J, Zhang C, Feng Z, Shi B, Zhai W, Yan Y, Wang Y. Excellent thermoelectric performance of BaMgSi driven by low lattice thermal conductivity: A promising thermoelectric material. *J Alloy Compd* (2020) 827:154342. doi:10.1016/j.jallcom.2020.154342

29. Babich AV, Rogachev M. Investigation of thermal properties and thermal stability of the Sn-Pb-Te system materials for the thermoelectric generator application. Proceeding of the 2020 IEEE Conference of Russian Young Researchers in Electrical and Electronic Engineering (EIConRus). January 2020, St. Petersburg and Moscow, Russia. IEEE (2020). 2111–4.

30. Zhan S, Hong T, Qin B, Zhu Y, Feng X, Su L, Shi H, Liang H, Zhang Q, Gao X, et al. Realizing high-ranged thermoelectric performance in $PbSnS_2$ crystals. *Nat Commun* (2022) 13:5937. doi:10.1038/s41467-022-33684-0

31. Xia Q, Xu Q, Xu B, Yi L. *Ab initio* prediction of thermoelectric performance of monolayer $BiSbTe_3$. *J Solid State Chem* (2021) 296:121963. doi:10.1016/j.jssc.2021.121963

32. Gangwar VK, Kumar S, Singh M, Ghosh L, Yufeng Z, Shahi P, Patil S, Schwier EF, Shimada K, Uwatoko Y. *Pressure induced superconductivity and location of Fermi energy at Dirac point in $BiSbTe_3$* (2019). *arXiv preprint arXiv*:1906.10336.

33. Giannozzi P, Andreussi O, Brumme T, Bunau O, Nardelli MB, Calandra M, Car R, Cavazzoni C, Ceresoli D, Cococcioni M, et al. Advanced capabilities for materials modelling with quantum ESPRESSO. *J Phys Condens Matter* (2017) 29:465901. doi:10.1088/1361-648X/aa8f79

34. Perdew JP, Zunger A. Self-interaction correction to density-functional approximations for many-electron systems. *Phys Rev B* (1981) 23:5048–79. doi:10.1103/physrevb.23.5048

35. Baroni S, Gironcoli SD, Corso AD, Giannozzi P. Phonons and related crystal properties from density-functional perturbation theory. *Rev Mod Phys* (2001) 73: 515–62. doi:10.1103/revmodphys.73.515

36. Gonze X. First-principles responses of solids to atomic displacements and homogeneous electric fields: Implementation of a conjugate-gradient algorithm. *Phys Rev B* (1997) 55:10337–54. doi:10.1103/physrevb.55.10337

37. Li W, Carrete J, Katcho NA, Mingo N. ShengBTE: A solver of the Boltzmann transport equation for phonons. *Comput Phys Commun* (2014) 185:1747–58. doi:10.1016/j.cpc.2014.02.015

38. Lu I-T, Zhou J-J, Park J, Bernardi M. First-principles ionized-impurity scattering and charge transport in doped materials. *Phys Rev Mater* (2022) 6:L010801. doi:10.1103/PhysRevMaterials.6.L010801

39. Peng P-P, Wang C, Li L-W, Li S-Y, Chen Y-Q. Research status and performance optimization of medium-temperature thermoelectric material SnTe. *Chin Phys B* (2022) 31(2022):047307. doi:10.1088/1674-1056/ac20c9

40. Gupta R, Dongre B, Carrete J, Bera C. Thermoelectric properties of the SnS monolayer: Fully *ab initio* and accelerated calculations. *J Appl Phys* (2021) 130:054301. doi:10.1063/5.0058125

41. Zhou J-J, Park J, Lu I-T, Maliyov I, Tong X, Bernardi M. Perturbo: A software package for *ab initio* electron–phonon interactions, charge transport and ultrafast dynamics. *Comput Phys Commun* (2021) 264:107970. doi:10.1016/j.cpc.2021.107970

42. Hieu NN, Phuc HV, Kartamyshev A, Vu TV. Structural, electronic, and transport properties of quintuple atomic janus monolayers Ga_2SX_2 (X= O, S, Se, Te): First-principles predictions. *Phys Rev B* (2022) 105:075402. doi:10.1103/physrevb.105.075402

43. Zhang G, Lu K, Wang Y, Wang H, Chen Q. Mechanical and electronic properties of α– M_2X_3 (M= Ga, in; X= S, Se) monolayers. *Phys Rev B* (2022) 105:235303. doi:10.1103/PhysRevB.105.235303

44. Chen Y, Wu Y, Hou B, Cao J, Shao H, Zhang Y, Mei H, Ma C, Fang Z, Zhu H, et al. Renormalized thermoelectric figure of merit in a band-convergent Sb_2Te_2Se monolayer: Full electron–phonon interactions and selection rules. *J Mater Chem A* (2021) 9: 16108–18. doi:10.1039/d1ta02107a

45. Marfoua B, Hong J. High thermoelectric performance in hexagonal 2D $PdTe_2$ monolayer at room temperature. *ACS Appl Mater.Interfaces* (2019) 11:38819–27. doi:10.1021/acsami.9b14277

46. Cheng L, Liu H, Zhang J, Wei J, Liang J, Shi J, Tang X. Effects of van der Waals interactions and quasiparticle corrections on the electronic and transport properties of Bi_2Te_3. *Phys Rev B* (2014) 90:085118. doi:10.1103/physrevb.90.085118

47. Sheng C, Fan D, Liu H. High thermoelectric performance can be achieved in two-dimensional $(PbTe)_2$ layer. *Phys Lett A* (2020) 384:126044. doi:10.1016/j.physleta.2019.126044

48. Batsanov SS. Van der Waals radii of elements. *Inorg Mater* (2001) 37:871–85. doi:10.1023/A:1011625728803

49. Gao Z, Dong X, Li N, Ren J. Novel two-dimensional silicon dioxide with in-plane negative Poisson's ratio. *Nano Lett* (2017) 17:772–7. doi:10.1021/acs.nanolett.6b03921

50. Yuan K, Sun Z, Zhang X, Gong X, Tang D A first-principles study of the thermoelectric properties of rhombohedral GeSe. *Phys Chem Chem Phys* 22, 1911, 22. doi:10.1039/c9cp05153h2020).

51. Lv B, Hu X, Wang N, Song J, Liu X, Gao Z Thermal transport property of novel two-dimensional nitride phosphorus: An *ab initio* study. *Appl Surf Sci* (2021) 559, 149463. doi:10.1016/j.apsusc.2021.149463

52. Peng B, Zhang H, Shao H, Xu Y, Zhang X, Zhu H Low lattice thermal conductivity of stanene. *Sci Rep* ,6, 20225, doi:10.1038/srep202252016).

53. Wang Y, Gao Z, Zhou J Ultralow lattice thermal conductivity and electronic properties of monolayer 1T phase semimetal $SiTe_2$ and $SnTe_2$. *Phys E* (2019) 108, 53–9. doi:10.1016/j.physe.2018.12.004

frontiers | Frontiers in Physics

TYPE Original Research
PUBLISHED 06 April 2023
DOI 10.3389/fphy.2023.1188513

OPEN ACCESS

EDITED BY
Guangzhao Wang,
Yangtze Normal University, China

REVIEWED BY
H.N. Dong,
Chengdu Normal University, China
Zhimin Wu,
Chongqing Normal University, China

*CORRESPONDENCE
Wei Kang,
283963423@qq.com

SPECIALTY SECTION
This article was submitted to Physical Chemistry and Chemical Physics, a section of the journal Frontiers in Physics

RECEIVED 17 March 2023
ACCEPTED 28 March 2023
PUBLISHED 06 April 2023

CITATION
Kang W, Du X, Wang J, Ye Z, Zhao J, Wang W, Wang Y, Wang L and Liu X (2023), Two-dimensional half-metallicity in transition metal atoms decorated $Cr_2Ge_2Te_6$. *Front. Phys.* 11:1188513. doi: 10.3389/fphy.2023.1188513

Two-dimensional half-metallicity in transition metal atoms decorated $Cr_2Ge_2Te_6$

Wei Kang*, Xue Du, Jintian Wang, Ziqin Ye, Jinghong Zhao, Wei Wang, Yan Wang, Lin Wang and Xiaoqing Liu

Key Laboratory of Optoelectronic Technology and System of Ministry of Education, College of Optoelectronic Engineering, Chongqing University, Chongqing, China

As one of the first experimentally found and naturally stable two-dimensional (2D) ferromagnetic materials, the monolayer $Cr_2Ge_2Te_6$ has garnered great interest due to its potential hires in electronics and spintronics. Yet, the Curie temperature of monolayer $Cr_2Ge_2Te_6$ is lower than the ambient temperature, severely restricting the creation of valuable devices. Using the first-principle calculations, we explored how the adsorption of 3*d* transition metals affects the electronic and magnetic properties of the monolayer $Cr_2Ge_2Te_6$ (from Sc to Zn). Our findings indicate that depending on the 3*d* transition metals to be adsorbed, the electronic properties of the $Cr_2Ge_2Te_6$ adsorption system may be adjusted from semiconductor to metal/half-metal. We found that the adsorption of Ti and Fe leads to a transformation from semiconductor to metal. While in $Cr_2Ge_2Te_6$@Sc, V, Co, Ni, and Cu, the absorption realizes the changes from semiconductor to half metal. Moreover, adsorption may modify the magnetic moment and Curie temperature of the adsorbed system to enhance the ferromagnetic stability of the monolayer $Cr_2Ge_2Te_6$. Furthermore, we are able to modulate the half-metallic of $Cr_2Ge_2Te_6$@Mn by means of electric fields. Hence, adsorption is a viable method for modulating the ferromagnetic half-metallic of 2D ferromagnets, paving the door for the future development of nano-electronic and spintronic devices with enhanced performance for 2D ferromagnetic materials.

KEYWORDS

monolayer Cr2Ge2Te6, 3d transition metal, electronic properties, ferromagnetism, half-metal, curie temperature

Introduction

Since Geim and Novoselov initially reported [1] the successful fabrication of graphene by the transparent tape exfoliation technique in 2004, there has been a continuous attempt to identify two-dimensional (2D) materials with superior characteristics. In the realm of contemporary materials research, atomic-level thickness layered van der Waals materials are suitable as a broad class of materials with excellent physical properties [2], and they are now gaining popularity among scientists. The van der Waals force interaction within the interlayer of layered 2D materials is a typical weak coupling interaction. In particular, with the discovery of boronene [3], MoS_2 [4], and black phosphorus [5], single or multiple-layer 2D layered materials, the interest in 2D semiconductor layered materials, and their relative heterostructures have been intensively studied. Yet, another essential attribute of materials, magnetic properties, has been of interest and is absent from many 2D van der Waals

materials. For example, graphene [6], a band-gapless, nonmagnetic 2D material, impedes its employment in spintronic devices. Hence, researchers are hopeful of discovering a series of 2D stacked magnetic materials.

Low-dimensional ferromagnetic semiconductors are urgently required to construct the next-generation of nanoscale spintronic devices. In recent years, there are some 2D half-metallic materials, for example, monolayer Mxene [7, 8] and multiferroic nanosheets ACr_2S_4 [9] (A = Li, Na, K Rb). The transition-metal trichalcogenides (TMTC), another class of typical layered van der Waals materials that possess both magnetic properties and a unique layered structure, have also attracted the interest of the public [10]. They are coupled between layers by weak van der Waals interactions; for instance, $MnPS_3$ has excellent physicochemical properties and is easy to prepare [11, 12]. In addition, the materials of this structure display diverse electronic properties, some as semiconducting and others as insulating, and they also have unique magnetic properties. As a potential candidate for 2D magnetic layered van der Waals materials, it has become the focus of recent research. In particular, as a member of the family of layered van der Waals materials, crystalline Cr-based transition metal trichloride has attracted significant interest. For example, the Curie temperature of $CrSiTe_3$ [13], one of the transition metal trisulfide materials, increases as the number of layers decreases. It is reported to be a well-known 2D ferromagnetic [14] semiconductor because both the block and monolayer exhibit different magnetic ground states. In addition, it has been reported [15] that the Curie temperature of CrI_3 is 45 K. Being a multilayer van der Waals insulator, its Curie temperature drops as the number of layers reduces, and it is also regarded as an excellent 2D ferromagnetic material. In recent years, $Cr_2Ge_2Te_6$ has also been selected by researchers because of its van der Waals geometry, intrinsic ferromagnetism, and higher Curie temperature than CrI_3. It has been stated [16] that V. Carteaux produced the first bulk of $Cr_2Ge_2Te_6$ in 1995. In 2017, a ferromagnetic monolayer, $Cr_2Ge_2Te_6$, with a Curie temperature of 61 K, in experimental, was exfoliated [17]. 2D layered $Cr_2Ge_2Te_6$ [18] of novel electronic, magnetic, optical, optoelectronic, piezoelectric, and thermoelectric properties are easily compatible with nanoelectronic devices. It was even reported [17] that ferromagnetism exists in the new $Cr_2Ge_2Te_6$ atomic layer and that the Curie temperature can be easily regulated by modulating the applied magnetic field. This finding suggests $Cr_2Ge_2Te_6$ is an ideal candidate for the study of 2D magnetic phenomena and spintronic device materials. On the other hand, the focus of research on this type of 2D layered van der Waals magnetic materials will also significantly advance our understanding of the magnetic properties of low-dimensional materials, which, when combined with their rich electronic and optical properties, will open up numerous application possibilities for 2D magnetoelectric and magneto-optical applications.

In particular, research on intrinsically magnetic semiconductors with high Curie temperatures, large band gaps, and high carrier mobility is of extraordinary significance for developing the next-generation of ultra-miniaturized, highly integrated spintronics and magneto-optics devices. Nevertheless, it is challenging to have long-range ordered ferromagnetic and semiconducting properties in 2D materials [19], thus hoping that the substrate material can be tuned by some conventional modifications to produce magnetic properties. In the past decades, many modifications, such as magnetic doping [20], nonmagnetic doping [21], or hole doping [22], have been used in an attempt to introduce long-range ordered ferromagnetic sequences in semiconductors. Functional adsorption is one of the most traditional techniques to modulate the electronic and magnetic properties of the material effectively. Many efforts have previously been devoted to studying metal atom interactions in 2D materials inducing magnetic for applications in spintronics. Particularly, graphene-like 2D materials interact with magnetic atoms to produce half metal, and this modulation has been considered as an effective and interesting means of application to spintronics. Some theoretical studies have shown that the adsorption of metal atoms on the graphene sheets significantly increases the Curie temperature up to 438 K [23]. The adsorption of transition metal atoms on the surface of black phosphorus also effectively modulates its electronic and magnetic properties [24]. It was reported that a strong orbital coupling between GaSe monolayer and transition metals was found to produce 100% spin-polarized currents [25]. A recent study also found that monolayer $Cr_2Ge_2Te_6$ nanosheet interacted with alkali metals, enhancing their ferromagnetism and exhibiting half-metallic properties [26]. Therefore, the combination of 2D layered van der Waals materials, intrinsic ferromagnetism, half-metallic properties, and adsorption will likely provide a good platform for applying new low-dimensional magnetic materials in the field of spintronics.

Using first-principles calculation, we want to examine the electronic and magnetic properties of 3*d* transition metals adsorbed on monolayer $Cr_2Ge_2Te_6$ nanosheet. We found that 3*d* transition metals adsorbed on the substrate $Cr_2Ge_2Te_6$ significantly change the magnetic moments of the system. Except for Ti and Cr adsorbed, the Curie temperature of the adsorption system (TM = Sc, V, Mn, Fe, Co, Ni, Cu, and Zn) is significantly enhanced by a factor of two, with an enhancement of Curie temperature increasing rate over to 200%. Based on the optimized structure of the adsorbed system, we analyzed the geometry, electronic structure, spin density of states, magnetic moments, and Curie temperature of the ten-absorbed system for first-principles calculation. We found that the adsorption energy changes significantly as the 3*d* transition metal is adsorbed at different positions. The degree of interaction between the transition metal atoms and monolayer $Cr_2Ge_2Te_6$ significantly differs at different adsorption positions. We also found that the 3*d* transition metals change the electronic properties of the absorbed system, especially $Cr_2Ge_2Te_6$@Ti and $Cr_2Ge_2Te_6$@Fe become metallic. At the same time, the Sc, V, Co, Ni, and Cu absorbed systems show half-metallic. In addition, we found that the adsorption of 3*d* transition metals can significantly increase the Curie temperature of the system. Therefore, the present study reveals that the monolayer $Cr_2Ge_2Te_6$ can change its electronic structure and magnetic properties by adsorption of 3*d* transition metal atoms, thus predicting the unlimited application prospects of monolayer 2D $Cr_2Ge_2Te_6$ ferromagnet in the next-generation of functional spintronic devices.

Methodology

Our density functional theory (DFT) calculations were performed using Vienna *ab initio* Simulation Package [27, 28].

The projector augmented wave formalism (PAW) [29, 30] describes the ion-electron potential. The exchange of correlation functions during the simulations is mainly handled by the generalized gradient approximation (GGA) [31] and is parameterized by the Perdew-Burke-Ernzerhofer (PBE) parameterization. Projection-enhanced wave functions have also been used to describe the electron-ion potential [27, 32]. The kinetic cut-off energy of the plane wave basis group is set as 400 eV. We set the condition of full convergence at ion relaxation as long as the total energy is less than 10^{-5} eV and the force on each atom is less than 0.01 eV/Å when the lattice constant, as well as the atomic positions, will be the most stable state of complete relaxation. To eliminate the interaction between periodic boundaries, we simulated the properties of the monolayer $Cr_2Ge_2Te_6$ using a 20 Å thick slab model in the z-direction. In addition, to fully characterize the van der Waals interactions between the adsorbed 3*d* transition metal and the monolayer $Cr_2Ge_2Te_6$, a DFT-D3 correction method [33, 34] with the Grimme scheme is used to perform the whole system study calculations. We adopted the 2 × 2 supercell structure for monolayer $Cr_2Ge_2Te_6$ with one transition metal. Besides, the Brillouin zone *k*-point mesh of 3 × 3 × 1 is used for optimizing, and a denser 8 × 8 × 1 *k*-point mesh is used for electronic structure computations. Here, we analyzed these results by utilizing the PBE + U functional to describe the high correlations between the electrons in the *d* shell. The on-site interactions U_{eff} are represented by the equation, $U_{eff} = U - J$, where U and J stand for the on-site Hubbard Coulomb and exchange parameters, respectively. U has been assigned values of 3.00 eV for Cr and 2.50 eV for other 3*d* transition metal atoms, respectively [35–38]. The values of J have been set to be 0.90 eV for Cr and 0.00 eV for 3*d* transition metals [39, 40]. Additionally, we computed the band structure of the monolayer $Cr_2Ge_2Te_6$ in a unit cell with and without the PBE + U. The Monte Carlo (MC) simulation based on the Ising model [41] was used to estimate the Curie temperature of the monolayer $Cr_2Ge_2Te_6$ and single-layer $Cr_2Ge_2Te_6$ absorbed transition metals.

Results and discussions

It is known from previous studies [42] that there is a large van der Waals gap in the structure of bulk $Cr_2Ge_2Te_6$, and the interlayer interactions are pretty weak, so it is possible to extract 2D $Cr_2Ge_2Te_6$ nanosheet by experimental peeling. Therefore, before studying the adsorption of transition metal atoms by the substrate monolayer $Cr_2Ge_2Te_6$, we first investigated the structural, electronic, and magnetic properties of the monolayer $Cr_2Ge_2Te_6$. Supplementary Figure S1A shows the top and side views of a monolayer $Cr_2Ge_2Te_6$ supercell (2 × 2). $Cr_2Ge_2Te_6$ is a hexagonal lattice structure. Each layer can be considered an octahedral $CrTe_6$ at the edge of the hexagonal lattice and a Ge dimer in the center [43]. After structural optimization, there are 40 atoms in the supercell (2 × 2) with lattice constants of $a = b = 13.65$ Å, $\alpha = 120^{\circ}$, and a bond length of 2.78 Å between the Cr atom and the nearest neighboring Te atom. Our calculated results are in agreement with previous literature [18]. The spin-polarized band structure shown in Supplementary Figure S1B explains the electronic properties of monolayer $Cr_2Ge_2Te_6$. It reveals that the monolayer $Cr_2Ge_2Te_6$ is a semiconductor whose band gap in the spin-down channel is indirect, with the valence band in the Γ point being the top of the valence band (VBM) and the bottom of conduction band (CBM) located in the *K* point, and the value of band gap in the spin-down channel is 0.52 eV; In the spin-up channel, we can see that the VBM is located at *Γ* point, while the CBM is located between K point and M point, and its indirect band gap value is 0.31 eV, which is consistent with the results of the literature [18, 44]. Supplementary Figure S1C shows the total density of states of the monolayer $Cr_2Ge_2Te_6$. We can see that near the Fermi surface, both the conduction band and the valence band are asymmetric in both spin channels, and the VBM in the spin-up channel is closer to the Fermi surface than its VBM in the spin-down energy band, while the CBM in the spin-up channel is closer to the Fermi surface than that in the spin-down channel, which also indicates that both the conduction band and the valence band edges near the Fermi surface are fully spin-polarized. Thus the band gap in the spin-up channel is smaller than that in the spin-down channel, implying that $Cr_2Ge_2Te_6$ is a bipolar magnetic semiconductor [45]. In addition, the contribution of the Cr atom in the spin-up is significantly larger than that in the spin-down, while the density of states of Te atoms is in the conduction band, where the electronic density of states in the spin-up is significantly larger than that in the spin-down. In addition, the valence band edge is mainly contributed by Te atoms, and at the conduction band edge, it is contributed primarily by Cr and Te atoms [18]. The spin polarization at the Fermi surface is also caused by the interaction between Cr and Te atoms. The valence band top is occupied by the *p* orbital of the Te atom, while the hybridized orbital of the d orbital of the Cr atom and the *p* orbital of the Te atom occupies the conduction band bottom.

To confirm the magnetic ground state of the most stable monolayer $Cr_2Ge_2Te_6$ nanosheet, we have calculated two different magnetic configurations for monolayer $Cr_2Ge_2Te_6$ nanosheet, i.e., ferromagnetic (FM) and antiferromagnetic (AFM) states. The energy difference (ΔE) is defined as the difference between the energy of AFM and FM per cell, that is $\Delta E = E_{AFM} - E_{FM}$, where E_{AFM} and E_{FM} represent the total energy of the antiferromagnetic $Cr_2Ge_2Te_6$ and the ferromagnetic $Cr_2Ge_2Te_6$ nanosheet. ΔE = 55.25 meV, showing that a 2D $Cr_2Ge_2Te_6$ has a higher energy per unit cell in AFM than in the FM state, which is more stable than in the AFM state. In addition, the literature [46] reported that the magnetic properties of $Cr_2Ge_2Te_6$ are mainly derived from the local magnetic moments on the Cr atomic sites; therefore. After calculations, we obtained the magnetic moment of the monolayer $Cr_2Ge_2Te_6$ as 24.00 μ_B, and the magnetic moment of each Cr atom is about 3.37 μ_B. This result is consistent with the literature [47]. We used Monte Carlo simulations to obtain the Curie temperature of the monolayer $Cr_2Ge_2Te_6$. The Monte Carlo simulation calculates the monolayer $Cr_2Ge_2Te_6$ nanosheet with a supercell of 20 × 20 × 1 to minimize the periodic reduction constraint. Each simulation was cycled for at least 10^5 steps to ensure the overall structure reached equilibrium at each temperature. As shown in Supplementary Figure S1D, the magnetic moment of the monolayer $Cr_2Ge_2Te_6$ start to decrease sharply at about 87 K. indicating a Curie temperature of about 87 K for the monolayer $Cr_2Ge_2Te_6$ nanosheet.

Previous work has shown [18] that low-dimensional materials are sensitive to external stimuli, which helps us investigate the adsorption system's fundamental properties. After studying the

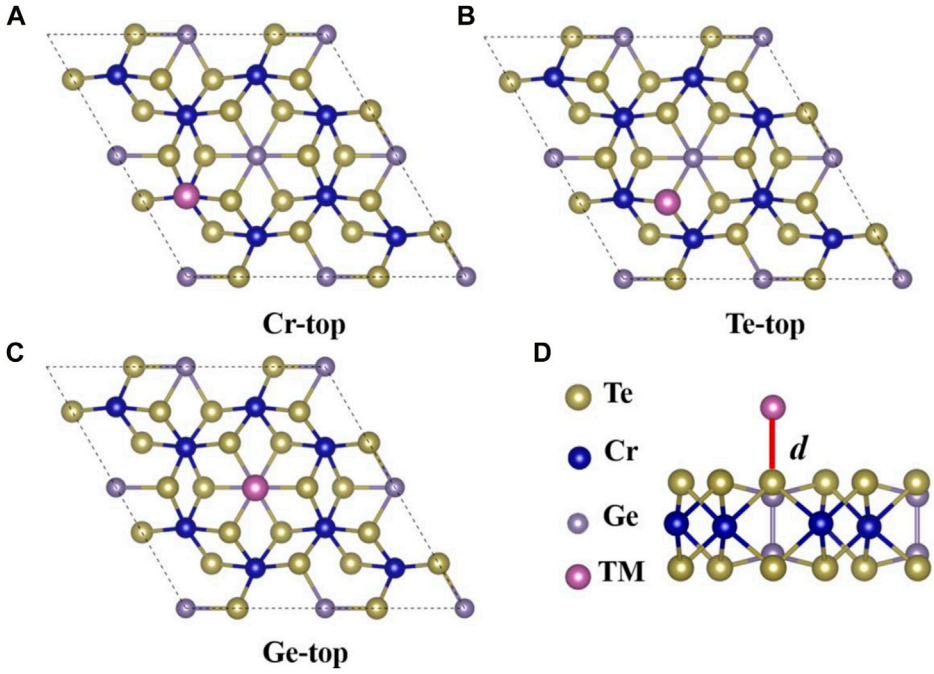

FIGURE 1
The top views of the crystalline structure of a 2 × 2 monolayer $Cr_2Ge_2Te_6$, with TM atoms absorbed at three different positions labeled as **(A)** Cr-top, **(B)** Te-top, and **(C)** Ge-top, respectively. The dotted black lines in the graph indicate the 2 × 2 supercell. **(D)** The side view of the monolayer $Cr_2Ge_2Te_6$ (2 × 2) nanosheet adsorbed by the transition metals, and the adsorption distance *d* is represented by the solid red line. The atoms of the Te, Cr Ge, and 3*d* transition metals are represented by the pale yellow, indigo, purple, and pink balls represent, respectively.

electronic properties and magnetic properties based on monolayer $Cr_2Ge_2Te_6$, we selected transition metal (TM = Sc, Ti, V, Cr, Mn, Fe, Co, Ni, Cu, and Zn) atoms and monolayer $Cr_2Ge_2Te_6$ nanosheet for the analytical study of the adsorption mechanism. Studying this class of transition metal adsorption will be a good guide for applying 2D magnetic materials in spintronic devices. We selected 2 × 2 supercell monolayer $Cr_2Ge_2Te_6$ as substrates for the adsorbing 3*d* transition metals from Sc atoms to Zn atoms sequentially. To find the most favorable adsorption sites, as shown in Figures 1A–C, we considered three locations where the monolayer $Cr_2Ge_2Te_6$ nanosheet adsorb the transition metal atoms. They are positions A (Cr-top), B (Te-top), and C (Ge-top), respectively. The adsorption distance (*d*) is the distance between 3*d* transition metal atoms and the substrate surface atoms, as shown in Figure 1D. To evaluate the interaction between the substrate and 3*d* transition metals, we calculated the adsorption energy of the adsorption system. We used the adsorption energy to describe the absorption stability with the following equation: $E_{ads} = E_{Cr_2Ge_2Te_6@TM-}(E_{Cr_2Ge_2Te_6} + E_{TM})$, where, $E_{Cr_2Ge_2Te_6@TM}$, $E_{Cr_2Ge_2Te_6}$, and E_{TM} are the total energy of 3*d* transition metal deposited on the monolayer $Cr_2Ge_2Te_6$ and the energy of the bare monolayer $Cr_2Ge_2Te_6$ and 3*d* transition metal, respectively. According to the definition, it is evident that when the value of adsorption energy E_{ads} is greater, then the more robust the interaction between 3*d* transition metal and monolayer $Cr_2Ge_2Te_6$, the more stable adsorption of the transition metal. After structural relaxation and static calculations for the structures of the monolayer $Cr_2Ge_2Te_6$ adsorbing transition metal at each of the three different sites, we obtained their respective adsorption energies E_{ads} and adsorption distances *d*.

Figure 2A shows the calculated adsorption energy at three positions after complete structural relaxation. All adsorption energies at all positions are negative, except for the Cr adsorbed at the Cr-top position and Ti atoms adsorbed at the Ge-top site. The adsorption energies are negative, indicating that this reaction is exothermic, suggesting the monolayer $Cr_2Ge_2Te_6$ can adsorb transition metals at three different positions, indicating that these adsorption systems are stable. Still, the interaction strength between the transition metal and the substrate differs from 3*d* transition metals. For the adsorption of Mn and Zn, there is no significant difference in the adsorption energies at the three different sites. Still, the adsorption energy of the $Cr_2Ge_2Te_6$@Mn fluctuating between −0.55 and −0.66 eV, is larger than that of the $Cr_2Ge_2Te_6$@Zn, indicating that the interaction strength in $Cr_2Ge_2Te_6$@Mn is stronger than that of the $Cr_2Ge_2Te_6$@Zn. For the systems adsorbed Sc, Ti, V, Cr, Fe, Co, Ni, and Cu, their adsorption energies significantly changed at different adsorption positions, implying the strength of interaction between 3*d* transition metals and the substrate was quite different. Similarly, from Supplementary Table S1, the adsorption distances of 3*d* transition metals adsorbed at different positions have significantly different variations. $Cr_2Ge_2Te_6$@Sc has relatively high adsorption energy, indicating a strong interaction between the Sc atoms and the substrate. However, for the $Cr_2Ge_2Te_6$@Zn, the adsorption distance fluctuates around 2.92 Å. In contrast, the adsorption energies at all three positions are small and almost negligible, indicating minimal interaction between the Zn atoms and the substrate material. On the other hand, for the adsorption systems of Ti, V, Cr, Mn, Fe, Co, Ni,

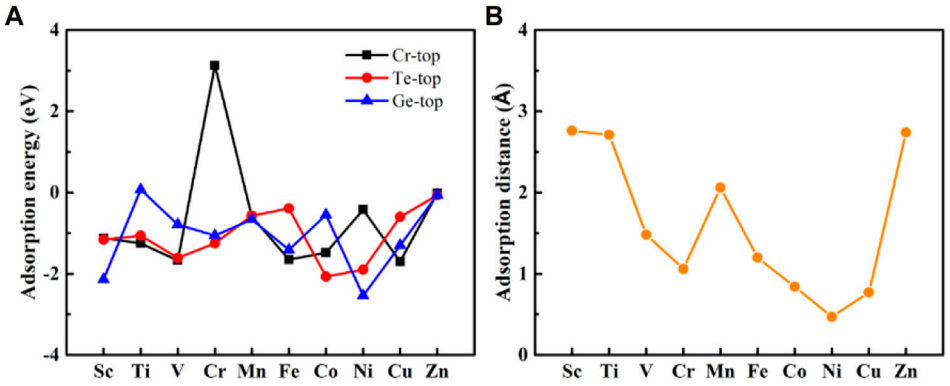

FIGURE 2
(A) The adsorption energy of monolayer $Cr_2Ge_2Te_6$ for transition metals at three distinct adsorption positions: Cr-top, Te-top, and Ge-top. **(B)** The adsorption distance of transition metals adsorbed by monolayer $Cr_2Ge_2Te_6$.

and Cu, the adsorption distance and adsorption energies obviously differ significantly at three different positions. For example, for the $Cr_2Ge_2Te_6$@Fe, we found that the value of the adsorption energy −1.65 eV at the Cr-top position is considerably larger than that of −0.39 eV at the Te-top position. At the same time, its adsorption distance of 1.20 Å is much larger than that of 2.79 Å at the Te-top position, indicating that the adsorption of Fe atoms at the Cr-top position is more stable than that at the Te-top position. More stable the absorption and their interactions are stronger.

We can determine the best adsorption site based on the minimum adsorption energy after structural relaxation. In $Cr_2Ge_2Te_6$@Fe, Co adsorbed at the Te-top position was significantly shifted and moved above the Cr atom, so the best adsorption site for the transition metal Co is at the Cr-top position. Similarly, we found that the Zn also moved from the Te-top site to the Ge-top site, so the best adsorption site for Zn is at the Ge-top position. Also, $Cr_2Ge_2Te_6$@Ni has a similar trend, having the Te-top position as the adsorption site. As a result (shown in Supplementary Table S1, S2), three categories may be used to group the best adsorption site for the ten absorption systems. The optimum adsorption site for Ti, V, Fe, Co, and Cu is at the Cr-top position (A site); the best adsorption site for Cr and Ni is at the Te-top position (B site); and the best adsorption site for Sc, Mn, and Zn is located at the Ge-top position (C site). Figure 2B shows the adsorption distance *d* at the best adsorption site. The $Cr_2Ge_2Te_6$@Zn has the smallest negative value of adsorption energy at −0.07 eV. As we all know, the outermost shell of the Zn atom is in an entire electron state. The Zn binds to the monolayer $Cr_2Ge_2Te_6$ through weak interaction, most likely as physical adsorption. Except for Zn absorbed, the E_{ads} values of the other absorption system are pretty large, ranging from −2.54 to −0.66 eV, indicating a strong bonding between 3*d* transition metals and the substrate. For Ti, V, Cr, Mn, Fe, Co, Ni, and Cu absorbed, the higher the negative values of the adsorption energy and, at the same time, the smaller their adsorption distance *d*, indicating strong bonding, most likely by chemical interaction. The adsorption energies of the adsorbed Sc and Ni atoms are the highest, reaching −2.14 and −2.54 eV, respectively, indicating that the bonding between Sc and Ni atoms and monolayer $Cr_2Ge_2Te_6$ is the strongest. For the adsorption system, the stability of 3*d* transition metal adsorption: $Cr_2Ge_2Te_6$@Ni > $Cr_2Ge_2Te_6$@Sc > $Cr_2Ge_2Te_6$@Co > $Cr_2Ge_2Te_6$@Cu > $Cr_2Ge_2Te_6$@V > $Cr_2Ge_2Te_6$@Fe > $Cr_2Ge_2Te_6$@Ti = $Cr_2Ge_2Te_6$@Cr > $Cr_2Ge_2Te_6$@Mn > $Cr_2Ge_2Te_6$@Zn. In addition, except for Sc, Ti, and V absorbed, the trend of adsorption energy change is consistent with the trend of its adsorption distance *d* change. In conclusion, by adsorbing 3*d* transition metals at various places, we determined that the optimal adsorption sites for various transition metals are situated at various locations. In general, the greater the negative value of their adsorption energy and the shorter the adsorption distance, the easier and stronger the mutual interaction between the substrate material and the transition metals.

Figure 3 depicts the spin-polarized band structure of the adhered nanosheet. As is evident, the transition metal has a considerable influence on the electronic structure of the monolayer $Cr_2Ge_2Te_6$ nanosheet of the substrate material. The half-metallic attribute of a material is that it exhibits metallic qualities and semiconductor or insulator properties for electrons with two distinct spin orientations. When the spin polarization rate is 100%, the material is half-metallic, meaning that the energy band in the spin-up channel is metallic while the energy band in the opposite spin direction is non-metallic. For $Cr_2Ge_2Te_6$@Sc, V, Cr, Co, Ni, and Cu, the spin-up energy bands cross the Fermi level showing the metallic. In contrast, the spin-down energy bands have band gaps, indicating that the spin-down energy bands are semiconducting in nature, suggesting that these systems become half metallic and supply 100% of the spin-polarized current due to their spin polarizabilities 100% at the Fermi level. For the half metallic adsorption systems, their corresponding half metallic gaps (E_g) were computed. The half metallic gap is the minimum between the lowest energy of spin-up (down) conduction bands in relation to the Fermi level and the greatest energy of spin-up (down) valence bands in absolute values. And the results showed that in the $Cr_2Ge_2Te_6$@Sc, V, Cr, Co, Ni, and Cu, half metallic gaps, E_g were 40.82, 121.14, 24.56, 100.78, 46.33, and 118.06 meV, indicating the half metallic of these adsorption systems is relatively stable. For the $Cr_2Ge_2Te_6$@Sc (Figure 3A), the spin-down channel retains the band structure of the pristine $Cr_2Ge_2Te_6$. The substrate material has acquired electrons because the spin-up energy band is heavily hybridized, and its conduction

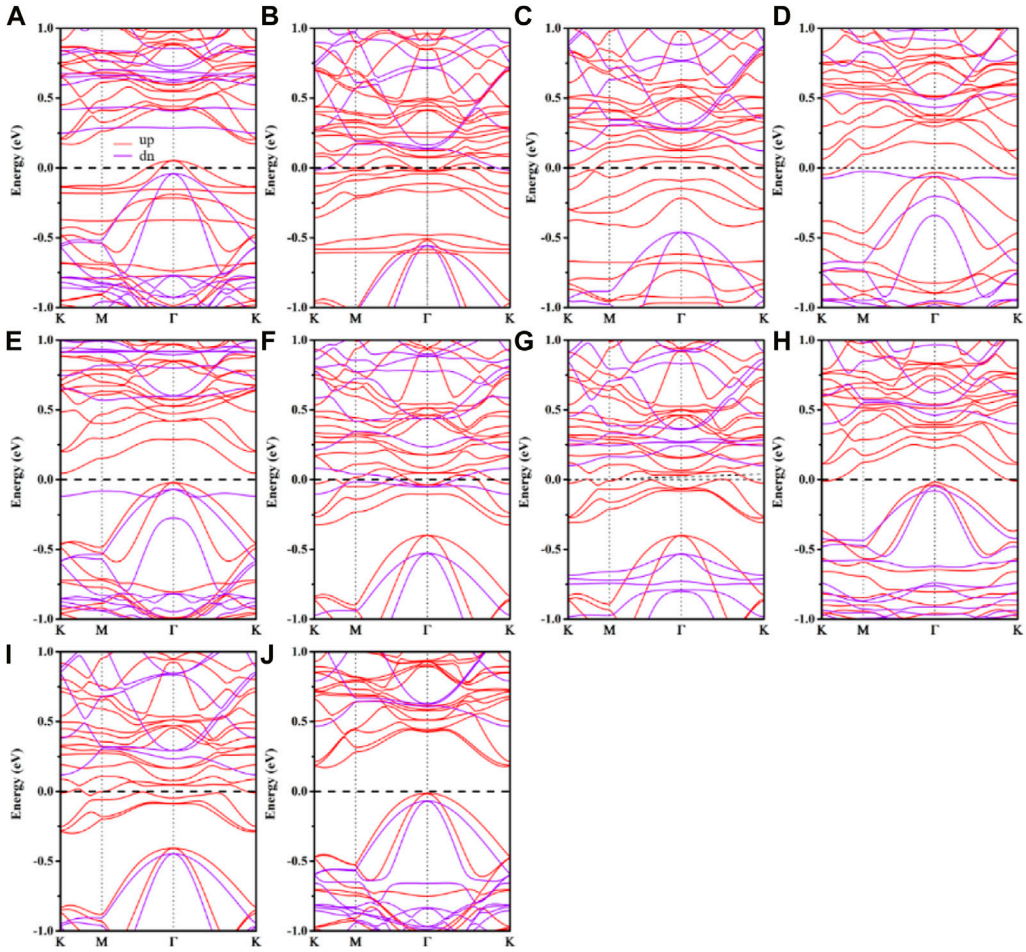

FIGURE 3
The calculated spin-polarized band structures of **(A)** $Cr_2G_2Te_6$@Sc, **(B)** $Cr_2G_2Te_6$@Ti, **(C)** $Cr_2G_2Te_6$@V, **(D)** $Cr_2G_2Te_6$@Cr, **(E)** $Cr_2G_2Te_6$@Mn, **(F)** $Cr_2G_2Te_6$@Fe, **(G)** $Cr_2G_2Te_6$@Co., **(H)** $Cr_2G_2Te_6$@Ni, **(I)** $Cr_2G_2Te_6$@Cu, **(J)** $Cr_2G_2Te_6$@Zn. In the band structures, the solid red lines correlate to the spin-up, while the solid purple lines correspond to the spin-down. The Fermi level is set to zero.

band is moved downward relative to intrinsic $Cr_2Ge_2Te_6$. With $Cr_2G_2Te_6$@V and Co, the spin-down exhibits a similar pattern; the spin-down energy band is visibly moved down relative to the intrinsic $Cr_2G_2Te_6$, and the spin-up is evidently annihilated, showing that 3*d* transition metal and the substrate have a strong interaction. As shown in Figures 3B, F, the $Cr_2Ge_2Te_6$@Ti and Fe have similar energy band structures, but their spin-up energy bands are more severely destroyed, indicating more intense energy band hybridization. Both the spin-up and spin-down energy bands exhibit metallic properties with conductivity, indicating the transition from semiconducting to metallic of the system. In the $Cr_2G_2Te_6$@Mn (Figure 3E), although the spin-down and spin-up valence bands preserve most of the intrinsic energy bands, the conduction bands exhibit notable change, suggesting that the Mn interacts with the substrate quite significantly. Yet, both spin-up and spin-down energy bands preserve the semiconductor character, with a very narrow band gap of 0.07 eV and 0.65 eV, respectively, showing that the entire system offers the semiconducting. $Cr_2G_2Te_6$@Zn (Figure 3J) preserves the intrinsic $Cr_2G_2Te_6$ energy band in both the spin-down and spin-up energy bands, indicating a very weak interaction and monolayer $Cr_2G_2Te_6$. It still exhibits semiconducting, with a band gap of about 0.18 eV in the spin-up and 0.48 eV in the spin-down. We also find that the energy band is slightly shifted downward, showing that $Cr_2G_2Te_6$ receives electrons. Hence, monolayer $Cr_2G_2Te_6$ energy bands are significantly hybridized with 3*d* transition metal except for Zn absorbed. As such, according to the interaction between the transition metal and the substrate material, it can be divided into four categories: half metal ($Cr_2Ge_2Te_6$@Sc, $Cr_2Ge_2Te_6$@V, $Cr_2Ge_2Te_6$@Cr, $Cr_2Ge_2Te_6$@Co, $Cr_2Ge_2Te_6$@Ni, and $Cr_2Ge_2Te_6$@Cu); metal ($Cr_2Ge_2Te_6$@Ti and $Cr_2Ge_2Te_6$6@Fe); semiconductor ($Cr_2Ge_2Te_6$@Mn and $Cr_2Ge_2Te_6$@Zn).

After that, we investigate the density of states of the adsorbed system, shown in Supplementary Figure S2. It should come as no surprise that the density of states is found to be asymmetric. In $Cr_2Ge_2Te_6$@Sc, the spin-up energy band near the Fermi level comes mostly from the 3*d* orbitals of Sc and partially from the 3*d* orbitals of Cr. In $Cr_2Ge_2Te_6$@V, the density of states near the Fermi energy level is predominantly provided by the 3*d* orbitals of V. Moreover, a portion of the density of states comes from the 3*d* orbitals of the Cr

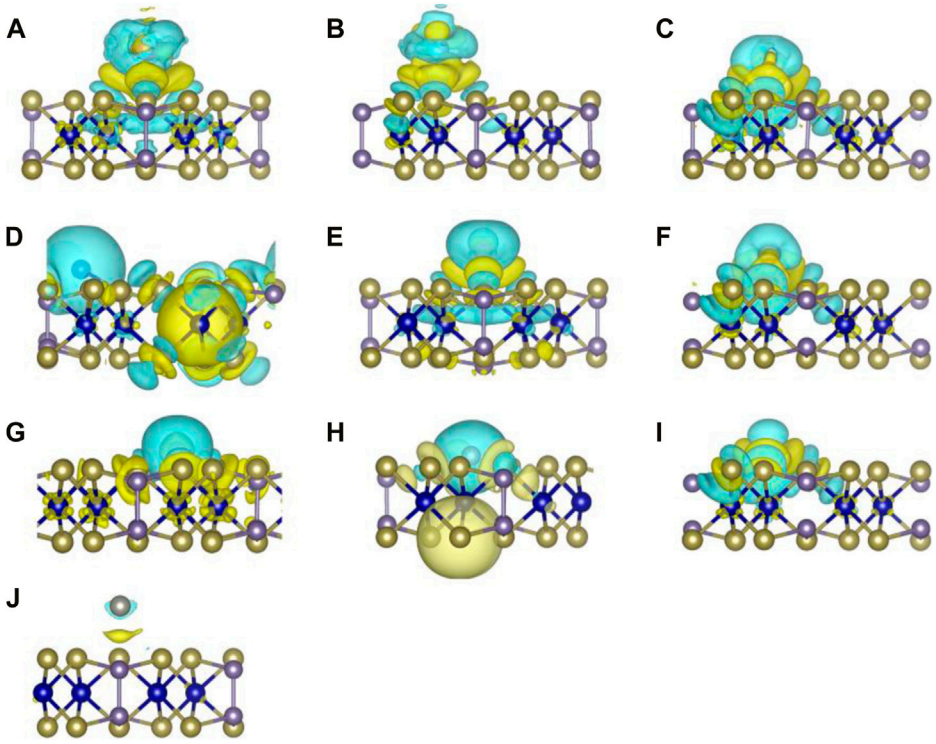

FIGURE 4
The differential charge density of **(A)** $Cr_2G_2Te_6$@Sc, **(B)** $Cr_2G_2Te_6$@Ti, **(C)** $Cr_2G_2Te_6$@V, **(D)** $Cr_2G_2Te_6$@Cr, **(E)** $Cr_2G_2Te_6$@Mn, **(F)** $Cr_2G_2Te_6$@Fe, **(G)** $Cr_2G_2Te_6$@Co., **(H)** $Cr_2G_2Te_6$@Ni, **(I)** $Cr_2G_2Te_6$@Cu, **(J)** $Cr_2G_2Te_6$@Zn. The isosurface value is set as 0.001 e/Å^3. Charge depletion (accumulation) is represented by the blue (yellow) isosurface in the graph.

atom that is close as well as the *p* orbitals of the Ge atom. It should be noted that the formation of half metal in $Cr_2Ge_2Te_6$@Co and Cu is exactly the same as in $Cr_2Ge_2Te_6$@V. In contrast, the half-metallic of $Cr_2Ge_2Te_6$@Ni is mostly due to the contribution of the 3*d* orbitals of Cr. Notably, $Cr_2Ge_2Te_6$@Cr exhibits half-metallic properties, mainly coming from the *d* orbitals of the Cr in the substrate. Its VBM in the spin-down channel results from the hybridization of the 3*d* orbitals of both the substrate and the adsorbed Cr and the *p* orbitals of the Ge atom. In $Cr_2Ge_2Te_6$@Ti and Fe, their metallic properties are mainly derived from the mutual hybridization between the Cr 3*d* orbitals, the Ge *p* orbitals, and the transition metal 3*d* orbitals. In both $Cr_2Ge_2Te_6$@Mn and $Cr_2Ge_2Te_6$@Zn, the conduction band bottom and valence band top at the Fermi plane are mainly contributed by the 3*d* orbitals of Cr atoms and partly by the *p* orbitals of Ge.

In order to get a comprehensive comprehension of the shifts in charge transfer that occur between 3*d* transition metals and monolayer $Cr_2Ge_2Te_6$, we carried out the differential charge density, as shown in Figure 4. We discovered that, with the exception of the charge that was transferred between the Zn and the monolayer $Cr_2Ge_2Te_6$, which was a very small amount, there was a large charge transfer in all of the other absorption systems. In addition, we used Bader charge [48] analysis to investigate the flow and magnitude of transferred charge between 3*d* transition metals and the monolayer $Cr_2Ge_2Te_6$. As shown in Supplementary Table S2, there is almost no charge transfer between Zn atom and the substrate, exactly in agreement with Figure 4J, indicating that the substrate material and transition metal interact weakly, matching the bandstructure (Figure 3J) and the very small adsorption energy (−0.07 eV). The charge transferred between Co and monolayer $Cr_2Ge_2Te_6$ is significantly more than that transferred in $Cr_2G_2Te_6$@Zn, as shown in Figure 4G. And the loss of charge accumulates near the Co, while the accumulation of charge clearly occurs at the surface of the monolayer $Cr_2Ge_2Te_6$, as well as slightly partial charge accumulation in the intermediate Cr atomic layer, indicating that strong chemical interaction between the Co atoms and monolayer $Cr_2Ge_2Te_6$, and a roughly 0.21 *e* loss of Co by Bader analysis. Furthermore, the charge transfer that occurs between Sc, Ti, V, Mn, Fe, and Cu and monolayer $Cr_2Ge_2Te_6$ is even much stronger, with charge loss occurring clearly around the 3*d* transition metals and charge accumulation apparently still present in the adsorbed intermediate region as well as around the surface and interlayer of monolayer $Cr_2Ge_2Te_6$. This suggests that the connection between the transition metals Sc, Ti, V, Mn, Fe, and Cu atoms and monolayer $Cr_2Ge_2Te_6$ is relatively robust and most likely involves chemisorption. Furthermore, in the $Cr_2Ge_2Te_6$@Cr and @Ni systems, the loss of charge occurs mainly around 3*d* transition metals, and electron accumulation is evident not only at the surface atoms of monolayer $Cr_2Ge_2Te_6$ but also more very evident on the Cr atom of the intermediate layer, suggesting equally strong hybridization in the absorbed system. In accordance with the Bader charge analysis, we conduct quantitative research to

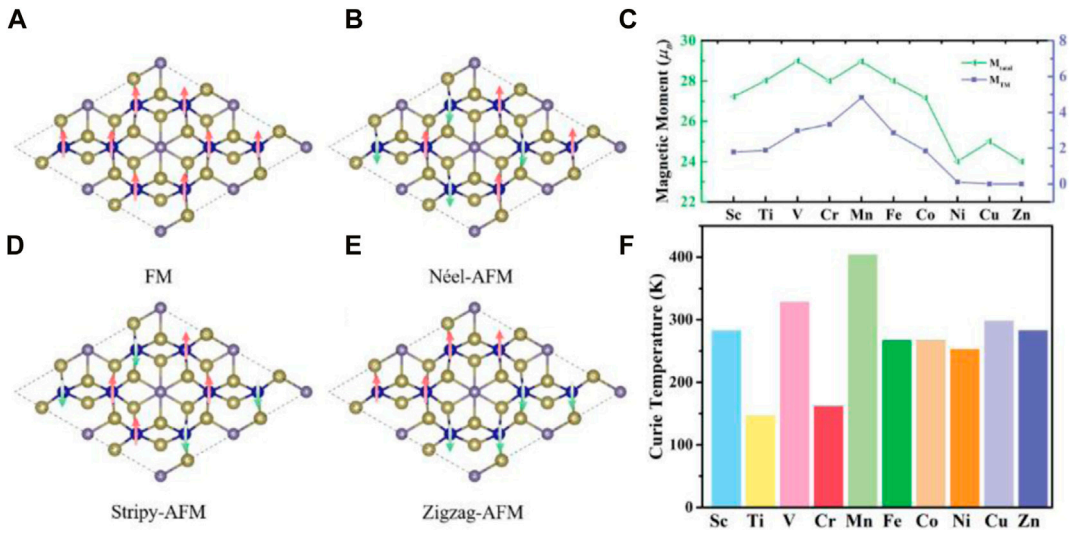

FIGURE 5
Schematics of four different magnetic structures: **(A)** FM, **(B)** Néel-AFM, **(C)** Stripy-AFM, and **(D)** Zigzag-AFM; **(E)** The total magnetic moment of the monolayer $Cr_2Ge_2Te_6$ absorbed with transition metals in the 2 × 2 supercell and the magnetic moment of transition metals in the monolayer $Cr_2Ge_2Te_6$ absorbed with transition metals. **(F)** The variation in the Curie temperature of monolayer $Cr_2Ge_2Te_6$ absorbed by conventional metals.

TABLE 1 The calculated total energy of the monolayer $Cr_2Ge_2Te_6$ absorbed the transition metals with four different magnetic configurations, the magnetic moment of the Cr atom near the absorption site (M_{Cr}), and the magnetic moment of transition metals in the monolayer $Cr_2Ge_2Te_6$ absorbed systems (M_{TM}).

TM-system	E_{FM}(eV)	$E_{Stripy\text{-}AFM}$(eV)	$E_{Zigzag\text{-}AFM}$(eV)	$E_{Néel\text{-}AFM}$(eV)	M_{Cr} (μ_B)	M_{TM} (μ_B)
Sc	−202.28	−201.06	−201.11	−200.78	3.38	1.78
Ti	−201.70	−200.75	−201.58	−201.52	3.42	1.88
V	−203.41	−203.13	−203.10	−203.00	3.58	2.97
Cr	−204.88	−204.65	−204.66	−204.67	3.34	3.34
Mn	−204.02	−203.72	−203.74	−203.50	3.33	4.83
Fe	−202.90	−202.64	−202.68	−202.58	3.47	2.86
Co.	−201.88	−201.32	−201.74	−201.55	3.51	1.85
Ni	−201.33	−201.14	−201.26	−201.01	3.35	0.11
Cu	−199.97	−199.79	−199.79	−199.60	3.58	0.00
Zn	−198.26	−198.06	−198.18	−197.93	3.35	0.00

determine the magnitude of the charge that is transmitted from the transition metal to the single layer $Cr_2Ge_2Te_6$. We discover that the number of transferred charges between Zn and monolayer $Cr_2Ge_2Te_6$ is very low, coming in at just 0.04 *e*, which suggests that the interaction between Zn and the substrate is relatively weak. Strong contact exists between monolayer $Cr_2Ge_2Te_6$ and the remainder of the 3*d* transition metals. The substrate $Cr_2Ge_2Te_6$ function as an acceptor to take up the lost electrons by the 3*d* transition metals. Just shown in Supplementary Table S2, the number of electrons transferred from Sc, Ti, V, Cr, Mn, Fe, Co, Ni, and Cu to monolayer $Cr_2Ge_2Te_6$ is 0.76, 0.65, 0.83, 0.71, 0.64, 0.40, 0.21, 0.54, and 0.39 *e*, respectively, indicating a significant increase in the number of charges transferred. This result lines up perfectly with the findings about the adsorption energy.

After that, we began to investigate how the adsorption of three-dimensional transition metals might affect the magnetic properties of a single layer of $Cr_2Ge_2Te_6$. In order to investigate the magnetic ground state of the monolayer $Cr_2Ge_2Te_6$ adsorbed with 3*d* transition metals, we took into account the four magnetic states that are depicted in Figures 5A–D. These states are, in order, ferromagnetic state, Néel-antiferromagnetic state, Stripy-antiferromagnetic state, and Zigzag-ferromagnetic state, respectively. As can be seen in Table 1, the ferromagnetic state is significantly lower after the adsorption of 3*d* transition metal compared to the other three magnetic states. This suggests that

the monolayer $Cr_2Ge_2Te_6$ absorbed with 3*d* transition metals is still relatively resistant in the ferromagnetic state. The ferromagnetic state is unaffected by the adsorption of 3*d* transition metals since it is an intrinsic magnetic state of the monolayer $Cr_2Ge_2Te_6$. In addition, we defined the energy difference between the Néel-antiferromagnetic and ferromagnetic states as ΔE_1:

$$\Delta E_1 = E(\text{Neel} - \text{AFM}) - E(\text{FM}) \quad (1)$$

where E (Neel-AFM) and E (FM) are the total energy of the absorbed system in the Néel-antiferromagnetic state and in the ferromagnetic state of the adsorbed transition metal, respectively. The energy difference of the ten absorbed systems is 1.50, 0.18, 0.41, 0.21, 0.52, 0.32, 0.33, 0.32, 0.37, and 0.34 eV, respectively. Clearly, there is a significant rise in the energy differences for adsorbed 3*d* transition metals. In an example, the energy difference of $Cr_2Ge_2Te_6$@Sc is about 1.50 eV, which is more than six times greater than the energy difference (ΔE_1 = 221.01 meV) of the pristine monolayer $Cr_2Ge_2Te_6$. Because of this, the results above indicate that the ferromagnetic state is the most stable for the absorbed system. Furthermore, the ferromagnetic state of the absorbed system is noticeably more stable when compared to the ferromagnetic state of the monolayer $Cr_2Ge_2Te_6$.

In the ferromagnetic state, the supercell 2 × 2 monolayer $Cr_2Ge_2Te_6$ with 8 Cr atoms, is expected to have a total magnetic moment of 24.00 μ_B. Furthermore, we calculated the magnetic moments of Cr near the optimal adsorption site (denoted by M_{Cr}) and the magnetic moments of the transition metals in the $Cr_2Ge_2Te_6$@TM adsorption system (represented by M_{TM}) separately. The findings are presented in Figure 5E. From Table 1, we can see that when 3*d* transition metals are absorbed, the magnetic moments of Cr near the optimal adsorption site do not vary, mainly in the range of 3.33–3.58 μ_B, which is significantly higher than 3.37 μ_B for monolayer $Cr_2Ge_2Te_6$. Among them, with the adsorption of V and Cu, the M_{Cr} reached a maximum of 3.58 μ_B; however, the M_{Cr} changed the least after adopting Mn, coming to 3.33 μ_B. On the other hand, we calculated the magnetic moments M_{TM} of the transition metals in the $Cr_2Ge_2Te_6$@TM adsorption system. And the results showed that from Sc to Zn atoms, the magnetic moments M_{TM} were 1.78, 1.88, 2.97, 3.34, 4.83 4.83, 2.86, 1.85, 0.11, 0.00和0.00 μ_B. The results are consistent with the results of Supplementary Figure S3. The 3*d* transition metals affect the magnetic properties of the adsorption system. In addition, we also calculated the total magnetic moments for the ten absorbed systems, as shown in Figure 5E. We discovered that the total magnetic moment first goes through an increase, then slightly decreases after the Cr adsorption, and then continues to increase again after Fe adsorption, all the way to the Zn, where the total magnetic moment falls; however, the decrease in the total magnetic moment for the Ni atom adsorption is greater than that for Cu atom adsorption. As we all know, the 4*s* orbitals from Sc to V are full of electrons, and the outermost 3*d* orbitals are unfilled with the number of electrons 3.00, 4.00, and 5.00 *e*. The total magnetic moments of the $Cr_2Ge_2Te_6$@Sc, Ti, and V systems are all integers, rising to 27.00, 28.00, and 29.00 μ_B in that sequence. This may be explained by the fact that the number of electrons in the outermost layer is connected to the total magnetic moments. When the Sc is absorbed, the total magnetic moments of $Cr_2Ge_2Te_6$@Sc increase by 3.00 μ_B, which coincides with the number of 4 *s*, 3*d* orbital electrons. In addition, from Mn to Co, the 4 *s* orbital is full of electrons, and the outermost 3*d* orbital is unfilled, with 5.00, 6.00, and 7.00 *e*, respectively. The total magnetic moments of the adsorbed systems of $Cr_2Ge_2Te_6$@Mn, $Cr_2Ge_2Te_6$@Fe, and $Cr_2Ge_2Te_6$@Co are also integers, decreasing linearly from a magnetic moment of 29.00 μ_B–27.00 μ_B, which is also related to the number of electrons in the outermost 3*d* orbitals. As we all know, the outermost 3*d* orbitals of Mn are arranged in 5.00 *e*. When Mn is adsorbed, the total magnetic moment of the $Cr_2Ge_2Te_6$@Mn reaches 29.00 μ_B. This is precisely 5.00 μ_B more than the total magnetic moment of the monolayer $Cr_2Ge_2Te_6$ without the adsorbed transition metal, which is 24.00 μ_B. This is due to the fact the outermost 3*d* orbitals of Mn have five unpaired electrons. Compared to 24.00 μ_B of the monolayer $Cr_2Ge_2Te_6$, the total magnetic moment of the $Cr_2Ge_2Te_6$@Fe is 28.00 μ_B, an increase of 4.00 μ_B. This can be interpreted as the Fe has 6 electrons in the outermost 3*d* orbitals but only 4 unpaired electrons. Compared to 29.00 μ_B for the $Cr_2Ge_2Te_6$@Mn, the total magnetic moment of the $Cr_2Ge_2Te_6$@Fe is reduced by 1.00 μ_B, and the total magnetic moment of the $Cr_2Ge_2Te_6$@Co adsorption system is reduced to 27.00 μ_B, which is likely to be the same reason. Since the 3*d* orbital of Cu is in the full electron state and the 4 *s* orbital is half full with only one electron, the total magnetic moment of the $Cr_2Ge_2Te_6$@Cu increases to 25.00 μ_B. Compared to 24.00 μ_B for a single layer of $Cr_2Ge_2Te_6$, the total magnetic moment of the $Cr_2Ge_2Te_6$@Cu increases by only 1 μ_B. Obviously, the magnetic moment of Zn, whose outermost 3*d* orbitals are in the full electron state, is zero; hence the total magnetic moment of the $Cr_2Ge_2Te_6$@Zn does not change.

On the other hand, we estimate the density of states of $Cr_2Ge_2Te_6$@TM shown in Figure 6. The total magnetic of the adsorption system is greater, the more asymmetric the spin-polarized density of states. It is noticeable that the spin-polarized density of states asymmetry becomes more and more pronounced with the absorption of Sc and V, indicating that $Cr_2Ge_2Te_6$@V has a greater total magnetic moment than that of $Cr_2Ge_2Te_6$@Sc. Similarly, the $Cr_2Ge_2Te_6$@Mn has a greater spin-polarized density of states asymmetry than the $Cr_2Ge_2Te_6$@Cu system, indicating a bigger total magnetic moment. While the asymmetry of the spin-polarized density of states of $Cr_2Ge_2Te_6$@Ni and $Cr_2Ge_2Te_6$@Zn is significantly weaker, so the total magnetic moments of these two transition metal adsorption systems are also the smallest. In order to investigate more progressively the origin of the total magnetic moment and magnetism of $Cr_2Ge_2Te_6$@TM, we also calculated the spin density distribution by the following equation:

$$\Delta\rho = \rho\uparrow - \rho\downarrow \quad (2)$$

Where $\Delta\rho$ is the spin density of $Cr_2Ge_2Te_6$@TM, $\rho\uparrow$ is the spin density in spin up and $\rho\downarrow$ is the spin density of spin down. Supplementary Figure S3 shows that the total magnetic moment mainly comes from the Cr of monolayer $Cr_2Ge_2Te_6$ and partly from the adsorbed 3*d* transition metals. In $Cr_2Ge_2Te_6$@Sc, Ti, V, Cr, Mn, Fe, and Co, the total magnetic moment mainly comes from transition metals; while for the adsorbed Ni, Cu, and Zn, the total magnetic moment is mainly derived from the Cr distribution of monolayer

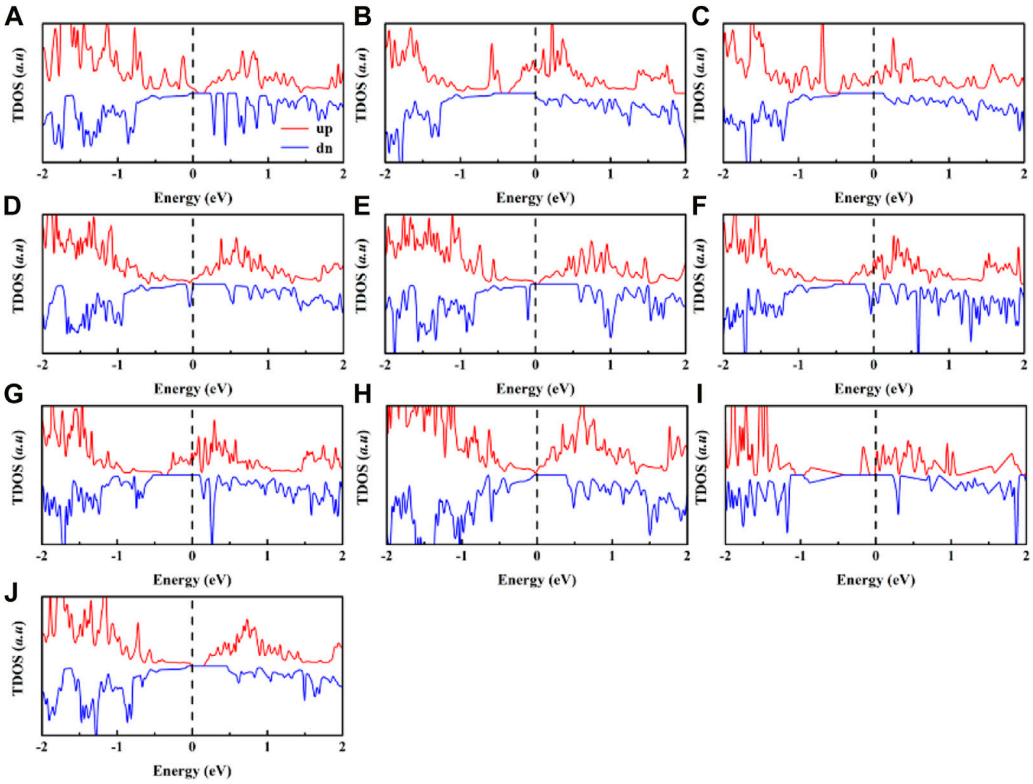

FIGURE 6
Spin-polarized total density of states in the **(A)** $Cr_2G_2Te_6$@Sc, **(B)** $Cr_2G_2Te_6$@Ti, **(C)** $Cr_2G_2Te_6$@V, **(D)** $Cr_2G_2Te_6$@Cr, **(E)** $Cr_2G_2Te_6$@Mn, **(F)** $Cr_2G_2Te_6$@Fe, **(G)** $Cr_2G_2Te_6$@Co., **(H)** $Cr_2G_2Te_6$@Ni, **(I)** $Cr_2G_2Te_6$@Cu, **(J)** $Cr_2G_2Te_6$@Zn. The Fermi level is set to zero.

$Cr_2Ge_2Te_6$. This result also agrees with the M_{TM} results of previously calculated transition metal magnetic moments.

In spintronic devices, the Curie temperature influences the transition temperature from ferromagnetic to paramagnetic and the stability of the ferromagnetic sequence. Calculating the Curie temperature of each adsorption system using Monte Carlo simulation is the next step to directly evaluate whether the ferromagnetic state coupling of the adsorbent system is improved. According to the literature [49, 50], based on the energy difference calculated above and Ising model simulations, we obtain the following expression for the spin exchange parameter *J*,

$$J = \Delta E_1 / 2NZS^2 \tag{3}$$

where N represents the number of magnetic atoms, Z represents the number of nearest neighbor magnetic atoms of Cr atoms, and ΔE_1 is the energy difference between the Néel-antiferromagnetic and ferromagnetic states that we calculated earlier. As shown in Figure 5F, the Curie temperatures of $Cr_2Ge_2Te_6$@Ti and Cr are slightly lower, around 150 K, while the Curie temperatures of other transition metal adsorption systems typically exceed 200 K. However, compared to that of the monolayer $Cr_2Ge_2Te_6$, the adsorption of 3*d* transition metals result in a significant increase in the Curie temperature of $Cr_2Ge_2Te_6$@TM and an improvement in the ferromagnetic coupling. According to the Goodenough-Kanamori rules [165,166], the ferromagnetic state coupling of monolayer $Cr_2Ge_2Te_6$ is the product of superexchange interaction and direct exchange interaction.

Since the bond length between Cr-Cr of the $Cr_2Ge_2Te_6$@TM system is relatively large, about 4.10 Å and the direct exchange interaction is mainly by the direct electron hopping of two adjacent Cr atoms showing the antiferromagnetic coupling, their direct exchange interaction is relatively weak. It is well knowledge that the superexchange contact will have a greater propensity to display ferromagnetic coupling. The superexchange interaction in the adsorbed system is generated by the Te atom acting as an intermediate anion. Since the bond angle of Cr-Te-Cr is mostly around 90°, this results in a more powerful superexchange interaction. Hence, the struggle between the two exchange interactions leads to the dominance of superexchange interactions in the adsorption system, which shows ferromagnetic coupling as a consequence. In view of this, the adsorption of 3*d* transition metals by the monolayer $Cr_2Ge_2Te_6$ leads to the enhancement of the ferromagnetic state. After that, we also define the Curie temperature increasing rate ε for the adsorption system by equation,

$$\varepsilon = \frac{Tc(Cr_2Ge_2Te_6@TM) - Tc(Cr_2Ge_2Te_6)}{Tc(Cr_2Ge_2Te_6)} \times 100\% \tag{4}$$

According to our calculation, the Curie temperature enhancement ratio of $Cr_2Ge_2Te_6$@TM reaches 224%, 68%, 277%,

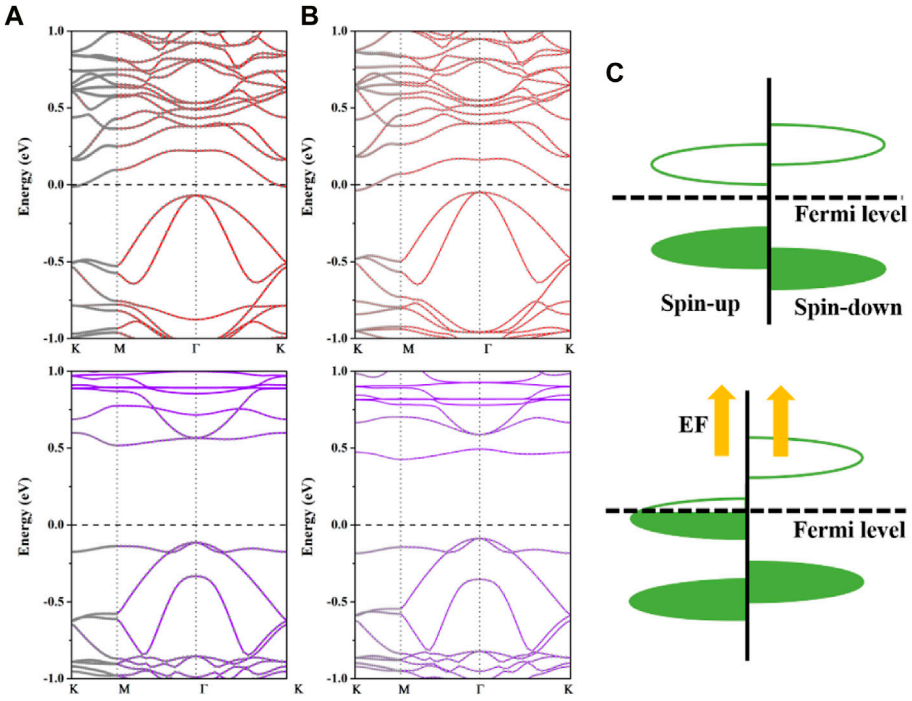

FIGURE 7
The calculated projected spin-up and spin-down band structures of $Cr_2Ge_2Te_6$@Mn with electric fields of **(A)** 0.1 and **(B)** 0.6 V/Å. In the band structures, the solid red lines correlate to the spin-up, while the solid purple lines correspond to the spin-down. The solid grey circles in the spin-up and spin-down band structures correspond to the contribution from the $Cr_2Ge_2Te_6$ layer. The Fermi level is set to zero. **(C)** A schematic illustration of the electric field-induced transition from a ferromagnetic semiconductor to a half metal.

85%, 367%, 207%, 207%, 190%, 242%, and 224%, respectively. All adsorbed transition metals improved their Curie temperatures by a factor of 2, with the exception of Ti and Cr atoms, whose adsorption Curie temperature improvement was less than 100%, suggesting that transition metals may dramatically increase their Curie temperatures.

In addition, we study how the electric field modulates the electrical characteristics of the adsorption system. According to earlier research, the $Cr_2Ge_2Te_6$@Mn system is a semiconductor; thus, we choose this system as an example and apply a positive electric field, that is, an electric field directed from the $Cr_2Ge_2Te_6$ to the adsorbed atoms. We discovered that the application of an additional positive electric field has a considerable influence on the electronic properties of the $Cr_2Ge_2Te_6$@Mn, particularly the spin-polarized electronic states of the monolayer $Cr_2Ge_2Te_6$. The calculated projected spin-up and spin-down band structures of the $Cr_2Ge_2Te_6$@Mn adsorption system under 0.10 and 0.60 V/Å electric fields are shown in Figures 7A, B, respectively. After applying the electric field, the spin-up energy band extended all the way to the Fermi level, whereas the spin-down energy band remained semiconducting. This caused a spin-polarization current with a spin-polarization rate of 100% at the Fermi level. In addition, compared to the energy band of the intrinsic monolayer $Cr_2Ge_2Te_6$, the conduction band in the spin-up channel of $Cr_2Ge_2Te_6$@Mn moves increasingly downward with an increasing positive electric field, suggesting that as its magnitude increases, the electric field increasingly impacted the conduction band in the spin-up channel. Consequently, the applied positive electric field transforms $Cr_2Ge_2Te_6$@Mn from a semiconductor to a half-metal, suggesting that the applied electric field has a distinct benefit in managing the electronic and magnetic properties of the absorbed system. In other words, as seen in Figure 7C, the applied positive electric field causes more charges initially localized in a certain energy band to shift in relative positions. Once the energy band at these positions crosses the Fermi energy level under the influence of the electric field, the materials also transform into a half-metal, i.e., one spin-up electronic state moves downward across the Fermi plane, while the electric field has little effect on the other spin-down electronic state, thus achieving a modulation of the electronic and magnetic properties of the absorbed system.

Conclusion

In conclusion, based on first-principles calculation, the electronic and magnetic properties of the monolayer $Cr_2Ge_2Te_6$ absorbed with 3*d* transition metal atoms have been investigated. Based on the calculated absorption energy, equilibrium absorption distance, and charge redistribution, the monolayer $Cr_2Ge_2Te_6$ absorbed Zn *via* a weak interaction. At the same time, the rest of the 3*d* transition metals are fascinated with the substrate *via* a strong interaction. Our results show that $Cr_2Ge_2Te_6$@TM can possess

different electronic properties. We found that the adsorption of Ti and Fe leads to a transformation from semiconductor to metal. While in $Cr_2Ge_2Te_6$@Sc, V, Co, Ni, and Cu, one of their spin energy bands appears to be metallic, the other spin energy band remains semiconductor, so the absorption realizes the changes from semiconductor to half metal. Furthermore, the ferromagnetic coupling is the most stable state in $Cr_2Ge_2Te_6$@TM, and their respective Curie temperatures are greatly enhanced by adsorption, demonstrating that adsorption may effectively boost the ferromagnetic state of monolayer $Cr_2Ge_2Te_6$. This relates to the outcome of the competition between direct exchange and superexchange. This research demonstrates a feasible method for not only modifying the electrical characteristics of the monolayer $Cr_2Ge_2Te_6$ but also enhancing their ferromagnetic stability. We are certain that this method can be experimentally achieved in the near future, which will considerably ease the deployment of CGT in nanoelectronic and spintronic devices.

Data availability statement

The original contribution presented in the study are included in the article/Supplementary Material, further inquiries can be directed to the corresponding author.

Author contributions

WK completed the computational analysis related to the paper and wrote the manuscript. XD and others helped me to check the grammatical problems of the manuscript and the corrections of the related icons.

Funding

This work was supported by the Natural Science Foundation of Chongqing (Grant No. cstc2020jcyj-msxmX0686), the Fundamental Research Funds for the Central Universities (2020CDJ-LHZZ-073), the National Natural Science Foundation of China (11674042), and the Thousand Youth Talents Program of China.

Conflict of interest

The authors declare that the research was conducted in the absence of any commercial or financial relationships that could be construed as a potential conflict of interest.

The reviewer ZW declared a shared affiliation with the author(s) to the handling editor at the time of review.

Publisher's note

Supplementary material

The Supplementary Material for this article can be found online at: https://www.frontiersin.org/articles/10.3389/fphy.2023.1188513/full#supplementary-material

References

1. Novoselov KS, Geim AK, Morozov SV, Jiang D, Zhang Y, Dubonos SV, et al. Electric field effect in atomically thin carbon films. *Science* (2004) 306:666–9. doi:10.1126/science.1102896

2. Geim AK, Novoselov KS. The rise of graphene. *Nat Mater* (2007) 6:183–91. doi:10.1038/nmat1849

3. Mannix AJ, Zhang Z, Guisinger NP, Yakobson BI, Hersam MC. Borophene as a prototype for synthetic 2D materials development. *Nat Nanotechnol* (2018) 13:444–50. doi:10.1038/s41565-018-0157-4

4. Manzeli S, Ovchinnikov D, Pasquier D, Yazyev OV, Kis A. 2D transition metal dichalcogenides. *Nat Rev Mater* (2017) 2:17033. doi:10.1038/natrevmats.2017.33

5. Kong X, Liu Q, Zhang C, Peng Z, Chen Q. Elemental two-dimensional nanosheets beyond graphene. *Chem Soc Rev* (2017) 46:2127–57. doi:10.1039/c6cs00937a

6. Geim AK. Graphene: Status and prospects. *Science* (2009) 324:1530–4. doi:10.1126/science.1158877

7. Liu J, Huang CC, Wang Y, Yao Q, Wang LY, Li DF. A promising robust intrinsic half-metallic MXene nanosheet Cr_2CuC_2 with high Curie temperature. *Phys E Low-dimens Syst Nanostructures* (2022) 143:115276. doi:10.1016/j.physe.2022.115276

8. Huang C-C, Wang Y, Yao Q, Li D-F, Liu J. MXene monolayer Mn_2ZnN_2: A promising robust intrinsic half-metallic nanosheet. *J Phys Condens Matter* (2022) 34:105301. doi:10.1088/1361-648x/ac3cb3

9. Liu J, Wang Y, Wang LY, Yao Q, Huang CC, Huang HY, et al. Several promising non-vdW multiferroic half-metallic nanosheets ACr_2S_4 (A = Li, Na, K, Rb): The first-principles researches. *Eur Phys J Plus* (2023) 138:224. doi:10.1140/epjp/s13360-023-03789-6

10. Sivadas N, Daniels MW, Swendsen RH, Okamoto S, Xiao D. Magnetic ground state of semiconducting transition-metal trichalcogenide monolayers. *Phys Rev B* (2015) 91:235425. doi:10.1103/physrevb.91.235425

11. Wang K, Ren K, Cheng Y, Chen S, Zhang G. The impacts of molecular adsorption on antiferromagnetic $MnPS_3$ monolayers: Enhanced magnetic anisotropy and intralayer dzyaloshinskii–moriya interaction. *Mater Horiz* (2022) 9:2384–92. doi:10.1039/d2mh00462c

12. Long G, Henck H, Gibertini M, Dumcenco D, Wang Z, Taniguchi T, et al. Persistence of magnetism in atomically thin $MnPS_3$ crystals. *Nano Lett* (2020) 20:2452–9. –9. doi:10.1021/acs.nanolett.9b05165

13. Lin M-W, Zhuang HL, Yan J, Ward TZ, Puretzky AA, Rouleau CM, et al. Ultrathin nanosheets of $CrSiTe_3$: A semiconducting two-dimensional ferromagnetic material. *J Mater Chem C* (2016) 4:315–22. –22. doi:10.1039/c5tc03463a

14. Casto LD, Clune AJ, Yokosuk MO, Musfeldt JL, Williams TJ, Zhuang HL, et al. Strong spin-lattice coupling in $CrSiTe_3$. *APL Mater* (2015) 3:041515. doi:10.1063/1.4914134

15. Huang B, Clark G, Navarro-Moratalla E, Klein DR, Cheng R, Seyler KL, et al. Layer-dependent ferromagnetism in a van der Waals crystal down to the monolayer limit. *Nature* (2017) 546:270–3. doi:10.1038/nature22391

16. Carteaux V, Brunet D, Ouvrard G, Andre G. Crystallographic, magnetic and electronic structures of a new layered ferromagnetic compound $Cr_2Ge_2Te_6$. *J Phys Condens Matter* (1995) 7:69–87. doi:10.1088/0953-8984/7/1/008

17. Gong C, Li L, Li Z, Ji H, Stern A, Xia Y, et al. Discovery of intrinsic ferromagnetism in two-dimensional van der Waals crystals. *Nature* (2017) 546:265–9. doi:10.1038/nature22060

18. Li X, Yang J. $CrXTe_3$ (X = Si, Ge) nanosheets: Two dimensional intrinsic ferromagnetic semiconductors. *J Mater Chem C* (2014) 2:7071. –6. doi:10.1039/c4tc01193g

19. Wolf SA, Awschalom DD, Buhrman RA, Daughton JM, von Molnár S, Roukes ML, et al. Spintronics: A spin-based electronics vision for the future. *Science* (2001) 294:1488–95. doi:10.1126/science.1065389

20. Tu NT, Hai PN, Anh LD, Tanaka M. High-temperature ferromagnetism in heavily Fe-doped ferromagnetic semiconductor (Ga,Fe)Sb. *Appl Phys Lett* (2016) 108:192401. doi:10.1063/1.4948692

21. Yazyev OV, Helm L. Defect-induced magnetism in graphene. *Phys Rev B* (2007) 75:125408. doi:10.1103/physrevb.75.125408

22. Červenka J, Katsnelson MI, Flipse CFJ. Room-temperature ferromagnetism in graphite driven by two-dimensional networks of point defects. *Nat Phys* (2009) 5:840–4. –4. doi:10.1038/nphys1399

23. Naji S, Belhaj A, Labrim H, Bhihi M, Benyoussef A, El Kenz A. Adsorption of Co and Ni on graphene with a double hexagonal symmetry: Electronic and magnetic properties. *J Phys Chem C* (2014) 118:4924–9. –9. doi:10.1021/jp407820a

24. Wang H, Zhu S, Fan F, Li Z, Wu H. Structure and magnetism of Mn, Fe, or Co adatoms on monolayer and bilayer black phosphorus. *J Magn Magn Mater* (2016) 401: 706–10. –10. doi:10.1016/j.jmmm.2015.10.131

25. Lu Y, Ke C, Fu M, Lin W, Zhang C, Chen T, et al. Magnetic modification of GaSe monolayer by absorption of single Fe atom. *RSC Adv* (2017) 7:4285–90. –90. doi:10.1039/c6ra27309b

26. Ilyas A, Wu H, Usman T, Khan SA, Deng R. The induction of half-metallicity and enhanced ferromagnetism in a $Cr_2Ge_2Te_6$ monolayer via electron doping and alkali metal adsorption. *J Mater Chem C* (2021) 9:5952–60. doi:10.1039/d1tc00006c

27. Kresse G, Furthmüller J. Efficient iterative schemes for *ab initio* total-energy calculations using a plane-wave basis set. *Phys Rev B* (1996) 54:11169–86. doi:10.1103/physrevb.54.11169

28. Kresse G, Furthmüller J. Efficiency of *ab-initio* total energy calculations for metals and semiconductors using a plane-wave basis set. *Comput Mater Sci* (1996) 6:15–50. doi:10.1016/0927-0256(96)00008-0

29. Blöchl PE. Projector augmented-wave method. *Phys Rev B* (1994) 50:17953–79. doi:10.1103/physrevb.50.17953

30. Kresse G, Joubert D. From ultrasoft pseudopotentials to the projector augmented-wave method. *Phys Rev B* (1999) 59:1758–75. doi:10.1103/physrevb.59.1758

31. Perdew JP, Burke K, Ernzerhof M. Generalized gradient approximation made simple. *Phys Rev Lett* (1996) 77:3865–8. –8. doi:10.1103/physrevlett.77.3865

32. Monkhorst HJ, Pack JD. Special points for Brillouin-zone integrations. *Phys Rev B* (1976) 13:5188–92. doi:10.1103/physrevb.13.5188

33. Grimme S, Antony J, Ehrlich S, Krieg H. A consistent and accurate *ab initio* parametrization of density functional dispersion correction (DFT-D) for the 94 elements H-Pu. *J Chem Phys* (2010) 132:154104. doi:10.1063/1.3382344

34. Grimme S. Semiempirical GGA-type density functional constructed with a long-range dispersion correction. *J Comput Chem* (2006) 27:1787–99. doi:10.1002/jcc.20495

35. Jiang P, Wang C, Chen D, Zhong Z, Yuan Z, Lu Z-Y, et al. Stacking tunable interlayer magnetism in bilayer CrI_3. *Phys Rev B* (2019) 99:144401. doi:10.1103/physrevb.99.144401

36. Tang C, Zhang L, Sanvito S, Du A. Electric-controlled half-metallicity in magnetic van der Waals heterobilayer. *J Mater Chem C* (2020) 8:7034–40. doi:10.1039/d0tc01541e

37. Chen S, Huang C, Sun H, Ding J, Jena P, Kan E. Boosting the Curie temperature of two-dimensional semiconducting CrI_3 monolayer through van der Waals heterostructures. *J Phys Chem C* (2019) 123:17987–93. doi:10.1021/acs.jpcc.9b04631

38. Liu M, Chen Q, Huang Y, Cao C, He Y. A first-principles study of transition metal doped arsenene. *Superlattices Microstruct* (2016) 100:131–41. doi:10.1016/j.spmi.2016.09.014

39. Zhang J, Zhao B, Yao Y, Yang Z. Robust quantum anomalous Hall effect in graphene-based van der Waals heterostructures. *Phys Rev B* (2015) 92:165418. doi:10.1103/physrevb.92.165418

40. Liechtenstein AI, Anisimov VI, Zaanen J. Density-functional theory and strong interactions: Orbital ordering in Mott-Hubbard insulators. *Phys Rev B* (1995) 52: R5467–70. doi:10.1103/physrevb.52.r5467

41. Tang C, Zhang L, Du A. Tunable magnetic anisotropy in 2D magnets *via* molecular adsorption. *J Mater Chem C* (2020) 8:14948–53. doi:10.1039/d0tc04049e

42. Xing W, Chen Y, Odenthal PM, Zhang X, Yuan W, Su T, et al. Electric field effect in multilayer Cr2Ge2Te6: A ferromagnetic 2D material. *arXiv* (2017) 4:024009. doi:10.48550/arXiv.1704.08862

43. Wang H, Qi J, Qian X. Electrically tunable high Curie temperature two-dimensional ferromagnetism in van der Waals layered crystals. *Appl Phys Lett* (2020) 117:083102. doi:10.1063/5.0014865

44. Tang X, Fan D, Guo L, Tan H, Wang S, Lu X, et al. Achieving higher thermoelectric performance for p-type $Cr_2Ge_2Te_6$ via optimizing doping. *Appl Phys Lett* (2018) 113:263902. doi:10.1063/1.5064787

45. Li X, Wu X, Li Z, Yang J, Hou JG. Bipolar magnetic semiconductors: A new class of spintronics materials. *Nanoscale* (2012) 4:5680. –5. doi:10.1039/c2nr31743e

46. Kang S, Kang S, Yu J. Effect of coulomb interactions on the electronic and magnetic properties of two-dimensional $CrSiTe_3$ and $CrGeTe_3$ materials. *J Electron Mater* (2019) 48:1441–5. –5. doi:10.1007/s11664-018-6601-2

47. Suzuki M, Gao B, Koshiishi K, Nakata S, Hagiwara K, Lin C, et al. Coulomb-interaction effect on the two-dimensional electronic structure of the van der Waals ferromagnet $Cr_2Ge_2Te_6$. *Phys Rev B* (2019) 99:161401. doi:10.1103/physrevb.99.161401

48. Clarendon Richard FWB. A theory of molecules: Atoms in molecules. A quantum theory. *Science* (1991) 5012:1566–7.

49. Naji S, Belhaj A, Labrim H, Bhihi M, Benyoussef A, El Kenz A. Electronic and magnetic properties of iron adsorption on graphene with double hexagonal geometry. *Int J Quan Chem.* (2014) 114:463–7. –7. doi:10.1002/qua.24592

50. El Hallani F, Naji S, Ez-Zahraouy H, Benyoussef A. First-principles study of the magnetic stability and the exchange couplings of $LaMn_2O_5$. *J Appl Phys* (2013) 114: 163909. doi:10.1063/1.4826263

Frontiers in Physics

Investigates complex questions in physics to understand the nature of the physical world

Addresses the biggest questions in physics, from macro to micro, and from theoretical to experimental and applied physics.

Discover the latest Research Topics

See more →

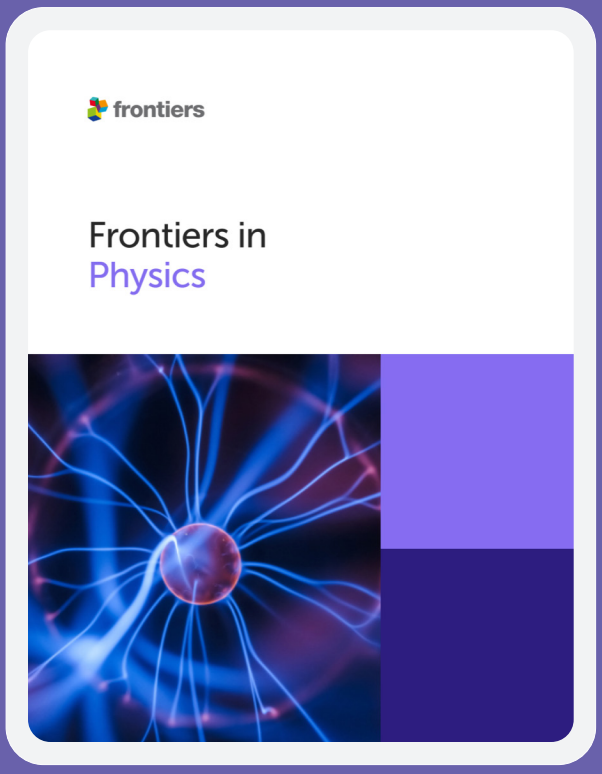

Frontiers

Avenue du Tribunal-Fédéral 34
1005 Lausanne, Switzerland
frontiersin.org

Contact us

+41 (0)21 510 17 00
frontiersin.org/about/contact